CENTRO INTERNACIONAL DE ESTUDOS
DE DOUTORAMENTO E AVANZADOS
DA USC (CIEDUS)

TESE DE DOUTORAMENTO

Characterisation and Optimisation of Radiation-Tolerant Silicon Sensors with Intrinsic Gain

Sofía Otero Ugobono

ESCOLA DE DOUTORAMENTO INTERNACIONAL

PROGRAMA DE DOUTORAMENTO EN FÍSICA NUCLEAR E DE PARTÍCULAS

SANTIAGO DE COMPOSTELA

2018

USC
UNIVERSIDADE
DE SANTIAGO
DE COMPOSTELA

UNIVERSIDADE DE SANTIAGO DE COMPOSTELA

Declaración da Autora da Tese

Characterisation and Optimisation of Radiation-Tolerant Silicon Sensors with Intrinsic Gain

Dna. Sofía Otero Ugobono

Presento a miña tese, seguindo o procedemento axeitado ao Regulamento, e declaro que:

1. A tese abarca os resultados da elaboración do meu traballo.
2. De selo caso, na tese faise referencia ás colaboracións que tivo este traballo.
3. A tese é a versión definitiva presentada para a súa defensa e coincide coa versión enviada en formato electrónico.
4. Confirmo que a tese non incorre en ningún tipo de plaxio doutros autores nin de traballos presentados por min para a obtención doutros títulos.

En Xenebra, 24 de xullo de 2018

Asdo.
Sofía Otero Ugobono

USC
UNIVERSIDADE
DE SANTIAGO
DE COMPOSTELA

Autorización do Director/Titor da Tese

Characterisation and Optimisation of Radiation-Tolerant Silicon Sensors with Intrinsic Gain

Dn. Abraham Antonio Gallas Torreira
Dn. Michael Moll

INFORMAN:

Que a presente tese, correspóndese co traballo realizado por Dna. Sofía Otero Ugobono, baixo a nosa dirección, e autorizamos a súa presentación, considerando que reúne os requisitos esixidos no Regulamento de Estudos de Doutoramento da USC, e que como directores desta non incorre nas causas de abstención establecidas na Lei 40/2015.

En Xenebra, 24 de xullo de 2018

Asdo.
Abraham Antonio Gallas Torreira

Asdo.
Michael Moll

USC
UNIVERSIDADE
DE SANTIAGO
DE COMPOSTELA

Si quelqu'un aime une fleur qui n'existe qu'à un exemplaire dans les millions et les millions d'étoiles, ça suffit pour qu'il soit heureux quand il les regarde. Il se dit: "Ma fleur est là quelque part..." Mais si le mouton mange la fleur, c'est pour lui comme si, brusquement, toutes les étoiles s'éteignaient!

Antoine de Saint-Exupéry, *Le Petit Prince*

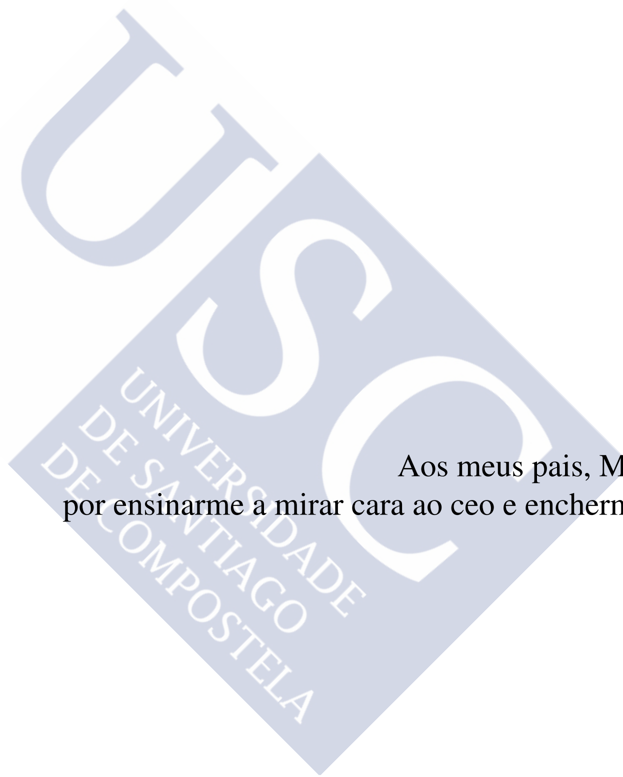

Aos meus pais, Mónica e Ariel,
por ensinarme a mirar cara ao ceo e enchermo de estrelas.

USC
UNIVERSIDADE
DE SANTIAGO
DE COMPOSTELA

Acknowledgements

I would like to dedicate a few lines to all the people without whom this PhD thesis would not have been possible. My apologies to anyone I may have inadvertently omitted.

First and foremost, I am grateful to my supervisors, **Michael Moll** and **Abraham Gallas Torreira**, for their support and guidance throughout this journey. Michael, thank you very much for mentoring me, and for giving me the opportunity to be part of the SSD team and the RD50 Collaboration. Abraham, I want to thank you for your continuous support, and for introducing me to the wonderful world of detector physics.

I want to thank **Matteo Centis Vignali**, **Marcos Fernández García**, and **Christian Gallrapp** for the many hours they dedicated to teach me, and to help me make sense of some of the rather puzzling results that appeared along the way. I do not owe you just a few beers but an entire brewery.

A sincere, warm, and cake-full thank you to everyone in the **SSD team**. You have always been, and remain to be, a constant source of knowledge, encouragement, support, and cheerfulness. These past three years would not have been half as wonderful if it were not for all of you.

My deepest gratitude to **CERN** for granting me the opportunity of carrying out the entirety of my PhD research work within the organisation. This experience has been unique from a professional, and a personal point of view. I am also grateful for the financial support provided by the European Union's **AIDA2020** project, which was essential for conducting all irradiation campaigns.

I would also like to show my appreciation to **Salvador Hidalgo Villena**, **Giulio Pellegrini**, and **María del Mar Carulla Areste** from CNM-Barcelona; and to **Mickel McClish** from RMD for providing me, not only with the sensors for my thesis, but also with valuable information regarding the devices that I could not have otherwise obtained.

Special thanks to everyone at the EP/DT Bond Lab, particularly to **Florentina Manolescu** for her assistance throughout these past three years, and her patience during the many hectic weeks of bonding and re-bonding irradiated samples. I also wish to thank **Jacopo Bronuzzi** and **Alessandro Mapelli** for their invaluable help during the planning and execution of clean-room operations at CMi-EPFL.

I must also thank **Iván Vila Álvarez**, **Sebastian White**, and **Rogelio Palomo Pinto** for their insightful comments on my work. I would also like to extend my gratitude to everyone within the **RD50 Collaboration** for their constructive feedback during these years. It has been an honour to be part of RD50.

Thanks should also go to **Veronique Wedlake**, and **Elvira Canosa Villar** for helping me sail through all the paperwork.

None of this work would have been possible without the unconditional support of friends and family. **Laura**! How can I possibly thank you for being the best office mate one could possibly ask for? I will miss you more than you can imagine. Thank you for the chats, the laughs, the tears, the hugs, and the support. I don't know where life will take us, but wherever we go my home will always have a place for you, and an oven for your pizzas! Grazie!

Moitísimas grazas a **Brais**, **Miguel**, **Pablo** e **Dani** por tódolos momentos compartidos dende que cheguei a Santiago.

Tamén lle quero dar as grazas a **Gonssa** por saber sacarme un sorriso mesmo nos momentos máis difíciles. Grazas: porque sei que sempre podo confiar en ti e porque aínda aturas os meus chistes malos.

Desexo, así mesmo, expresalo meu máis sincero agradecemento a **José Manuel Sánchez de Santos** por tódala axuda que me brindou no meu particular *camiño de Santiago*.

No quiero olvidarme de darle las gracias a **José Edelstein**. Cómo puedo agradecerte toda la ayuda que me brindaste desde antes siquiera de venir a Santiago. No sólo jugaste un papel fundamental en que pudiera cumplir mi sueño de estudiar acá, sino que también me ayudaste a sobrellevar mis primeros meses lejos de casa.

A mi abuelo, **Julio**, gracias por estar siempre ahí, porque siempre supe que podía contar con vos y por acompañarme incluso en la distancia. A mi tía, **Edit**, por ser como una hermana para mí y por demostrarme que, por muchos obstáculos que la vida te ponga por delante, siempre hay que seguir avanzando. ¡Te quiero mucho, Edu!

Por último, gracias a mis padres, **Mónica** y **Ariel**, por siempre creer en mi y motivarme a seguir mi propio camino. Por nunca poner en duda mis sueños y por ayudarme a hacerlos realidad. Porque siempre supe que, pasara lo que pasara, podía contar con un abrazo de ustedes y todo iba a estar mejor. Si llegué hasta acá es en buena medida gracias a todo el esfuerzo que ustedes hicieron y al apoyo incondicional que me brindaron. Ari, por desgracia nunca vas a leer estas palabras, pero me consuelo con saber que si estuvieras acá tendrías una sonrisa de oreja a oreja.

Finally, I cannot but conclude by quoting the wise words of Gustavo Cerati,

Gracias totales.

USC UNIVERSIDADE DE SANTIAGO DE COMPOSTELA

Contents

Resumo v

Abstract xiii

List of Figures xv

List of Tables xxv

1 Introduction 1

2 Silicon Detectors 3

2.1 Energy bands in a semiconductor 4

2.2 Intrinsic carrier concentration at thermal equilibrium 4

2.3 Extrinsic silicon: donors and acceptors 6

2.4 PN-junction 7

2.4.1 Capacitance 9

2.5 Charge collection 9

3 Radiation Damage 11

3.1 Surface damage 11

3.2 Bulk damage 13

3.2.1 NIEL-scaling hypothesis 15

3.2.2 Trapping 17

USC UNIVERSIDADE DE SANTIAGO DE COMPOSTELA

3.2.3 Space charge sign inversion 19
3.2.4 Annealing 21
3.2.5 Acceptor removal 23
3.3 Leakage current 25
3.3.1 Dependence with fluence 25
3.3.2 Dependence with temperature 25

4 Experimental Techniques **27**
4.1 CV/IV measurements 27
4.1.1 Probe station 31
4.1.2 Climate chamber 33
4.2 Transient Current Technique 33
4.2.1 TCT+ set-up 34
4.3 Two-Photon Absorption TCT 41
4.4 Radioactive source measurements 43
4.5 Irradiation facilities 46
4.5.1 PS-IRRAD Proton Facility at CERN 46
4.5.2 TRIGA Mark III reactor at IJS 46

5 4D Tracking **47**
5.1 Acquisition of timing information 49
5.1.1 Timing at each point 49
5.1.2 Timing in the event reconstruction 49
5.2 Timing considerations 51
5.2.1 Time resolution 51
5.2.2 Detector requirements for timing 54

USC UNIVERSIDADE DE SANTIAGO DE COMPOSTELA

6 Silicon Detectors with Intrinsic Gain **57**

6.1 Low Gain Avalanche Detectors 61

6.2 Deep Diffused Avalanche Particle Detectors 63

7 Characterisation of LGADs **67**

7.1 Capacitance and leakage current 68

7.1.1 Capacitance 68

7.1.2 Leakage current 73

7.2 Homogeneity analysis 77

7.3 Charge collection with voltage 84

7.3.1 ^{90}Sr voltage scans 84

7.3.2 TCT voltage scans 86

7.4 Gain study 96

7.5 Detailed study of samples irradiated up to 10^{14} n_{eq}/cm^2 101

7.5.1 Waveforms at different temperatures 101

7.5.2 Leakage current 105

7.5.3 Annealing and influence of the guard ring on TCT scans 105

7.5.4 Characterisation of the electric field 110

8 Characterisation of DD-APDs **115**

8.1 First Set of 2×2-mm^2 DD-APDs 116

8.1.1 Homogeneity analysis 117

8.1.2 Charge collection with voltage 121

8.1.3 Capacitance 124

8.1.4 Leakage current 124

8.2 Second Set of 2×2-mm^2 DD-APDs 129

USC UNIVERSIDADE DE SANTIAGO DE COMPOSTELA

8.2.1 Homogeneity analysis 130
8.2.2 Charge collection with voltage 136
8.2.3 Capacitance 142
8.2.4 Leakage current 143
8.3 8×8-mm^2 DD-APDs 149

9 Conclusions **155**

Appendices **163**

Appendix A Silicon crystal growth **165**

Appendix B LGADs and PiN diodes: waveforms at different temperatures **169**

Appendix C Optical effects caused by glue on 2×2-mm^2 DD-APDs **179**

Appendix D About voltage scans on 2×2-mm^2 DD-APDs with very high gain **181**

Appendix E IV curves of 2×2-mm^2 DD-APDs at different temperatures **187**

Bibliography **193**

USC UNIVERSIDADE DE SANTIAGO DE COMPOSTELA

Resumo

Esta tese, realizada no marco da Colaboración RD50 e do Programa de Estudos do Doutoramento do CERN (dentro do equipo EP-DT-DD SSD), ten como obxectivo principal contribuír á investigación e desenvolvemento de sensores de silicio tolerantes a radiación para a actualización a altas luminosidades do Gran Colisionador de Hadróns do CERN (HL-LHC). Este traballo vai en paralelo cos numerosos esforzos realizados por ATLAS, CMS, RD50 e outros proxectos de I+D que desenvolven dispositivos capaces de soportar os niveis de radiación previstos no HL-LHC, que chegarán ata aproximadamente unhas $1,6 \times 10^{16}$ partículas/cm^2 nos detectores máis internos. A maior luminosidade do HL-LHC implica un aumento na acumulación de eventos agardados. Para afrontar isto, novas tecnoloxías estanse a propoñer para acadar resolucións temporais para partículas mínimamente ionizantes da orde dos $\sim$ 10 ps sen perder precisión espacial. Ademais, xorde outro gran desafío dos altos niveis de radiación agardados, a degradación da eficiencia da recolección de carga e a posterior perda de rendemento do sensor. Para afrontar estes problemas, unha liña de investigación estuda a posibilidade de producir sensores de silicio tolerantes á radiación con ganancia intrínseca. O obxectivo é mellorar a amplitude do sinal despois de irradiar e, simultaneamente, mellorar as capacidades de resolución temporal dos dispositivos.

Esta tese enfócase na análise de dúas das tecnoloxías propostas para ser empregadas en detectores con resolución temporal en futuros colisionadores de alta luminosidade: os detectores de avalancha de baixa ganancia (ou LGADs, polas súas siglas en inglés) e os detectores de avalancha de difusión profunda (ou DD-APDs, polas súas siglas en inglés). Ambos tipos de dispositivos baséanse no mesmo principio básico: grazas á ionización de impacto os sensores posúen ganancia intrínseca. A multiplicación interna destes sensores debería mellorar as súas capacidades de resolución temporal e aumentar a amplitude dos seus sinais, mesmo despois de seren irradiados.

Neste traballo caracterizáronse LGADs e DD-APDs antes e despois de ser irradiados para estudar a degradación do rendemento destes dispositivos (perda de sinal e ganancia, resposta espacial inhomoxénea, etc.) en función da fluencia da radiación. O obxectivo destes estudos é axudar a comprender os procesos físicos fundamentais que conducen á deterioración do mecanismo de ganancia nos dispositivos de silicio con ganancia intrínseca. Ademais, esta tese bota luz sobre os moitos fenómenos que ocorren dentro dos dispositivos de silicio tras ser expostos a altos niveis de radiación, tanto con protóns como con neutróns. Finalmente, ao mesmo tempo que se pretendía optimizar o rendemento destes detectores, obtivéronse límites de aplicación claros para os LGADs e DD-APDs

en termos de tolerancia á radiación. Estes resultados servirán ao HL-LHC e a outros experimentos como guía á hora de considerar o uso de dispositivos con ganancia intrínseca para aplicacións en reconstrucción de trazas, calorimetría e para a realización de medidas temporais de precisión.

LGADs

Un conxunto de 16 LGADs e diodos PiN, fabricados polo CNM-Barcelona, caracterizáronse antes e despois de ser irradiados con protóns. Todos os dispositivos teñen un espesor de 285 μm, unha área activa de 3×3 mm^2, un anel de garda (GR) e o que se coñece como unha extensión da terminación da unión (ou JTE, polas súas siglas en inglés). A caracterización dos sensores foi realizada a través de medicións CV/IV, medicións de recolección de carga cunha fonte radioactiva, escaneamentos TCT, eTCT e TPA-TCT a diferentes tensións e temperaturas. O obxectivo era analizar os efectos da radiación sobre a ganancia; a homoxeneidade da recolección de carga; o inicio da multiplicación; e a evolución do campo eléctrico, da carga recollida e o dopado efectivo coa tensión, a fluencia e temperatura. Os diodos PiN foron medidos para seren empregados como referencia para os cálculos de ganancia.

As mostras estudadas proveñen da partida 7859 do CNM, e de catro obleas de silicio diferentes (W1, W2, W3 e W4):

- W1 e W2 cunha dose de implantación na capa de multiplicación de $1,8 \times 10^{13}$ cm^{-2},
- W3 e W4 cunha dose de implantación na capa de multiplicación de $2,0 \times 10^{13}$ cm^{-2}.

No que se refire aos parámetros eléctricos destes sensores, antes de irradiar, todos tiñan unha capacidade final de $\sim 4,1$ pF, e unha corrente inversa de saturación total (pad + GR) de menos de 0,21 μA á tensión de baleiramento e a 20°C. Os resultados obtidos nesta tese compáranse cos de estudos anteriores. Segundo estes estudos os LGADs pódense clasificar pola a súa corrente inversa de saturación antes de irradiar, definindo como dispositivos de baixa corrente aos que presentan unha corrente inversa de saturación total inferior a 1 μA á tensión de baleiramento e a 20°C. Supoñendo que a corrente inversa de saturación é proporcional ao volume activo do dispositivo, nos LGADs analizados nesta tese o limiar de 1 μA fixado no estudos anteriores, previamente mencionados, correspóndese a 0,34 μA, debido ao menor volume activo dos sensores. Como xa se indicou, todas as mostras (agás o sensor LGAD_4_W4_I3_1, posteriormente irradiado ata unha fluencia de 10^{12} n$_{eq}$/cm^2) teñen unha corrente inversa de saturación inferior aos 0,21 μA á tensión de baleiramentoe a 20°C.

As mostras foron enviadas á instalación IRRAD do CERN para ser irradiadas con protóns de 24 GeV/c, con fluencias de entre 10^{12} e 10^{15} n$_{eq}$/cm^2. Despois de irradiar, e

antes da súa caracterización, os detectores foron sometidos a un proceso de recocido a 60°C durante 80 min.

A distribución espacial da recolección de carga foi examinada nalgúns dispositivos, antes e despois de irradiar, a través de medidas TCT co láser vermello. A distribución resulta homoxénea antes de irradiar, cunha desviación máxima da media inferior ao 5 %. Despois de irradiar a fluencias non superiores aos 10^{14} n_{eq}/cm^2, a desviación máxima da media variou entre un 2 % e un 20 %, dependendo da mostra e iluminación (frontal ou posterior). Non obstante, a unha fluencia de 10^{15} n_{eq}/cm^2 atopáronse unhas inhomoxeneidades significativas. De feito, observouse un padrón a raias con diferentes niveis de recolección de carga e a desviación máxima da media variaba entre o 13 % e o 100 % (visto en TCT co láser vermello e iluminación posterior). Para comprender mellor a orixe destas inhomoxeneidades, realizáronse escaneamentos TCT nun díodo PiN irradiado ata 10^{14} n_{eq}/cm^2. A distribución espacial de recolección de carga resultou ser moito máis homoxénea que para un LGAD irradiado á mesma fluencia. Por conseguinte, é razoable concluír que a principal fonte de inhomoxeneidades na recolección de cargas é o efecto da radiación na capa de multiplicación p+.

Un dos principais obxectivos deste traballo foi analizar a evolución coa fluencia da tensión de inicio da multiplicación. Para isto, tomouse como referencia un estudo anterior sobre LGADs similares irradiados con neutróns, pións de 200 MeV/c e protóns de 800 MeV/c. Nese estudo atopouse que a tensión de inicio da multiplicación diminuía coa fluencia. Este efecto sería consecuencia do que se denomina xeralmente como *remoción efectiva de aceptores*. Non obstante, nesta tese, onde se caracterizaron LGADs irradiados con protóns de 24 GeV/c, o estudo da recolección de carga coa tensión mostrou que nestes dispositivos e con este tipo de irradiación a tensión de inicio da multiplicación aumenta coa fluencia. Isto é consistente coa inversión de signo da carga espacial inicialmente de tipo p a tipo n debido á captura de ocos. Ademais, a través de medidas de TPA-TCT e simulacións TCAD, que permitiron a análise da evolución do campo eléctrico dentro dun dos LGADs irradiados ata 10^{14} n_{eq}/cm^2, foi posible deducir que hai un *efecto de triple unión* que se produce no dispositivo con inversión de tipo. Curiosamente, tamén se descubriu que co recocido a tensión de inicio da multiplicación diminúe e a ganancia recupérase ao 60-70 % do valor antes de irradiar. A medida que as mostras se recocen, estas tenden a un estado semellante ao que tiñan antes de ser irradiadas. Isto implica que o recocido xoga un papel importante no rendemento dos LGADs e poderíase aproveitar na operación de LGADs a longo prazo. Máis campañas de irradiación e estudos sistemáticos de recocido deben levarse a cabo en sensores semellantes para comprender mellor estes fenómenos.

Con respecto á ganancia, demostrouse que este parámetro diminúe co aumento da fluencia. Ata fluencias por baixo dos 10^{14} n_{eq}/cm^2, é posible recuperar a ganancia aumentando a tensión de polarización. Non obstante, a fluencias máis altas, non é posible recuperar a ganancia a valores previos á irradiación por medio do aumento da tensión de polarización aplicada. En realidade, á máxima fluencia evaluada (10^{15} n_{eq}/cm^2) a carga recollida polos LGADs, independentemente do seu dopado na capa de multiplicación, era

case igual ao dun díodo PiN normal sen multiplicación interna de carga. Esta diminución da ganancia interna pódese atribuír á triple unión mencionada anteriormente, ou máis especificamente, á inversión de signo da carga espacial debido á captura de ocos. Antes de irradiar, a unha tensión de polarización específica o campo eléctrico ten un máximo claro na capa de multiplicación. Despois de irradiar, ao aplicar esa mesma tensión de polarización hai dous picos no campo eléctrico que *compiten* entre si: un na parte posterior do dispositivo e outro na parte dianteira. Isto implica que se require unha maior tensión de polarización para acadar a mesma intensidade do campo eléctrico na capa de multiplicación e, polo tanto, a mesma ganancia que había antes de irradiar. Tamén é posible que a causa desta diminución da ganancia sexa realmente unha combinación de dous efectos, a inversión de signo da carga espacial e a remoción de aceptores. Estudos adicionais, particularmente a 10^{15} n_{eq}/cm^2, deben ser realizados para determinar se a diminución observada na ganancia é debido a unha combinación do efecto de triple unión e á remoción de aceptores.

DD-APDs

Dous conxuntos de DD-APDs cun área activa de 2×2 mm^2 foron caracterizdos, antes e despois de ser irradiados con neutróns, para avaliar a súa tolerancia á radiación. A caracterización de todos os DD-APD de 2×2 mm^2 incluíu a realización de escaneamentos TCT de superfcie e de tensión, así como a medida da capacitancia e a corrente inversa de saturación con respecto á tensión. Esta tese abrangue o estudo máis completo feito ata o momento sobre a resistencia á radiación dos DD-APDs. Tamén foron caracterizados dous dispositivos cunha area activa de 8×8 mm^2. Estes sensores non foron irradiados, o estudo centrouse na análise da uniformidade da amplitude do sinal.

2×2 mm^2

Nesta tese estudouse o efecto da radiación con neutróns sobre DD-APDs de 2×2 mm^2. Para facelo, dous conxuntos de DD-APDs de 2×2 mm^2 caracterizáronse antes e despois de ser irradiados con neutróns. O primeiro conxunto constaba de 7 DD-APDs e o segundo de 8. Despois do estudo do primeiro conxunto de detectores descubríuse que antes de irradiar é imperativo analizar todos e cada un dos sensores. Isto débese a que cada sensor pode proceder de diferentes obleas de silicio, con distintas ganancias, perfís de dopado, e mesmo distintos espesores e profundidades da unión pn. Debido a que isto non era coñecido durante o traballo no primeiro set de sensores, os resultados non foron concluíntes. Por iso, un segundo conxunto de DD-APDs foi solicitado a RMD e todos os sensores foron avaliados antes de iniciar a campaña de irradiación.

Cinco dos sete DD-APDs do primeiro conxunto foron irradiados con neutróns ata fluencias de entre 3×10^{13} n_{eq}/cm^2 e 1×10^{15} n_{eq}/cm^2. Os dous dispositivos restantes non foron irradiados e mantivéronse como referencia. Os detectores non foron sometidos a ningún tratamento térmico tras a irradiación. Con todo, estimouse que, debido ao seu manexo, as mostras experimentaron un recocido total de 60 min a 21°C.

Os escaneamentos TCT de superficie realizáronse para analizar a homoxeneidade espacial da recolección de carga. As mostras non irradiadas mostraron inhomoxeneidades por efectos puramente ópticos. Tras a irradiación, atopouse unha redución da área activa dos sensores dependente da fluencia. Ademais, nas mostras irradiadas a fluencias maiores aos 6×10^{13} n_{eq}/cm^2, unha rexión de maior recolección de carga apareceu no centro dos dispositivos nos escaneamentos co láser vermello, a natureza deste efecto aínda non está clara.

As curvas IV demostraron que neste conxunto a corrente inversa de saturación parece estar dominada pola corrente de xeración superficial. Como se prevía, hai un aumento da corrente coa fluencia. A partir das medidas IV a 200 V, onde non se espera que haxa multiplicación interna, foi posible estimar α, que é a *taxa de dano relacionada coa corrente*. O valor obtido de $8,22 \times 10^{-19}$ A/cm resultou da orde de magnitude agardada. A dependencia entre a corrente inversa de saturación e a temperatura foi avaliada para unha das mostras irradiadas ata 3×10^{14} n_{eq}/cm^2 e determinouse a enerxía efectiva. O valor obtido foi $(1,221 \pm 0,008)$ eV, que é consistente co valor esperado de 1,21 eV.

A partir das medidas CV, constatouse que a unha tensión específica a capacitancia diminúe coa fluencia. Supoñendo unha área activa similar, isto implicaría un aumento no espesor da rexión de baleiramento coa irradiación, que vai na dirección dos resultados obtidos con simulacións. Dito isto, os escaneamentos TCT de superficie mostraron unha redución na área activa. A diminución da capacidade podería ser unha combinación de ambos efectos.

Escaneamentos TCT de tensión foron realizados para avaliar o cambio na recollida de carga coa fluencia. Atopouse que a maior nivel de irradiación, menor é a recolección de carga. De feito, a unha fluencia de 3×10^{14} n_{eq}/cm^2 sería necesario aplicar unha tensión de polarización de ~ 2500 V para recuperar o valor de recolección de carga que tiña o sensor a 1700 V antes de ser irradiado. Non obstante, a conclusión máis importante derivada destas medidas non estivo relacionada coa tensión de operación dos sensores despois de irradiar. Ao comparar os escaneamentos de dispositivos que, en principio, deberían terse comportado de forma idéntica, descubríronse variacións significativas na resposta. Isto foi observado mesmo nos DD-APD non irradiados. Estas variacións tamén se atoparon durante as medidas CV/IV. Despois de consultar co fabricante, RMD, soubose que os sensores podían provir de diferentes obleas de silicio. Isto implicaba que a súa ganancia, perfil de dopado, espesor e profundidade de unión pn tamén podían diferir. Por tanto, fíxose patente que era crucial medir e probar todas as mostras antes dunha campaña de irradiación. Finalmente, en función destes resultados, decidiuse estudar un novo conxunto de DD-APDs para ter unha mellor comprensión do seu comportamento.

O novo conxunto de dispositivos constaba de 8 DD-APDs, todos eles foron caracterizados antes e despois de ser irradiados con neutróns. Para ter resultados máis concluíntes, todas as mostras foron irradiadas a pares, cada par a unha fluencia diferente: 3×10^{13}, 6×10^{13}, 3×10^{14}, and 1×10^{15} $\mathrm{n_{eq}/cm^2}$. Non se realizaron pasos de recocido despois da irradiación. Non obstante, estimouse que o recocido total das mostras debido ao su manexo e ao desenvolvemento de medidas a diferentes temperaturas foi de 73 min a 21°C. As probas realizadas neste novo conxunto de dispositivos foron as mesmas que no conxunto anterior.

Igualmente ao observado no primeiro conxunto, os escaneamentos TCT de superficie mostraron que a área activa redúcese coa fluencia. Ademais, a fluencias superiores a 6×10^{13} $\mathrm{n_{eq}/cm^2}$, atopouse a mesma inhomoxeneidade no centro do detector nos escaneamentos TCT de superficie co láser vermello.

As curvas IV presentaron o incremento previsto coa fluencia, e a corrente inversa de saturación semella estar dominada pola corrente de produción do sutrato, tanto antes como despois da irradiación. Unha vez máis, a partir das medidas de corrente inversa de saturación a 200 V, estimouse a taxa de dano relacionada coa corrente, que resultou ser de $8,66 \times 10^{-19}$ A/cm, que é da orde de magnitude esperada. Tamén se realizou unha análise da dependencia da corrente inversa de saturación coa temperatura. Unha mostra non irradiada e todos os sensores irradiados foron medidos a varias temperaturas. A enerxía efectiva foi determinada para todos e cada un deles. O valor medio da enerxía efectiva sobre todos os sensores e a súa desviación estándar foron calculados. O valor obtido foi de $(1,15 \pm 0,05)$eV, que está lixeiramente por debaixo do agardado 1,21 eV.

Respecto ás medidas CV, os resultados foron análogos aos do conxunto anterior de sensores. A capacitancia diminúe coa fluencia, o que podería implicar un aumento no espesor da rexión de baleiramento coa fluencia, consistente cos resultados obtidos por medio de simulacións. Non obstante, este comportamento tamén se pode explicar cunha redución da área activa, que de feito se observa nos escaneamentos TCT de superficie. Posiblemente, a diminución da capacitancia é causada por unha combinación de ámbolos dous efectos.

Finalmente, os escaneamentos TCT de tensión mostran unha diminución na recolección de carga coa fluencia, como se agardaba. Neste conxunto, os resultados foron bastante consistentes entre si para mostras irradiadas á mesma fluencia e para todas as mostras antes da irradiación. As medicións demostraron que para fluencias de ata 6×10^{13} $\mathrm{n_{eq}/cm^2}$, a recolección de carga pódese recuperar aumentando a tensión de polarización. Pola contra, a fluencias por riba de 3×10^{14} $\mathrm{n_{eq}/cm^2}$, a tensión de polarización necesaria para recuperar os niveis de recolección previos á irradiación non se podería alcanzar, xa que se estima sería superior a 3000 V.

Deberían realizarse máis estudos no intervalo entre 6×10^{13} e 3×10^{14} $\mathrm{n_{eq}/cm^2}$ para obter límites de operación máis precisos. Dito isto, os estudos de resistencia á radiación realizados apuntan a que os DD-APDs non son unha tecnoloxía prometedora para aplica-

cións en física de altas enerxías con niveis de radiación superiores a 3×10^{14} n_{eq}/cm^2.

8×8-mm^2

O traballo realizado en DD-APDs cunha área activa de 8×8 mm^2 centrouse no estudo da homoxeneidade da amplitude do sinal sobre a área do detector, unha propiedade particularmente importante para a realización de medidas temporais de precisión. En estudos previos atopouse que a amplitude do sinal nos DD-APDs depende fortemente da posición. Baséandose neses estudos propúxose a idea de facer un acoplamento capacitivo entre o lado frontal do DD-APD e unha malla metálica, usando kapton como dieléctrico. O obxectivo do estudo realizado nesta tese foi verificar esta dependencia espacial mediante medidas TCT, identificar a súa causa e probar a posibilidade de empregar un método máis simple para solucionar o problema da non uniformidade.

Dous DD-APDs de 8×8 mm^2 foron analizados por medio de escaneamentos TCT de superficie. Un mantívose inalterado e o outro foi metalizado no CMi-EPFL a través da deposición de aluminio por medio dunha pulverización catódica. Para evitar a interferencia dos efectos ópticos (como reflexións) no estudo da uniformidade espacial da amplitude do sinal, analizouse a relación entre a amplitude do sinal e a carga recollida.

A mostra non metalizada foi sometida a escaneamentos TCT de varios tipos: frontais co láser vermello e infravermello, e posteriores co láser infravermello. Para a iluminación frontal, pódese ver que os mapas do cociente amplitude/carga teñen unha dependencia clara coa distancia ao punto de lectura. O cociente amplitude/carga diminúe coa distancia ao punto de lectura. O mesmo foi observado nos escaneamentos TCT co láser infravermello, onde hai un claro gradiente de amplitude, o máximo do cal atópase debaixo do punto de lectura na parte frontal. A diferenza máxima do cociente amplitude/carga observada a través de TCT co láser infravermello foi dun 75 % a unha distancia de 7 mm. Mediante un estudo cualitativo deste fenómeno atopouse que a relación entre a amplitude do sinal e a carga dependía da distancia ao contacto debido á resistividade superficial do dispositivo. En consecuencia, a aplicación dunha capa condutora na superficie dos DD-APDs (a metalización previamente mencionada) podería ser unha solución á non uniformidade espacial da amplitude do sinal.

Só se realizaron escaneamentos TCT co láser infravermello no DD-APD metalizado, xa que os sinais obtidos co láser infravermello son os máis semellantes aos previstos durante a operación habitual do detector. Un escaneamento TCT superficial frontal pouco detallado foi feito para identificar a área completa do sensor. En base a ese escaneamento inicial, escolléronse catro rexións do sensor de $0,5 \times 0,5$ mm^2 cada unha para realizar escaneamentos máis detallados. Estas medidas demostraron que a uniformidade do cociente amplitude/carga dos DD-APDs podería mellorarse notablemente metalizando a superficie dos dispositivos. As non uniformidades foron inferiores ao 8 %, cando se compara a diferenza do cociente amplitude/carga a unha distancia de 7 mm. Estes primeiros resultados

son bastante prometedores. Con todo, deberíanse realizar máis estudos para confirmar a viabilidade deste método.

Observacións finais

Para resumir, o traballo realizado sobre os LGADs demostrou que estes dispositivos poden manter as súas capacidades de ganancia ata fluencias de 1×10^{14} $\mathrm{n_{eq}/cm^2}$. De feito, por baixo dese nivel de irradiación, é posible recuperar a ganancia aumentando a tensión de polarización aplicada. Tamén se concluíu que os dispositivos poden ser fabricados para ter unha resposta homoxénea en toda a súa área activa. Finalmente, no caso de exposición a protóns altamente enerxéticos, o recocido das mostras podería mellorar o rendemento destes dispositivos durante o seu uso en experimentos de física de altas enerxías.

A partir dos estudos de resistencia a radiación realizados en DD-APD concluíuse que esta tecnoloxía non é tan prometedora para ser aplicada en experimentos de física de altas enerxías con niveis de radiación superiores a 3×10^{14} $\mathrm{n_{eq}/cm^2}$. A fluencias máis altas, as tensións necesarias para recuperar os valores de ganancia previos á irradiación superan amplamente o rango operativo dos sensores. O deseño dos DD-APDs debe ser adaptado para poder usar este tipo de detectores nas condicións agardadas para o HL-LHC.

Abstract

The research work of this PhD thesis is performed in the framework of the RD50 Collaboration, working on the development and characterisation of radiation tolerant silicon detectors for high luminosity colliders. The main focus is on silicon sensors for tracking applications within the HL-LHC experiments. Sensors with intrinsic charge multiplication are presently under investigation within RD50. In this thesis, Low Gain Avalanche Detectors (LGADs) and Deep Diffused Avalanche Particle Detectors (DD-APDs) are studied, as they allow to multiply the charge generated by traversing particles. The subsequent increase in the signal produced by the detectors has the potential to improve the signal-to-noise ratio, and with it the efficiency and the time resolution of the detectors. Unfortunately, these devices suffer from serious radiation damage when exposed to particle fluences higher than about 10^{14} particles/cm^2.

The aim of this thesis is to characterise LGADs and DD-APDs before and after exposure to radiation, and study the performance degradation (loss of signal, loss of gain, inhomogeneous spatial response, etc.) as a function of radiation fluence. The origin of the differences in performance is evaluated, and new optimised designs are proposed based on some of the results obtained. The performed work helps understand the fundamental physical processes that are leading to the deterioration of the gain mechanism in silicon devices with intrinsic gain. Whilst aiming for performance optimisation, clear application limits for LGAD and DD-APD devices in terms of radiation hardness are obtained. From a solid-state physics point of view, this thesis sheds light on the many phenomena occurring inside silicon devices after heavy irradiation, both with protons and neutrons. From the perspective of detector physics and detector technology, these findings will serve the HL-LHC and other experiments as guidelines for considering the use of devices with intrinsic gain for tracking, calorimetry, or timing applications.

USC
UNIVERSIDADE
DE SANTIAGO
DE COMPOSTELA

List of Figures

2.1 Energy band structures with respect to momentum of Si and GaAs. 5

2.2 Schematic of the covalent bonds in intrinsic, n-type, and p-type silicon. . 6

2.3 Schematic of the space charge, electric field, and energy bands of a pn-junction in thermal equilibrium. 8

3.1 Schematic of the process of permanent surface damage. 12

3.2 Graphical representation of point defects. 12

3.3 Emission and capture processes through intermediate states. 14

3.4 Simulation of the distribution of defects for different incident particles and energies. 15

3.5 Normalised displacement damage cross sections as a function of energy for neutrons, protons, pions and electrons. 16

3.6 Depletion voltage and N_{eff} with respect to fluence for n-type silicon. . . . 20

3.7 Change in N_{eff} with annealing time. 23

3.8 Structure of the B_iO_i defect complex. 24

3.9 Depletion voltage as a function of fluence in p-type silicon, and acceptor removal coefficient c with respect to initial acceptor concentration, for different devices and irradiations. 24

4.1 Example of a typical CV measurement on a PiN diode. 28

4.2 Sketches of the electrical connections in the CV/IV probe station. 29

4.3 Pictures of the CV/IV probe station. 30

4.4 Parallel and serial equivalent circuits for a silicon sensor 32

USC UNIVERSIDADE DE SANTIAGO DE COMPOSTELA

4.5 Pictures of the CV/IV set-up inside a climate chamber. 32

4.6 Sketches of signal generation with TCT. 34

4.7 Simplified schematic of the TCT+ set-up. 35

4.8 Photographs of the PCBs used in this thesis. 36

4.9 Photographs of the TCT+ set-up at the EP-DT-DD SSD laboratory at CERN. 37

4.10 Schematics of the cooling, and linear stage systems of the TCT+ set-up. . 38

4.11 Optical system of the TCT+ set-up. 40

4.12 Photographs comparing the light absorption in a fluorescent solution when illuminated with a laser diode (single-photon absorption), and with a femtosecond pulsed laser (two-photon absorption). 41

4.13 Pictures of the TPA-TCT set-up at the Singular Laser Facility of the UPV/EHU. 42

4.14 Energy spectrum expected for electrons emitted by a ^{90}Sr source, and energy deposition of electrons in silicon. 45

4.15 Picture of the radioactive source measurements set-up. 45

4.16 Average signal from 20000 waveforms, and charge distribution obtained from ^{90}Sr source measurements on an unirradiated 300-μm diode. 45

5.1 Illustration of real CMS events, expected beam spot at the HL-LHC, and a sketch of the intersection of two bunches. 48

5.2 Schematic of the reconstruction of tracks by associating time-compatible hits. 50

5.3 Graphical explanation of how a timing layer can be used to discriminate vertices. 50

5.4 Schematic of the main components of a time-tagging detector. 51

5.5 Graphical representation of time walk. 52

5.6 Simulated weighting field of two segmented devices. 55

5.7 Representation of time jitter. 55

6.1 Schematic cross section of an LGAD pad with a JTE structure. The laser configuration of the TCT set-up can also be seen. Also, a simulation of the electric field at two different bias voltages inside a thin (50 μm) and a thick (300 μm) LGAD. 59

6.2 Photographs of the metallisation structure of CNM run 7859 LGADs and PiN diodes. 60

6.3 Examples of waveforms obtained with red-back, red-front, and IR TCT on a fully depleted LGAD and a PiN diode. 60

6.4 Schematic of the fabrication process of DD-APDs. 64

6.5 Cross-section schematic, and diagram of the edge of a DD-APD. 64

6.6 Pictures of one of the 2×2-mm^2 DD-APDs measured in this thesis. . . . 65

6.7 Pictures of an 8×8-mm^2 DD-APDs with an AC-coupled read-out on the p-side, and a sintered gold layer on the n-side. 65

7.1 CV curves before and after irradiation for all the LGADs from run 7859. . 70

7.2 CV curves before and after irradiation for all the PiN diodes from run 7859. 71

7.3 Full depletion voltage with respect to fluence for all the LGADs and PiN diodes from run 7859. 72

7.4 IV curves before and after irradiation for all LGADs from W1 and W2 (multiplication-layer dose: 1.8×10^{13} cm^{-2}). 74

7.5 IV curves before and after irradiation for all LGADs from W3 and W4 (multiplication-layer dose: 2.0×10^{13} cm^{-2}). 75

7.6 Close-up at low voltages of the total current for all LGADs before irradiation. 76

7.7 IV curves before and after irradiation for all PiN diodes from run 7859. . 76

7.8 TCT surface scans before and after irradiation on LGAD_7859_4_W2_E3_1. 79

7.9 TCT surface scans before and after irradiation on LGAD_7859_4_W4_I3_1. 80

7.10 TCT surface scans before and after irradiation on LGAD_7859_7_W3_C2_3. 81

7.11 TCT surface scans before and after irradiation on LGAD_7859_9_W1_F10_3. 82

7.12 TCT surface scans after irradiation on PiN_7859_4_W3_I8_1. 83

7.13 ^{90}Sr charge collection curves of all LGADs and PiN diodes before irradiation. 85

7.14 Charge collection in PiN diodes as a function of voltage, before and after irradiation, measured with red-front TCT. 87

7.15 Charge collection in PiN diodes as a function of voltage, before and after irradiation, measured with red-back TCT. 88

7.16 Charge collection in PiN diodes as a function of voltage, before and after irradiation, measured with IR TCT. 89

7.17 Detail of the voltage scans, and IV curves of PiN_7859_4_W1_I8_1. 90

7.18 Voltage scans of LGADs, before and after irradiation, measured with red-front TCT. 93

7.19 Voltage scans of LGADs, before and after irradiation, measured with red-back TCT. 94

7.20 Voltage scans of LGADs, before and after irradiation, measured with IR TCT. 95

7.21 Multiplication-onset voltage, also referred to as threshold voltage, as a function of fluence. 96

7.22 Gain at 700 V and -20°C as a function of fluence for LGADs. 99

7.23 Before-irradiation voltage scans for the PiN diodes used as reference from W3 and W4. 99

7.24 *Type-1 gain* of LGADs as a function of voltage and fluence for IR pulses. 100

7.25 Red-front and red-back TCT voltage scans and waveforms at 300 V of LGAD_7859_4_W2_I3_1 (mult. layer dose: 1.8 $\times$ 10^{13} cm^{-2}, fluence: 10^{14} n$_{eq}$/cm^2) at 20, 10, 0, -10, and -20°C. 103

7.26 Red-front and red-back TCT voltage scans and waveforms at 300 V of LGAD_7859_7_W3_C2_3 (mult. layer dose: 2.0 $\times$ 10^{13} cm^{-2}, fluence: 10^{14} n$_{eq}$/cm^2) at 20, 10, 0, -10, and -20°C. 104

7.27 Leakage current curves before irradiation for samples LGAD_7859_4_W2_I3_1 and LGAD_7859_7_W3_C2_3. 106

7.28 Charge collection as a function of voltage obtained with red-front TCT on an unirradiated LGAD at 20°C and -20°C, with and without a GR connection. 108

7.29 Evolution with time of the multiplication-onset voltage and the gain for both LGADs irradiated up to 10^{14} n_{eq}/cm^2 (LGAD_7859_4_W2_I3_1 and LGAD_7859_7_W3_C2_3). 108

7.30 Red-front TCT voltage scans performed on both LGADs irradiated up to 10^{14} n_{eq}/cm^2 (LGAD_7859_4_W2_I3_1 and LGAD_7859_7_W3_C2_3). . . 109

7.31 Drift velocity profiles obtained through eTCT on LGAD_7859_7_W3_C2_3, irradiated up to 10^{14} n_{eq}/cm^2, at 20°C and -20°C. 112

7.32 Drift velocity profiles obtained through eTCT (20°C and -20°C) and TPA-TCT (0°C and -20°C) on LGAD_7859_4_W2_I3_1, irradiated up to 10^{14} n_{eq}/cm^2.112

7.33 Red-front TCT voltage scan, and eTCT ZY-scans of LGAD_7859_4_W2_I3_1 (irradiated up to 10^{14} n_{eq}/cm^2). 113

7.34 Schematic of the hypothetical *triple-junction* structure in an LGAD; and low-voltage detail of the IV curves of samples LGAD_7859_4_W2_I3_1 and LGAD_7859_7_W3_C2_3, both before and after irradiation. 114

8.1 View of a 2×2-mm^2 DD-APD mounted on a TCT PCB by means of a custom-made adaptor. 116

8.2 IR and red-front TCT surface scans of DD-APDs 394_1_7 and 394_1_8, both unirradiated. 118

8.3 Photograph of DD-APD 394_1_7, and of the alumina supports of samples 394_1_7 and 394_1_5, after elimination of the silicon sensors. 118

8.4 IR and red-front TCT surface scans on DD-APD 394_1_1, irradiated up to 3×10^{13} n_{eq}/cm^2. 119

8.5 IR and red-front TCT surface scans on DD-APD 394_1_3, irradiated up to 6×10^{13} n_{eq}/cm^2; and waveforms obtained through red-front TCT. . . . 119

8.6 IR and red-front TCT surface scans on DD-APDs 394_1_4 and 394_1_5, irradiated up to 3×10^{14} n_{eq}/cm^2. 120

8.7 IR TCT voltage scans of all 2×2-mm^2 DD-APDs from the first set. . . . 122

8.8 Capacitance with respect to voltage for all 2×2-mm^2 DD-APDs from the first set. 123

8.9 Capacitance at 500 V with respect to fluence. Measurements done at -20°C and 1 kHz. 123

8.10 Leakage current for all 2×2-mm^2 DD-APDs from the first set. Measurements done at -20°C. 125

8.11 Leakage current at 200 V and -20°C with respect to fluence for all 2×2-mm^2 DD-APDs from the first set. 127

8.12 Leakage current with respect to voltage for DD-APD 394_1_5 at five different temperatures. 128

8.13 IR and red-front TCT surface scans on DD-APD APD_2B_1, before and after irradiation up to 3×10^{13} n_{eq}/cm^2. 132

8.14 IR and red-front TCT surface scans on DD-APD APD_2B_3, before and after irradiation up to 3×10^{13} n_{eq}/cm^2. 132

8.15 IR and red-front TCT surface scans on DD-APD APD_2B_5, before and after irradiation up to 6×10^{13} n_{eq}/cm^2. 133

8.16 IR and red-front TCT surface scans on DD-APD APD_2B_11, before and after irradiation up to 6×10^{13} n_{eq}/cm^2. 133

8.17 IR and red-front TCT surface scans on DD-APD APD_2B_6 before irradiation, and photograph of the surface of the device. 134

8.18 IR and red-front TCT surface scans on DD-APD APD_2B_4, before and after irradiation up to 3×10^{14} n_{eq}/cm^2. 134

8.19 IR and red-front TCT surface scans on DD-APD APD_2B_7, before and after irradiation up to 1×10^{15} n_{eq}/cm^2. 135

8.20 IR and red-front TCT surface scans on DD-APD APD_2B_9, before and after irradiation up to 1×10^{15} n_{eq}/cm^2. 135

8.21 IR TCT voltage scans of all 2×2-mm^2 DD-APDs from the second set before and after irradiation. 137

8.22 Red-front TCT voltage scans of all 2×2-mm^2 DD-APDs from the second set before and after irradiation. 138

8.23 Detail at intermediate voltages of IR and red-front TCT voltage scans of all 2×2-mm^2 DD-APDs from the second set before and after irradiation. 139

8.24 Detail at high voltages of IR and red-front TCT voltage scans of all 2×2-mm^2 DD-APDs from the second set before and after irradiation. 140

8.25 Gain as a function of fluence for 2×2-mm^2 DD-APDs from the second set before and after irradiation. 141

USC UNIVERSIDADE DE SANTIAGO DE COMPOSTELA

8.26 Capacitance with respect to voltage for all 2×2-mm^2 DD-APDs from the second set. 142

8.27 Capacitance at 500 V with respect to fluence. Measurements done at -20°C and 10 kHz. 143

8.28 Leakage current for all 2×2-mm^2 DD-APDs from the second set. Measurements done at -20°C. 144

8.29 Leakage current at 200 V (where no multiplication is expected) and -20°C with respect to fluence for all 2×2-mm^2 DD-APDs from the second set. . 145

8.30 Leakage current at 200 V with respect to $1/kT$ for DD-APDs, from the second set, irradiated up to 3×10^{13} n_{eq}/cm^2, 6×10^{13} n_{eq}/cm^2, 3×10^{14} n_{eq}/cm^2, and one unirradiated device. 147

8.31 Leakage current at 200 V with respect to $1/kT$ for DD-APDs from the second set irradiated up to 1×10^{15} n_{eq}/cm^2. 148

8.32 Effective energy of DD-APDs of the second set as a function of fluence. . 148

8.33 Photographs of an 8×8-mm^2 DD-APD with no surface metallisation. . . 150

8.34 Photographs of a metallised 8×8-mm^2 DD-APD. 150

8.35 Charge collection, signal amplitude, and amplitude/charge ratio maps obtained with IR-front TCT on the p-side of an 8×8-mm^2 DD-APD with no surface metallisation. 151

8.36 Charge collection, signal amplitude, and amplitude/charge ratio maps obtained with IR-back TCT on the n-side of an 8×8-mm^2 DD-APD with no surface metallisation. 151

8.37 Charge collection, signal amplitude, and amplitude/charge ratio maps obtained with red-front TCT on the p-side of an 8×8-mm^2 DD-APD with no surface metallisation. 152

8.38 IR-front TCT scans done to the n-side of a metallised 8×8-mm^2 DD-APD.154

8.39 Picture of the metallic grid on the 8×8-mm^2 DD-APD measured. This was the first device to be metallised. 154

A.1 Schematic drawing of the Czochralski crystal puller. 166

A.2 Schematic of the different steps of the Czochralski process. 166

A.3 Schematic drawing of the float-zone process, and a photograph taken during the procedure. 167

B.1 Red-front TCT waveforms from (left) LGAD_7859_4_W2_I3_1 (1.8×10^{13} cm^{-2}) and (right) PiN_7859_7_W1_C9_3 (PiN diode), from W2 and W1, irradiated up to 10^{14} n_{eq}/cm^2, at 20, and 10°C. 170

B.2 Red-front TCT waveforms from (left) LGAD_7859_4_W2_I3_1 (1.8×10^{13} cm^{-2}) and (right) PiN_7859_7_W1_C9_3 (PiN diode), from W2 and W1, irradiated up to 10^{14} n_{eq}/cm^2, at 0, -10, and -20°C. 171

B.3 Red-back TCT waveforms from (left) LGAD_7859_4_W2_I3_1 (1.8×10^{13} cm^{-2}) and (right) PiN_7859_7_W1_C9_3 (PiN diode), from W2 and W1, irradiated up to 10^{14} n_{eq}/cm^2, at 20, and 10°C. 172

B.4 Red-back TCT waveforms from (left) LGAD_7859_4_W2_I3_1 (1.8×10^{13} cm^{-2}) and (right) PiN_7859_7_W1_C9_3 (PiN diode), from W2 and W1, irradiated up to 10^{14} n_{eq}/cm^2, at 0, -10, and -20°C. 173

B.5 Red-front TCT waveforms from (left) LGAD_7859_7_W3_C2_3 (2.0×10^{13} cm^{-2}) and (right) PIN_7859_4_W3_I8_1 (PiN diode), from W3, irradiated up to 10^{14} n_{eq}/cm^2, at 20, and 10°C. 174

B.6 Red-front TCT waveforms from (left) LGAD_7859_7_W3_C2_3 (2.0×10^{13} cm^{-2}) and (right) PIN_7859_4_W3_I8_1 (PiN diode), from W3, irradiated up to 10^{14} n_{eq}/cm^2, at 0, -10, and -20°C. 175

B.7 Red-back TCT waveforms from (left) LGAD_7859_7_W3_C2_3 (2.0×10^{13} cm^{-2}) and (right) PIN_7859_4_W3_I8_1 (PiN diode), from W3, irradiated up to 10^{14} n_{eq}/cm^2, at 20, and 10°C. 176

B.8 Red-back TCT waveforms from (left) LGAD_7859_7_W3_C2_3 (2.0×10^{13} cm^{-2}) and (right) PIN_7859_4_W3_I8_1 (PiN diode), from W3, irradiated up to 10^{14} n_{eq}/cm^2, at 0, -10, and -20°C. 177

C.1 IR TCT surface scans of a 2×2-mm^2 DD-APD to study unexpected charge collection areas outside the silicon die. 180

C.2 IR TCT surface scans of a partially covered DD-APD to study unexpected charge collection areas outside the silicon die. 180

D.1 High-voltage detail of IR and red TCT voltage scans on DD-APDs, the voltages indicated are those provided by the power supply. 183

D.2 High-voltage detail of the leakage current in DD-APDs during IR and red TCT voltage scans, the voltages indicated are those provided by the power supply. 183

D.3 Schematic of the biasing and read-out circuitry used during TCT measurements on DD-APDs. 183

D.4 High-voltage detail of IR and red TCT voltage scans on DD-APDs, the voltages indicated are those actually applied to the sensor. 184

D.5 Waveforms obtained at -20°C, before irradiation, through IR and red TCT on samples APD_2B_1 and APD_2B_7. 184

D.6 IR TCT voltage scans obtained from sample APD_2B_4 with three different intensities: 129 μW, 69 μW, and 22 μW. 185

E.1 IV curves at different temperatures before irradiation, sample APD_2B_6. 188

E.2 IV curves at different temperatures after irradiation to 3×10^{14} n_{eq}/cm^2, sample APD_2B_4. 188

E.3 IV curves at different temperatures after irradiation to 3×10^{13} n_{eq}/cm^2, sample APD_2B_1. 189

E.4 IV curves at different temperatures after irradiation to 3×10^{13} n_{eq}/cm^2, sample APD_2B_3. 189

E.5 IV curves at different temperatures after irradiation to 6×10^{13} n_{eq}/cm^2, sample APD_2B_5. 190

E.6 IV curves at different temperatures after irradiation to 6×10^{13} n_{eq}/cm^2, sample APD_2B_11. 190

E.7 IV curves at different temperatures after irradiation to 1×10^{15} n_{eq}/cm^2, sample APD_2B_7. 191

E.8 IV curves at different temperatures after irradiation to 1×10^{15} n_{eq}/cm^2, sample APD_2B_9. 191

USC UNIVERSIDADE DE SANTIAGO DE COMPOSTELA

USC
UNIVERSIDADE
DE SANTIAGO
DE COMPOSTELA

List of Tables

2.1 Basic properties of some semiconductors and diamond at 300 K. 4

7.1 Irradiation details for all LGADs and PiN diodes from run 7859. 68

7.2 *Type-1 gain* values obtained through ^{90}Sr measurements on LGADs from run 7859 before irradiation, at 700 V, and 20°C. 98

8.1 Irradiation details for all 2×2-mm^2 DD-APDs from the first set of sensors analysed. 117

8.2 *Current related damage rates* (α), after 60 min at 21°C, obtained from the experimental data at 200 V, and calculated for a PiN diode with active volume 6×10^{-4} cm^3. 126

8.3 Irradiation details for all 2×2-mm^2 DD-APDs from the second set of sensors analysed. 129

8.4 *Current related damage rates* (α), after 73 min at 21°C, obtained from the experimental data at 200 V, and calculated for a PiN diode with active volume 6×10^{-4} cm^3. 144

USC
UNIVERSIDADE
DE SANTIAGO
DE COMPOSTELA

Chapter 1

Introduction

In view of the High Luminosity upgrade of the CERN Large Hadron Collider (HL-LHC), radiation tolerant silicon sensors are being developed in the framework of ATLAS[1], CMS[2], RD50 and other sensor R&D projects. The HL-LHC beam parameters and hardware configuration should enable the collider to reach a peak instantaneous luminosity (rate of collisions) of 5×10^{34} cm^{-2}s^{-1}, and an integrated luminosity (total collisions created) of 250 fb^{-1}/year with the goal of 3000 fb^{-1} after about 12 years of operation. This will imply a factor 5 increase in instantaneous luminosity, and 10 in integrated luminosity with respect to the LHC. Furthermore, the equipment is being designed with a 50 % margin with respect to the wanted peak luminosity. This margin should make it possible to push the peak instantaneous luminosity to $7-7.5 \times 10^{34}$ cm^{-2}s^{-1}, and the integrated luminosity to $300-350$ fb^{-1}/year with the goal of 4000 fb^{-1} after the full operation period [1]. This increase in luminosity will also imply a factor 4 rise in the expected pile-up with respect to that observed during Run 2 of the LHC in ATLAS and CMS [1, 2, 3]. Lastly, at the end of the operation period, radiation levels are expected to reach values above 1.6×10^{16} fast hadrons/cm^2 at the innermost detectors [4].

To cope with the increase in pile-up, silicon sensors with timing capabilities of the order of ~ 10 ps are being developed [5]. Given the expected radiation levels, the radiation-tolerance of these devices is of the utmost importance. In recent years it was proven that in order to meet the radiation-tolerance requirements of the new experiments a combination of readout at the segmented n+ electrodes; high voltage operation; a thoroughly planned annealing scheme; and proper electrode design, both for planar and 3D sensors, are needed [6]. However, the degradation of the charge collection efficiency, and the subsequent loss of sensor performance, remain the main obstacles in detector operation. In order to tackle these issues, one line of research investigates the possibility of producing radiation tolerant silicon sensors with intrinsic charge gain. The aim is to improve the signal height after irradiation as well as the timing capabilities of silicon sensors. This thesis is focused on two of the technologies under consideration: Low Gain Avalanche Detectors (LGADs) [7], and Deep Diffused Avalanche Particle Detectors [8]. Said devices are

[1] A Toroidal LHC ApparatuS.
[2] Compact Muon Solenoid.

characterised by their intrinsic charge gain. Internal multiplication should improve their timing capabilities as well as increase their signal height, even after irradiation.

In the particular case of LGADs, several production runs have already been fabricated, first by CNM-Barcelona[3], followed by Hamamatsu Photonics K.K. (HPK), and Fondazione Bruno Kessler (FBK). Moreover, during the past years there has been a continuous effort to conduct radiation-hardness and timing tests on thick ($\sim 300\ \mu$m) and thin ($\sim 50\ \mu$m) LGADs [10, 11, 12, 13, 14, 15, 16]. The development of LGADs is considerably advanced, with ATLAS and CMS already foreseeing the use of LGADs in their detectors [17, 18, 19].

In the case of DD-APDs, manufactured by Radiation Monitoring Devices Inc. (RMD), during the past years studies have been carried out on the timing capabilities of the devices and on the homogeneity of response over the sensor area. In fact, it was found that the signal amplitude in DD-APDs is highly dependent on position [20, 21]. To tackle this issue, the solution proposed was to make a capacitive coupling between the front side of the DD-APD and a metallic mesh, using kapton as a dielectric. These devices are currently under production and study. So far, the radiation-hardness studies performed on DD-APDs had been limited to fluences of the order of $10^{12}\ n_{\text{eq}}/\text{cm}^2$ [22], well below the expected fluence in the HL-LHC. Currently, there is a particular effort on assessing the effect of high levels of radiation on the timing properties of these detectors [21, 23, 24]. As regards the general radiation-tolerance of DD-APDs, this thesis contains the most comprehensive study carried out so far.

UNIVERSIDADE DE SANTIAGO DE COMPOSTELA

[3] Centre Nacional de Microelectrònica, IMB-CNM-CSIC, Barcelona, Spain [9].

Chapter 2

Silicon Detectors

Semiconductor sensors are widely used in high energy physics (HEP). In particular, silicon detectors are used mainly for tracking applications, due to their fast response, and high spatial resolution. Silicon presents the added advantage of being an abundant material, and that the techniques used for the purification and growth of monocrystalline silicon, as well as for microfabrication, are shared with the microelectronics industry. The principle of operation is similar to that of an ionisation chamber. In this case the silicon acts as the active material, each end of the sensor is an electrode, and a potential difference is applied between them. The absorption of a photon or the passage of a charged particle through the material causes it to get ionised, creating pairs of electrons and holes (e^-/h^+). These *charge carriers* move under the influence of the electric field created by the applied voltage. As the charge pairs move through the electric field, they induce and electrical current at the electrodes which can be picked up by the appropriate electronics [25]. The number of charge carriers produced is directly related to the deposited (or absorbed) energy and the *ionisation energy*. The mean ionisation energy is the average energy required for ionisation to occur, which in silicon corresponds to the creation of an e^-/h^+ pair. The ionisation energy depends on the material and the temperature. For instance, this energy is of about 30 eV for gases, and of 3.6 eV for silicon [25]. In Table 2.1 the material properties at 300 K of a few semiconductors are indicated [26]. The combination of low ionisation energy, large enough *bandgap* for room-temperature operation to be possible, and high carrier mobility[1], make of silicon an optimal choice for tracking applications. In addition, its rigidity, and the available microelectromechanics techniques allow for the mechanisation of support structures in the same material. Thus reducing the coefficient of thermal expansion[2] mismatch between the sensor and the support, as well as simplifying the possibility of adding additional features to the substrate [27]. Finally,

[1]**Charge carrier mobility ($[\mu]$ = $cm^2V^{-1}s^{-1}$):** velocity of a charge carrier (cm/s) moving under the influence of an electric field (V/cm) inside a material.

[2]**Coefficient of thermal expansion (CTE):** represents the size change of an object with respect to variations in temperature.

Table 2.1: Basic properties of some semiconductors and diamond at 300 K. From [26].

	Si	Ge	GaAs	Diamond
Atomic number (Z)	14	32	31/33	6
Bandgap (E_g) [eV]	1.12	0.66	1.42	5.47
	indirect	indirect	direct	indirect
Mean ionisation energy [eV]	3.6	2.9	4.3	13
Radiation length [cm]	9.4	2.3	2.3	18.8
Density [g/cm^3]	2.33	5.32	5.32	3.51
Electron mobility (μ_e) [cm^2/Vs]	1450	3900	8500	1800
Hole mobility (μ_h) [cm^2/Vs]	450	1900	400	1200

2.1 Energy bands in a semiconductor

All semiconductors have an energy band or level structure where the electrons of the material are distributed following a Fermi-Dirac distribution (Equation 2.1). The energy level structure in question is related to the structure of the lattice itself. However, all semiconductors share the same characteristic of possessing a forbidden energy range where there are no allowed energy states. Above and below this range there are permitted energy bands. The upper bands are the *conduction bands*, and those below are the *valence bands*. The energy separation between the lowest conduction band and the highest valence band is the *bandgap* [28]. Figure 2.1 shows the energy band structure of Si and GaAs with respect to momentum. The valence-band maximum and the conduction-band minimum can be aligned or misaligned. The latter implies that the minimum energy needed for a band-to-band transition to occur is given by the bandgap plus some additional energy that goes into phonon excitation, i.e. a transfer of momentum through lattice vibrations. When the extrema are misaligned, as in Si, there is a variation in momentum between bands, thus the material is defined as *indirect*. If both extrema are aligned, as in GaAs, no momentum transferral is required, making the material *direct* [25, 28, 29].

2.2 Intrinsic carrier concentration at thermal equilibrium

Previously it was explained that in all semiconductors, hence also silicon, the probability that an electron occupies an electronic state with energy E is given by the Fermi–Dirac distribution function:

$$F(E) = \frac{1}{1 + \mathrm{e}^{(E-E_F)/kT}}\,, \tag{2.1}$$

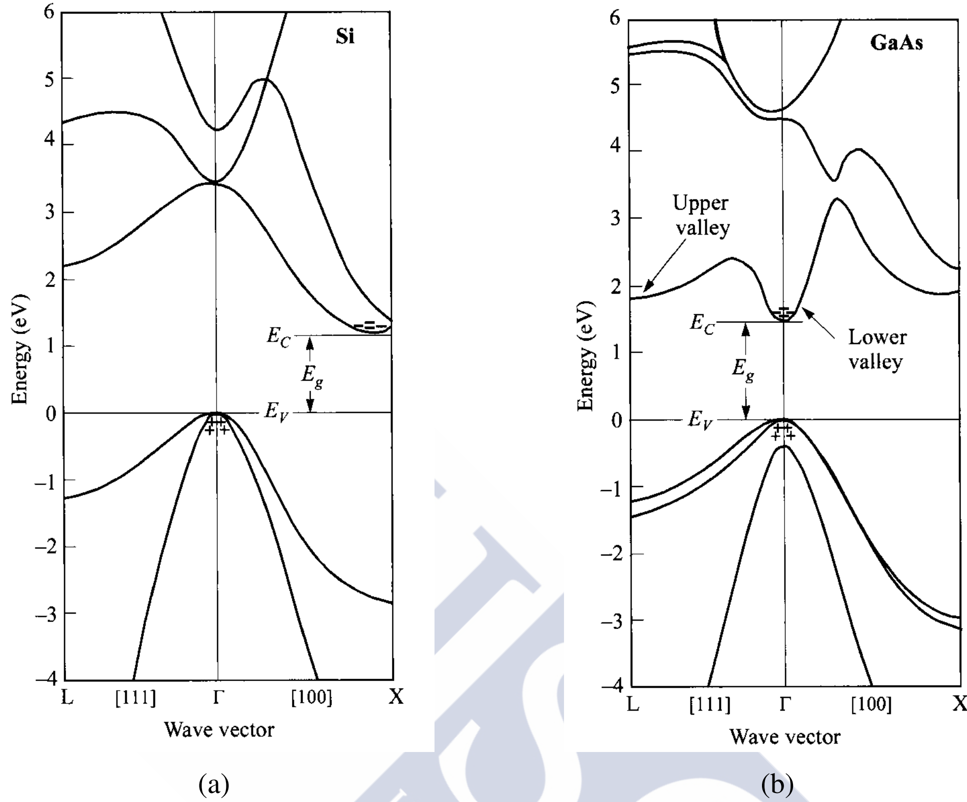

Figure 2.1: Energy band structures with respect to momentum of (a) Si and (b) GaAs. Plus signs (+) indicate holes in the valence bands and minus signs (-) indicate electrons in the conduction bands. From Sze and Kwok 2007 [28]. ©John Wiley Sons, reproduced with permission.

where k is the Boltzmann constant, T is the absolute temperature in degrees Kelvin, and E_F is the energy of the Fermi level, i.e. the energy at which the probability of occupation by an electron is exactly one-half [30]. Specifically, in intrinsic (pure) silicon in thermal equilibrium, the number of electrons in the conduction band (n) is equal to that of holes in the valence band (p) [30]. Hence, the intrinsic carrier density in thermal equilibrium (n_i) is given by:

$$n_i = \sqrt{np} = \sqrt{N_C N_V}\, e^{-E_g/2kT} \propto (kT)^{3/2} e^{-E_g/2kT}, \tag{2.2}$$

where N_C and N_V are the effective densities of states in the conduction and valence band. To go from Equation 2.1 to Equation 2.2, a series of approximations and considerations must be made, for a detailed explanation see [25, 28].

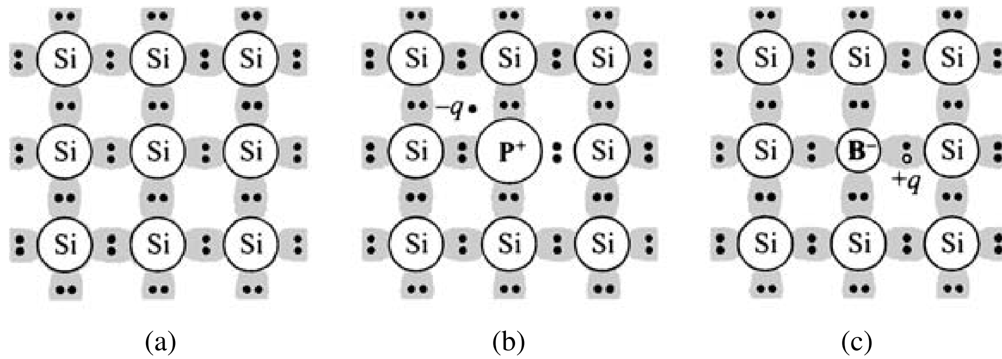

(a) (b) (c)

Figure 2.2: Schematic of the covalent bonds in (a) intrinsic, (b) n-type, and (c) p-type silicon. From Sze and Kwok 2007 [28]. ©John Wiley Sons, reproduced with permission.

2.3 Extrinsic silicon: donors and acceptors

In practice, the silicon used for detectors always has some degree of impurities as a by-product of crystal growth. In fact, for detector applications, impurities, called *dopants*, are purposefully introduced into the silicon to control its conductivity [25]. Figure 2.2a shows a schematic of the covalent bonds between silicon atoms in the lattice. Silicon belongs to Group 14[3] in the periodic table, which means it has 4 valence electrons. In intrinsic silicon, each atom shares its 4 valence electrons with the neighbouring atoms, forming four covalent bonds [28].

A silicon atom can be substituted by an atom from Group 15[4] (e.g. P, As), which have 5 valence electrons. Only 4 of these electrons are used to form covalent bonds with the Si. The remaining electron is *donated* to the conduction band. This is illustrated in Figure 2.2b, where the dopant, referred to as *donor*, is phosphorous [28]. This *donated* electron is lightly bound and can move freely under the influence of an electric field [25]. Silicon doped with donors is known as *n-type* silicon.

Instead, if an atom from Group 13[5] (e.g. B, Ga) is introduced, it will only have 3 valence electrons to share with its neighbouring silicon atoms. To close its electronic shell, the Group 13 atom must extract, or *accept*, an electron from a lattice atom in the vicinity. This type of dopant is called an *acceptor*. The extraction of an electron from the valence band, to form four covalent bonds, creates a *hole* that can move freely through the crystal[6]. Silicon doped with acceptors is known as *p-type* silicon. Figure 2.2c depicts the resulting bond structure of p-type silicon.

[3]Modern IUPAC notation for *Group IV* [31]

[4]Modern IUPAC notation for *Group V* [31]

[5]Modern IUPAC notation for *Group III* [31]

[6]The idea of a *hole* with positive charge moving through the lattice is a manner of visualising the movement of electrons within the valence band towards vacant spaces.

2.4 PN-junction

As explained earlier, p-type and n-type silicon are doped with acceptor and donor impurities, respectively. Now, a silicon crystal could be doped in such a way that, within the same crystal, there were two adjoining regions: one doped with acceptors (p-type), and one doped with donors (n-type). This is called a *pn-junction* [25]. Let us assume that the concentration of dopants changes abruptly from acceptors (N_A) to donors (N_D). The condition $N_A \ll N_D$ (or vice versa) implies that the pn-junction is abrupt. For a detailed description of the dynamics of a more realistic non-abrupt pn-junction see [28].

Initially, the p- and n-type regions are electrically neutral. However, due to the large carrier concentration gradients at the junction, carriers will thermally diffuse across it. As holes diffuse from the p-side towards the n-side, negative acceptor ions, fixed in the lattice, remain near the junction creating a negatively charge region within the p-side of the junction. Analogously, electrons diffuse from the n-side to the p-side, leaving behind positively charged donor ions. Consequently, a positive space charge region is formed on the n-side, and a negative one, of equal net charge, is formed on the p-side of the junction, see Figure 2.3a. This space charge builds up a potential and creates an electric field from the positive charge towards the negative, as shown in Figure 2.3b. The electric field opposes the diffusion gradient for each type of charge carrier (see Figure 2.3b). As a result, the diffusion depth for holes and electrons is limited by the *built-in* potential of the space charge. If the potential matches the available energy for thermal diffusion, then the diffused region cannot continue to extend. The magnitude of said potential depends on the doping concentrations of donors (N_D) and acceptors (N_A), and is equal to the difference between the respective Fermi levels of the n- and p-regions: $V_{bi} = E_{Fn} - E_{Fp}$ [25, 30]

As a consequence of the diffusion of carriers across the junction, a region devoid of mobile carriers is generated, the so-called *depletion region*. In thermal equilibrium, the width of this region depends solely on the doping concentrations. If one side is more heavily doped than the other, then the depletion region will extend further into the less doped side. The net charge on both sides of the junction must be equal [26]. Strictly speaking, the depletion region is not entirely free of mobile carriers, as the diffusion profile is a gradual transition. Even so, given the substantial difference in carrier concentration, for future calculations it will be convenient to treat the depletion zone as an abrupt transition between non-depleted bulk and zero carrier concentration [25].

So far, only the situation of a pn-junction at thermal equilibrium has been discussed. If an external potential is applied to the junction, the situation is significantly altered. When a negative voltage is applied to the n-side and a positive to the p-side (known as *forward biasing*), the potential barrier in the junction is reduced. This means that the flow of holes and electrons through the junction will increase, and that the depleted region will shrink. If, instead, the junction is *reverse biased*, i.e. positive voltage to the n-side and a negative to the p-side, the potential barrier increases and the depletion region grows [25]. Hence, the depletion region width w_d depends on the external voltage applied. Whilst w_d

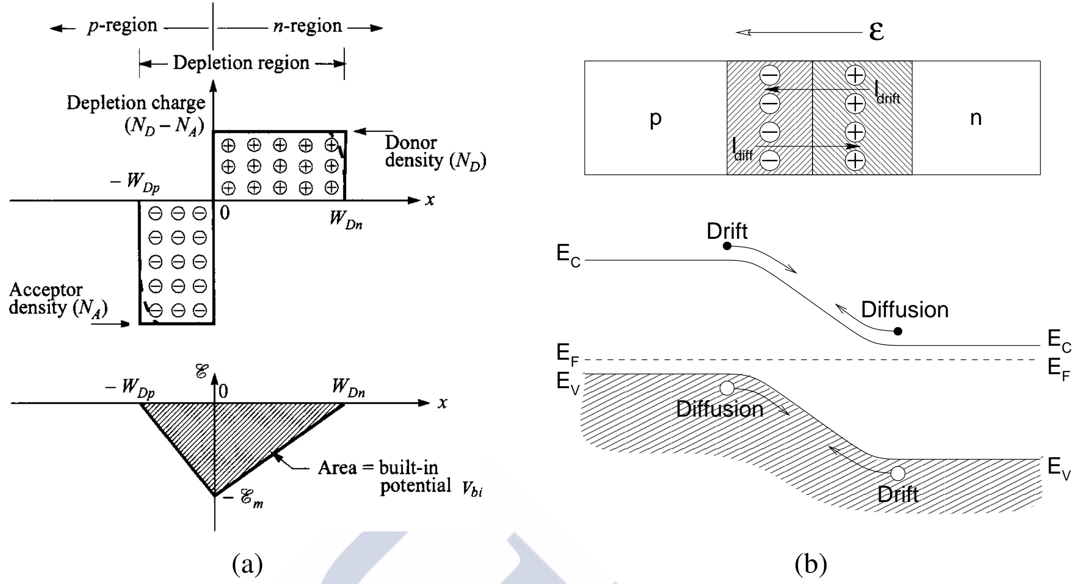

Figure 2.3: (a) Space charge and electric field distribution of a pn-junction in thermal equilibrium. From Sze and Kwok 2007 [28]. ©John Wiley Sons, reproduced with permission. (b) Electric field direction in the depletion region, and energy band diagram of a pn-junction in thermal equilibrium. From [32].

is smaller than the depth of the device d, its growth follows

$$w_d(V) = \sqrt{\frac{2\varepsilon\varepsilon_0}{q_0|N_{eff}|}(V_{bi}+V)} \quad \text{for} \quad w_d \leq d\,, \tag{2.3}$$

$$\text{with} \;\; N_{eff} = N_D - N_A$$

N_{eff} is the *effective doping concentration*, given by the difference between the concentration of ionised donors and acceptors in the space charge region [26]. Eventually, a voltage is reached so that the device is *fully depleted*, i.e. the depletion region occupies the full depth of the sensor. The corresponding voltage is called *full depletion voltage* V_{dep}, and it is given by

$$V_{dep} = \frac{q_0}{2\varepsilon\varepsilon_0}|N_{eff}|d^2 + V_{bi}\,. \tag{2.4}$$

Generally, the built-in voltage V_{bi} is neglected as in most cases it is an order of magnitude smaller than the depletion voltage [26]. These expressions are valid under the assumption that the bulk is lightly doped in comparison to the implant. The depletion region extends predominantly into the bulk, and the contribution to the depletion width of the heavily doped region can be neglected [25].

2.4.1 Capacitance

The capacitance per unit area of a pn-junction is defined as

$$C = \frac{dQ}{dV} = \frac{dQ}{dw_d}\frac{dw_d}{dV}. \tag{2.5}$$

Here, dQ is the incremental change in depletion charge on each side of the junction for an increment dV in the applied voltage. The full charge of a depletion region with volume $V = Aw_d$ is $Q = q_0 N_{eff} A w_d$. The differential is then given by $dQ = q_0 N_{eff} A dw_d$. Applying this, and the derivative with respect to V of Equation 2.3, in Equation 2.5, the following expression is obtained:

$$C = \varepsilon\varepsilon_0 \frac{A}{w_d(V)} = A\sqrt{\frac{\varepsilon\varepsilon_0 q_0 |N_{eff}|}{2(V+V_{bi})}} \quad for \quad w_d \leq d, \quad \text{i.e.} \quad V \leq V_{dep}. \tag{2.6}$$

From Equation 2.6 it can be drawn that, up to full depletion, the capacitance decreases with increasing voltage following the relation $C \propto 1/\sqrt{V}$. Once the device is fully depleted, the capacitance achieves a constant value of

$$C_{end} = \frac{\varepsilon\varepsilon_0 A}{d}. \tag{2.7}$$

Sometimes referred to as *end* or *geometrical capacitance*, this value only depends on the geometry of the diode. Once the device is fully depleted, increasing the applied voltage does not alter the capacitance.

2.5 Charge collection

Inside a semiconductor charge carriers can move either through diffusion or drift. As explained in the previous section, diffusion is driven by a concentration gradient. Thermal energy makes carriers move in random directions. The presence of a concentration gradient implies that carriers will collide more frequently on the direction of the higher concentration. Consequently, the net motion of the charges will be in the direction of the lower concentration [25].

The situation is rather different if an external voltage is applied. Under these conditions, an electric field is created, and the charge carriers move, on average, parallel to this field. Said movement is called *drift*. The *drift velocity* of carriers is proportional to the applied electric field:

$$\vec{v} = \mu \vec{E}\,, \tag{2.8}$$

where μ is the mobility. Electrons and holes have different mobilities. In silicon at 300 K, and up to fields of about 10^4 V/cm, the mobility for electrons is of 1450 cm^2/Vs, and for holes is of 450 cm^2/Vs. In this regime, the mobility is only dependent on temperature. At higher fields, the interactions between the charge carriers and the lattice increase. In fact, at high fields the mobility decreases following $\mu \propto 1/E$. The drift velocity no longer increases linearly with the electric field, and it saturates at a constant velocity, commonly denoted as *saturation velocity* [25, 28].

For the operation of silicon sensors, a reverse bias voltage is applied. This voltage allows for the growth of the depletion region (reaching full depletion in many detector designs), and consequently creates an electric field inside of the sensor. When a particle traverses a silicon detector or when a photon is absorbed, electrons and holes are produced. If they are created within the depletion region, or if they reach it, they will start drifting under the influence of the electric field. Due to their opposite charge, e^- and h^+ move in opposite directions. The time required for each charge to traverse the full sensitive volume of the device is known as *collection time*. The collection time can be significantly reduced by increasing the bias voltage above full depletion. As the carriers move, they instantaneously induce a current pulse on the electrodes of the device. The current induced by a single charge carrier can be described by Ramo's Theorem:

$$i(t) = -q\vec{v}\cdot\vec{E}_W = -q\mu\vec{E}\cdot\vec{E}_W\,. \tag{2.9}$$

The induced current is dependent on the drift velocity of the charge carrier in question, and on the *weighting field* ($\vec{E}_W$). The weighting field describes the coupling of a charge at any position to a given electrode. The weighting field should not be confused with the actual electric field. The electric field determines the trajectory of the charges and their velocity. Instead, the weighting field determines how charge motion induces a current on a specific electrode, and it is dependent solely on geometry.

Chapter 3

Radiation Damage

Semiconductor devices are not immune to the effects of radiation. The damage produced by radiation in silicon can be divided into two categories, *ionisation damage* and *displacement damage*. Each of these affects the bulk and the surface of the devices differently. For instance, ionisation causes no damage in the bulk, it creates e^-/h^+ pairs that are driven away from the sensitive volume of the sensor. On the contrary, ionisation creates fixed positive charges inside the oxide layer on the surface of the sensor, modifying the electric field. This damage to the surface can affect the read-out in segmented devices, and can increase the surface generation current. On the other hand, the effect of displacement damage on the surface is negligible. However, the changes it causes in the bulk affect basic detector properties such as leakage current, capacitance, effective doping, signal formation, electric field profile, etc [25, 33].

3.1 Surface damage

Ionisation can cause permanent damage to the insulating layers of sensors (usually SiO_2), and to the interface with the bulk. Figure 3.1 shows schematically the process that leads to permanent surface damage [33]. The incident ionising particle creates e^-/h^+ pairs, most of which recombine immediately, (b) and (c). Just as in silicon, electrons have a high mobility in SiO_2 ($\mu_e \approx 20\text{cm}^2/\text{Vs}$), so they are rapidly collected at the positive electrode. Holes have a lower mobility ($\mu_h \approx 2 \times 10^{-5}\text{cm}^2/\text{Vs}$), meaning that they move slowly towards the SiO_2-Si interface, (d) and (e). Some of these holes may get trapped in the oxide and in the interface, (f). In turn, those trapped holes will attract electrons from the silicon bulk. These accumulations of electrons can form conducting channels between detector electrodes, which affects the read-out of the device. Also, due to displacement damage, additional energy levels are created in the silicon bulk (see following sections). When close to the SiO_2-Si interface, these additional energy states can alter the surface generation current properties of the material, thus increasing the surface leakage current [25, 33].

UNIVERSIDADE DE SANTIAGO DE COMPOSTELA

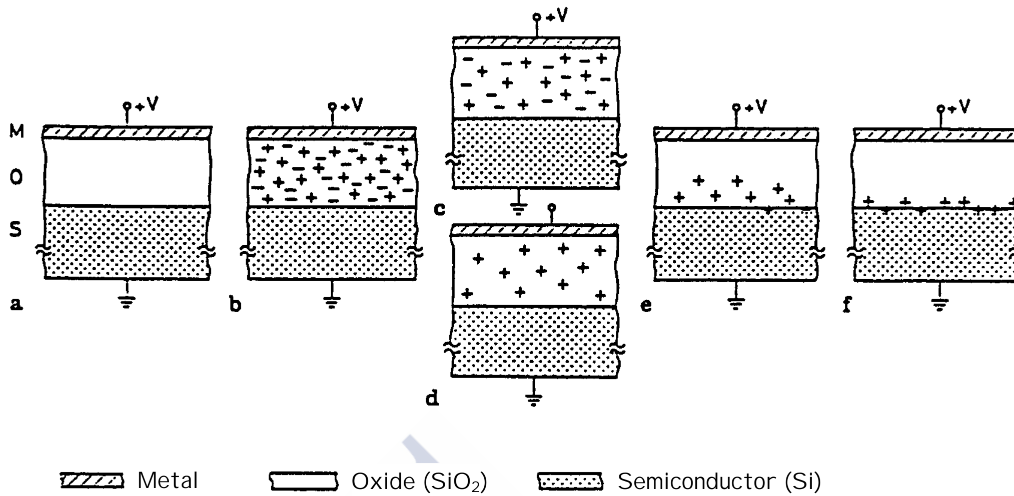

Figure 3.1: Schematic of the damage produced on the surface of a silicon sensor through ionisation. Modified from [33].

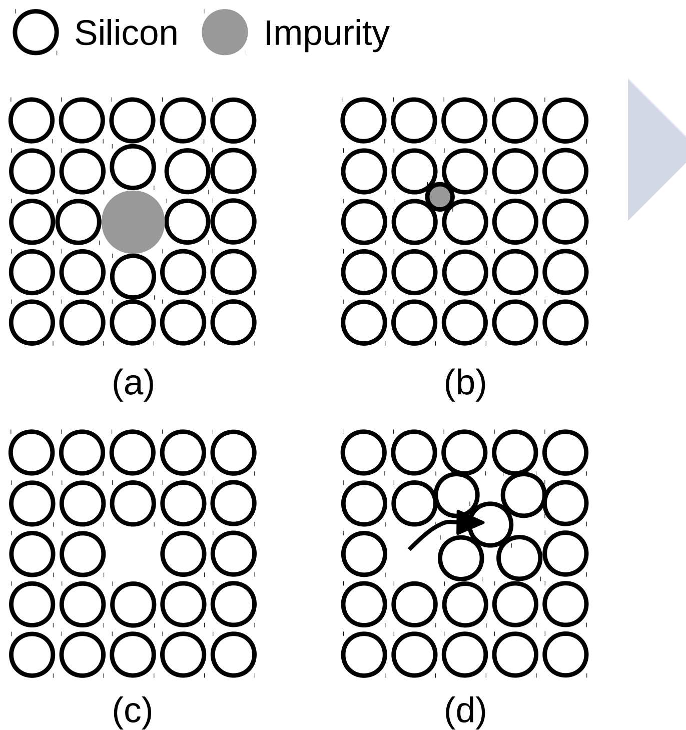

Figure 3.2: Point defects. (a) Substitutional impurity. (b) Interstitial impurity. (c) Lattice vacancy. (d) Frenkel defect. After [30].

3.2 Bulk damage

Bulk properties define in great extent the characteristics of a silicon sensor, thus displacement damage is the chief damage mechanism in HEP applications. The radiation that the devices are meant to detect is the same that damages them. The interaction between radiation and the electron cloud is the basis of the detection method, and is a transient effect with no long-lasting repercussions. Instead, the interaction with the lattice may lead to permanent material changes, which often are of detrimental nature [29]. Since displacement damage is caused by the transfer of energy and momentum to the lattice, it depends on the non-ionising energy loss (NIEL) of the impinging particle. This, in turn, depends on the mass and energy of the incident particle [25]. The probability of displacing a silicon atom from its lattice location, and its recoil energy, depend on the type and energy of the impinging radiation. On the one hand, the elastic cross section for scattering on silicon depends on the type of radiation. Charged particles interact electrostatically with the partially screened nucleus, whilst neutral particles scatter elastically with the nucleus only. On the other hand, the energy transfer and kinematics of the interaction depend on the mass of the incident particle [29].

The principal processes leading to bulk damage are the displacement of lattice atoms, thus generating *point defects*; nuclear interactions, such as neutron capture and nucleus transmutation; and the formation of damage *clusters* at the end of the recoil path of energetic displaced lattice atoms. If the energy of the recoil is above 25 eV, point defects will be created. For recoil energies between 2 keV and 12 keV, the energy is high enough to create one defect cluster and additional point defects. Recoil energies above 12 keV result in several clusters and additional point defects.

The aforementioned point defects can be classified into four different types: *substitutional defects*, i.e. there is a different type of atom at a lattice site than expected; *interstitials*, i.e. atoms located at a normally unoccupied site of the lattice; *vacancies*, i.e. empty lattice sites caused by the removal of an atom from its lattice site; and *Frenkel defects*, the combination of an interstitial next to a vacancy [29]. All of these are represented in Figure 3.2.

At room temperature, most primary defects are mobile and cannot be considered stable. For instance, an interstitial may fill the place of a vacancy. However, they may also interact with other lattice defects, either already present in the crystal or caused by radiation. This can lead to the formation of a new type of defect that is both immobile and stable at room temperature [29]. The most notable manifestations of displacement damage are three [25]:

- Formation of mid-gap states. These intermediate states in the forbidden band facilitate the transition of electrons from the valence to the conduction band (*generation*), and vice versa (*recombination*). Both transitions occur in steps of electron and hole

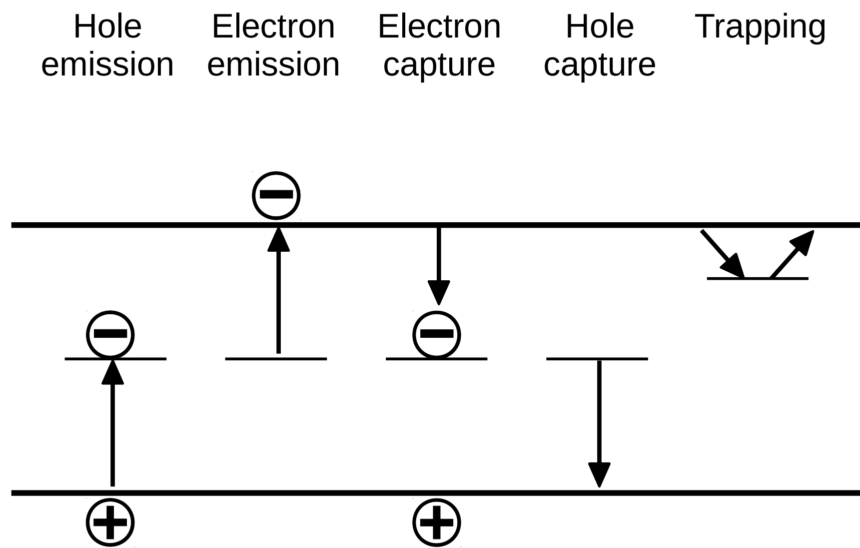

Figure 3.3: Emission and capture processes through intermediate states. The arrows show the direction of electron transitions. After [25].

capture or emission. These individual steps are illustrated in Figure 3.3. In depleted regions, where the conduction band is underpopulated, generation dominates, i.e. the leakage current of the reverse-biased pn-junction increases. In forward-biased junctions or non-depleted regions, the conduction band has a higher carrier concentration, hence recombination prevails, i.e. there is charge loss.

- Formation of defect energy levels close to a band edge. Electrons or holes can be captured and emitted after a certain time. This phenomenon is referred to as *trapping*, and it is illustrated in Figure 3.3. If the emission times of these *traps* are longer than the acquisition time of the detector, the signal is reduced. Also, the presence of temporarily fixed charges can induce changes in the space charge.
- Changes in the doping characteristics. Defects can act as donors, acceptors or be electrically neutral. If electrically active, in sufficient concentration they can change the effective donor and/or acceptor concentration, which will impact on the charge density of the space charge. Macroscopic properties, such as the full depletion voltage, will be affected.

In the following sections, the effects of these defects in the sensor properties will be discussed in greater detail.

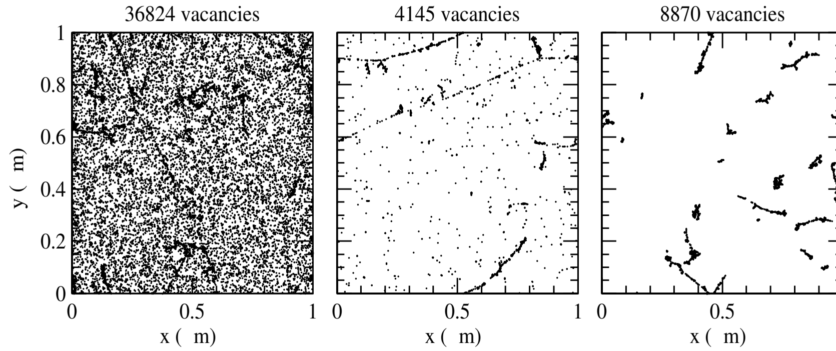

Figure 3.4: Simulation of the distribution of defects (vacancies) produced by (left) 10-MeV protons, (middle) 24-GeV/c protons, and (right) 1-MeV neutrons, up to a fluence of 10^{14} cm^{-2}. The plots are projections over 1 μm of depth (z). From Huhtinen 2002 [34]. ©Elsevier Science B.V., reproduced with permission.

3.2.1 NIEL-scaling hypothesis

Previously it was explained that bulk damage depends on the energy and type of incident particle, as the interactions with the lattice will be different. Charged particles interact electrostatically with the partially screened nucleus, whilst neutral particles scatter elastically with the nucleus only. Figure 3.4 shows the expected distribution of defects in silicon after irradiation, up to the same fluence, with 10-MeV protons, 24-GeV/c protons, and 1-MeV neutrons. This raises the question of how to compare the damage caused by different types of radiation. To solve this issue, the so-called *Non-Ionising Energy Loss scaling hypothesis* was proposed.

The basic assumption of the NIEL-scaling hypothesis is that the bulk damage caused by energetic particles can be described as being proportional to the energy deposited in collisions leading to displacement, i.e. the NIEL, also referred to as the displacement damage cross section D. The displacement damage cross section can be calculated by using the cross sections (σ_ν) and recoil-energy distributions (E_R) of each interaction leading to displacement damage. The fraction of the total energy loss of the impinging particle that actually contributes to the NIEL ($P(E_\mathrm{R})$) must also be considered. Finally, the contribution of all possible interactions between the incoming particle of energy E and the lattice must be considered. The expression for D is then

$$D(E) := \sum_\nu \sigma_\nu(E) \int_0^{E_\mathrm{R}^{\mathrm{max}}} f_\nu(E, E_\mathrm{R}) P(E_\mathrm{R}) dE_\mathrm{R}. \tag{3.1}$$

Here the integration is done over all possible recoil energies. $f_\nu(E, E_\mathrm{R})$ is the probability of occurrence of each interaction.

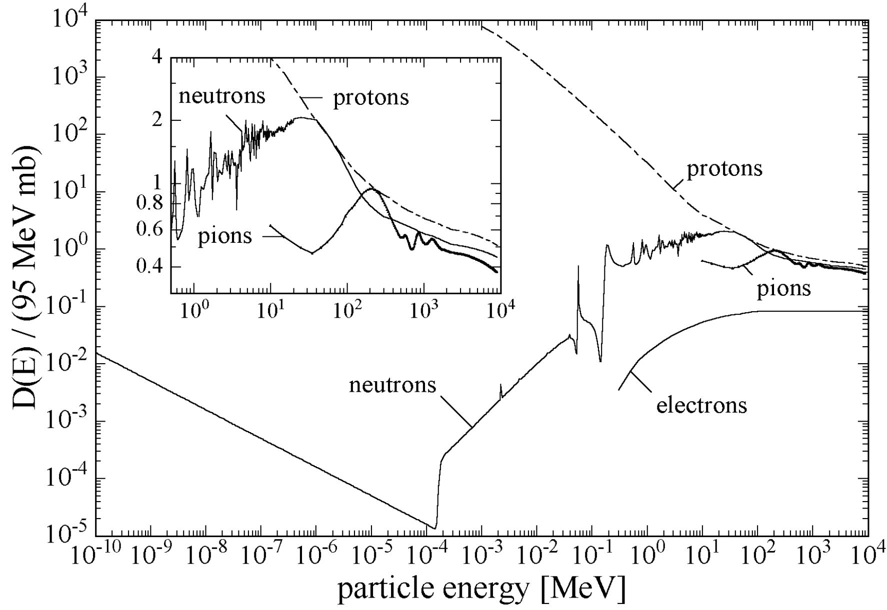

Figure 3.5: Normalised displacement damage cross sections as a function of energy for neutrons, protons, pions and electrons. From [26].

Now that the displacement damage cross section has been defined, it can be used to compare the damage efficiency of different radiation sources with different particles, and a given energy distribution of their fluence ($\phi(E)$). In order to normalise all damage efficiencies to that of a given particle and energy, a *hardness factor* κ was defined. The hardness factor compares the damage efficiency of a specific irradiation to the damage which would have been produced by the same fluence of 1-MeV neutrons:

$$\kappa = \frac{\int D(E)\phi(E)dE}{D(E_n = 1\text{ MeV})\int \phi(E)dE}\,, \tag{3.2}$$

with $D(E_n = 1\text{ MeV}) = 95\text{ MeV mb}$.

By means of the hardness factor of a specific radiation source it is possible to define the equivalent 1 MeV neutron fluence ϕ_{eq}:

$$\phi_{eq} = \kappa \int \phi(E)dE. \tag{3.3}$$

Figure 3.5 shows the normalised displacement damage cross sections as a function of energy for neutrons, protons, pions and electrons. For further details about the experimental determination of the hardness factor see [26].

It should be mentioned that the NIEL-scaling hypothesis should not be regarded as universally valid. Exceptions to this rule have been found, for instance, comparing the effect that neutrons and charged hadrons have on the effective space charge. Nevertheless, to get an approximation of what could be expected from different particles and energies, the NIEL-scaling hypothesis gives fairly reliable results [35].

3.2.2 Trapping

Semiconductor crystals present imperfections in the lattice either from the crystal growth process or caused by radiation damage. Defects such as vacancies, dislocations or impurities introduce additional energy levels in the bandgap that can trap charge carriers. As a charge carrier moves through the sensor, the probability of it being trapped is proportional to the elapsed time. The trapping probability is actually defined as the inverse of the *carrier lifetime* τ, i.e. the time a charge carrier can spend traversing the crystal before getting trapped. After injection into a device of a certain amount of charges, if some of the charge carriers get trapped, the mobile charges available for signal formation will decrease following

$$Q(t) = Q_0\,\mathrm{e}^{-t/\tau_{e,h}}. \tag{3.4}$$

Q_0 is the initial charge that will decay exponentially as carriers get trapped. Assuming that thermal velocity (v_{th}) dominates over drift velocity, so that $\tau_{e,h}$ is proportional to v_{th} [25], the trapping probability caused by radiation damage is defined as

$$\frac{1}{\tau_{e,h}} = \sum_t N_t(1 - P_t^{e,h}(T))\sigma_{t_{e,h}} v_{th_{e,h}}. \tag{3.5}$$

N_t is the trap concentration, $\sigma_{t_{e,h}}$ and $v_{th_{e,h}}$ are the capture cross section and the thermal velocity of electrons and holes. $P_t^{e,h}(T)$ refers to the occupation probability of a trap of energy E_t for either electrons or holes [36]. Under the approximation that the space charge region is void of charge carriers (reasonable assumption for reverse-biased devices) [37], the occupation probabilities for electrons and holes are

$$P_t^e(T) = \frac{1}{\frac{c_e}{c_h}\chi_t^2 + 1}, \tag{3.6}$$

$$P_t^h(T) = 1 - P_t^e(T) = 1 - \frac{1}{\frac{c_e}{c_h}\chi_t^2 + 1}, \tag{3.7}$$

$$\text{with} \quad \chi_t = \mathrm{e}^{(E_t - E_i)/kT} \quad \text{and} \quad c_{e,h} = \sigma_{t_{e,h}} v_{th_{e,h}}. \tag{3.8}$$

Considering that $v_{th} \propto \sqrt{T}$, and that the capture cross section scales with temperature as $\sigma(T)/\sigma(T_0) = (T/T_0)^m$ with m between -2 and 2 [36], the trapping probability at a given temperature is described by

$$\frac{1}{\tau_{eff_{e,h}}} \propto \phi_{eq} \frac{1 - P_t^{e,h}(T)}{1 - P_t^{e,h}(T_0)} \left(\frac{T}{T_0}\right)^{m+1/2}. \tag{3.9}$$

Here it has been assumed that the concentration of radiation-induced traps is proportional to the fluence ϕ_{eq}, specifically to the *equivalent fluence* (see Section 3.2.1) [36].

Based on the previous expression, it is evident that the trapping probability depends on both the fluence and the temperature. According to the results from the study in [36], the trapping probability increases linearly with fluence, and decreases with increasing temperature.

Another important parameter associated to traps is the *emission probability*, as this is related to the actual time the charge carriers remain trapped. Let us remember that, if the emission time of the traps is longer than the acquisition time, there is a reduction in collected charge, i.e. the integral of the signal measured within the acquisition time. On the contrary, if the charge is released before the end of the acquisition time period, then the charge collection is not affected. The emission probabilities for holes (e_p) and electrons (e_n) are given by the following expressions:

$$e_p = v_{th_h} \sigma_{t_h} N_V \, \mathrm{e}^{-(E_t - E_V)/kT}, \tag{3.10}$$
$$e_n = v_{th_e} \sigma_{t_e} N_C \, \mathrm{e}^{-(E_C - E_t)/kT}. \tag{3.11}$$

The emission probability of holes e_p grows exponentially as the energy level of the trap E_t approaches the valence band E_V. Analogously, e_n increases exponentially as the trap approaches to the conduction band E_C. Finally, e_p and e_n are highly dependent on temperature. As the temperature decreases the emission probability decreases as well, so the charge carriers remain trapped for a longer period at lower temperatures [38].

3.2.3 Space charge sign inversion

Radiation induced defects can alter the doping profile of a silicon sensor. In particular, it is possible for the space charge to undergo an inversion of sign due to the created damage.

3.2.3.1 Type inversion

In the case of n-type silicon, it was found that after low levels of irradiation the effective doping decreases until it appears intrinsic (undoped). For instance, a device with an initial N_{eff} of about $10^{11} - 10^{12}$ cm^{-3} becomes intrinsic after irradiation up to a fluence of the order of $10^{12} - 10^{13}$ $n_{\text{eq}}/\text{cm}^2$. At higher fluences, the effective doping (or space charge) increases, but with the opposite sign to the one it had before irradiation, i.e. it behaves as if it were p-type silicon, see Figure 3.6. A combination of processes occur to give place to this phenomenon. Firstly, the transformation from n-type to intrinsic-like (positive space charge to neutral) could be attributed to *donor removal*. This does not imply the actual physical removal of donor atoms, but the formation of complexes between donors and defects that render the donors electrically inactive or neutral. In particular, the formation of vacancy-phosphorus (V-P) complexes reduces the number of active phosphor donors. This reaction, however, does not explain the observed *type inversion*. As a matter of fact, this is consistent with the creation of acceptor-like states, which form a negative space charge by capturing electrons from the bulk through thermal excitation. Divacancy complexes (V-V) are one of the candidates for these acceptor-like defects. Initially they contribute to the reduction of the effective donor concentration by neutralising donor states. Eventually, at a certain fluence, they balance each other out, so the space charge is zero, i.e. intrinsic. At higher fluences, the acceptor-like states dominate and result in a net negative space charge (p-like). The change in space charge after irradiation up to a fluence ϕ is

$$N_C(\phi) = N_{C0}(1 - \mathrm{e}^{-c\phi}) + g_C\phi. \tag{3.12}$$

The first term describes donor removal, where N_{C0} is the concentration of removable donors, and c the removal constant. The second term describes the generation of acceptor states. g_C is the introduction rate of *stable acceptors*, i.e. defects that are independent of annealing.

To operate a device that has undergone space charge sign inversion, no change is needed in bias polarity. However, for the full device to be depleted, i.e. to establish the electric field in the full volume of the sensor, the biasing voltage will have to be raised proportionally to the increase in space charge (remember that $V_{\text{dep}} \propto |N_{eff}|$, see Equation 2.4) [25, 39].

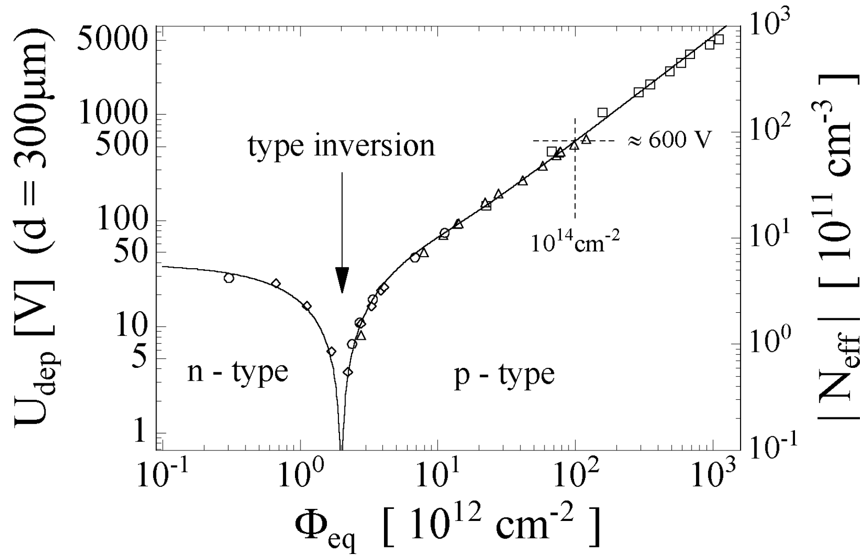

Figure 3.6: Depletion voltage and absolute effective doping with respect to fluence for an initially n-type silicon. From [26].

3.2.3.2 Trapping-induced N_{eff}

Another source of space charge sign inversion is trapping. At low temperatures the electric field inside of a sensor may be affected by the increasing effect of trapping centres. As explained in Section 3.2.2, the trapping probability and the emission time increase with decreasing temperature. The lower the temperature, the more carriers will be trapped, and the more inefficient the detrapping will be. These additional trapped charges could alter the effective doping concentration N_{eff}, which would modify the electric field distribution, and in turn the charge collection properties of the sensor [40]. This trapping-induced space charge sign inversion can occur due to the injection of carriers into the depleted region of an irradiated detector or due to the carriers from the leakage current of the device itself [10, 41].

Consider the situation of a large number of electrons being injected in the depleted region of an irradiated device at low temperatures. In the n-type region of the sensor (positive space charge), electron trapping could convert the positive space charge into negative, i.e. into p-like. Similarly, if holes were the ones being injected, the negative space charge of the p-type region could convert into positive, i.e. n-like [40]. If the temperature of the device were to be increased, the emission times of the traps would decrease. Consequently, a lower number of trapped carriers would contribute to the space charge, thus reverting the effect [41].

This effect has been observed as well in irradiated p+/n/n+ detectors with a type-inverted bulk. As explained earlier, after highly irradiating a device with an n-type bulk, the n-type region (positive space charge) undergoes type inversion and behaves as if it were p-type (negative space charge). This eventually results in an increase of the depletion voltage. At low temperatures, a continuous injection of holes would lead, first, to a compensation of the negative space charge. Afterwards, the sign of the space charge would invert from negative to positive, thus recovering the before-irradiation space charge sign, and decreasing the depletion voltage. If the temperature of the device were increased, the emission times would decrease. Fewer trapped holes would contribute to the space charge which would go back to being negative. Interestingly, if instead of continuously injecting holes at low temperatures, electrons were injected, the space charge of the type-inverted bulk would become yet more negative. As a result, the depletion voltage would further increase [41, 42].

3.2.4 Annealing

After irradiation of a device it is seen that the observed damage to the detector (increase in leakage current, change in space charge, trapping probability, etc.) diminishes with time. The rate at which this occurs is dependent on the temperature at which the device is kept during that period. This effect, called *beneficial annealing*, is caused by a series of mechanisms that alter the irradiation-induced defects. Defects might recombine (e.g. a vacancy being filled by a silicon interstitial), they can transform and create complexes by association with other defects, also, complexes may dissociate into their components. The change in space charge caused by beneficial annealing (N_A) is usually described by

$$N_A(t) = \phi g_a \mathrm{e}^{-t/\tau_a}. \tag{3.13}$$

The factor g_a is the average introduction rate of defects. The time constant τ_a scales with temperature as

$$\frac{1}{\tau_a} = k_{0a} \mathrm{e}^{-E_a/kT_a}. \tag{3.14}$$

T_a is the temperature at which the device is annealed. E_a is the activation energy of the mechanisms causing the annealing, and the factor k_{0a} is the *attempt-to-escape frequency* [26, 29]. To better understand the physics behind Equation 3.14, imagine an interstitial vibrating in the lattice at a frequency k_{0a}, and approaching periodically an energy barrier E_a for migration to a vacancy. The probability of the interstitial having enough energy to surpass this barrier, and thus recombine with a vacancy, is given by the factor $\exp(-E_a/kT_a)$. Hence, $1/\tau_a$ is the probability that a given interstitial has sufficient energy to recombine with a given vacancy times the frequency of approach to the barrier,

the so-called attempt-to-escape frequency k_{0a} [43].

In the long term, the effect of annealing may no longer be beneficial for detector performance. In fact, radiation-induced defects may interact causing originally electrically inactive defects to become active. This process is called *reverse annealing*. The change in effective space charge caused by reverse annealing (N_Y) can be parameterised with the following function:

$$N_Y(t) = g_Y \phi \left(1 - \frac{1}{1 + t/\tau_Y}\right). \tag{3.15}$$

Here g_Y is the average introduction rate of defects, and τ_Y a time constant that can be expressed by the relation

$$\frac{1}{\tau_Y} = k_{0Y} \mathrm{e}^{-E_Y/kT_a}. \tag{3.16}$$

T_a is the temperature at which the device is kept during the annealing process. E_Y is the activation energy, and k_{0Y} is the attempt-to-escape frequency [26, 29]

Equation 3.17 summarises the cumulative effect of the phenomena that affect the space charge, except for trapping: type inversion, beneficial annealing, and reverse annealing.

$$\Delta N_{eff}(t) = N_{eff,0} - N_{eff}(\phi, t(T_a)) = N_C(\phi) + N_A(\phi, t(T_a)) + N_Y(\phi, t(T_a)), \tag{3.17}$$

$N_{eff,0}$ is the effective space charge before irradiation. $N_{eff}(\phi, t(T_a))$ is the effective space charge after irradiation to a fluence ϕ, and after an annealing period t at temperature T_a. $N_C(\phi)$ represents the donor removal observed in type inversion, see Equation 3.12. $N_A(\phi, t(T_a))$ and $N_Y(\phi, t(T_a))$ are the change in space charge due to beneficial (Equation 3.13) and reverse (Equation 3.15) annealing, respectively.

An example is show in Figure 3.7 of the evolution with time of the change in effective doping concentration at 60°C of an irradiated PiN diode irradiated. The three aforementioned components are indicated (N_C, N_A and N_Y). At times below $\sim$ 100 min, beneficial annealing reduces the change in space charge, later reverse annealing dominates.

Finally, given the temperature dependence of these processes, lowering the temperature of the sensor has a significant effect on the evolution of N_{eff}. At low temperatures the annealing process slows down, and reveres annealing is delayed. This is one of the reasons why in HEP silicon detectors are not only operated at low temperature (this is also to decrease leakage current, see Section 3.3), but they are cooled even when not in operation.

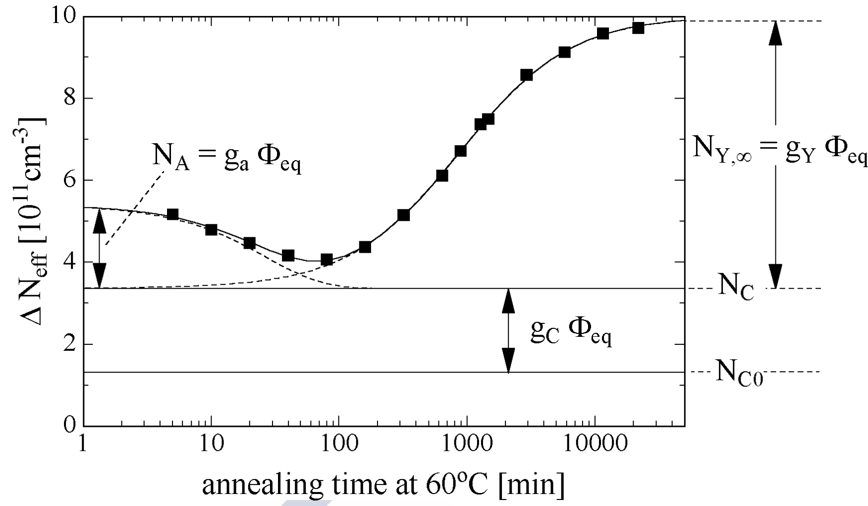

Figure 3.7: Evolution with time of the change in effective doping concentration (ΔN_{eff}) at 60°C of a PiN diode irradiated up to 1.4×10^{13} cm^{-2}. From [26].

In fact, the detectors are only warmed up during maintenance. During cooling, beneficial annealing is suppressed too. However, the time spent at room temperature during maintenance is usually more than enough for beneficial annealing to take place [25, 26, 44].

3.2.5 Acceptor removal

Previously, the concept of donor removal in irradiated n-type silicon was explained. After irradiation of p-type silicon an analogous effect called *acceptor removal* occurs. The origin of acceptor removal has yet to be fully understood. It is thought that due to irradiation, boron atoms are removed from their lattice locations (substitutional state) and get electrically deactivated by forming complexes with other elements [45]. Various complexes can be formed, however, the chief candidate for acceptor removal is the combination of one boron and one oxygen interstitial: B_iO_i, see Figure 3.8 [46]. The observed dependence of the acceptor concentration with fluence is an exponential decay:

$$N_A(\phi) = N_{A,0}\, \mathrm{e}^{-c\phi}. \tag{3.18}$$

$N_{A,0}$ is the acceptor concentration before irradiation, and c is the *acceptor removal coefficient* [10].

Given that the depletion voltage is proportional to the effective doping (see Equation 2.4), if the concentration of acceptors decreases, i.e. if less acceptors are electrically active, the depletion voltage will decrease too, see Equation 3.19.

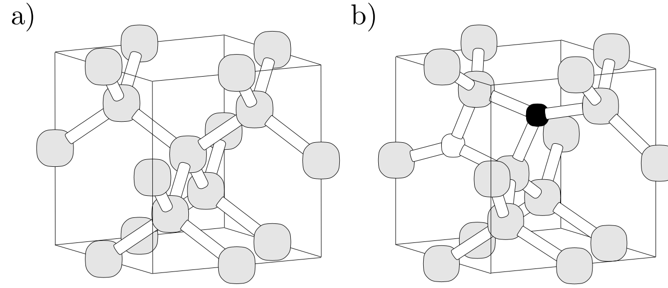

Figure 3.8: Lattice structure of (a) pure silicon, and (b) silicon with a B_iO_i defect complex. Grey balls represent silicon, small black are boron, and small white are oxygen. From [46].

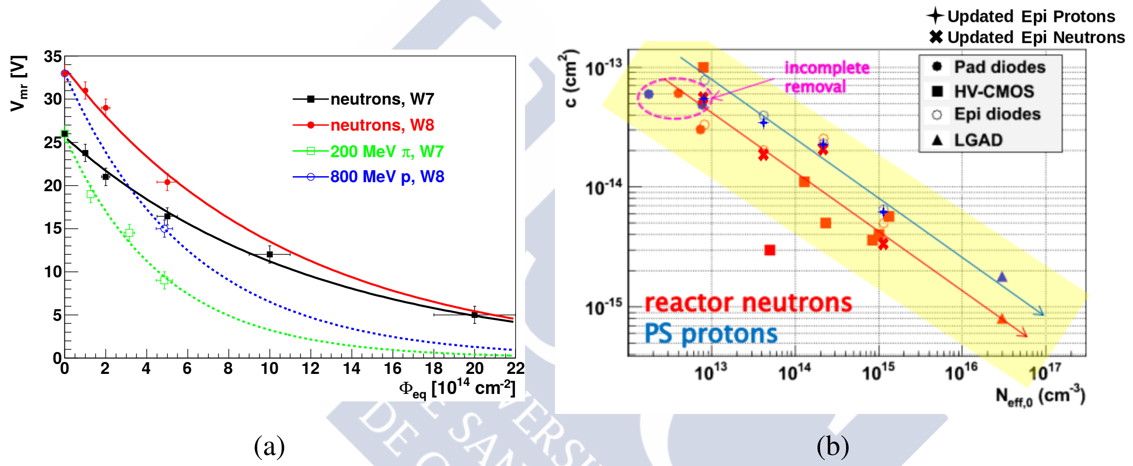

Figure 3.9: (a) Depletion voltage as a function of fluence in p-type silicon. From [10]. (b) Acceptor removal coefficient c with respect to initial acceptor concentration, for different devices and irradiations. From [47].

$$V_{dep}(\phi) \propto V_{dep,0}\, \mathrm{e}^{-c\phi}. \tag{3.19}$$

Where $V_{dep,0}$ is the initial depletion voltage (before irradiation) [10].

As regards the acceptor removal coefficient c, it was found experimentally that this value is dependent on the type of irradiation, and on the initial concentration of acceptors. Figure 3.9a shows the depletion voltage[1] as a function of fluence for different types of irradiation, namely neutrons, pions, and protons. The data show that c is larger for irradiation with charged hadrons. Figure 3.9b shows how, for different devices and irradiations, the acceptor removal coefficient decreases with increasing initial acceptor concentration [47].

[1]It should be clarified that these data correspond, not to the full depletion voltage of a device, but to the depletion voltage of the multiplication layer of various Low Gain Avalanche Detectors. This topic will be discussed in detail in Chapters 6 and 7.

3.3 Leakage current

3.3.1 Dependence with fluence

As explained at the beginning of this chapter, the creation of mid-gap states after irradiation causes an increase in leakage current. Experimentally it has been found that the increase in leakage current is proportional to the fluence:

$$\Delta I = \alpha \phi V. \tag{3.20}$$

ΔI is the difference between the leakage current after and before irradiation. V is the active volume of the device, and the proportionality factor α is called *current related damage rate*. α depends on the annealing history of the sensor (annealing temperature and time), but has been found to be independent of fluence in the range $\phi_{eq} = [10^{11}, 10^{14}]$ cm^{-2}, for further details see [26].

3.3.2 Dependence with temperature

Another important feature of leakage current is its strong dependence with temperature. Leakage current decreases with temperature, so after irradiation it is possible to maintain the current at low values and away from thermal runaway by refrigerating the sensors. Both the surface and the bulk generation current decrease with temperature. In fact, the same temperature dependence is expected for the two. The explanation for this is as follows. Both currents are described by the following equations [48]:

$$I_s = qn_is_gA \ , \quad I_{\text{bulk}} = \frac{qn_iw_dA}{\tau_g} \ , \tag{3.21}$$

where q is the charge, A the active area, w_d the depletion depth, n_i is the intrinsic charge carrier concentration, τ_g is the bulk generation lifetime, and s_g is the surface generation velocity.

Assuming that the bulk current is generated through a trap level of energy E_t and density N_t, the bulk generation lifetime τ_g is described by

$$\tau_g = \frac{1}{N_t}\left(\frac{\exp\left(\frac{\Delta_t}{kT}\right)}{v_{th_h}\sigma_{t_h}} + \frac{\exp -\left(\frac{\Delta_t}{kT}\right)}{v_{th_e}\sigma_{t_e}}\right) , \tag{3.22}$$

where $\Delta_t = E_t - E_F$ is the difference between the trap level and the intrinsic Fermi level. $v_{th_{e,h}}$ and $\sigma_{t_{e,h}}$ are the thermal velocities and the trapping cross sections for electrons and holes [48, 49].

Similarly, the surface current is assumed to be generated through a trap level of energy E_{it} and density N_{it}. The surface generation velocity is given by

$$s_g = N_{it}\,\frac{\sigma_{s_e} v_{th_e} \cdot \sigma_{s_h} v_{th_h}}{\sigma_{s_e} v_{th_e} \exp[\Delta_t/kT] + \sigma_{s_h} v_{th_h} \exp[-(\Delta_t)/kT]}\,. \tag{3.23}$$

Here, once again, $\Delta_t = E_{it} - E_F$ is the difference between the interface trap level and the intrinsic Fermi level; $v_{th_{e,h}}$ refers to the thermal velocities of electrons and holes; and $\sigma_{s_{e,h}}$ to the trapping cross sections for the interface trap.

The usual assumption will be made that $v_{th_e}\sigma_{t_e(s_e)} \approx v_{th_h}\sigma_{t_h(s_h)}$ [49]. Based on the premise that the energy level of traps, in the bulk and the surface, is close to the intrinsic Fermi level, $1/\tau_g$ and s_g can be assumed to be proportional to $\sqrt{T}$ [48, 49]. If instead, $|\Delta_t/kT| > 1.5$, then the dependence with temperature of $1/\tau_g$ and s_g is mainly given by $\exp(-\Delta_t/kT)$ [49]. Putting all of these together, and remembering the expression for the intrinsic charge carrier concentration (Equation 2.2), it is found that both the bulk and the surface generation current are expected to have an identical dependence on temperature:

$$I(T) \propto T^2 \exp\left(-\frac{E_g + 2\Delta_t}{2kT}\right). \tag{3.24}$$

Generally, to parameterise the dependence of leakage current with temperature, an effective energy $E_{eff} = E_g + 2\Delta_t$ is introduced. E_{eff} represents the effective energy required for the generation of current through a mid-gap level. This energy is also referred to as activation energy (E_a), where $E_a = E_{eff}/2$. Finally, the usual parameterisation used is given by

$$I(T) \propto T^2 \exp\left(-\frac{E_{eff}}{2kT}\right) = T^2 \exp\left(-\frac{E_a}{kT}\right). \tag{3.25}$$

Within the temperature range 250-415 K (203-295 K for the surface) the effective energy is near 1.21 eV [49, 50].

Chapter 4

Experimental Techniques

To characterise, before and after irradiation, the devices under study in this thesis, 6 methods were employed: IV measurements, i.e. leakage current as a function of voltage; CV measurements, i.e. capacitance as a function of voltage; radioactive source measurements, i.e. charge collection as a function of voltage; the Transient Current Technique (TCT) [51]; edge-TCT [52]; and Two-Photon Absorption (TPA) TCT [53]. Each of these methods provides insight into different aspects of the sensor performance, and radiation damage. The particularities of said techniques will be discussed in the following sections. In addition, a brief description of the facilities were the irradiation campaigns took place is included.

USC UNIVERSIDADE DE SANTIAGO DE COMPOSTELA

4.1 CV/IV measurements

Characterising the electrical properties of sensors is fundamental for the evaluation of their quality and performance. From IV curves the breakdown voltage, and power consumption can be determined. Also, the magnitude of the leakage current can be directly related to the amount of lattice imperfections, caused by radiation or production issues, that form intermediate energy levels within the bandgap (see Section 3.3). CV curves will provide information about the effective doping concentration, and the depletion voltage of the sensors. As explained in Section 2.4.1, before full depletion, the capacitance of a sensor follows the proportionality relation $C \propto 1/\sqrt{V}$. After full depletion, the capacitance remains constant for all voltages (end capacitance). Figure 4.1 shows a typical plot of $1/C^2$ with respect to V for a normal PiN diode. Before full depletion, it is possible to describe the data with a linear fit that increases with voltage (green line in Figure 4.1). After full depletion, the capacitance is constant so the plot of $1/C^2$ with respect to V reaches a plateau, which can be described through a constant linear fit (red line in Figure 4.1). The depletion voltage is defined as the voltage at which these two fits intersect [54].

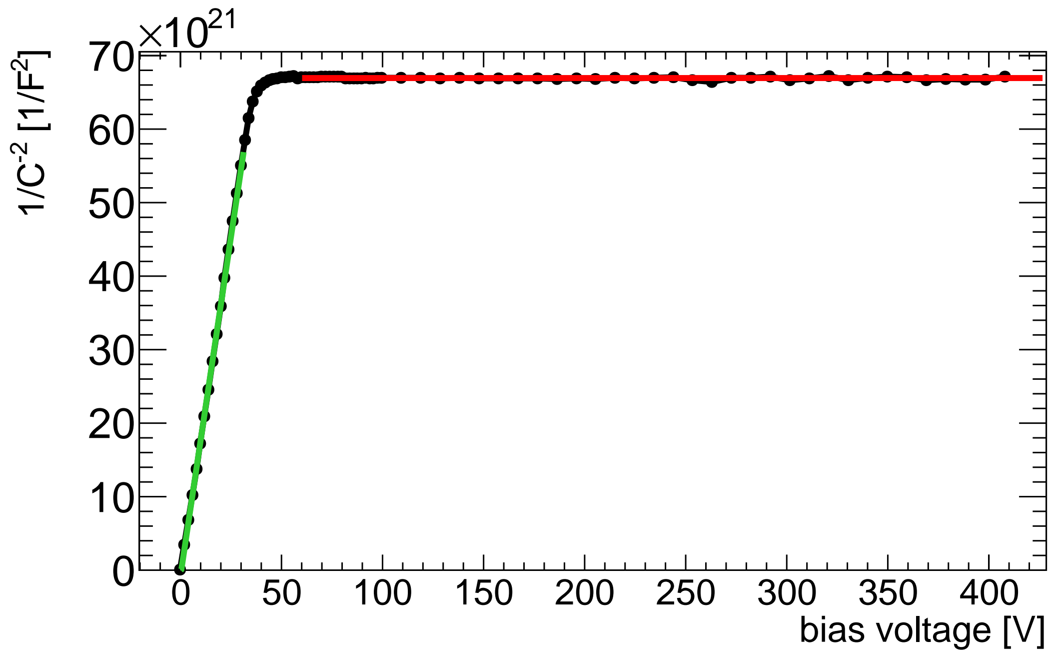

Figure 4.1: Example of a typical CV measurement on a PiN diode. Before full depletion, $1/C^2$ increases linearly with voltage (green fit). After full depletion, the capacitance is constant, which is seen in the plot as a plateau (red fit).

The EP-DT-DD Solid State Detectors (SSD) team at CERN possesses two different set-ups for the realisation of CV/IV measurements. The basis of their operation is the same, the main difference lies in the cooling system used and the mounting of the device under test (DUT). One of the set-ups consists in a *probe station*, where thermal contact is achieved via physical contact between the sensor and a temperature-controlled chuck. Also, the electrical contact is done by means of probe needles and micromanipulators. Because of this, only bare-die sensors with metallised electrodes can be tested there. Instead, the other set-up is mounted inside a climate chamber, where the cooling of the sample is achieved not by direct contact but by cooling down the air within the chamber. This allows for the testing of devices mounted on printed circuit boards (PCB), which expands the range of devices that can be studied. The data acquisition and control of both set-ups is done through a LabVIEW user interface.

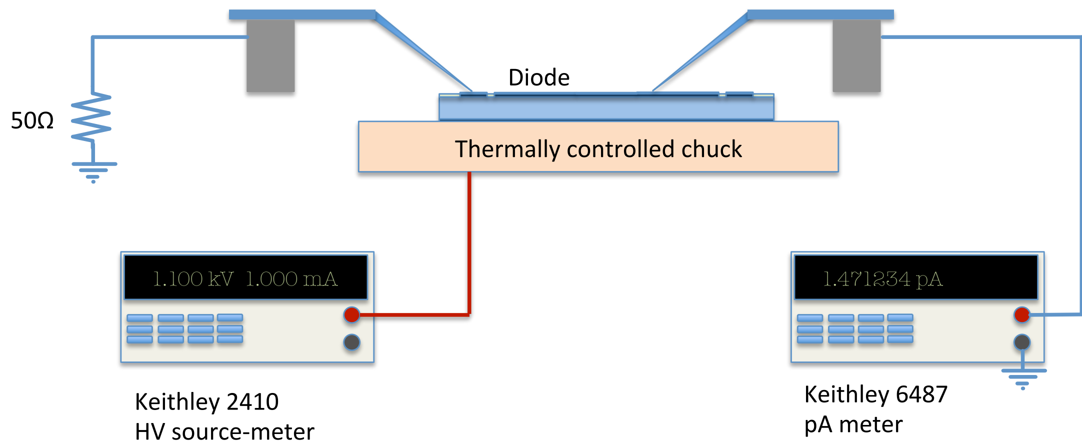

(a)

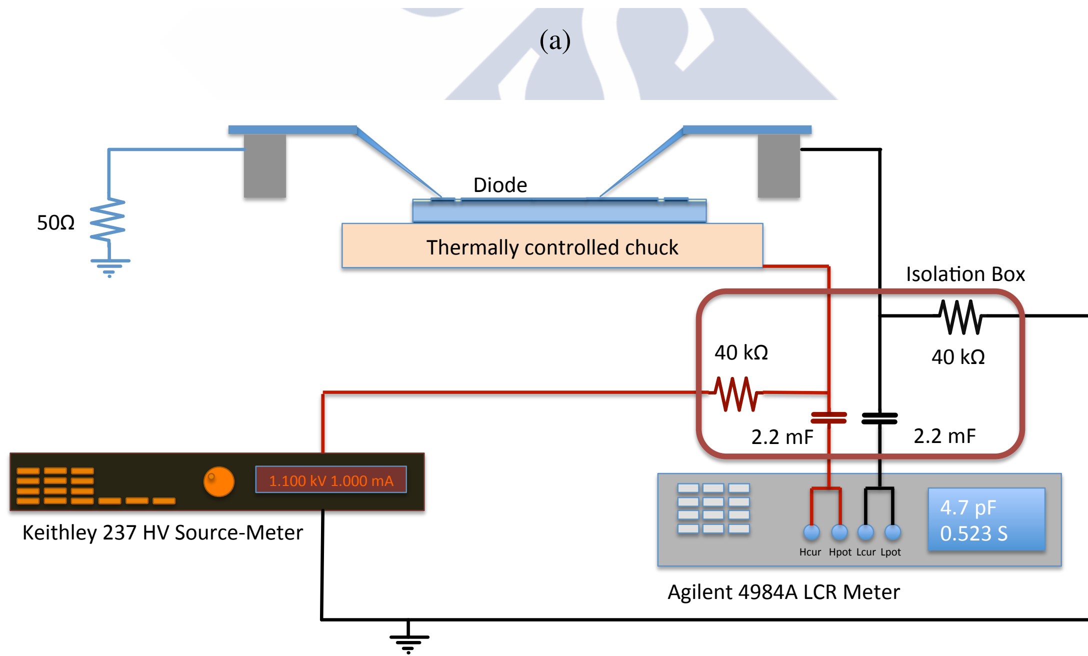

(b)

Figure 4.2: Sketches of the electrical connections in the probe station for (a) IV and (b) CV measurements. From [55].

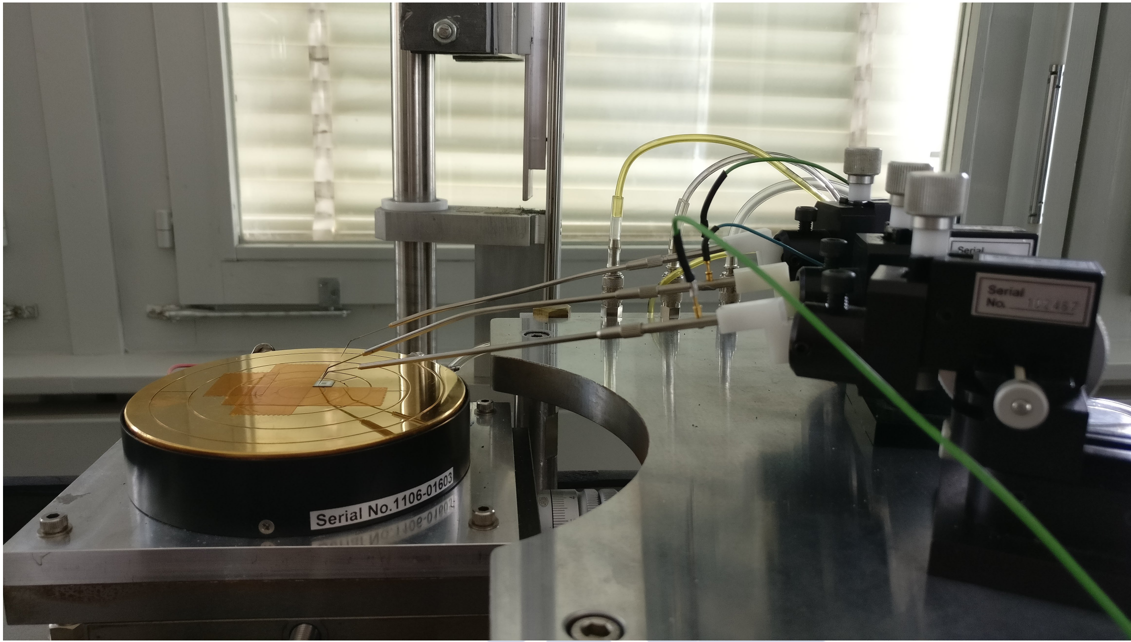

(a)

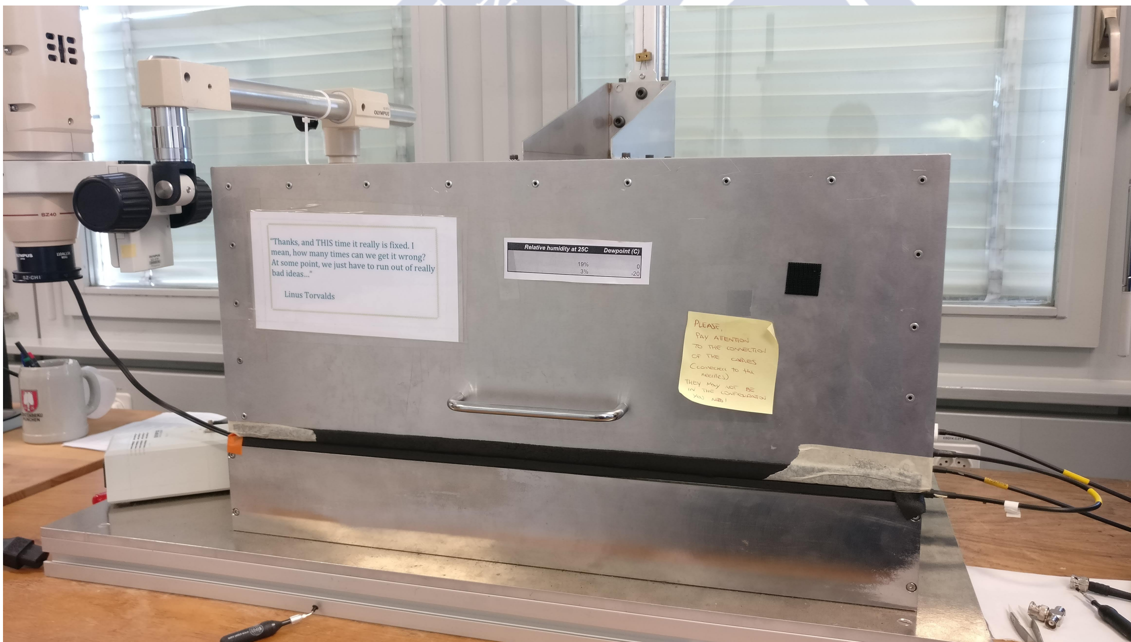

(b)

Figure 4.3: Pictures of the CV/IV (a) probe station, and of the (b) set-up as seen closed.

4.1.1 Probe station

In this set-up, the DUT is mounted on a thermally controlled chuck (produced by ATT Systems). If the sensor can be biased from the back plane, the bias voltage is also provided by the chuck. The circuit is closed by connecting the front-side electrode of the sensor to ground through a probe needle that is connected to the ground of the power supply. If the sensor has a guard ring, this can also be grounded through a probe needle, see Figure 4.2. Both probe needles have a 20-μm tungsten tip, and are attached to a micromanipulator by means of a probe holder. To ensure that neither the micromanipulators nor the sensor move, these are held through suction by a vacuum pump. The temperature at the chuck is controlled by means of integrated Peltier elements that are cooled down through a liquid ethanol circuit connected to a chiller (Huber). The whole station is located inside a Faraday cage that also acts as a dark box, to stop light from interfering with IV measurements. The box also allows for the control of the humidity conditions of the set-up. To avoid condensation or frost whilst working at low temperatures, a continuous flow of dry air with a dew point below $-100°$C is injected inside the box. Pictures of the set-up can be found in Figure 4.3.

In this set-up the high voltage is provided by a Keithley 2410 power supply (maximum voltage: ± 1100 V). During IV measurements the total leakage current of the device, i.e. the pad current plus the guard ring current, is measured with that same instrument. However, the pad current is measured with a Keithley 6487 picoammeter. A sketch of the electrical connections used during IV measurements can be seen in Figure 4.2a. CV measurements are somewhat more complex. Two voltage sources must be used simultaneously: one provides an alternate voltage, necessary to measure the impedance of the sensor; and the other a direct voltage, used for biasing the device. In this set-up the bias voltage is provided by a Keithley 237, and the AC is provided by the LCR-meter (Agilent HP-E4980A) used for measuring the impedance of the DUT. To disentangle both voltages, a decoupling circuit is connected between both sources and the sensor. A sketch of the electrical connections used during CV measurements can be seen in Figure 4.2b. Before each CV measurement, an *open circuit correction* must be performed to determine the impedance of the set-up itself, without a sample. This ensures that the following CV measurements reliably characterise the behaviour of the DUT. Finally, to obtain the capacitance value for a given sensor, it is necessary to define a circuit model for the device. This model will allow the LCR-meter to calculate the capacitance of the sensor from the measured impedance (Z). In this thesis the model used was that of a resistor R_p in parallel with a capacitor C_p (Figure 4.4a), where the resistor represents the leakage current of the sensor. Another possibility, not used in this thesis, is to assume that the sensor can be described as a resistor R_s in series with a capacitor C_s (Figure 4.4b). Regardless of the model chosen, since both circuits represent the same measured data, knowing the frequency ν of the AC-signal used, they can be converted from one to the other [26]:

$$C_s = \frac{1+\omega^2 R_p^2 C_p^2}{\omega^2 R_p^2 C_p} \quad \text{and} \quad R_s = \frac{R_p}{1+\omega^2 R_p^2 C_p^2} \qquad with \omega = 2\pi\nu. \tag{4.1}$$

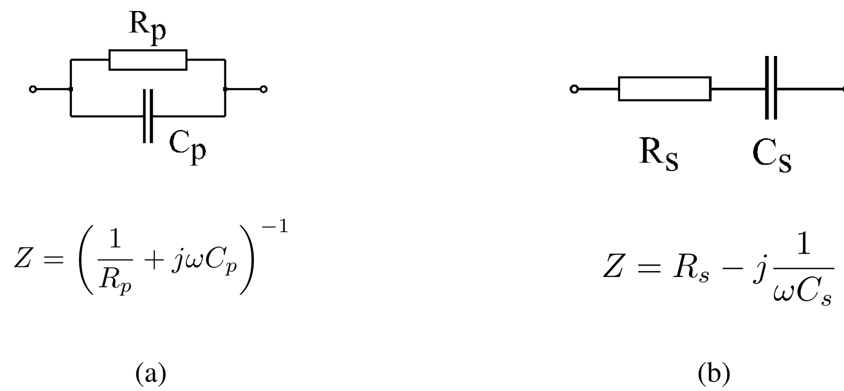

(a) (b)

Figure 4.4: (a) Parallel and (b) serial equivalent circuits for a silicon sensor. Modified from [26].

(a) (b)

Figure 4.5: (a) Climate chamber. (b) Detail of the connections for CV/IV measurements inside the climate chamber.

4.1.2 Climate chamber

As previously mentioned, another CV/IV set-up is available for measuring devices that have either already been mounted on a PCB, or that must be mounted on one in order to be measured. In this case, the devices with its PCB are mounted on a metallic support within a climate chamber (Binder MKT115) that can be operated in a temperature range from -70°C to 180°C. Figure 4.5 shows both the chamber and the mounted sample. The electrical connections between the equipment and the sensor are done through coaxial cables attached to the SMA connectors of the PCB, see Figure 4.5b. The bias voltage in this set-up can be provided by either of two power supplies: a Keithley 2410, with a maximum output of ±1100 V; or an iseg SHW 222M, which can supply up to ±2000 V. The leakage current is measured through a Keithley 6487 picoammeter, and the capacitance with a Keysight 4980A. Also, a Keithley 2000 multimeter is used to measure the temperature of the sample by means of a Pt1000 glued to the PCB.

4.2 Transient Current Technique

The Transient Current Technique (TCT) is based on the analysis of the current induced by the movement of charge carriers inside a sensor [51]. The charge carriers are generated by illuminating silicon sensors with picosecond laser pulses. Changing the used wavelength it is possible to vary the penetration depth of the light. By illuminating a silicon sensor with an infrared (1064 nm) laser providing ps-wide pulses, the response of the sensor to minimum ionising particles (MIP) is simulated[1]. The infrared (IR) laser has an absorption length in silicon of about 1 mm, hence it recreates the charge carriers' path caused by a MIP traversing the detector, however, without the statistical charge fluctuations[2]. The signal produced in the DUT by the IR laser is formed by a superposition of the signals induced by the moving electrons and holes, see Figure 4.6.

On the other hand, if red (660 nm) laser pulses are used, since the absorption length of red light in silicon is of a few micrometers, e^-/h^+ pairs are produced close to the illuminated surface. To visualise the resulting signals from red TCT, the example of an n+/p/p+ device will be described. In the case of red-front illumination (on the n+ electrode), the electrons produced are immediately collected by the front electrode whilst holes have to drift all through the device to reach the back electrode (p+). For this reason, in an n-on-p device, red-front illumination is equivalent to the injection of holes, see Figure 4.6. Analogously, red-back illumination (on the p+ electrode) corresponds to the injection of electrons [57], see Figure 4.6. This behaviour makes red light TCT a useful

[1] Minimum ionising particles (MIP): particles that have mean energy loss rates close to the minimum, such as most relativistic charged particles [56].

[2] Every IR pulse generates the same number of charge carriers, however, with MIPs a Landau-Vavilov distribution of charge deposition is observed [25]. This will be discussed in greater detail in Section 4.4 and in Chapter 5.

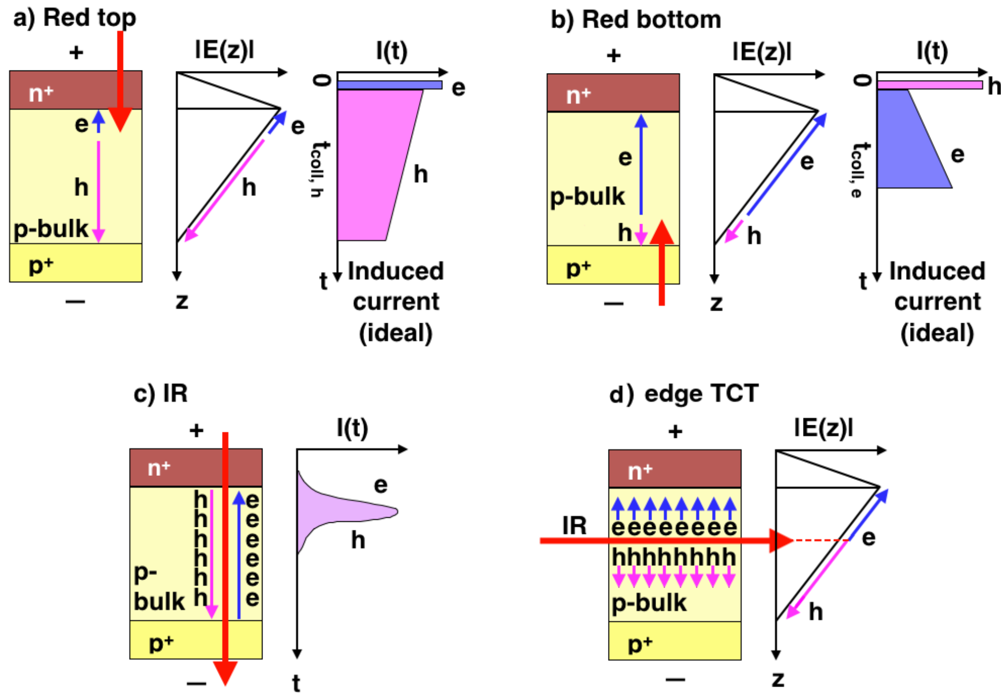

Figure 4.6: Sketches of signal generation with TCT. Modified from [54].

tool to characterise the movement of electrons (e^-) and holes (h^+), and the electric field inside a device. Remember from Equation 2.9 that the signal induced by charge carriers is proportional to the electric field. In red TCT the signal is given by the contribution of only one type of charge carrier that must traverse the full thickness of the sensor. The output signal is a representation of the electric field inside the sensor.

Another variation of TCT is the so-called edge-TCT (eTCT). This technique consist in illuminating the edge of the sensor with a ps-pulse IR laser. The side illumination characteristic of eTCT and the penetration length of IR light in silicon result in eTCT being a method for probing the electric field all through the thickness of the device, see Figure 4.6. This type of illumination is useful for the study of sensor properties such as the depletion depth, the charge collection efficiency, the instantaneous drift velocity, and the electric field [52].

4.2.1 TCT+ set-up

The TCT+ set-up available at the EP-DT-DD SSD laboratory at CERN combines all three measurement techniques: front and back TCT with IR or red laser pulses; eTCT with IR laser pulses. The set-up as a whole can be divided into several subsystems that have to interact and communicate during operation: the cooling system, the linear stage system, the optical system, and the electrical and readout system. The entire system is controlled

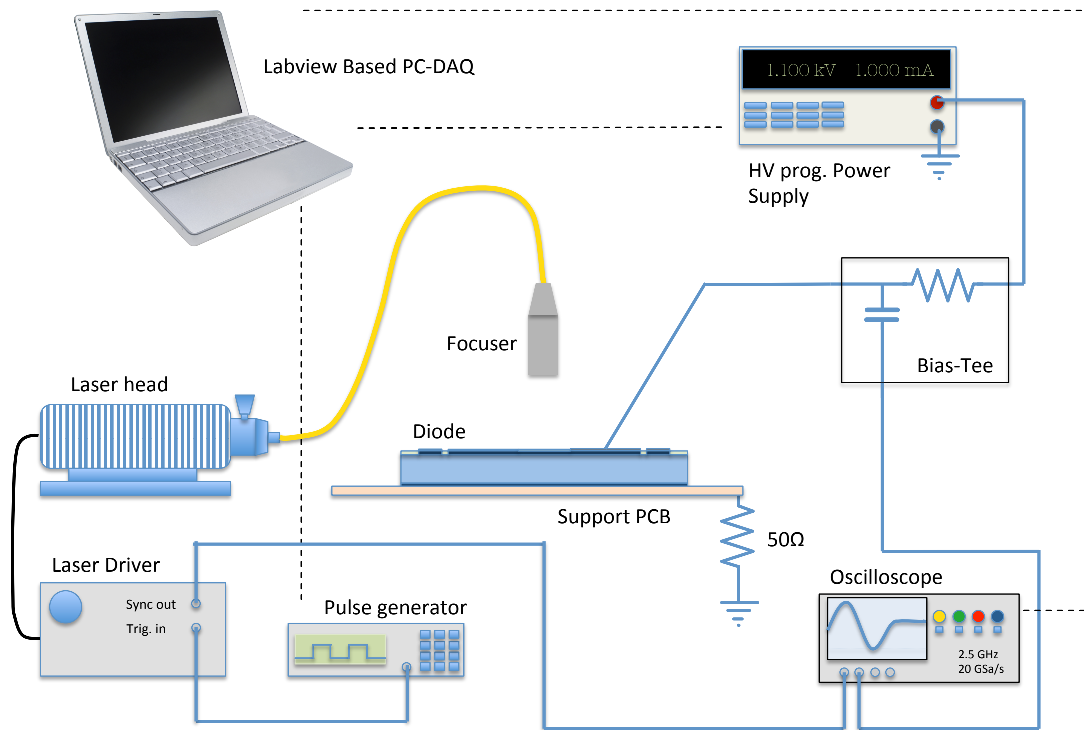

Figure 4.7: Simplified schematic of the TCT set-up. From [55].

UNIVERSIDADE DE SANTIAGO DE COMPOSTELA

by a LabVIEW based software, which is also in charge of the data acquisition. Figure 4.7 shows a simplified schematic of the set-up, notice that eTCT and back illumination are not included in this sketch.

In order to measure a device, it must be mounted on a PCB. Most sensors are attached by means of a conductive glue, such as silver paint, which also creates an electrical connection to the back of the device. The frontal connections are done by means of wire-bonds[3]. Figure 4.8 shows pictures of all the PCBs used in this thesis. Inside the set-up, the PCB is mounted on top of a copper base that gives both mechanical support, and thermal contact to control the temperature of the DUT. The functioning of the cooling system will be explained further on. To avoid interference from environmental noise, the TCT+ system is enclosed in a Faraday cage. The cage works also as a dark box, and allows for the control of the humidity conditions of the set-up. Figure 4.9 shows pictures of the TCT+ set-up.

[3]Wire-bonds are done by the CERN Wire Bonding and Reliability Testing Service.

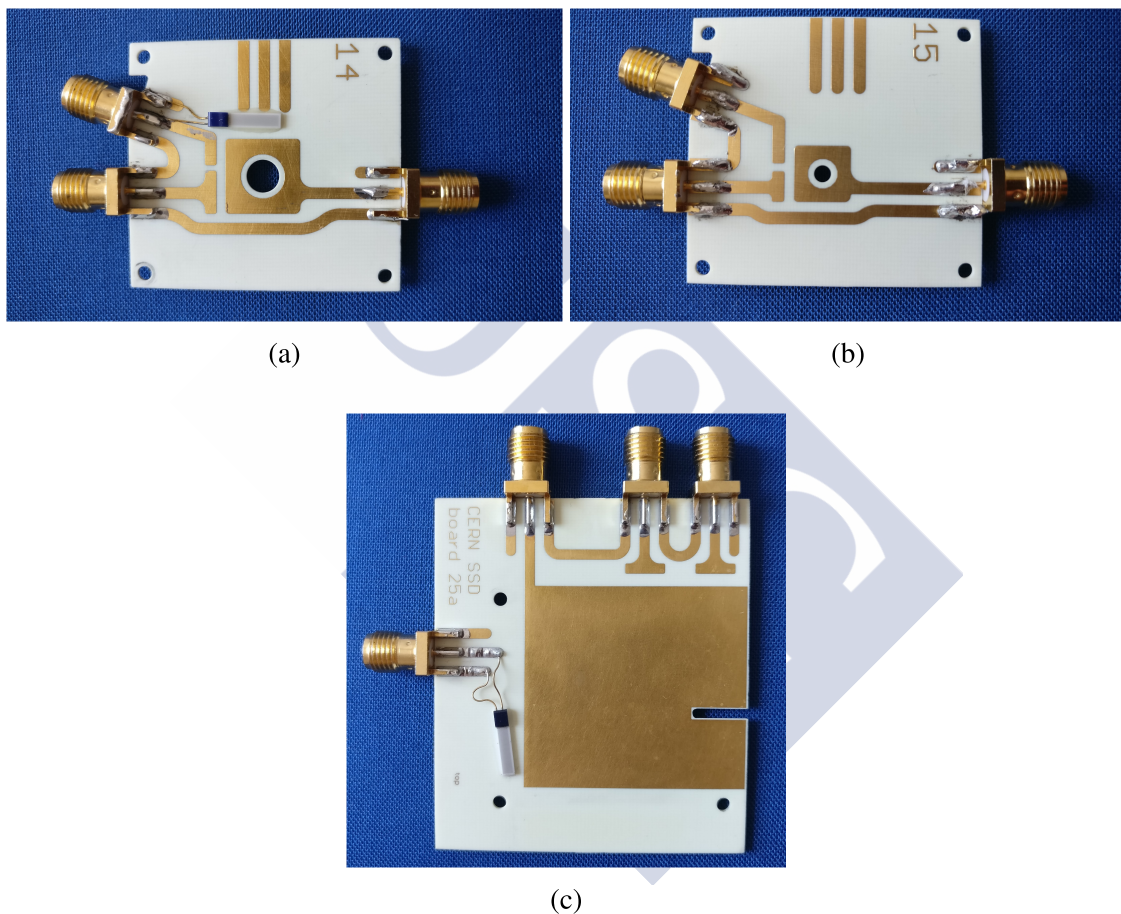

(a) (b)

(c)

Figure 4.8: (a) PCB 14 and (b) PCB 15, both used for front and back TCT. (c) PCB 25a, used for front, back and edge TCT. In this thesis, PCB 14 was used to mount DD-APDs. PCB 15 and 25a were used for mounting LGADs.

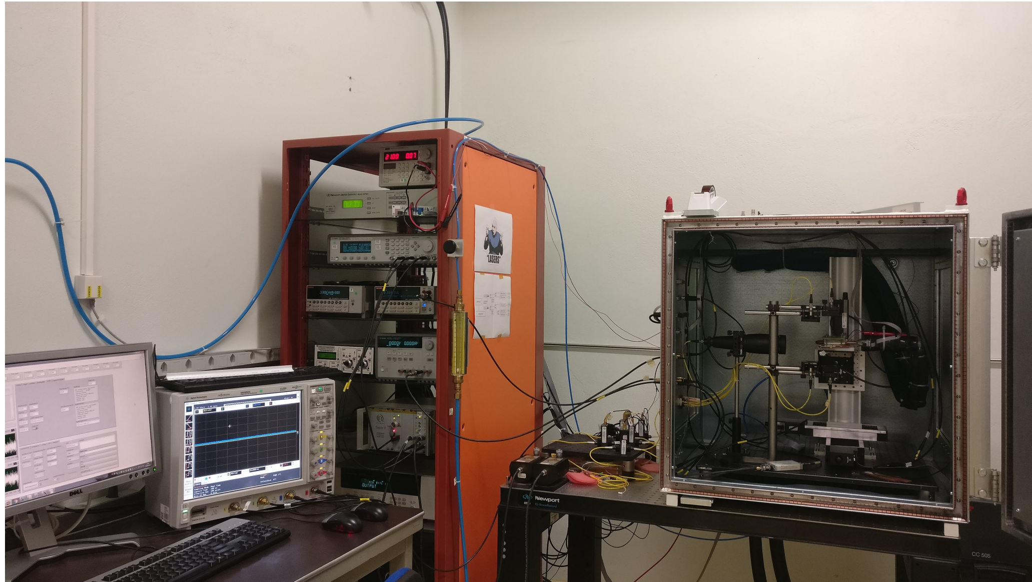

(a)

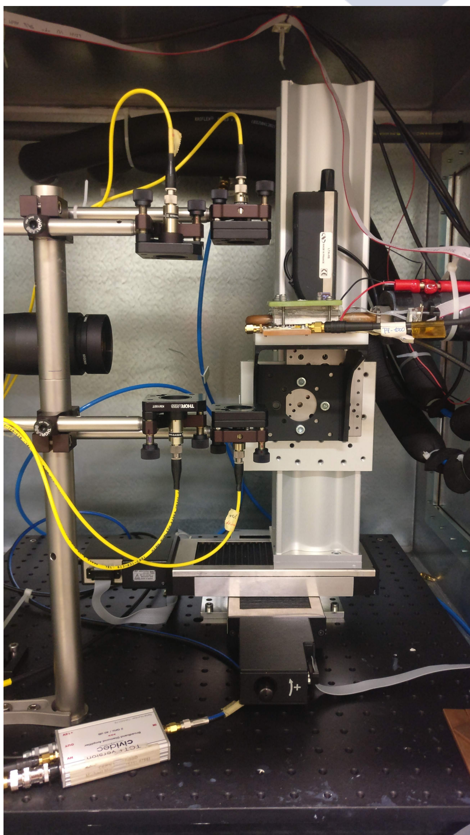

(b)

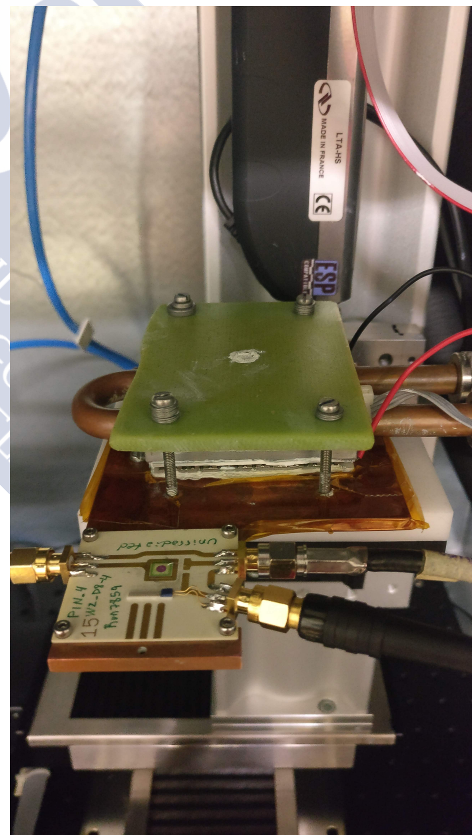

(c)

Figure 4.9: Photographs of the TCT+ set-up. (a) Wide view of the full set-up (the chiller is not visible). (b) Detailed view inside the Faraday cage. (c) Detail of the copper support with the Peltier element, and a PCB with a sample.

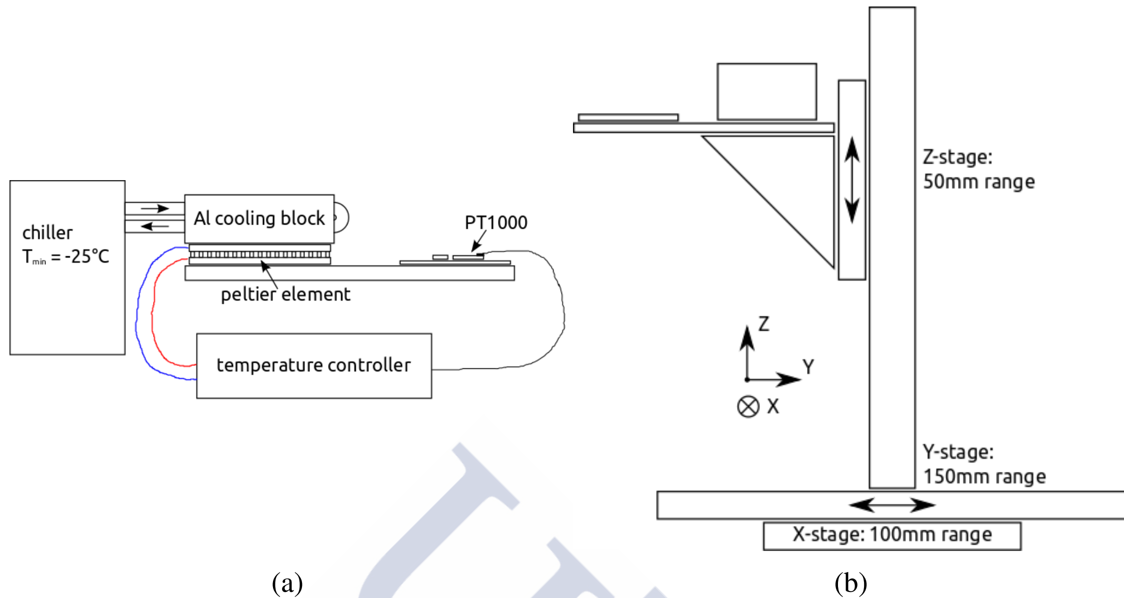

Figure 4.10: Schematics of the (a) cooling, and (b) linear stage systems of the TCT+ set-up. From [58].

To perform measurements at temperatures between -20°C and 20°C, the TCT+ set-up has a cooling system. The system consists of a chiller (Huber), a PID temperature controller (LairdTech PR-59), and a Peltier element (Adaptive ET-241-14-15). The Peltier element is attached to the cooper support where the PCB is mounted, the copper base works as a thermal conductor between the two, see Figure 4.9c. The Peltier element is cooled down by a chiller that pumps a solution of deionised water and ethanol. The temperature is regulated by the PID temperature controller, which compares the requested temperature with that measured on the PCB through a Pt1000. A schematic of the system is shown in Figure 4.10a.

A vital part of the TCT+ set-up is the linear stage system, in charge of moving the DUT with microprecision (minimum step width of 1 μm) to perform high resolution scans. The system, shown in Figure 4.10b, consists of three stages, and a stage controller (Newport ESP301-3N). The copper support where the PCB and the Peltier element are mounted is fixed to the Z-stage (Newport LTA-HS stage). This stage is used to take the sample towards the focal point of the laser used, so as to obtain the highest resolution possible. The Z-stage is, in turn, fixed to an aluminium rail attached to the X-stage (Newport UTS100CC stage), which is itself mounted on the Y-stage (Newport UTS100CC stage), see Figure 4.9b. The X- and Y-stages allow for the alignment with the chosen laser, and for the movement of the sample during scans.

The core of the TCT+ set-up is the optical system, the layout of which can be found in Figure 4.11. A pulse generator (Agilent 8110A) is connected to a laser driver (PicoQuant PDL 828 “Sepia II”) with two channels. Each channel controls a picosecond pulsed diode laser head, each emitting 200-ps-wide laser pulses with a wavelength of 660 nm (red)

and 1064 nm (IR). The laser pulses are transported all through the optical system towards the inside of the Faraday cage through optical fibres. The laser beams at the output of each fibre are collimated and focused. For both the red and IR laser, a 10 μm-diameter beam spot can be achieved, both with front and back illumination. To synchronise the data taking with the laser pulses, the signal from the pulse generator is also used for triggering. The pulse rate used, 200 Hz, was chosen so that there is enough time between measurements for the sample to reach a state of equilibrium.

The intensity of the lasers is set to 40 % and 60 % of the maximum the red and the IR lasers can provide, respectively. In addition, both laser heads are equipped with manual attenuators. These permit to vary the laser intensity, i.e. the charge injected in the DUT, without altering the pulse shape of the laser. After passing through the attenuator, each beam is split, with 10 % of the light going towards a reference photodiode. The reference photodiodes, based on silicon and InGaAs, are used to monitor the laser intensity during measurements. The remaining 90 % of the laser light goes through a series of beam splitters and shutters. These enable the selection of the wanted wavelength (red or IR), as well as the illumination direction (front, back or edge). For red TCT the beam goes through a 50:50 beam splitter, to obtain the beams for front and back TCT. Accordingly, the laser intensity during red-front or red-back TCT is 45 % of the beam intensity right after the laser-head attenuator. For IR TCT the beam first goes through a 50:50 beam splitter, where one of the outputs goes to the optics for eTCT. The other output goes to an extra 50:50 beam splitter, which divides the beam for IR-front and back TCT. In the end, the beam intensity for eTCT is 45 % of the initial one, and 22.5 % for front and back TCT.

Of special importance is the electrical and readout system. This system handles the biasing of the DUT; the amplification of the signal; and its transfer to the oscilloscope. The latter also receives the triggering signal from the pulse generator, and the reference-diode signal. During read-out, the signal from the DUT gets amplified by a high bandwidth current amplifier (CIVIDEC C2-HV), and is then recorded by a 2.5-GHz digital oscilloscope (Agilent DSO9254A). The data are then acquired and stored by the LabVIEW software that controls the entire set-up. It should be noted that each stored waveform is, in fact, the average of 256 signals. This is done to reduce the noise in the measurements.

Finally, there are two general read-out and biasing schemes possible: biasing and reading out the sensor through the same electrode, or biasing through one electrode and reading out from the other. When the biasing is done through the same electrode as the read-out, to avoid breaking the amplifier by applying a high DC bias to it, a *bias T* must be included in the circuit (see Figure 4.7). A bias T is a passive device, consisting of a capacitor and a resistor (or an inductor), which separates the direct current of the power supply from the alternate current of the induced signal. The amplifier model used in the TCT+ set-up has an integrated bias T that can withstand up to $\pm$1000 V.

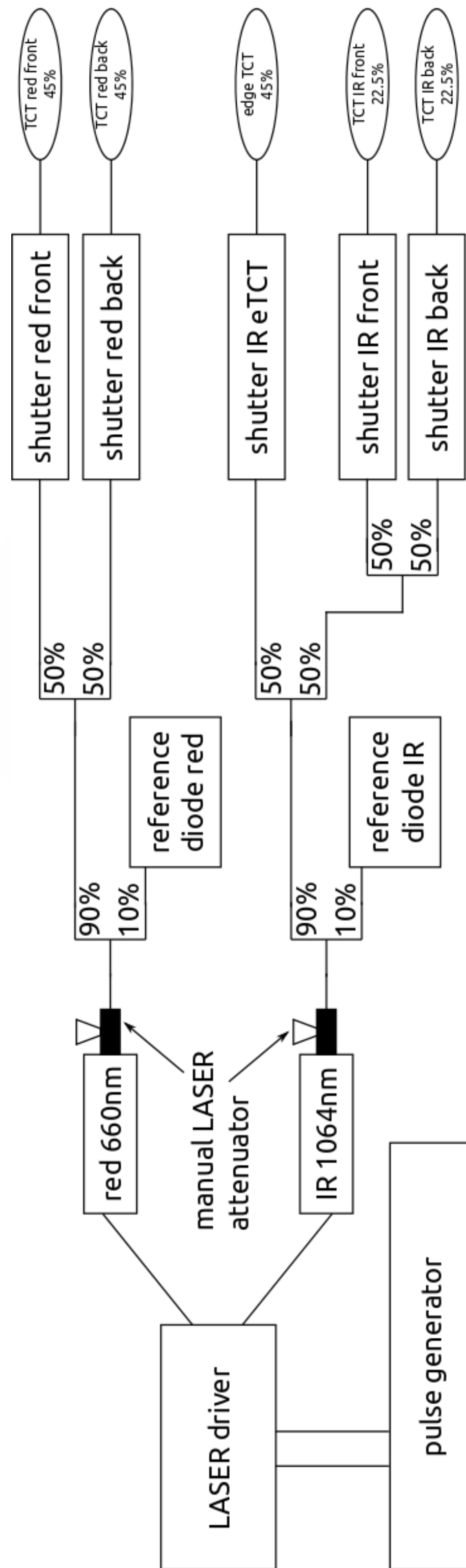

Figure 4.11: Optical system of the TCT+ set-up. From [58].

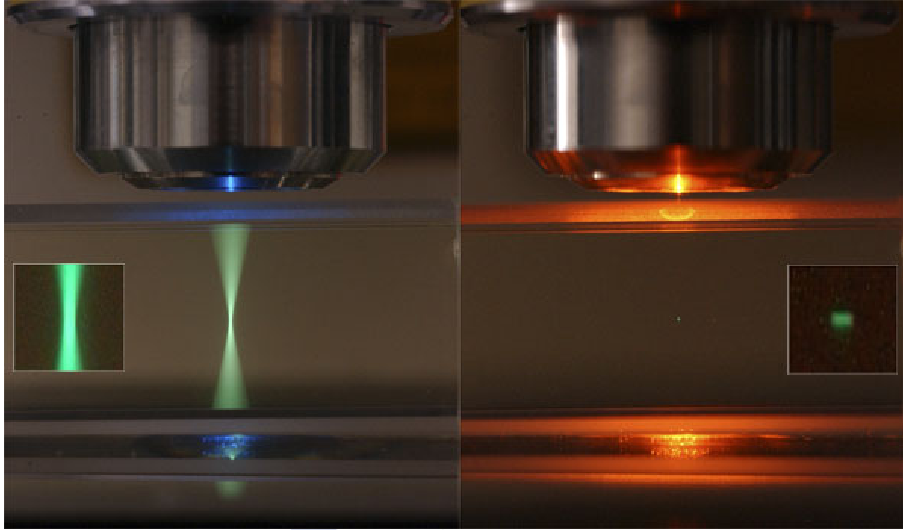

Figure 4.12: Photographs comparing the light absorption in a fluorescent solution when illuminated with a (a) laser diode (single-photon absorption), and with a (b) femtosecond pulsed laser (two-photon absorption). From [59].

4.3 Two-Photon Absorption TCT

In the previous section, *Single-Photon Absorption* TCT was described. However, there is another technique available for laser characterisation of sensors: *Two-Photon Absorption TCT* (TPA-TCT). The theoretical basis for Two-Photon Absorption TCT is that due to the time-energy uncertainty principle it is possible to produce an e^-/h^+ pair by means of the absorption of two photons. Two photons that individually possess an energy lower than that of the bandgap, but that the sum of both their energies is equal or higher than it, could be absorbed by means of an intermediate virtual state. For this to be possible, both photons must interact with the e^- to be excited in an interval of less than 1 fs [60]. Experimentally this is achieved by means of a femtosecond pulsed mode-locked laser, and under sufficiently intense laser illumination [53]. Figure 4.12 shows two pictures comparing the light absorption in a fluorescent solution when illuminated with a laser diode, and with a femtosecond pulsed laser. In the former, the light is absorbed through single-photon absorption all along the path of the beam inside the solution. On the contrary, when the solution is illuminated with the femtosecond pulsed laser, the absorption occurs only in the focal point of the laser. The underlying principle is that, only in the focal point is the density of photons high enough so that the second photon can interact with the electron, and promote it from the virtual state within the lifetime of the state itself ($\sim$ 1 fs). As a consequence, when this technique is used for testing silicon sensors, the electron-hole generation is extremely localised, making it possible to perform a three-dimensional probing of the electric field [53].

USC UNIVERSIDADE DE SANTIAGO DE COMPOSTELA

(a)

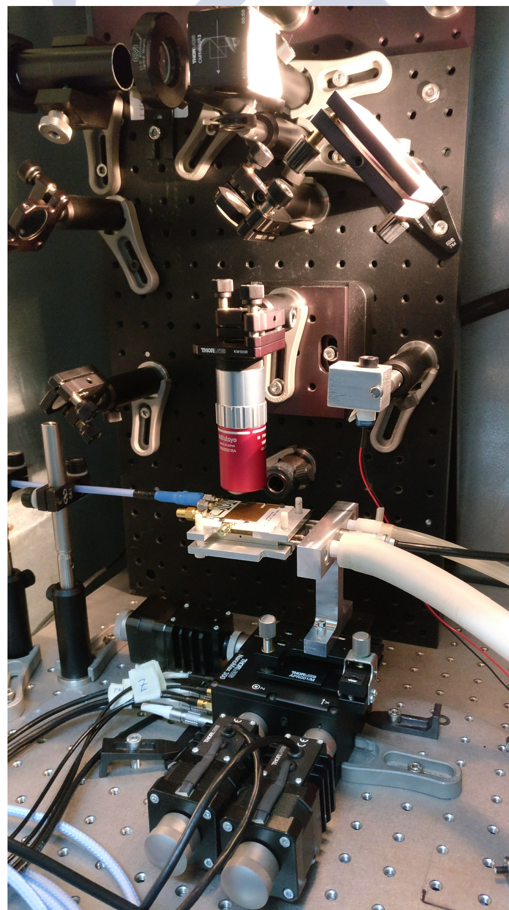

(b)

Figure 4.13: (a) View of the full TPA-TCT set-up at the Singular Laser Facility of the UPV/EHU. From [61]. (b) Close-up of the inside of the Faraday cage.

In this thesis, all TPA-TCT measurements were conducted at the Singular Laser Facility of the UPV/EHU[4] in Bilbao, Spain. The facility is extremely flexible, with a tunable laser system where the intensity, wavelength, and pulse duration can be adjusted. As in the TCT+ set-up, the sensor must be first mounted on a PCB. This is then mounted on a 3-axis optical stage with sub-micron resolution (Thorlabs NanoMax 300) located inside a Faraday cage, see Figure 4.13. As in other previously described set-ups, the Faraday cage not only avoids interference from external noise, but also acts as a dark box, and allows for the control of the atmospheric conditions to which the DUT is exposed. During measurements a constant flow of dry air is injected into the box to avoid any kind of condensation. Measurements below room temperature (down to -20°C) can be achieved by means of a cooling system based on a circuit of liquid nitrogen.

In this work the laser wavelength used is 1300 nm, and the pulse width is of 60 fs. As explained before, this method uses the laser to generate charge carriers in a point-like volume located at the focal point of the laser. It is particularly important to find the focal point before each series of measurements on a specific device, and after any change in temperature to compensate for changes in position due to the expansion or contraction of the DUT support. The laser used in this facility has an ellipsoidal focal point with a section of $\sim 1\mu$m, and a length of $\sim 10\mu$m.

4.4 Radioactive source measurements

To study the signals and the energy deposition distribution of MIPs in a silicon sensor, radioactive source measurements must be performed. In this thesis, said scans have been carried out by means of a Strontium-90 (^{90}Sr) source, with an activity of 26.68 MBq. ^{90}Sr is a radioactive isotope, with a half-life of 28.9 years, which decays to ^{90}Y through a β^- decay with a Q-value[5] of 0.546 MeV. ^{90}Y also undergoes a β^- decay to ^{90}Zr (stable) with a Q-value of 2.28 MeV and a half-life of 64.1 hours [63]. As a result, ^{90}Sr can be used as a source of electrons, Figure 4.14a shows the energy spectrum expected for electrons emitted by a ^{90}Sr source, including the contribution from ^{90}Y. Considering the energy deposition of electrons in silicon, described by the Bethe-Bloch formula, and shown as a function of electron energy in Figure 4.14b, it can be concluded that electrons with an energy of the order of 1 MeV can be considered to be MIPs [64]. Consequently, by exposing a silicon detector to a ^{90}Sr source it is possible to study the response of the device to MIPs.

The radioactive source measurements set-up available at the EP-DT-DD SSD laboratory at CERN is installed inside a climate chamber (the same used for CV/IV measurements, see Section 4.1.2). The DUT must be mounted on a PCB to be tested in this set-up. The Pt1000 on the PCB is used to control that measurements are done at the wanted tem-

[4] Access to this facility was granted via the RD50 Collaboration.

[5] The total energy released in the decay process [62].

perature. The biasing of the sensor is done by a power supply (Keithley 2410) that can provide a maximum voltage of ± 1100 V. Inside the chamber there is 2-axis stage system (Newport), attached to it there is a support where the PCB can be screwed. On top the sample there is a movable platform where the ^{90}Sr source, together with a collimator, can be placed. The function of the collimator is to control the beam spot under the radioactive source, and the trigger rate. The latter depends on the aperture of the collimator, ranging from ~ 50 Hz with an aperture of 1 mm in diameter, to ~ 200 Hz for 3 mm. The platform is generally adjusted to be as close as possible to the DUT. Also, by means of the XY-stages, the DUT is aligned with the source, and with the scintillator located below it. The scintillator is used for triggering, as only the electrons energetic enough to fully traverse the silicon sensor (MIPs) will be capable of reaching the scintillator. Figure 4.15 shows a picture of the set-up inside the climate chamber.

The read-out of the sample is done through a charge amplifier (CIVIDEC Cx), the output signal of which has an amplitude proportional to the collected charge, with a proportionality constant of 12 mV/fC. Figure 4.16a shows the average signal from 20000 waveforms obtained from an unirradiated 300 μm diode. Both the signal from the sensor, and from the scintillator (trigger) are read by a digital oscilloscope (Agilent DSO9254). The data are then acquired and stored by the LabVIEW software that controls the whole set-up. For each voltage point at which the sensor is measured, 2000 events are measured in order to get the charge collection distribution.

During the data analysis, the amplitude of each signal pulse is determined. Also, the electronic noise is evaluated by calculating the root mean square (RMS) over the first 100 ns of the waveform. For each bias voltage used, a charge distribution histogram, which also includes the electronic noise distribution, is obtained. Figure 4.16b shows the charge distribution for an unirradiated 300-μm diode, here the collected charge is indicated in mV, as the conversion from amplitude to charge has not yet been done. The electronic noise distribution ought to be centred around 0, as it is in Figure 4.16b, and can be described by a Gaussian fit. The charge distribution from the sensor can be described by the convolution of a Landau and a Gaussian distribution. The fluctuations in deposited energy by a MIP in silicon are accurately described by the Landau distribution. On the other hand, the Gaussian acts as a correction of the Landau, as it describes the noise distribution [65]. From such a fit the most provable value for the charge collection can be obtained.

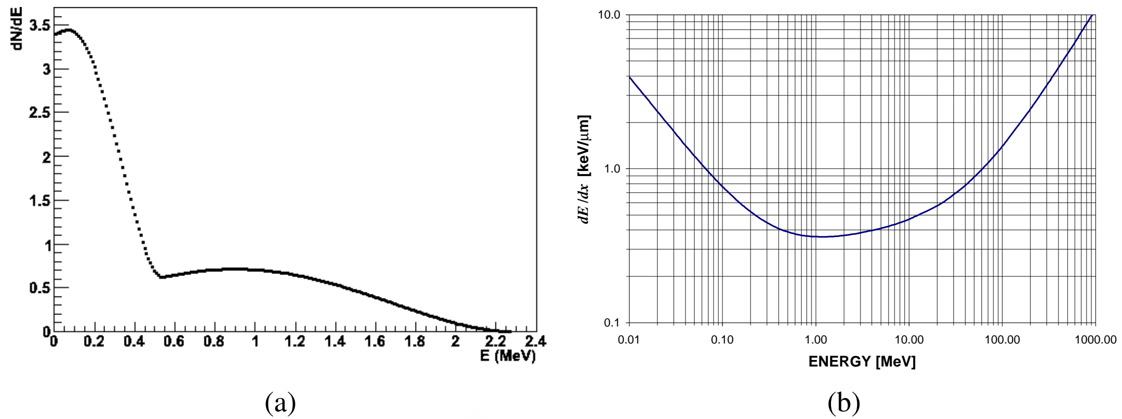

(a) (b)

Figure 4.14: (a) Energy spectrum expected for electrons emitted by a ^{90}Sr source, including the contribution from ^{90}Y. From [66]. (b) Energy deposition of electrons in silicon as a function of the energy of the electron. From [64].

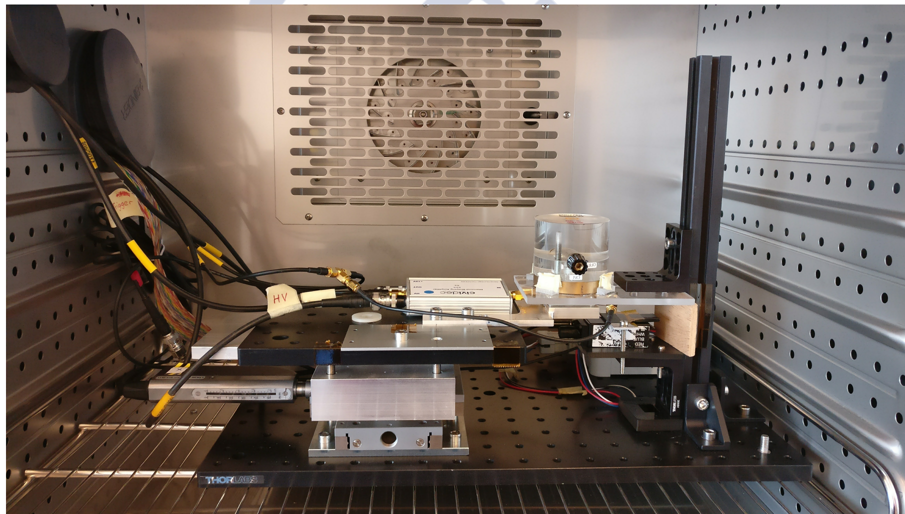

Figure 4.15: Close-up of the radioactive source measurements set-up.

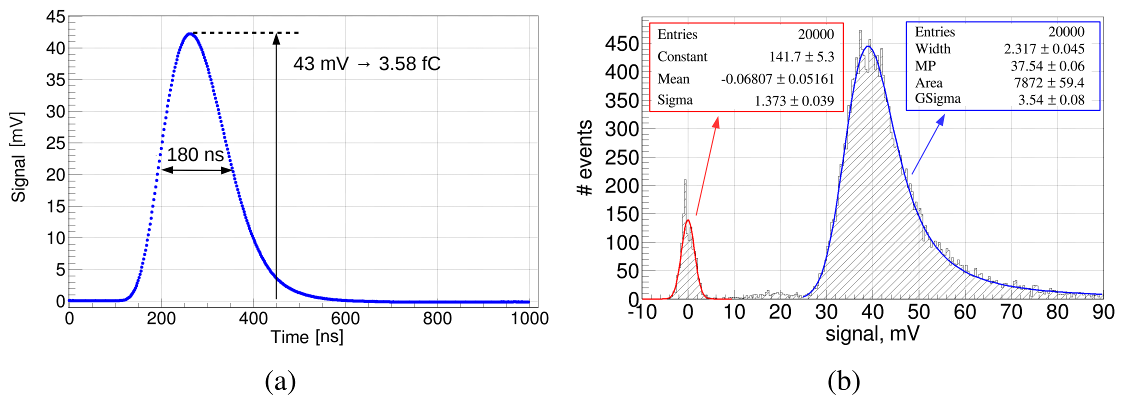

(a) (b)

Figure 4.16: (a) Average signal from 20000 waveforms, and (b) charge distribution obtained from ^{90}Sr source measurements on an unirradiated 300-μm diode. The electronic noise was fitted with a Gaussian (red), and the collected charge with a Landau-Gaussian convolution (blue). From [67].

4.5 Irradiation facilities

To study the effects of radiation on silicon sensors it is necessary to irradiate said samples. For this thesis, devices were exposed to 24-GeV/c protons, at the PS-IRRAD proton facility at CERN; or to neutrons, at the Jožef Stefan Institute neutron irradiation facility in Ljubljana. All irradiation campaigns in this thesis were done within the AIDA2020 project, funded by the European Union's Horizon 2020 Research and Innovation programme under Grant Agreement no. 654168 [68].

4.5.1 PS-IRRAD Proton Facility at CERN

The PS-IRRAD proton facility is at CERN, in Geneva, Switzerland. Specifically, on the T8 beam-line of the East Area at the Proton Synchrotron (PS) accelerator. The facility provides a Gaussian beam of 24-GeV/c protons. The beam spot size can be adjusted from $\sim 5 \times 5$ mm^2 to $\sim 20 \times 20$ mm^2 (FWHM). The proton beam is delivered in spills of ~ 400 ms duration, and a maximum intensity of 5×10^{11} protons per spill. The average flux is higher than 8×10^{13} p/cm^2/h [69]. Irradiations are performed at room temperature, consequently uncontrolled annealing may occur during the process [70]. The hardness factor of the facility, as determined in 2015, is of 0.56 [71].

4.5.2 TRIGA Mark III reactor at IJS

The neutron facility at the Jožef Stefan Institute consists of a TRIGA Mark III nuclear reactor, which provides neutrons with a continuous energy spectrum of up to a several MeV. The power of the reactor can be regulated from a few Watts to a maximum of 250 kW, enabling irradiation with different neutron fluxes ($1 - 4 \times 10^{12}$ n/cm^2/s). The hardness factor of the facility is of 0.9 [72, 73].

USC UNIVERSIDADE DE SANTIAGO DE COMPOSTELA

Chapter 5

4D Tracking

As mentioned in Chapter 1, the upgrade of the LHC to the HL-LHC implies that the instantaneous luminosity (rate of collisions) will be 5-7 times higher than the current value [1]. As a result, the number of interactions per bunch crossing, or pile-up, will be proportionally higher. During Run 2 of the LHC the pile-up observed at ATLAS and CMS was of $\sim$ 50 [2, 3], their expected pile-up at the HL-LHC is of between 140-200 [3, 74]. The primary vertex (*pp* collision) reconstruction efficiency during Run 2 was of $\sim$ 99 %. For these reconstructions solely spatial information (3D tracking) was used [75]. This was possible because most interactions occur in clearly distinguishable locations, as can be seen in Figure 5.1a. However, at the HL-LHC the density of interactions (*pp* collisions per unit volume) will be such that with spatial information alone the reconstruction efficiency would be significantly diminished. With the current spatial resolution of ATLAS and CMS ($\sim$ 300 μm) about 10-15 % of vertices would be in fact two *overlapped* interactions, i.e. vertices separated in space by a distance smaller than the spatial resolution of the detector [76]. A depiction of a high-pile-up bunch crossing, with 78 reconstructed vertices, taken during a special run in 2012 at CMS, is shown in Figure5.1b [3]. In order to avoid the loss of primary vertices, the degradation of track reconstructions, and to exploit the full potential of the luminosity capability of the HL-LHC, timing information must be included [76]. Figure 5.1c shows the expected time spread of the beam spot in the HL-LHC when two bunches overlap entirely, see Figure 5.1d. Under these conditions, the pile-up density is maximal and the spread in time is of $\sim$ 180 ps. A time resolution of at least $\sim$ 30 ps would be sufficient to disentangle overlapping vertices [17].

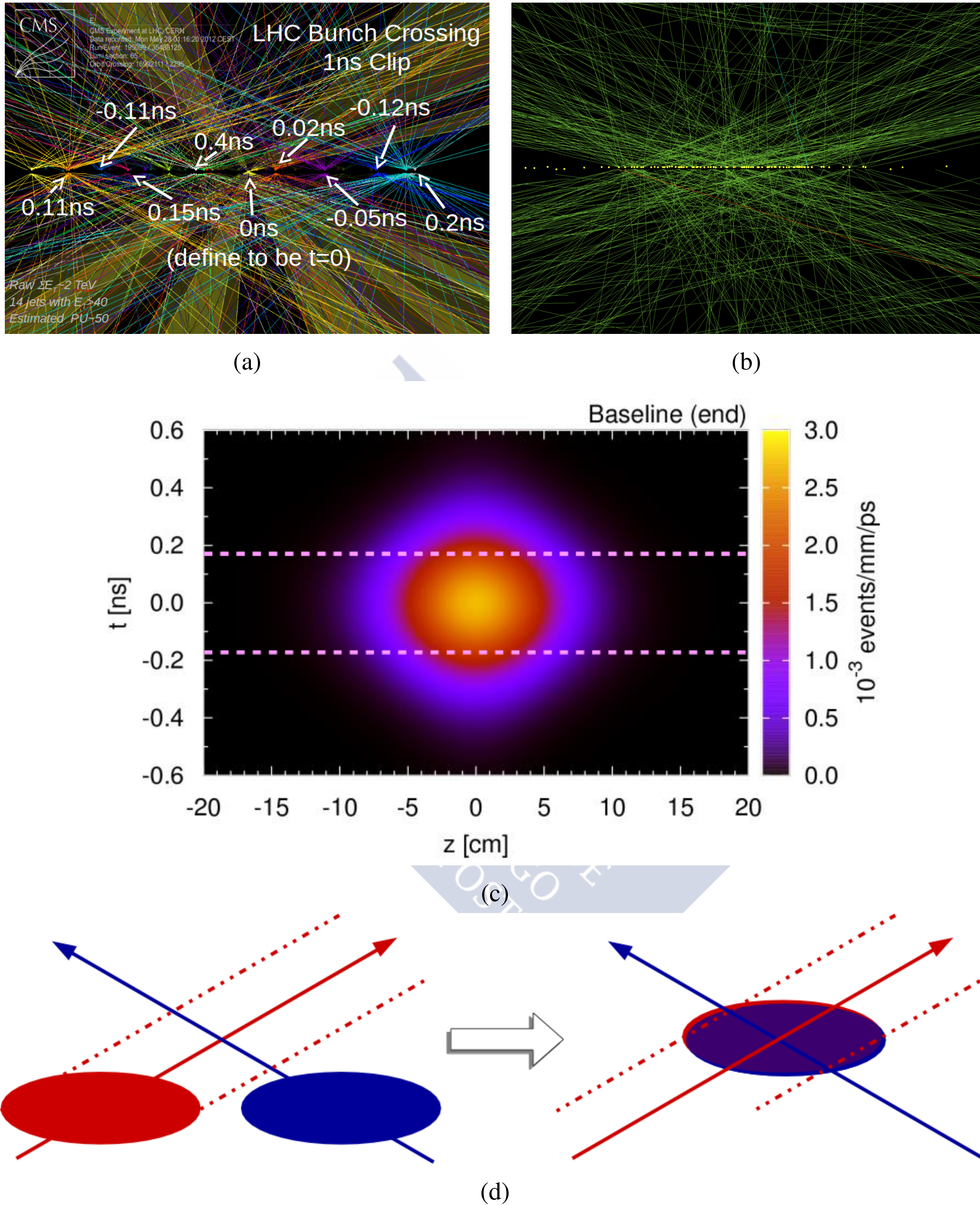

(a) (b) (c) (d)

Figure 5.1: (a) Illustration of a real CMS event with a pile-up of ~ 50. From [77]. (b) Depiction of a high-pile-up bunch crossing, with 78 reconstructed vertices, taken during a special run in 2012 at CMS. From [78]. (c) Expected baseline-scenario beam spot at the HL-LHC at the end of fill. From [79]. (d) Simple graphical representation of how the maximum spatial spread in z of the intersection of two bunches is reached when they overlap entirely.

5.1 Acquisition of timing information

The timing information required to properly reconstruct events can be obtained, and applied to the reconstruction process, at different stages. One option is to associate a timestamp to every single hit on the tracking system, i.e. to each point of a track. Another option is to assign a timestamp to each track, thus allowing to distinguish events overlapping in space. Below there is a more thorough description of both timing methods.

5.1.1 Timing at each point

This method associates timing information to each point of a track, i.e. to every hit in the tracking system. Such precise time-tagging of the hits allows for the suppression of noise hits, as they would not be compatible with the expected time of passage of the particles. In this particular method, both the timing and 3D-tracking information are included in the low level trigger of the experiment. Thus, the time and position measurements of particles are used directly in the real-time track-reconstruction algorithm implemented in an FPGA processing board. A schematic diagram of how precise time-tagging can provide the necessary information to disentangle overlapping events is shown in Figure 5.2. Developing a tracking system of these characteristics is a major challenge, not only from the point of view of the detectors themselves, but from the point of view of the read-out electronics. There is the option of avoiding this difficulty altogether by time-tagging tracks rather than individual hits (see following section). However, in experiments, such as LHCb Upgrade[1], where the goal is to attain a hit time resolution of $\sim$ 10 ps, and a hit position resolution of $\sim$ 10 μm, 4D information of each hit is crucial. There is ongoing work in the development of firmware capable of performing fast track reconstruction, so far with encouraging results [80, 81].

5.1.2 Timing in the event reconstruction

An alternative to the previously described method is that of associating a timestamp to each track rather than each hit. In this case the timing information is used during the event reconstruction. Such a method reduces the demands on the read-out and processing electronics, as the timing is performed uniquely on dedicated *timing layers* located inside or outside the tracker volume. As a result of the timing being done in a different layer, this method requires minimal changes to the main tracker hardware. Figure 5.3 shows a simplified diagram of how the time information provided by the timing layer can be used to distinguish two vertices that overlap in space. Analogously to hit-timing method, the 4D information obtained from the tracker and the timing layer can be used to improve the low level trigger [76].

[1] Large Hadron Collider beauty

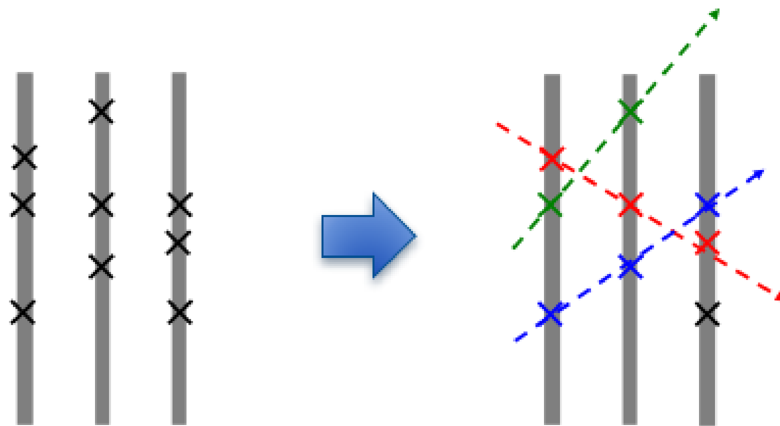

Figure 5.2: Using spatial information only, it would not be possible to unequivocally reconstruct the tracks from this pattern of hits (left). Including precise timing information enables the reconstruction of tracks by associating time-compatible hits (right). From [80].

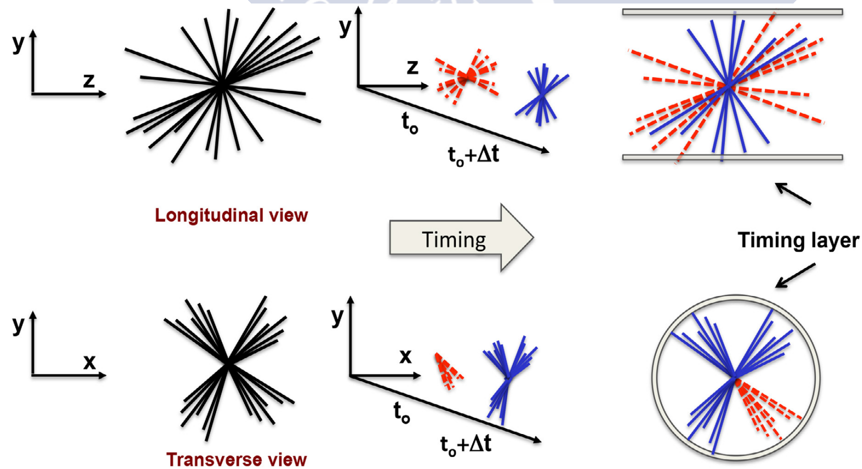

Figure 5.3: Simplified graphical explanation of how time-tagging tracks by means of a timing layer can be used to distinguish two vertices that overlap in space. From [76].

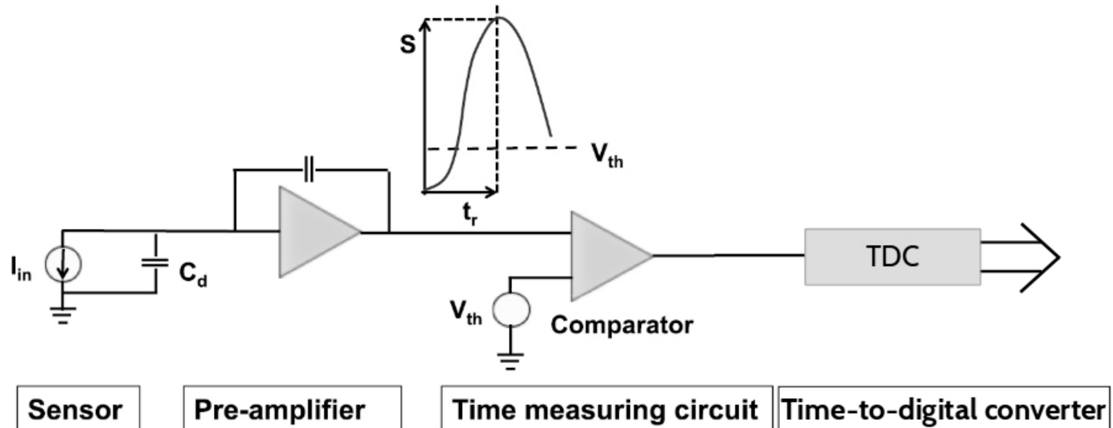

Figure 5.4: Schematic of the main components of a time-tagging detector. The sensor is represented by a capacitor with a current source in parallel. Modified from [82].

5.2 Timing considerations

5.2.1 Time resolution

The importance of accurate time measurements for future HEP experiments has been established. For the purpose of developing new detector technologies that can cater for these timing needs, it is also of importance to consider the characteristics these sensors must possess. In particular, the device and the read-out electronics must be so that the electronics can determine the time of passage of a particle using the signals generated by the sensor as input. For these measurements to be reliable, the signal must have a constant shape that scales with the amount of energy deposited [76]. This is not the only factor that affects the timing capabilities of a detector. In order to go through all the parameters that affect the timing resolution, we must first indicate the main components of a time-tagging detector, see Figure 5.4. The silicon sensor, indicated as a capacitor with a current source in parallel, is read out by a preamplifier. The preamplifier output is then compared to a threshold (V_{th}) to determine the time of arrival (t_0). Lastly, the comparator output is digitised in a time-to-digital converter (TDC). Each step in the read-out process, and any effect that changes the shape of the signal has a different impact in the time resolution. In fact, the time resolution can be expressed as the sum of various terms, as seen in Equation 5.1, each associated to a different effect [82].

$$\sigma_t^2 = \sigma_{\text{Time walk}}^2 + \sigma_{\text{Landau noise}}^2 + \sigma_{\text{Distortion}}^2 + \sigma_{\text{Jitter}}^2 + \sigma_{\text{TDC}}^2 \tag{5.1}$$

A detailed description of each one of these terms can be found in the following pages.

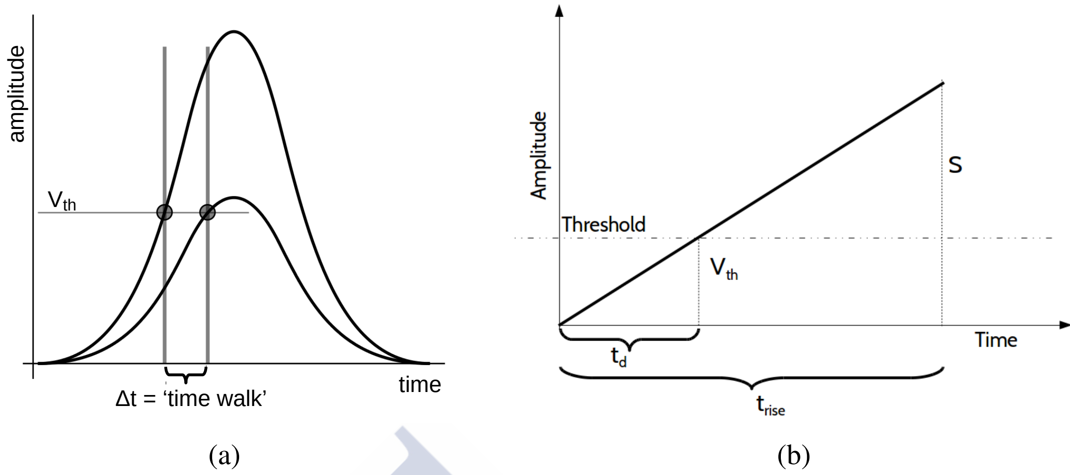

Figure 5.5: (a) *Time walk* is the variation in time of arrival produced by the difference in signal amplitude. The higher the amplitude, the sooner the signal will surpass the threshold used to determine the time of arrival. Modified from [83]. (b) Linear signal with a maximum amplitude S, and a rise time t_{rise}. The signal crosses the threshold V_{th} at t_d.

5.2.1.1 Time walk

The time of arrival was previously defined as the time when the signal crosses a fixed threshold. The time at which this occurs will inevitably depend on the pulse height. As the amplitude varies, the time of arrival shifts. The higher the amplitude, the sooner the signal will surpass the threshold, giving an earlier time of arrival than a lower signal. This phenomenon, which is illustrated in Figure 5.5a, is called *time walk* [25]. Let us illustrate this effect by means of a linear signal, see Figure 5.5b. The maximum amplitude of said signal is S, its rise time is t_{rise}, and the time at which the signal crosses the threshold (V_{th}) is t_d. According to the intercept theorem, these parameters can be related as follows, $t_d/t_{rise} = V_{th}/S$. Thus, the time at which the signal crosses the threshold can be defined as $t_d = t_{rise} \cdot V_{th}/S$. The *time walk* is defined as the RMS of t_d:

$$\sigma_{\text{Time walk}} = [t_d]_{RMS} = \left[\frac{V_{th}}{S/t_{rise}}\right]_{RMS} \propto \left[\frac{N\sigma_n}{dV/dt}\right]_{RMS}; \tag{5.2}$$

where it has been taken into consideration that the threshold is usually expressed in multiples of the system noise ($N\sigma_n$), and that $S/t_{rise} = dV/dt$ [76].

From Equation 5.2 it can be deduced that time walk can be reduced by setting the threshold to the lowest possible level, by minimising the noise, by maximising the slew rate[2], and by using amplitude compensating circuitry. This last point is related to the

[2] Change of voltage or current per unit of time (dV/dt).

fact that the time measurement can be significantly corrected, i.e. the time walk can be reduced, if the signal amplitude is known [25, 76]. For this purpose, two techniques are commonly used: Time-over-Threshold (ToT) and Constant Fraction Discriminator (CFD). Further details of these two methods can be found in [76].

5.2.1.2 Landau noise

When a MIP traverses a silicon sensor, the energy deposition, and hence the charge distribution created, follow a Landau-Vavilov distribution [25]. This means that the signal produced by a MIP crossing a sensor varies on an event-by-event basis. Such variations cause a change in signal magnitude, which, as explained before, is at the core of the time walk phenomenon. In addition, for a given event, the amount of deposited energy per unit length is not uniform. These additional fluctuations, specific to each event, produce irregularities in the current signal, referred to as *Landau noise* [84]. Landau noise is intrinsic to how energy is deposited in silicon detectors by MIPs. As a consequence, it can be minimised, but not fully compensated as, for instance, time walk. It has been found that Landau noise sets a physical limit to the precision of a silicon sensor. In the case of thin sensors ($\sim 50\mu$m) this limit is of the order of 20 ps, the value increases with sensor thickness [84]. Nevertheless, Landau noise can be minimised by setting the threshold as low as possible, and by using thinner detectors [84].

5.2.1.3 Signal distortion: drift velocity and weighting field

As explained in Chapter 2, the induced current signal of a silicon detector can be calculated using the Ramo-Shockley theorem [25]. As seen in Equation 2.9, according to this theorem, the current induced by a charge carrier is proportional to the drift velocity, and the weighting field. These variables must be considered when developing a device for timing applications. For instance, inhomogeneities in the drift velocity throughout the active volume of the sensor will inevitably lead to variations in signal shape as a function of the hit position. To achieve the required uniformity, the simplest solution is to have a high enough electric field ($\mathscr{E} > 30$ kV/cm) so that carriers move with saturated drift velocity [84]. As regards the weighting field, uniformity is also of the essence. As previously explained in Chapter 2, the weighting field depends only on the geometry of the sensor and determines how charge motion couples to a specific electrode [25]. If the weighting field depends on the hit position along the implant pitch[3], then the resulting signal will have a different shape for each point of incidence. In devices with a pitch similar to the electrode width the weighting field along the electrode pitch is fairly constant, see Fig 5.6a. On the contrary, if the electrode width is much smaller than the pitch, the weighting field is concentrated solely underneath the implant, see Figure 5.6b. In short,

[3]Distance between the centres of adjacent electrodes.

segmented sensors need to have an electrode width similar to the pitch, and both of these must be larger than the sensor thickness [76].

5.2.1.4 Jitter

The presence of noise in the signal itself or in the electronics results in the fluctuation of the time of threshold crossing, causing the early or late triggering of the comparator. This in turn leads to a timing variance referred to as *jitter* [76]. As can be seen in Figure 5.7, by simple geometrical projection the jitter is determined by the following equation:

$$\sigma_{\mathrm{Jitter}} = \frac{\sigma_n}{\mathrm{dV/dt}} \approx \frac{\mathrm{t_{rise}}}{S/\sigma_n}, \tag{5.3}$$

where, as in Section 5.2.1.1, a linear leading edge has been assumed: $\mathrm{dV/dt} = S/\mathrm{t_{rise}}$ [25]. It is then apparent that in order to minimise the jitter, timing detectors must have low intrinsic noise, and very fast slew rates. Also, the read-out electronics must have low noise as well [76].

5.2.1.5 TDC effects

To be able to store in memory the timing measurements these must be digitised, a time-to-digital converter (TDC) is used for this purpose. When digitised, the time of arrival obtained through the comparator is stored in a time bin of width ΔT. The contribution to the timing resolution is $\Delta T/\sqrt{12}$ [76]. There have been extensive improvements in the performance of TDCs. Actually, TDCs have reached sub-picosecond time resolution, rendering the contribution of TDC binning negligible compared to the other terms [86].

5.2.2 Detector requirements for timing

From the factors affecting the time resolution mentioned above it is possible to draw some conclusions regarding the properties timing detectors must have. Firstly, the devices must have very fast slew rates and low intrinsic noise, the latter is also required from the read-out electronics. These properties ensure the minimisation of both the jitter and the time walk. Secondly, to reduce as much as possible the Landau noise it is recommendable to use thin detectors. Thirdly, the electric field in the sensor must be high enough so that charge carriers move with saturated drift velocity. This ensures a uniform drift velocity and, consequently, reduces signal distortions. Lastly, signal distortions can be mitigated by designing devices with an electrode width much larger than the sensor thickness.

UNIVERSIDADE DE SANTIAGO DE COMPOSTELA

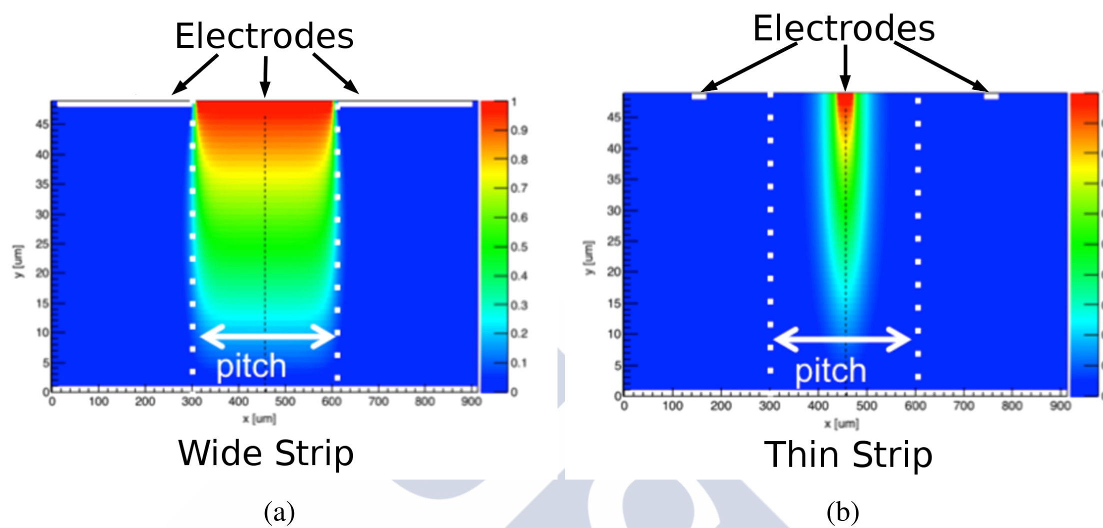

(a) (b)

Figure 5.6: Plots obtained by simulating the weighting field in two segmented devices with (a) wide strips, and (b) thin strips. From [84].

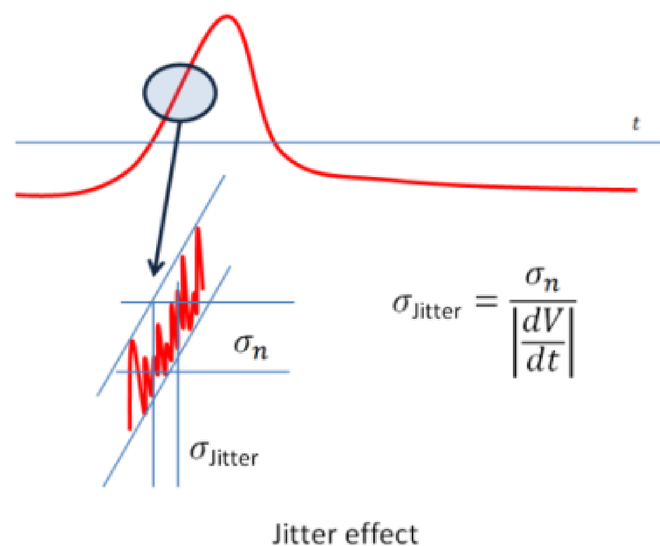

Figure 5.7: The signal noise can produce variations in the time at which the signal crosses the fixed threshold. This fluctuation is known as *jitter*. Modified from [85].

USC
UNIVERSIDADE
DE SANTIAGO
DE COMPOSTELA

Chapter 6

Silicon Detectors with Intrinsic Gain

A conventional silicon detector is a diode that, when operated at reverse bias, gives a response proportional to the amount of charge generated by primary ionisation (see Chapter 2). The performance of these devices can be improved by increasing their signal via the incorporation of internal gain. The mechanism through which this multiplication of the charge is achieved is called *impact ionisation*. If inside the sensor there is a high enough electric field (>200 kV/cm [7]), charge carriers will gain sufficient energy to eject other charges when interacting with the crystal lattice. For devices with a long enough multiplication region[1], the gain due to the impact ionisation of one type of charge carrier within a length d is accurately described by the following equation:

$$G_q = e^{\alpha_q d} \,, \tag{6.1}$$

where α_q is the ionisation probability of the charge carrier. This magnitude is highly dependent on the electric field ($\mathscr{E}$) and is defined by Equation 6.2:

$$\alpha_q = \alpha_{q0} \cdot e^{-\mathscr{E}_q/|\mathscr{E}|} \,. \tag{6.2}$$

The ionisation probability depends on the electric field, the material, the type of charge carrier (electrons or holes), and the temperature [25]. In fact, the coefficients α_{q0} and $\mathscr{E}_q$ increase with temperature, for both electrons and holes. As the exponential term dominates, α_q decreases with temperature [90]. Consequently, the lower the temperature, the higher the gain. Regarding the dependence with the type of carrier and material,

[1]Charge carriers should not be assigned any ionisation probability right after being generated. Carriers must travel a certain distance before they actually gain enough kinetic energy from the electric field to have an appreciable ionisation probability [87]. This distance is usually referred to as *dead space* or *dead length*. The dead space can be ignored if it is significantly smaller than the thickness of the multiplication region. On the contrary, if the multiplication region is narrow, i.e. of the order of a *few* dead spaces, then the dead space of the carriers cannot be ignored. This means that, under the latter circumstances, Equation 6.1 is no longer accurate. For a detailed study of the accurate gain expression in the case of sensors with a short multiplication region see [88, 89].

in silicon the ionisation probability for hole-induced ionisation (α_h) is lower than that of electrons (α_e). The ratio between these two coefficients, $\kappa = \alpha_h/\alpha_e$, tends to unity with increasing electric field. At lower electric fields it is electrons that undergo impact ionisation. That said, at a high enough electric field, the holes produced by primary ionisation will also start charge avalanches through impact ionisation. When this occurs, the *secondary charges*, those produced through multiplication, can create further avalanches, causing a self-sustaining process, and leading to the *breakdown* of the device [91]. The strong dependence of the ionisation probability with the electric field has a direct impact in the design and performance of devices with intrinsic gain. Even small inhomogeneities in the doping or crystal defects in the multiplication region may result in parts of the device undergoing breakdown, whilst in others there is proportional amplification. For this reason, it is of the utmost importance to ensure the homogeneity of the sensors, which explains the complexity of producing large-area (more than a few mm^2) devices [29].

The properties inherent to silicon detectors with intrinsic gain make them clear candidates to be used in timing applications. For this particular purpose, the objective is to design detectors that will minimise the time resolution σ_t, given by Equation 5.1. Below there is a detailed explanation of how detectors with intrinsic gain can prove helpful at optimising the parameters in Equation 5.1 [92].

- **Jitter**

  In Section 5.2.1.4 it was already discussed that the jitter can be minimised by using detectors with low intrinsic noise, and very fast slew rates, i.e. high signal amplitude and short rise time. Detectors with internal gain can provide signals with a high amplitude whilst maintaining fairly low noise levels. As for the fast slew rate, sensors with short drift distances are the best option. Thin detectors with intrinsic gain deliver signals of the same amplitude as a thick sensor, but with a much shorter rise time [93].

- **Time walk and Landau noise**

  According to Equation 5.2 the time walk can be reduced by setting the threshold to the lowest possible level, by minimising the noise, by maximising the slew rate, and by using amplitude compensating circuitry. Of these parameters, the ones that can be controlled through the appropriate design of the sensor are the noise level and the slew rate. In the same way as for the jitter, detectors with intrinsic gain provide an optimum solution.

  As far as Landau noise is concerned, it is impossible to eliminate it, as it is intrinsic to how energy is deposited in silicon detectors by MIPs. Having said that, it is possible to reduce it by employing thin devices, vindicating the idea of using sensors with internal gain.

UNIVERSIDADE DE SANTIAGO DE COMPOSTELA

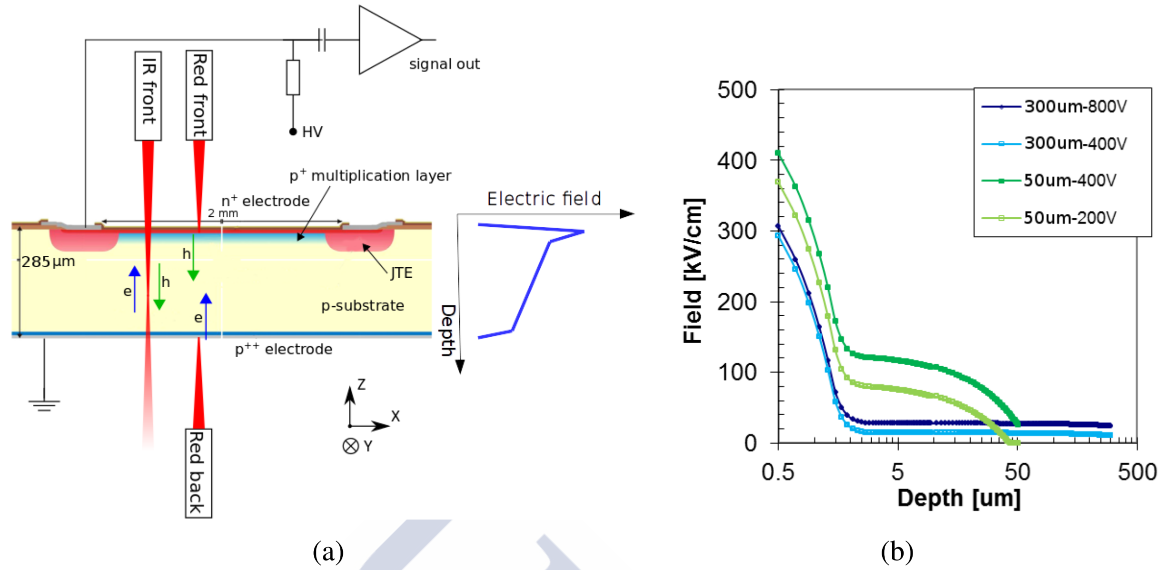

(a) (b)

Figure 6.1: (a) Schematic cross section of an LGAD pad with a JTE structure. The laser configuration of the TCT set-up can also be seen, where hole and electron injection is accomplished using red and infrared laser pulses. Right: simplified depiction of the electric field inside a fully depleted LGAD. (b) Simulation of the electric field at two different bias voltages inside a thin (50 μm) and a thick (300 μm) LGAD. From [94].

- **Signal distortion: drift velocity and weighting field**

  As discussed in Section 5.2.1.3, the drift velocity must be homogeneous throughout the entire active volume of the sensor, and the weighting field must be uniform along the implant pitch. The first is achieved by inducing a high enough electric field ($\mathscr{E} > 30$ kV/cm) so that carriers move with saturated drift velocity. Detectors with internal gain guarantee that, at least within the region of multiplication, the drift velocity will saturate. However, to ensure its saturation over the full active volume, there are special design and operation aspects to be considered. For instance, in the case of LGADs these conditions can be achieved by applying higher bias voltages to thick detectors (300 μm), or by using thinner devices (50 μm), see Figure 6.1b. Finally, the weighting field uniformity can be fulfilled by designing the geometry of the electrodes properly, irrespective of gain.

- **TDC effects**

  The contributions of TDC discretisation can be reduced not by optimising the silicon detector itself, but by using the proper bin size.

Having appraised detectors with intrinsic gain for the purpose of accurate timing, it is reasonable to conclude that they are a potentially excellent choice. In the following pages, the specific detector technologies analysed in this thesis are described.

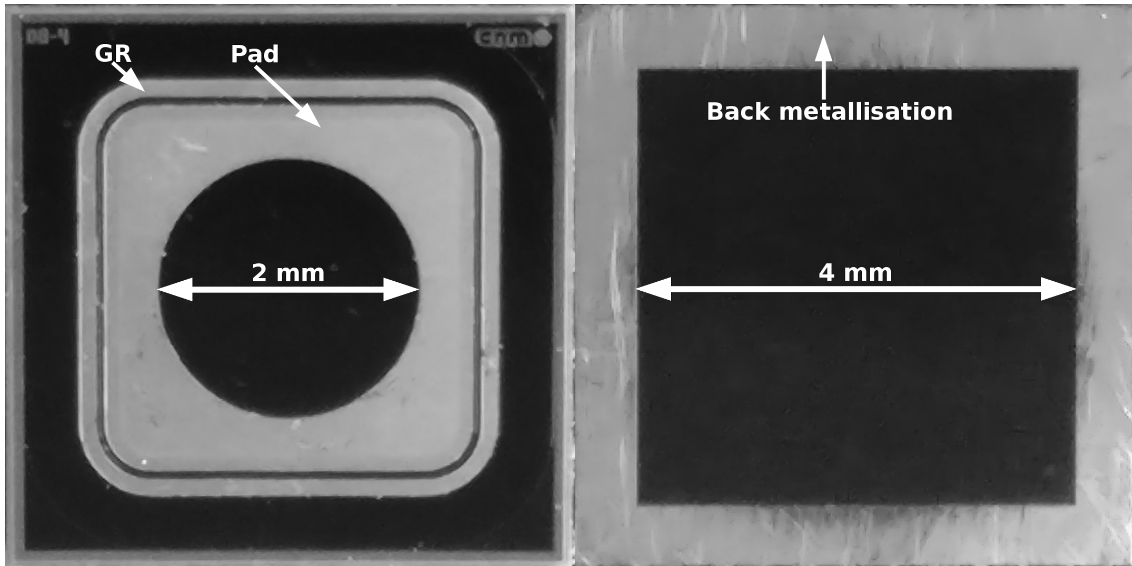

Figure 6.2: Front (left) and back (right) view of the CNM devices characterised in this thesis. Both LGADs and PiN diodes have the same metallisation structure.

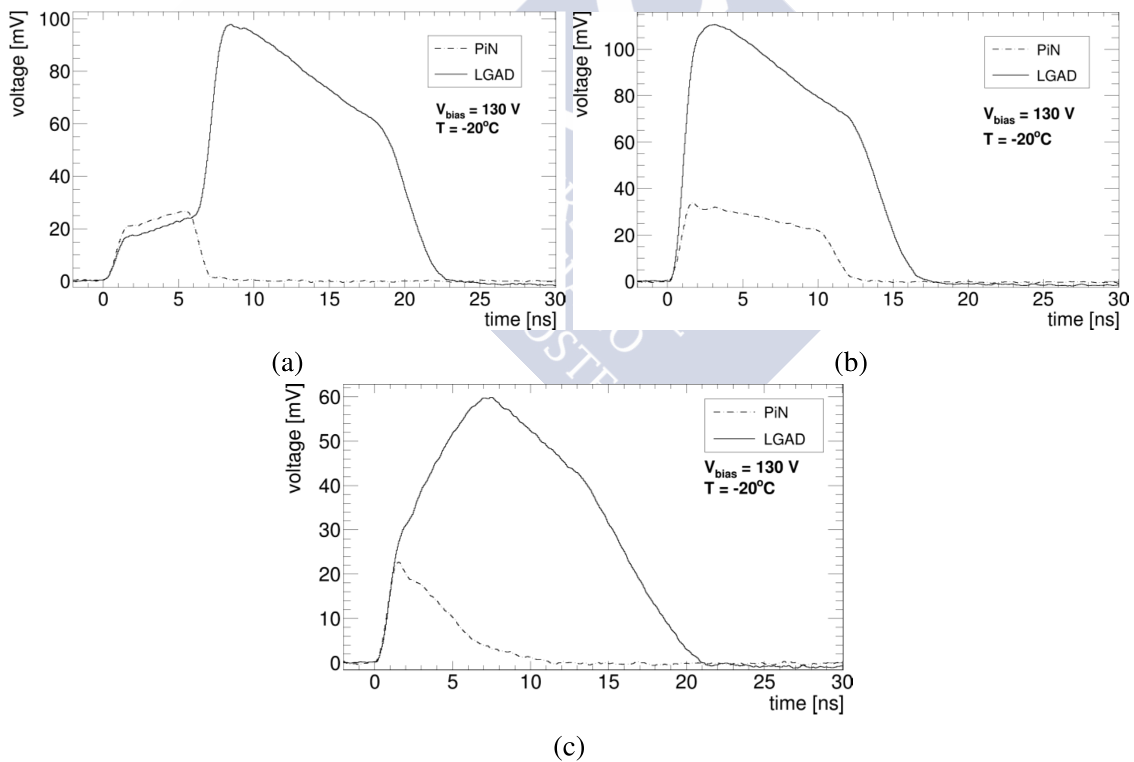

Figure 6.3: Waveforms obtained with (a) red-back TCT, (b) red-front TCT, and (c) IR TCT on an LGAD (solid line) and on an n-in-p diode (dashed line), both sensors have a thickness of 285 μm. These signals were obtained at -20°C, applying 130 V, and using the same laser intensities for both sensors. The full depletion voltages of the sensors are $\sim$ 42 V for the PiN, and $\sim$ 71 V for the LGAD.

6.1 Low Gain Avalanche Detectors

Low Gain Avalanche Detectors (LGADs) are planar silicon sensors that consist of a p-type bulk with a p++ ohmic contact, an n+ electrode, and a diffused p+ (multiplication) layer just below the n+ electrode, see Figure 6.1a. If the sensor is reverse biased, a high electric field is produced in the multiplication layer region. When charge carriers reach this region, if the field is high enough (>200 kV/cm), they will undergo impact ionisation, producing additional charge carriers. The extent of said ionisation, and thus the gain of the sensor, is directly dependent on the doping concentration of the p+ layer as well as on the bias voltage applied and the temperature of operation [90, 95].

The doping concentration of the p+ layer is chosen to generate a gain between 10 and 100, much lower than the usual gain of, for instance, a SiPM (10^4) [5]. By limiting the gain to lower values, many drawbacks are averted, such as: the gain-induced increase in sensor noise, the difficulties in sensor segmentation (due to the very high fields), and the high power consumption after irradiation. The main idea behind the development of LGADs is to design thin detectors with the lowest gain necessary to perform accurate single particle time measurements [76]. As mentioned in Section 5.2.1.3, to improve time resolution it is advisable to saturate the drift velocity. A sufficiently high bias voltage guarantees that the electric field in the bulk of the sensor is almost as high in an LGAD as it would be in a sensor without gain (without the p+ layer). Therefore, the drift velocity saturates, and signals with fast rise time and uniform shapes are obtained. For all of these to be possible, LGADs are designed so that a high external voltage can be applied without the detectors reaching breakdown. [5, 96].

A part of the devices under study in this thesis are pad PiN diodes[2] and LGADs from run[3] 7859. They were all manufactured by the Centre Nacional de Microelectrònica (CNM) in Barcelona. These PiN diodes and LGADs were processed on p-doped float-zone[4] silicon wafers with a resistivity of 12 kΩ·cm. Each sensor has an active area of 3×3 mm^2, a thickness of 285 μm, a guard ring (GR), and a junction termination extension (JTE) (see Figure 6.1a). The JTE is an n-type diffusion that overlaps with the edge of the main junction. Its purpose is to increase the operational voltage range by making the electric field more homogeneous at the junction [97]. Additionally, all samples have openings in the metallisation, both on the front and the back, with the purpose of allowing for laser measurements, see Figure 6.2. The details regarding doping concentrations of the devices, irradiation campaigns, etc. are indicated in Chapter 7.

[2]These PiN diodes come from the same wafers as the LGADs and have the same properties except for the fact that PiN diodes have no multiplication layer.

[3]Batches of sensors coming from several wafers produced with the same mask design. Within each run LGADs with different multiplication-layer doping may be produced.

[4]For a detailed description of the properties and crystal growth method of float-zone silicon see Appendix A.

For the purpose of understanding some of the results obtained in this thesis, which will be discussed in Chapter 7, it is important to go through the expected signal shapes in LGADs, and in PiN diodes of the same characteristics, barring the multiplication layer. In particular the focus will be on waveforms obtained through all available TCT illuminations: red front, red back, and infrared (see Section 4.2).

- **Red-back TCT $\equiv$ electron injection**

  The typical waveforms obtained through red-back TCT (electron injection) on an n-in-p diode (PiN diode) and an LGAD are shown in Figure 6.3a. The different components of the signals can be clearly identified. In the case of the LGAD, first there is the drift of the injected electrons (e^-), which coincides with the expected signal from the PiN diode. Whilst for the PiN diode there is only the drift of e^-, the LGAD waveform presents the onset of the multiplication right after the e^- drift. The multiplication ends at around 7 ns and it is followed by the drift of the secondary holes (produced in the multiplication). The end of the signal is a tail caused by diffusion and the read-out electronics.

- **Red-front TCT $\equiv$ hole injection**

  The signal obtained with red-front TCT (hole injection) on an LGAD is similar in shape to that obtained with a PiN diode, see Figure 6.3b. The PiN diode signal is produced by the drift of holes from the front side of the device towards the back electrode. On the other hand, in the LGAD there are two overlapping components to the signal: the primary holes drifting towards the back electrode, as in the PiN diode; and the secondary holes generated by the impact ionisation of the electrons created by the impinging laser. As these two mechanisms of generation of holes occur in the same time scale, it is impossible to discriminate each contribution to the signal. What can be noticed, however, is the difference in amplitude between signals, a direct consequence of the multiplication in LGADs. It should be noted, though, that the gain expected for hole injection (red-front TCT) is lower than that expected for electron injection (red-back TCT). In red-front TCT the electrons are created so close to the front electrode that some of them might not travel a long enough distance through the multiplication region to actually undergo impact ionisation.

- **Infrared TCT $\sim$ MIPs**

  As explained in Section 4.2, infrared TCT provides a method to emulate the response of a silicon sensor to minimum ionising particles, excluding statistical charge fluctuations. The signal obtained is a combination of drifting electrons and holes, which are created all through the path of the laser beam. In Figure 6.3c the signals obtained through IR TCT on a PiN diode and an LGAD are shown.

6.2 Deep Diffused Avalanche Particle Detectors

Deep Diffused Avalanche Particle Detectors (DD-APDs) are sensors with intrinsic gain, and as such they have a high electric field region where charge carriers undergo impact ionisation. The p-n junction is located towards the centre of the device, rather than close to the surface (Figure 6.5a). A high reverse bias voltage must be applied to achieved the desired gain. Even so, the devices remain under-depleted, with a depletion region of $\sim 150\ \mu$m near breakdown (1.8 kV) [98]. Nevertheless, the multiplication region of these devices has a lower and wider electric field compared to other devices, such as *reach-through APDs* (see [91]). This results in higher gain values, and lower κ, i.e. the ratio between hole and electron ionisation rates, mentioned at the beginning of this chapter. Those properties cause a reduction in noise levels, and, at a given gain, an increase in stability with respect to changes in bias voltage, temperature or local fluctuations in impurity concentration [99].

Having said that, the high voltage applied creates a strong enough electric field so that it could present some issues along the edge of the device, where electrical breakdown might occur at a lower voltage than in the bulk [98]. Reducing the electric field on the edges and surface of the sensor inhibits breakdown at the edges, which would otherwise contribute to leakage current and device noise [100]. Such a reduction is accomplished by properly shaping the doping profile. RMD (Radiation Monitoring Devices Inc.) does this by means of a planar production process, a schematic of the complete production process is shown in Figure 6.4. Grooves are machined on both sides of an n-type neutron transmutation doped[5] silicon wafer. Afterwards, the deep diffusion of p-type dopants is performed by exposing the wafers to a vapour rich in gallium and aluminium. This process takes several days (more than 150 hours) and is done at high temperatures ($\sim$ 12000°C) [100]. The presence of the grooves on the surface of silicon causes the doping profile to be curved [98]. The p-type region then encloses an n-well, and the p-n junction is formed between the interfaces of these two regions, see Figure 6.5b. The wafer is then ground to remove excess material from both wafer surfaces. On the bottom side, enough material is removed so that the n-region forms part of the surface [100]. Non-metallic conductive layers are diffused into the front (p+) and back (n+) of the device. Lastly, on the n+ side the contact electrode is etched into a mesa structure; a polyimide passivation layer is applied on the entire back side, except the n+ electrode; and the wafer is diced [100]. The DD-APDs manufactured by RMD can be diced into discrete devices with a size ranging between 3 mm^2 to 10 cm^2. Also, monolithic, multi-element DD-APD arrays having up to 28×28 elements can be manufactured [102].

[5]Neutron Transmutation Doping (NTD) is the process by which a semiconductor is doped through thermal-neutron irradiation. Natural silicon has a 3.10 % abundance of ^{30}Si. This isotope can capture a slow neutron, resulting in ^{31}Si which is unstable, and decays to ^{31}P through a beta decay. The final product is an n-type doped silicon material [101].

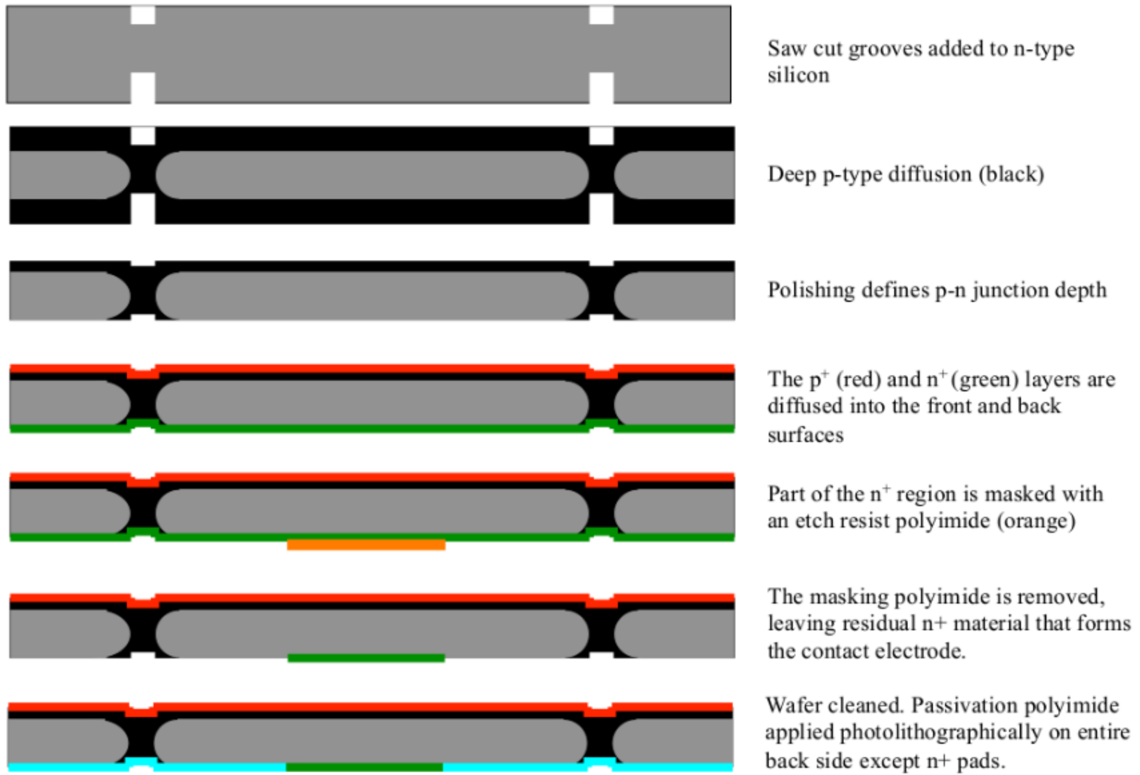

Figure 6.4: Schematic of the fabrication process of DD-APDs. From [103].

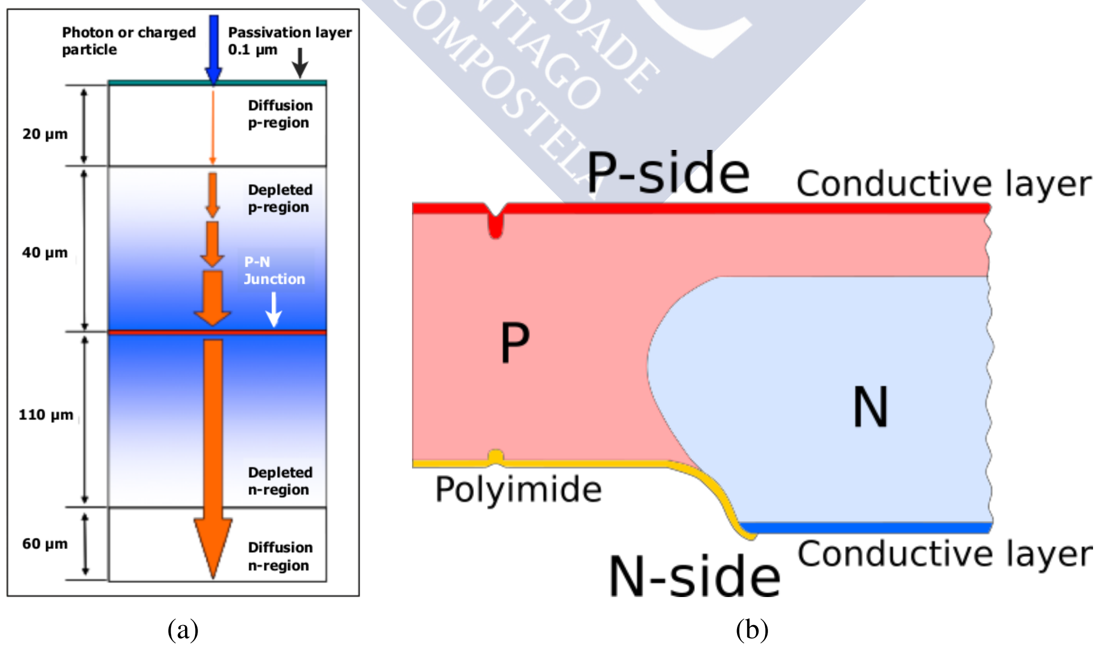

(a) (b)

Figure 6.5: (a) Cross-section schematic of a DD-APD. (b) Diagram of the edge of a DD-APD. From [24].

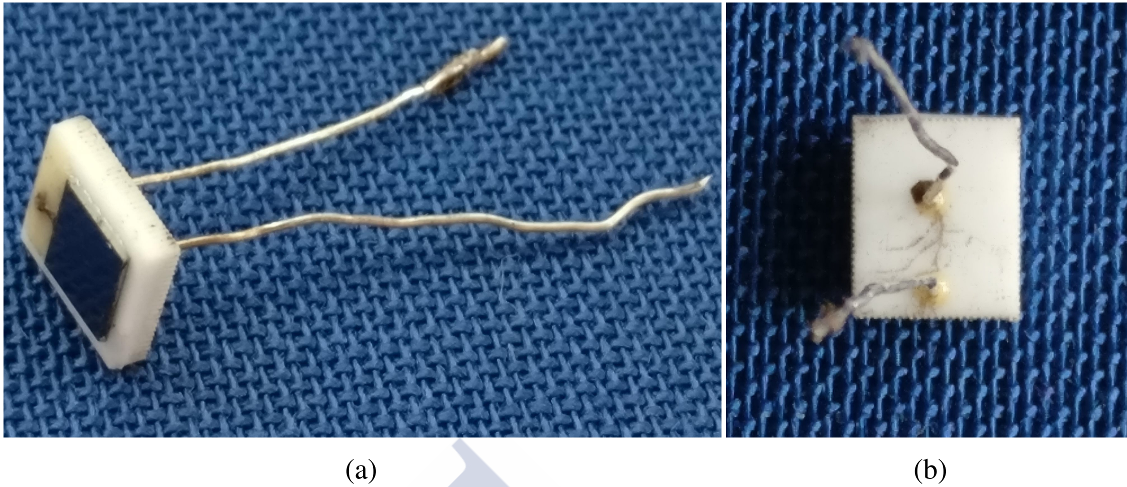

(a) (b)

Figure 6.6: Pictures of one of the 2×2-mm^2 DD-APDs measured in this thesis. (a) Side view, and (b) back view.

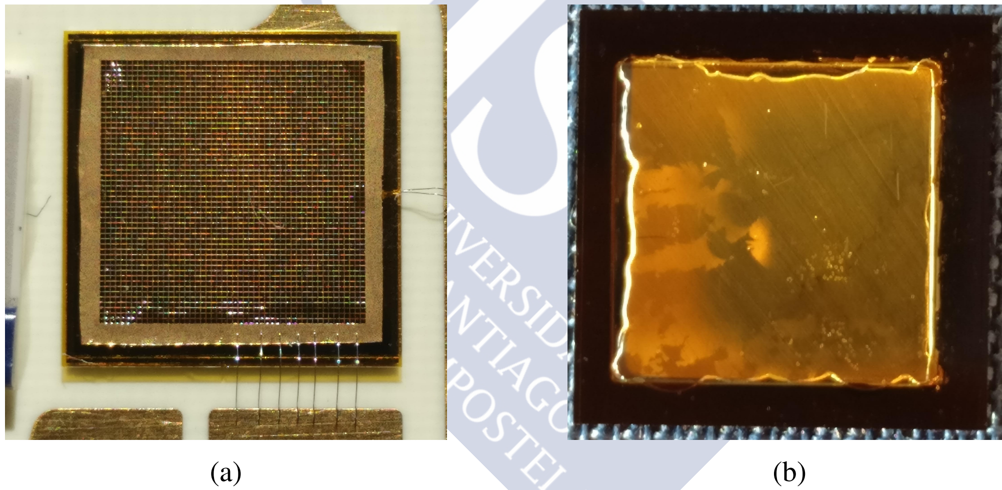

(a) (b)

Figure 6.7: Pictures of an 8×8-mm^2 DD-APDs with an (a) AC-coupled read-out on the p-side, and a (b) sintered gold layer on the n-side.

Studies performed during the past years on this type of devices have shown that the signal amplitude in DD-APDs is highly dependent on position [20, 21]. This is a highly important issue for timing applications. To improve the uniformity of response it was proposed that the devices should be customised so as to enable an AC-coupled readout of the p-side of the detector. Tests were performed on DD-APDs with a die size of 10×10 mm^2, and an active area of 8×8 mm^2 [20]. Various read-out and bias configurations were tested. It was concluded that the best results for spatial uniformity, time walk and jitter were obtained with the configuration consistent of a kapton layer and a metallic mesh on the p-side (Figure 6.7a); and a layer of sintered gold on the n-side (Figure 6.7b), to improve its conductivity [20].

In this thesis, RMD DD-APDs with an active area of 2×2 mm^2, and 8×8 mm^2 were studied. The research focuses mainly on the effects of neutron irradiation on DD-APDs with an active area of 2×2 mm^2, mounted on an alumina substrate with feed-through connectors, see Figure 6.6. The electrical connections between the DD-APD electrodes and the leads are made with conductive epoxy bumps. Also, the space between the DD-APD and the alumina substrate is filled with a non-conducting underfill material to provide mechanical support and environmental protection to the DD-APD [100]. No AC-coupling was added to these sensors, i.e. they do not have a mesh. The specific details of the devices, the mounting, the irradiation campaigns, the read-out methods, etc. are all explained in Chapter 8. A brief report on the spatial dependence of the signal amplitude in 8×8-mm^2 DD-APDs without the addition of a mesh is also included, see Section 8.3. The objective was to verify this spatial dependence by means of TCT measurements, identify its cause, and test the possibility of employing a simpler method to fix the non-uniformity problem: metallisation of the electrodes.

Chapter 7

Characterisation of LGADs

The following sections are dedicated to the presentation and discussion of the results obtained from the characterisation, before and after proton irradiation, of a batch of LGADs and PiN diodes. All the devices, manufactured by CNM-Barcelona, have a thickness of 285 μm, an active area of 3×3 mm^2, a guard ring (GR), and a junction termination extension (JTE). The characterisation of the sensors was done by performing current and capacitance measurements as a function of voltage (IV and CV), radioactive source measurements, TCT scans, eTCT and TPA-TCT Z-scans at different voltages and temperatures. The objective is to analyse the effects of radiation on several properties of LGADs, namely the gain; the charge collection homogeneity; the multiplication onset; and the evolution with voltage, fluence and temperature of the electric field, the collected charge, and the space charge. The main use of including PiN diodes in this study is to serve as a reference for gain calculations. The average peak power of the laser beams used for front and back illumination were 47.4 μW for red TCT, and 29.5 μW for IR TCT.

The samples studied come from CNM run 7859, and from four different wafers: W1, W2, W3 and W4. W1 and W2 have the same multiplication-layer implant dose: 1.8×10^{13} cm^{-2}. Correspondingly W3 and W4 have both a multiplication-layer implant dose of 2.0×10^{13} cm^{-2}. Regarding the electrical parameters of these sensors, they all have an end capacitance before irradiation of ~ 4.1 pF, and a total leakage current (pad + GR) of less than 0.21 μA at full depletion and 20°C.

The samples were sent to be irradiated with 24-GeV/c protons at the CERN IRRAD facility (hardness factor of 0.56 in 2015) [70, 71]. In order to study the effects of different fluences, the samples were separated in four sets of four detectors each. Every set consisted of 2 PiN diodes and 2 LGADs, each of these pairs was formed by one sample from W1 or W2 and another one from W3 or W4. Each set was irradiated up to a different fluence (see Table 7.1): 10^{12}, 10^{13}, 10^{14}, and 10^{15} n$_{eq}$/cm^2. After irradiation, and before their characterisation, the detectors were annealed at 60°C for 80 min.

Table 7.1: Irradiation details for all LGADs and PiN diodes from run 7859.

Fluence [1 MeV $n_{eq}cm^{-2}$]	LGADs	PiN diodes
0	LGAD_7_W1_C2_3	-
	LGAD_4_W4_D7_1	-
10^{12}	LGAD_4_W2_E3_1	PIN_4_W2_I8_1
	LGAD_4_W4_I3_1	PIN_4_W3_H9_1
10^{13}	LGAD_4_W2_D8_2	PIN_4_W2_J6_1
	LGAD_4_W3_E8_1	PIN_5_W4_A6_4
10^{14}	LGAD_4_W2_I3_1	PIN_7_W1_C9_3
	LGAD_7_W3_C2_3	PIN_4_W3_I8_1
10^{15}	LGAD_9_W1_F10_3	PIN_4_W1_I8_1
	LGAD_7_W3_D1_4	PIN_4_W4_A6_3

7.1 Capacitance and leakage current

To properly characterise the devices and to be able to compare the results obtained through TCT with those measured in other studies, it is of the utmost importance to obtain the IV and CV curves of the sensors before and after irradiation. The measurements were performed in the probe station described in Section 4.1.1, applying a negative bias to the p-side of the devices, and connecting the GR to ground. Before irradiation all measurements were conducted at 20°C and after irradiation at -20°C.

7.1.1 Capacitance

Figures 7.1 and 7.2 shows the curves of inverse square capacitance with respect to voltage for all PiN diodes and LGADs, both before and after irradiation. Before irradiation, at low voltages, as the device depletes, the curves for PiN diodes grow linearly until after full depletion, where the capacitance is constant so a plateau is reached (see Chapter 2). In contrast, the linear increase with voltage of $1/C^2$ in LGADs starts after a certain *threshold voltage*. For W1 and W2 (multiplication-layer dose: 1.8×10^{13} cm^{-2}) the threshold voltage is of approximately 30 V, for W3 and W4 (multiplication-layer dose: 2.0×10^{13} cm^{-2}) it is of $\sim$ 32 V. This *foot* indicates that the depletion of the bulk does not commence until the multiplication layer has been depleted. This threshold voltage will be discussed in greater detail further on in this chapter, as it is associated with the multiplication onset.

As explained in Chapter 2, it is possible to extract the depletion voltage of the sensors from 1/C^2 curves. Figure 7.3 presents the depletion voltage values of all LGADs and PiN diodes from run 7859 before and after irradiation. Firstly, before irradiation LGADs had, on average, a full depletion voltage of $\sim$ 66 V for W1 and W2 (multiplication-layer dose: 1.8 $\times$ 10^{13} cm^{-2}), and $\sim$ 71 V for W3 and W4 (multiplication-layer dose: 2.0 $\times$ 10^{13} cm^{-2}). Such a difference in depletion voltage is consistent with the difference in multiplication-layer dose. LGADs from W3 and W4 require a higher voltage to deplete the multiplication layer, and consequently the full device. On the other hand, PiN diodes had a lower full depletion voltage: $\sim$ 40 V for W1 and W2, and $\sim$ 44 V for W3 and W4. Such behaviour was expected as PiN diodes do not have a multiplication layer to deplete.

After irradiation, it was found that at lower fluences ($\leq 10^{13}$ n$_{\mathrm{eq}}$/cm^2) the depletion voltage of PiN diodes from W3 and W4 decreased slightly, whilst for PiN diodes from W1 and W2 the depletion voltage was constant within considering uncertainties. At higher fluences ($\geq 10^{14}$ n$_{\mathrm{eq}}$/cm^2) the depletion voltage of all PiN diodes increased, as expected (see Chapter 3). For LGADs from W1 and W2 there is a moderate tendency towards lower values of depletion voltage up to a fluence of 10^{14} n$_{\mathrm{eq}}$/cm^2 ($V_{\mathrm{dep}(1\mathrm{E}14\mathrm{n_{eq}/cm^2})} = 52 \pm 7$ V). Although the device irradiated up to 10^{13} n$_{\mathrm{eq}}$/cm^2 (LGAD_4_W2_D8_2) presents an unusually high depletion voltage. As a matter of fact, as will be discussed in the following section, also the leakage current of that sample was higher than expected, even at voltages below the so-called threshold voltage, or *multiplication-onset voltage*. Meanwhile, LGADs from W3 and W4 presented a clear decrease in depletion voltage up to a fluence of 10^{14} n$_{\mathrm{eq}}$/cm^2. This decrease in depletion voltage could be an indicator of *acceptor removal* in the multiplication layer, which (as explained in Chapter 3) consists in the decrease of the effective acceptor concentration (N_a), i.e. the a decrease in the number of active acceptors [10, 45]. If the effective doping of the multiplication layer decreases, then so does the required voltage to deplete it ($V_{dep} \propto N_a$) [25]. In line with this result, at a fluence of 10^{15} n$_{\mathrm{eq}}$/cm^2 LGADs, regardless of the wafer, the depletion voltage of both LGADs is higher, and coincides within the error range with that of PiN diodes irradiated to the same fluence. This would indicate that at a fluence of 10^{15} n$_{\mathrm{eq}}$/cm^2 LGADs behave as PiN diodes, meaning that effectively there is no longer a multiplication layer.

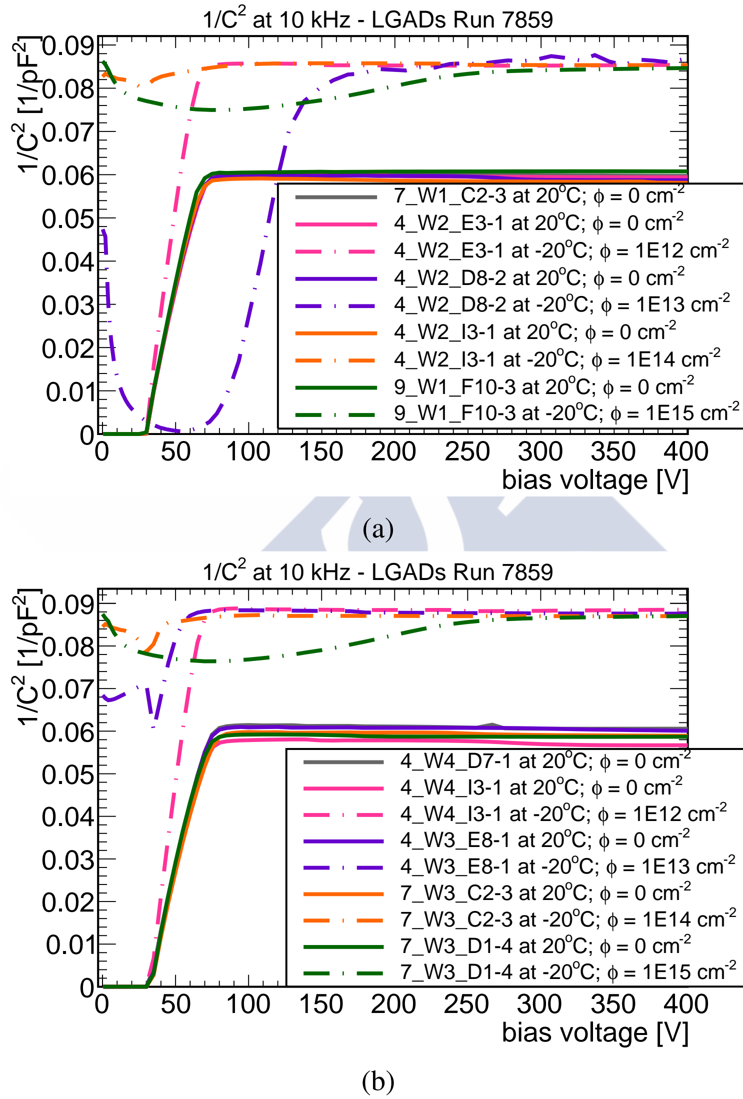

Figure 7.1: Inverse square capacitance with respect to voltage, before and after irradiation, for all (a) LGADs from W1 and W2 (multiplication-layer dose: 1.8×10^{13} cm^{-2}), (b) LGADs from W3 and W4 (multiplication-layer dose: 2.0×10^{13} cm^{-2})

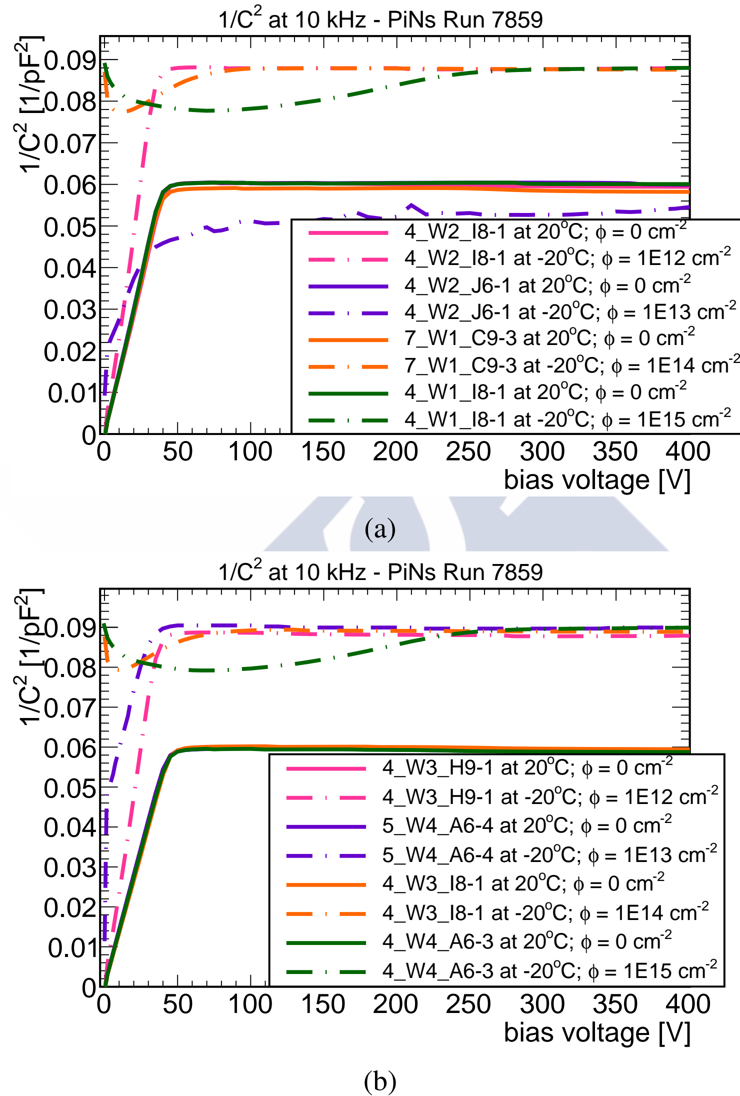

Figure 7.2: Inverse square capacitance with respect to voltage, before and after irradiation, for all (a) PiN diodes from W1 and W2, and (b) PiN diodes from W3 and W4. The measurements were done at 20°C before irradiation, and at -20°C after irradiation.

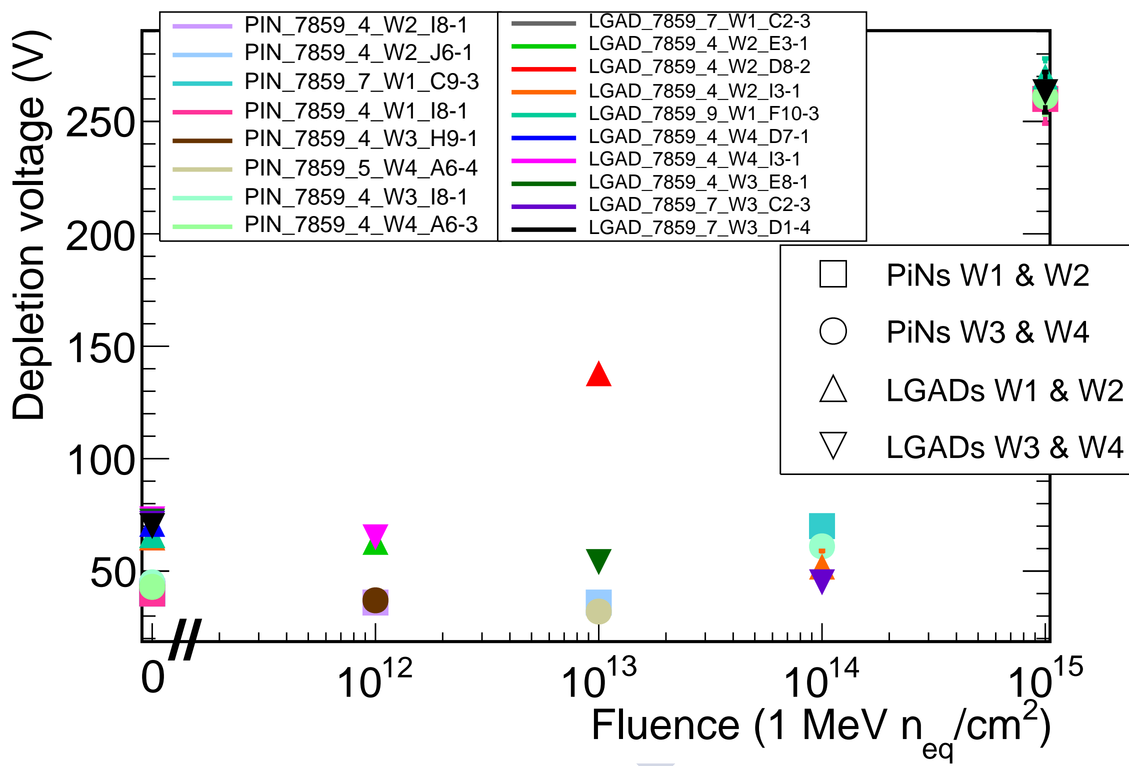

Figure 7.3: Full depletion voltage with respect to fluence for all the LGADs and PiN diodes from run 7859.

7.1.2 Leakage current

As regards the IV curves, Figures 7.4 to 7.7 show the total (pad + GR) and the pad leakage current before and after irradiation for all the measured LGADs and PiN diodes from run 7859. It was found that before irradiation at full depletion voltage and 20°C the total leakage current for LGADs was lower than 0.21 μA for all devices (see Figure 7.6). Only a sensor from W4 (LGAD_4_W4_I3_1) had an unusually high total leakage current, $\sim$ 35 μA at full depletion, which is why the device was chosen to be irradiated up to a fluence of 10^{12} n_{eq}/cm^2. By comparing for each device the leakage current before and after irradiation it can be seen that after irradiation the pad leakage current is higher, even though the measurements after irradiation were done at a lower temperature (-20°C).

Another important aspect that can be examined in these measurements is the threshold voltage, also referred to as multiplication-onset voltage. In the case of $1/C^2$ curves, the threshold voltage was identified as the minimum voltage as from which $1/C^2$ increases linearly with voltage. In IV curves, the link between the threshold voltage and multiplication becomes more apparent, as it is at this voltage that an increase in leakage current is observed. By observing the IV curves at low voltages, it is possible to clearly identify this voltage.

Figure 7.4c and 7.5c show the pad leakage current curves for all LGADs from W1 and W2 (multiplication-layer dose: 1.8×10^{13} cm^{-2}), and W3 and W4 (multiplication-layer dose: 2.0×10^{13} cm^{-2}), respectively, between 0 and 80 V. Before irradiation all samples but one have a threshold voltage of the order of 30 V. The sample with an unusually high leakage current (LGAD_9_W1_F10_3) has the particularity of not having a JTE, unlike all other LGADs and PiN diodes.

After irradiation to fluences not higher than 10^{14} n_{eq}/cm^2, the same threshold voltage is observed, in fact the general shape of the IV curves is similar to that before irradiation. Only one device from W2 (LGAD_4_W2_D8_2), irradiated up to 10^{13} n_{eq}/cm^2, has an unexpectedly high leakage current, even at voltages below the threshold voltage. In fact, the after-irradiation leakage current of this device is the highest of all the irradiated LGADs, regardless of the wafer. This is the same sample that had an unusually high depletion voltage after irradiation (see previous section). Nevertheless, at about 30 V the leakage current of said sample increases as well. Finally, at a fluence of 10^{15} n_{eq}/cm^2 no threshold voltage is observed, regardless of the wafer. This implies that there is no onset of multiplication at this fluence. The result is consistent with what was observed in the previous section, where the depletion voltage of LGADs irradiated up to 10^{15} n_{eq}/cm^2 was found to be the same as that of PiN diodes irradiated up to the same fluence. Both results are a clear indication that at 10^{15} n_{eq}/cm^2 there is no multiplication.

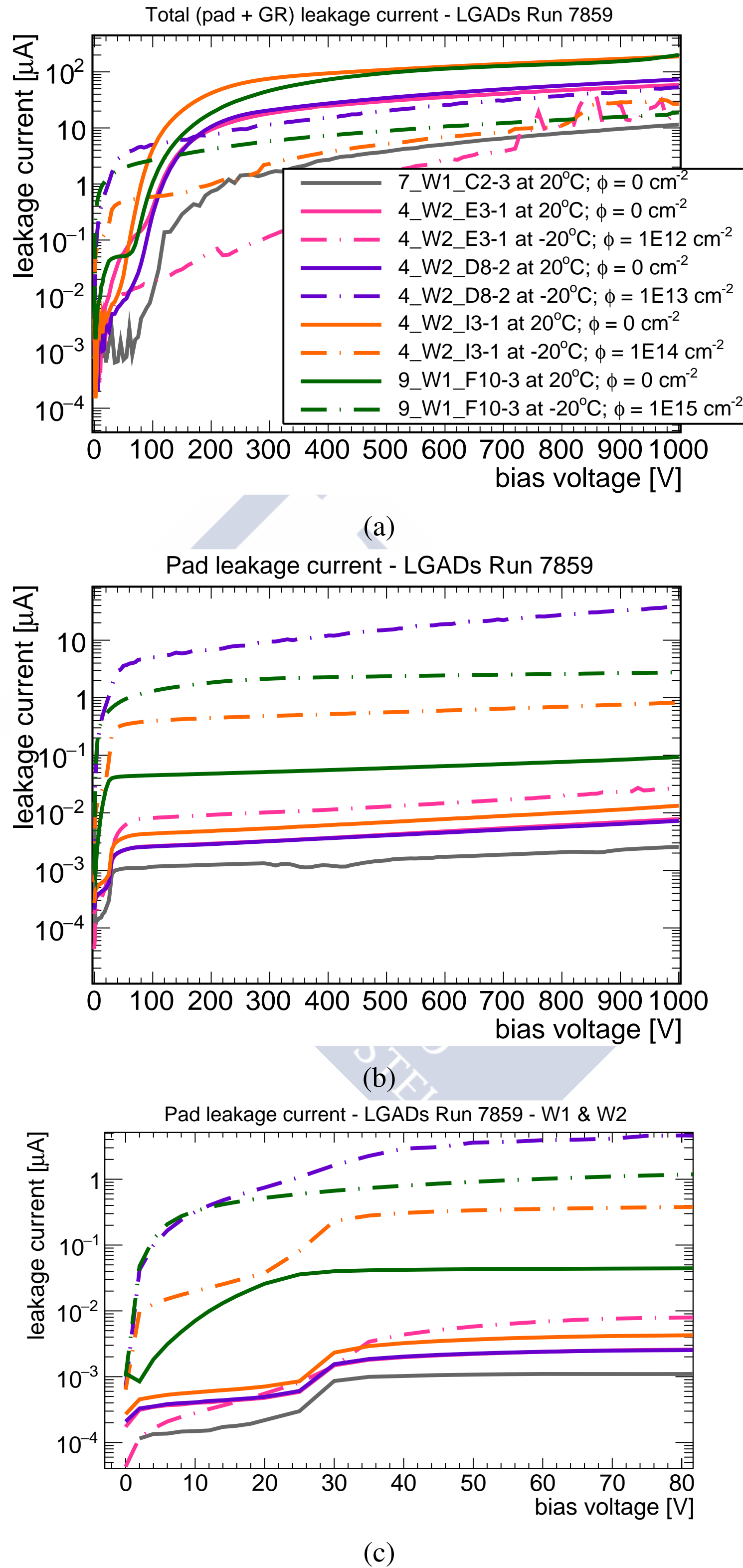

Figure 7.4: (a) Total (pad + GR), (b) pad leakage current, and (c) close-up at low voltages of the pad current before and after irradiation for LGADs from W1 and W2 (multiplication-layer dose: 1.8×10^{13} cm^{-2}); all plots share the same legend. The measurements were done at 20°C before irradiation, and at -20°C after irradiation.

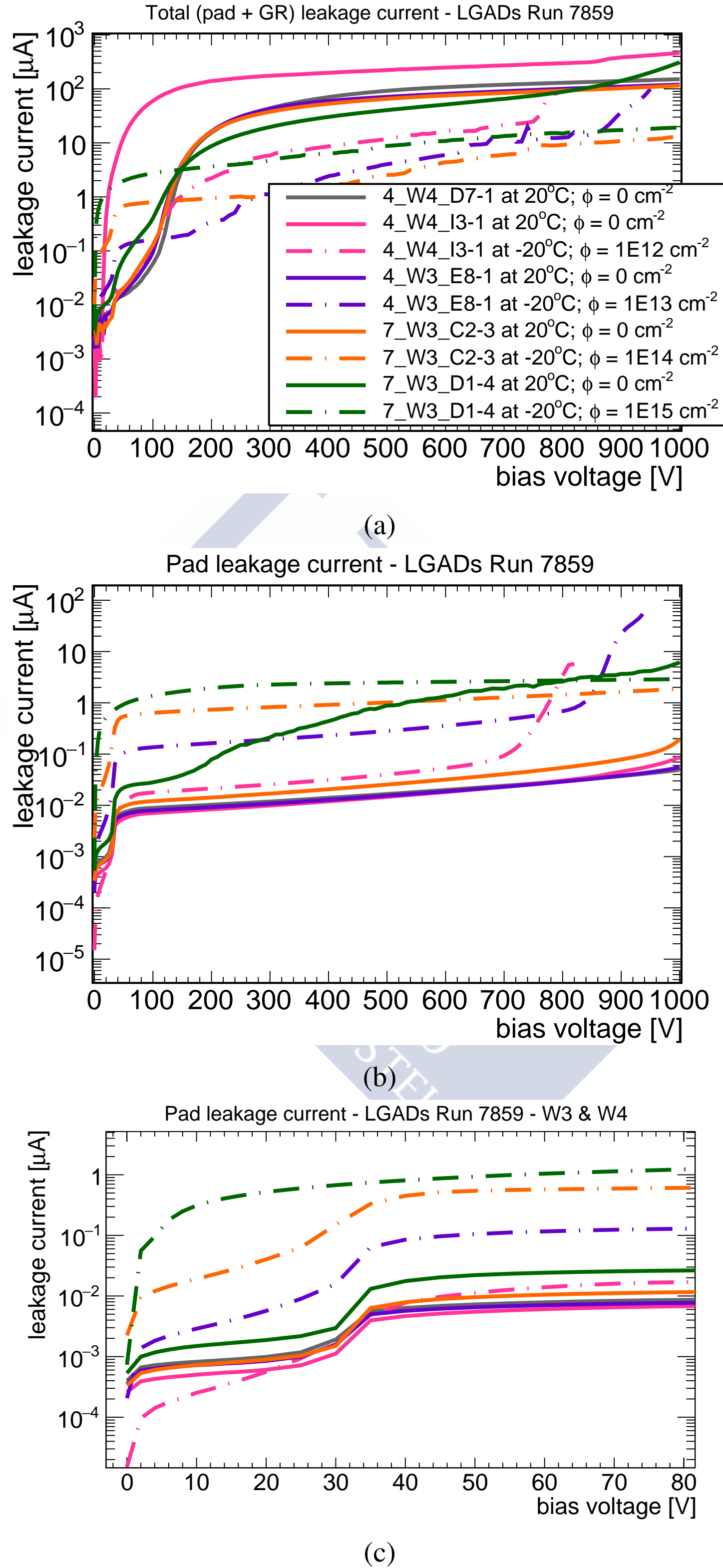

Figure 7.5: (a) Total (pad + GR), (b) pad leakage current, and (c) close-up at low voltages of the pad current before and after irradiation for LGADs from W3 and W4 (multiplication-layer dose: 2.0×10^{13} cm^{-2}); all plots share the same legend. The measurements were done at 20°C before irradiation, and at -20°C after irradiation.

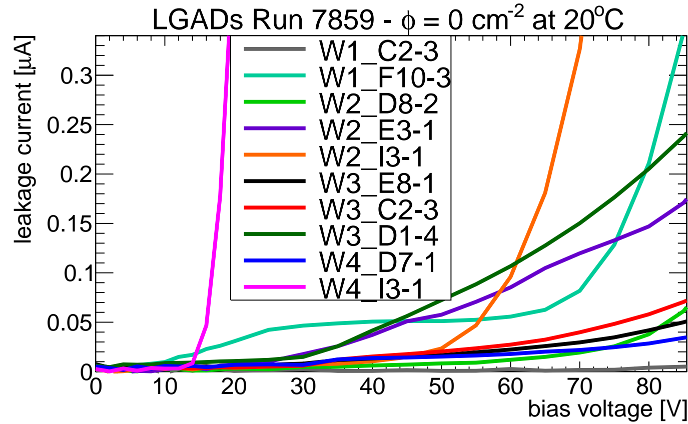

Figure 7.6: Close-up at low voltages of the total current for all LGADs before irradiation. At full depletion voltage the current was lower than 0.21 μA for all devices but one (W4_I3_1). The measurements were done at 20°C.

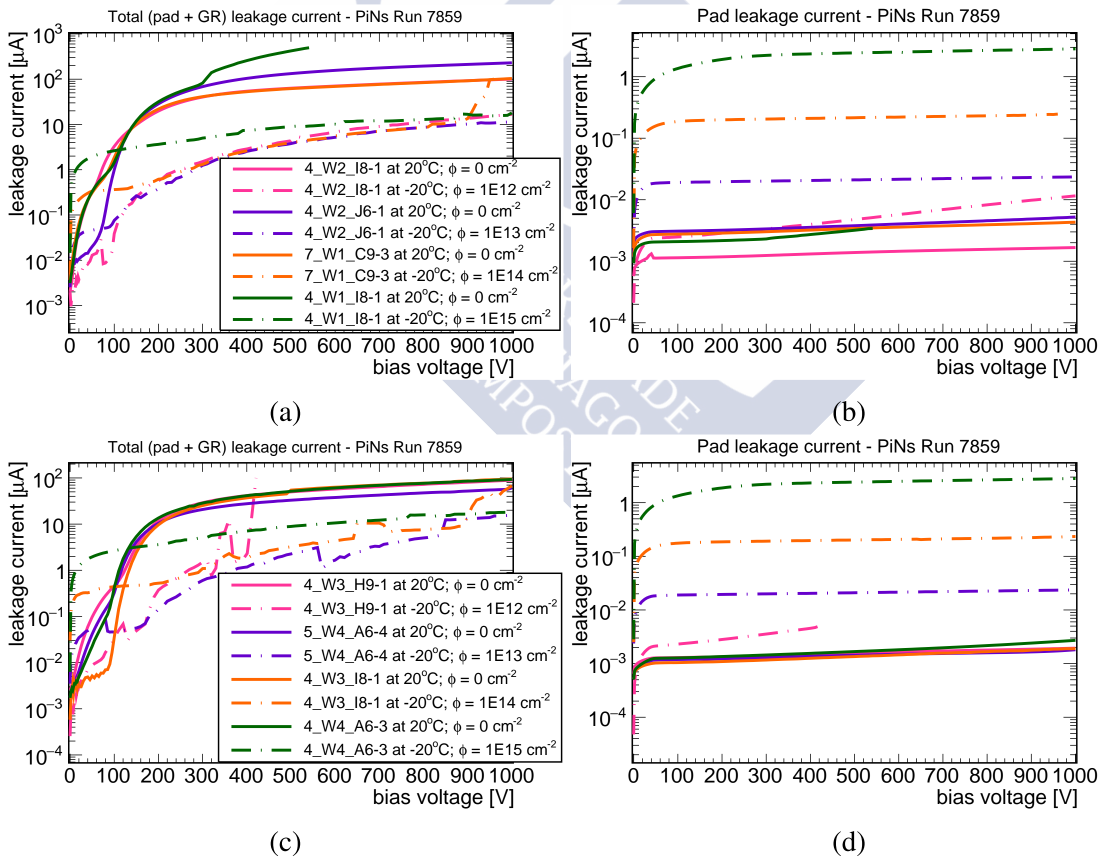

Figure 7.7: (a) Total (pad + GR), and (b) pad leakage current before and after irradiation for PiN diodes from W1 and W2; both plots share the same legend. (c) Total, and (d) pad leakage current before and after irradiation for PiN diodes from W3 and W4; both plots share the same legend. The measurements were done at 20°C before irradiation, and at -20°C after irradiation.

7.2 Homogeneity analysis

Surface scans, also referred to as XY scans, were performed in order to verify the homogeneity of charge collection in this set of LGADs. During surface (spatial position) scans the bias voltage remains constant and the laser beam spot is moved all over the surface of the sample. A measurement is performed at each location and a 2D map of charge collection can be generated after integrating every signal obtained. The specific concern about this property arises from the inhomogeneous behaviour observed in LGADs from a previous CNM run: 7062 (multiplication-layer dose: 1.6×10^{13} cm^{-2}) [14]. In this earlier study, it was observed that before irradiation the collected charge had a homogeneous distribution across the sensors at voltages above 200 V. After irradiation with 800-MeV protons up to a fluence of 10^{14} n$_{eq}$/cm^2, it was observed that the inhomogeneities were present even at a bias voltage of 1000 V [104]. To test the homogeneity of the LGADs from run 7859, XY scans with electron and hole injection were performed before and after irradiation, covering an area of at least 1×1 mm^2. The main interest lay in the samples irradiated to the highest fluences. That is why two of the sensors irradiated up to 10^{14} and 10^{15} n$_{eq}$/cm^2 were tested before and after irradiation. The before-irradiation measurements were performed at 100 V (over-depletion[1]), to verify if there were any inhomogeneities below the 200-V threshold indicated in [14] (voltage at which, before irradiation, the charge collection was homogeneous in run 7062). After irradiation the scans were done at 300 V, so that the bias voltage would be above the 200-V threshold, and above the full depletion voltage. In addition, the two LGADs irradiated up to the lowest fluence (10^{12} n$_{eq}$/cm^2) were both measured before and after irradiation at 100 V. Given the low level of irradiation, no major changes in charge collection homogeneity were expected even at lower voltages, and at 100 V the devices would be over-depleted.

For all devices it was found that before irradiation the charge collection was homogeneous (Figures 7.8 to 7.11). In some sensors certain structures were seen, however they were all consistent with optically observed scratches or residues from the metallisation process or otherwise. Excluding those effects, generally, the maximum deviation of the charge from the mean value was below ~ 5 %. Also, the variations between the mean and the mode of the charge collection distribution were, on average, below 0.2 %. Scratches and metallisation remnants cannot be removed. However, to avoid the interference of other types of residues, after irradiation all sensors were thoroughly cleaned, and inspected under the microscope before performing the measurements here presented.

The two LGADs irradiated up to 10^{12} n$_{eq}$/cm^2 presented a certain degree of inhomogeneity after irradiation, with the maximum deviation from the mean ranging between 2 % and 15 % depending on the sample and the illumination (front or back). The LGAD from W2 (LGAD_7859_4_W2_E3_1, Figure 7.8) presented a higher charge collection towards the centre in the red-front TCT scan, whilst the opposite behaviour was observed in the red-back TCT measurement. As for the device from W4 (LGAD_7859_4_W4_I3_1,

[1]When the bias voltage applied is higher than the full depletion voltage.

Figure 7.9), it displayed some higher charge collection structures, most noticeably in the red-back TCT scan.

In Figure 7.10 the results from the red-back and red-front TCT surface scans performed on sample LGAD_7859_7_W3_C2_3, before and after irradiation up to 10^{14} n_{eq}/cm^2, are shown. After irradiation, the charge collection map for hole injection (red-front TCT, see Figure 7.10c) shows a difference between mean and mode of ~ 0.8 %, and a maximum deviation from the mean of ~ 6 %. There is only one point with a 10 % deviation from the mean, consistent with an optically observed metal residue spot on the front side of the device. As for the map for electron injection (red-back TCT), the maximum deviation from the mean is almost 20 %, and there is a 4 % deviation between mean and mode (see Figure 7.10d).

Finally, surface scans were also performed on sample LGAD_7859_9_W1_F10_3, which was irradiated up to 10^{15} n_{eq}/cm^2. After irradiation, significant inhomogeneities were found, see Figure 7.11. In fact, a striped pattern of different charge collection levels was seen, most evident in the red-front TCT scan. For this particular sample, the maximum deviation from the mean varied between 13 % up to a staggering 100 % (seen in red-back TCT). In addition, the mode differs significantly from the mean in both after-irradiation scans: 13 % for red-back TCT, and 33 % for red-front TCT.

To better understand the source of these inhomogeneities, scans were carried out on a PiN diode (PiN_7859_4_W3_I8_1) irradiated up to 10^{14} n_{eq}/cm^2. Figure 7.12 shows the results obtained. The red-front TCT (hole injection) scan presented no difference between mean and mode, and the maximum variation from the mean was lower than 5 % (barring two bins towards the centre of the plot, consistent with a speck of dust later observed through the microscope). As for the red-back TCT (electron injection) scan, there is a difference of 1 % between the mode and the mean. The maximum variation from the mean was, as for red-front TCT, lower than 5 %. This value stands for all but one of the measurement points, which presented an unusually high charge collection (15 % above the mean). The source of this charge fluctuation is unknown. This point notwithstanding, the general observation is that after irradiation of a PiN diode up to 10^{14} n_{eq}/cm^2, the charge collection spatial distribution is much more homogeneous than for an LGAD irradiated up to the same fluence (compare Figures 7.10 and 7.12). Ergo, it seems reasonable to conclude that the main source of charge collection inhomogeneities is the effect of radiation on the p+ multiplication layer.

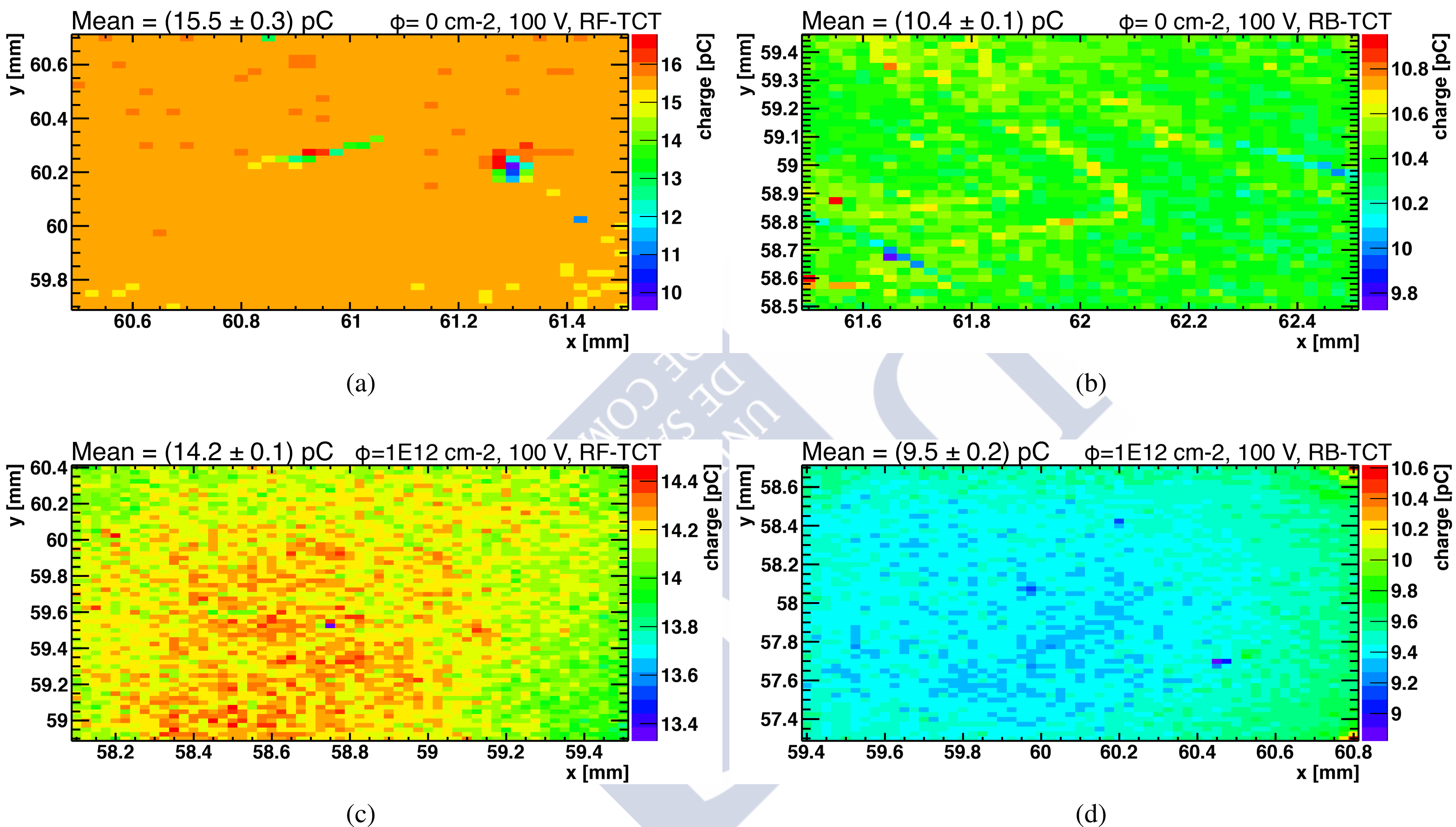

Figure 7.8: TCT surface scans on LGAD_7859_4_W2_E3_1 (multiplication-layer dose: 1.8×10^{13} cm^{-2}) at 100 V: before irradiation with (a) hole (red-front TCT) and (b) electron (red-back TCT) injection; after proton irradiation (10^{12} n_{eq}/cm^2) with (c) hole and (d) electron injection. The inhomogeneities observed on non-irradiated devices are due to residues and/or scratches. The mean charge collection and standard deviation of each scan are specified.

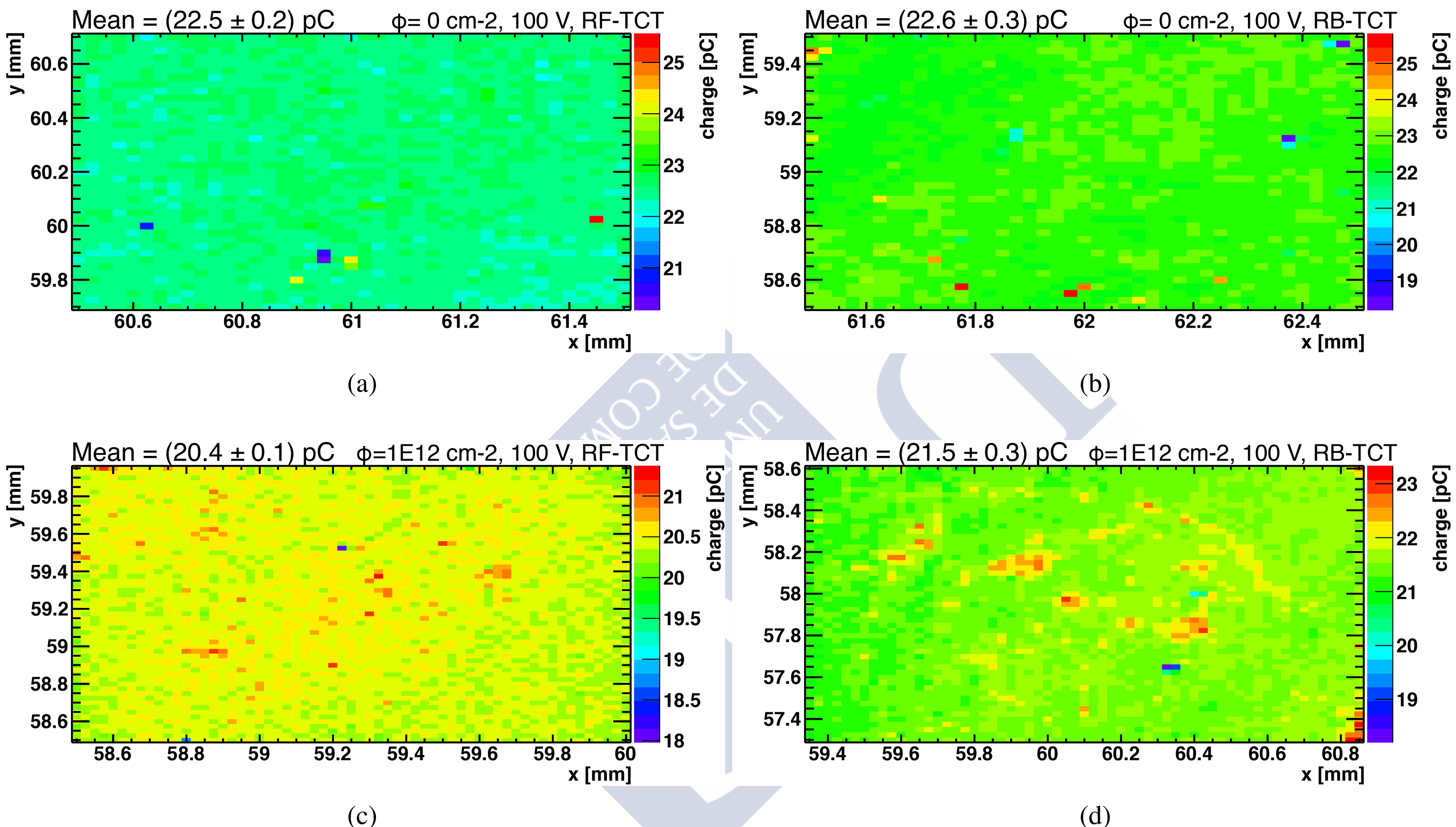

Figure 7.9: TCT surface scans on LGAD_7859_4_W4_I3_1 (multiplication-layer dose: 2.0×10^{13} cm^{-2}) at 100 V: before irradiation with (a) hole (red-front TCT) and (b) electron (red-back TCT) injection; after proton irradiation (10^{12} n$_{eq}$/cm^2) with (c) hole and (d) electron injection. The inhomogeneities observed on non-irradiated devices are due to residues and/or scratches. The mean charge collection and standard deviation of each scan are specified.

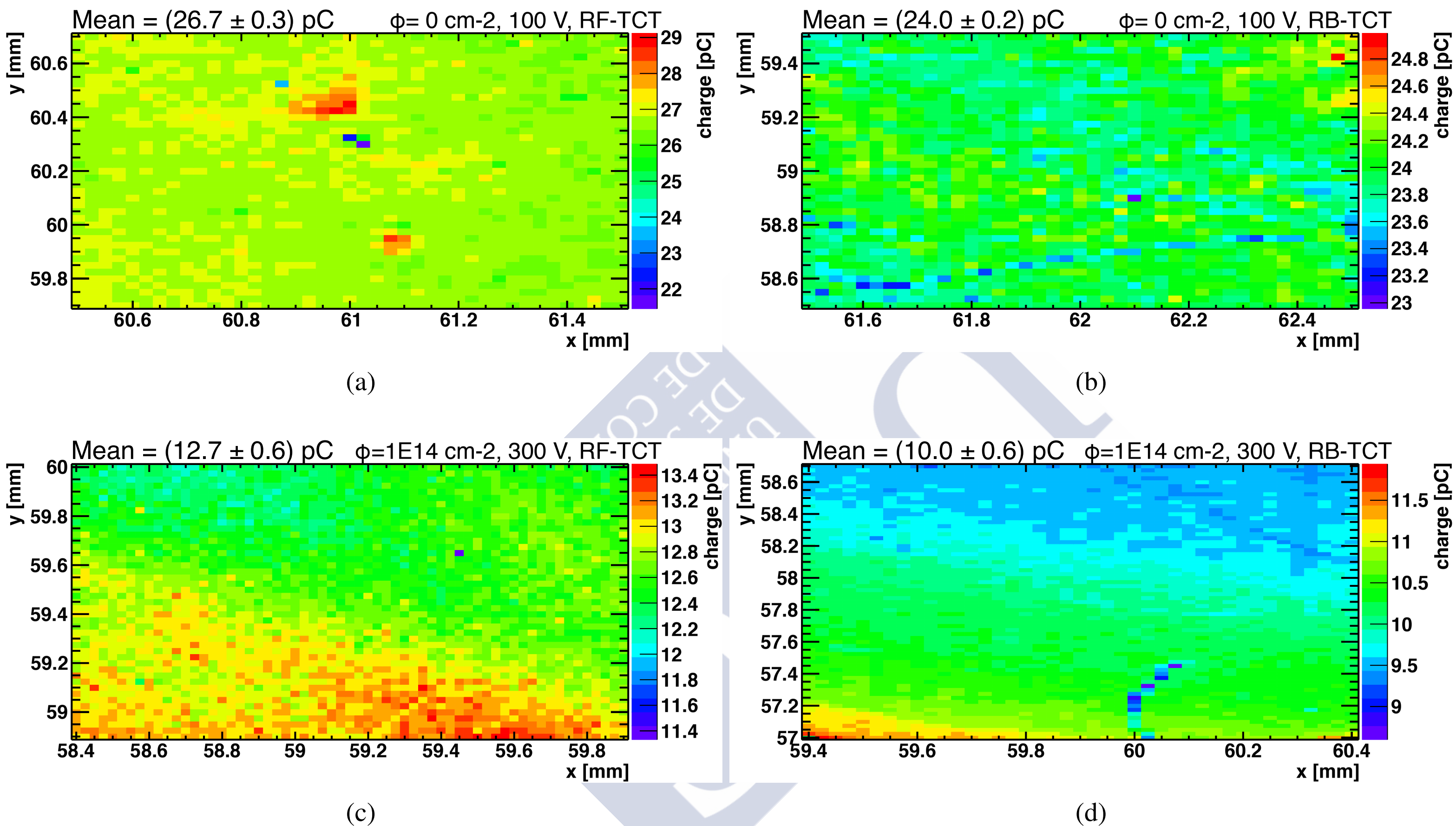

Figure 7.10: TCT surface scans on LGAD_7859_7_W3_C2_3 (multiplication-layer dose: 2.0×10^{13} cm^{-2}): before irradiation with (a) hole (red-front TCT) and (b) electron (red-back TCT) injection at 100 V; after proton irradiation (10^{14} n_{eq}/cm^2) with (c) hole and (d) electron injection at 300 V. The inhomogeneities observed on non-irradiated devices are due to residues from the metallisation process. After irradiation the maximum deviation from the mean charge is of $\sim$ 6 % for hole injection and of $\sim$ 20 % for electron injection. The mean charge collection and standard deviation of each scan are specified.

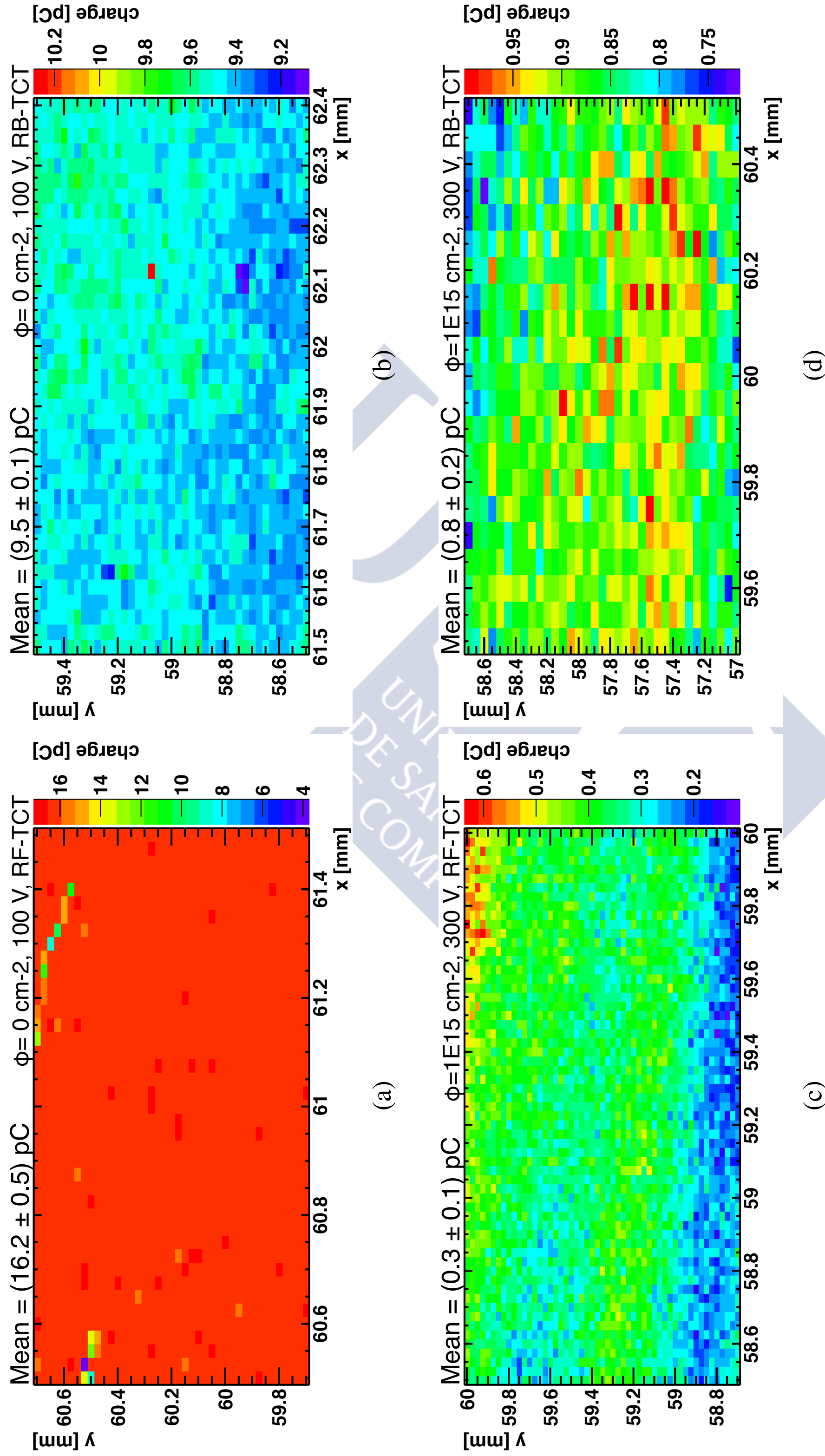

Figure 7.11: TCT surface scans on LGAD_7859_9_W1_F10_3 (multiplication-layer dose: 1.8×10^{13} cm^{-2}): before irradiation with (a) hole (red-front TCT) and (b) electron (red-back TCT) injection at 100 V; after proton irradiation (10^{15} n_{eq}/cm^2) with (c) hole and (d) electron injection at 300 V. The mean charge collection and standard deviation of each scan are specified.

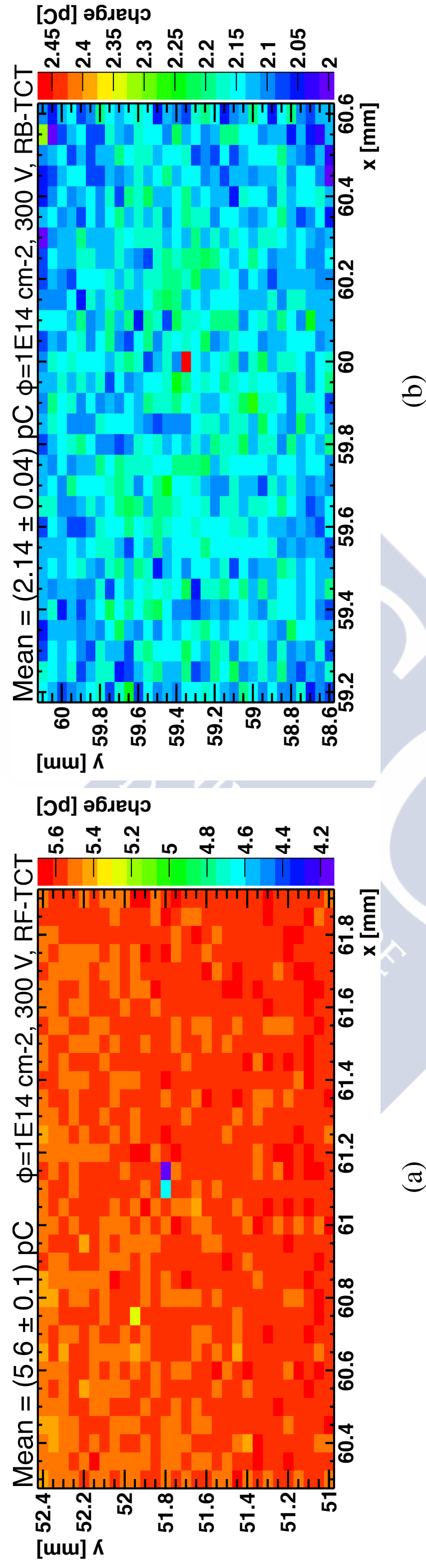

Figure 7.12: TCT surface scans on a PiN diode (PiN_7859_4_W3_I8_1) after proton irradiation (10^{14} n_{eq}/cm^2) with (a) hole and (b) electron injection at 300 V. The mean charge collection and standard deviation of each scan are specified.

7.3 Charge collection with voltage

7.3.1 ^{90}Sr voltage scans

As explained in Section 4.2, IR TCT measurements give results similar to those of MIPs. However, those measurements do not reproduce the expected statistical charge fluctuations characteristic of MIP-induced signals. To study those signals and the energy deposition distribution of MIPs in the devices, radioactive source measurements must be performed. In this thesis, said scans have been carried out, before irradiation, by means of a ^{90}Sr source, at 20°C. After irradiation, the devices presented excessive noise levels that made it impossible to perform accurate measurements, even at -20°C.

As described in Section 4.4, the ^{90}Sr source produces electrons via β^- decay. These electrons reach both the DUT and the scintillator, used for triggering, positioned right beneath it. The signal induced in the DUT is recorded to then analyse the charge collection with respect to the bias voltage. In the case of PiN diodes, it is expected that after full depletion the collected charge will be constant. Conversely, for the LGADs, one expects the charge collected to continue increasing even after full depletion. This is due to the fact that, the higher the bias voltage, the higher the electric field in the multiplication layer; thus, the higher the charge multiplication. Evidently, at a given bias voltage and temperature, a higher gain is expected from the LGADs with a higher multiplication-layer implant dose.

Figure 7.13 shows the charge collection[2] with respect to bias voltage (*charge collection curves*) of all the LGADs and PiN diodes, before irradiation and at 20°C. The plots look exactly as expected, there are solely some abnormal fluctuations in the signal from some PiN diodes. As anticipated, LGADs have a higher charge collection

On average, the charge collected by PiN diodes was of (2.9 ± 0.3) fC. This was calculated as the average the charge collected at all voltages measured, since after full depletion PiN diodes have a constant charge collection. For comparison, assuming that a MIP generates an average of 80 e^-/h^+ per μm path length in silicon [25], the charge collection expected was of ~ 3.7 fC. Finally, the charge collected, at 700 V, by LGADs with a multiplication-layer dose of 1.8×10^{13} cm^{-2} and 2.0×10^{13} cm^{-2} was of (12.2 ± 0.3) fC and (33.1 ± 0.8) fC, respectively. The uncertainties here indicated were obtained by calculating the error of the mean, not the standard deviation.

From the results here presented it was possible to study the gain of the analysed LGADs before irradiation. This is discussed in detail in Section 7.4.

[2] As explained in Chapter 4, when analysing radioactive source measurements, the charge collection at a given voltage is obtained by fitting the distribution of deposited charge with the convolution of a Landau and a Gaussian distribution. The charge collection is defined as the most probable value extracted from the Landau fit.

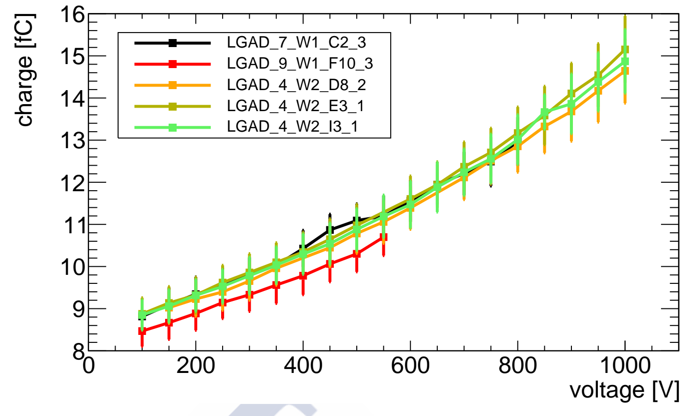

(a)

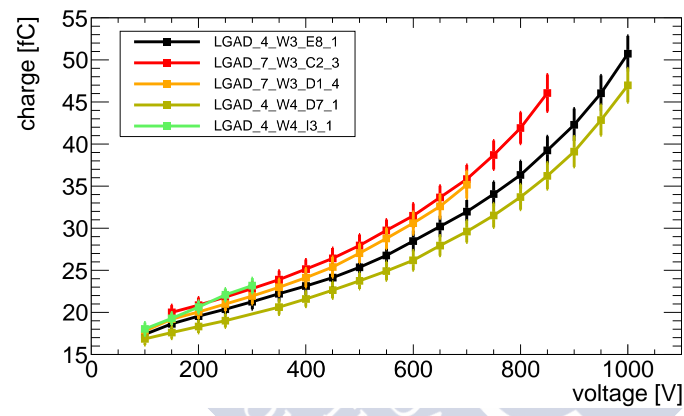

(b)

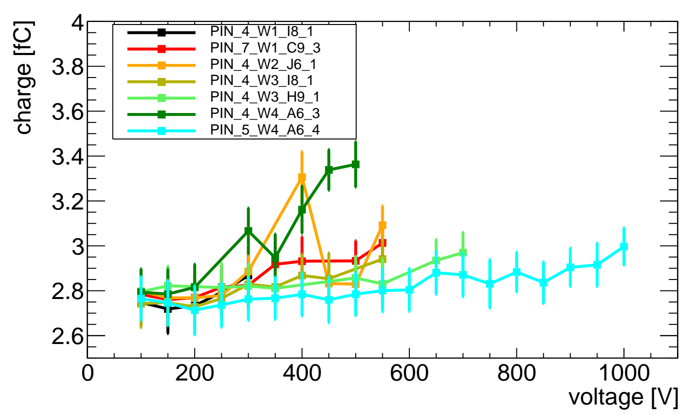

(c)

Figure 7.13: Charge collection curves obtained, before irradiation, through ^{90}Sr source measurements at 20°C for LGADs with a multiplication-layer does of (a) 1.8 $\times$ 10^{13} cm^{-2}, and (b) 2.0 $\times$ 10^{13} cm^{-2}, and for (c) PiN diodes.

7.3.2 TCT voltage scans

Voltage scans were performed on all devices both before and after irradiation, and with all available illuminations, i.e. red-back, red-front, and IR TCT. Voltage scans are performed by maintaining the position of the laser beam spot constant whilst the bias voltage applied to the DUT is changed, thus obtaining a response signal from the sensor at each voltage. The voltage range covered was from 0 to 1000 V, although in some scans the full voltage range could not be covered. If the leakage current during the TCT measurements reached, before 1000 V, values deemed to high for the safe operation of the detector, the measurements were interrupted.

Figures 7.14 to 7.16 show charge collection as a function of voltage before and after irradiation for all PiN diodes at -20°C. Before irradiation, both for red-front and IR illumination there is a continuous increase in charge collection from 0 V onwards, until, after full depletion, the charge collection stabilises. For red-back TCT, the behaviour is rather different. As the illumination is done on the backside of the device, the injected electrons produce little to no signal until the sensor is almost fully depleted. That is why at voltages below full depletion there is nearly no charge collection. Once the full-depletion voltage is reached, charge collection increases abruptly to then remain constant.

In the particular cases of hole injection and IR pulses, it was found that the charge collected by PiN diodes from W4 was lower than that of PiN diodes from W3, this can be seen in Figures 7.14b and 7.16b. The LGADs from these wafers presented a similar behaviour (see Figures 7.18b and 7.20b). This result is unexpected since wafers 3 and 4 were manufactured so as to be identical. Since the laser intensity remained constant through all scans, this difference can only be attributed to the wafers themselves. Also, as the effect is seen with red-front TCT and not red-back TCT, the difference must be in the front side of the devices. The manufacturer, CNM-Barcelona, of the devices suggested this difference could be due to a difference in thickness of the passivation layer. Spectroscopic reflectometry measurements were carried out independently at CNM-Barcelona, and at CMi-EPFL[3]. Both studies concluded that there was a difference between wafers in the thickness of the SiO_2 layer. The thickness of the passivation layer alters the reflectance of the surface, which subsequently affects the amount of charge deposited when measuring with lasers. However, this variation in the passivation has no effect in the behaviour of the detectors when exposed to particles.

Furthermore, a rather abnormal behaviour was observed, before irradiation, in one of the samples from W1 (PiN_7859_4_W1_I8_1). The sample presents a steep drop in charge collection at a voltage of 340 V, for all illuminations. As can be seen in Figure 7.17, the drop coincides with an abrupt increase in leakage current between 300 V and 350 V.

[3]This work was performed by M. Carulla and D. Quirion at CNM-Barcelona; and by A. Mapelli and D. Bouvet at CMi-EPFL (`https://cmi.epfl.ch/`).

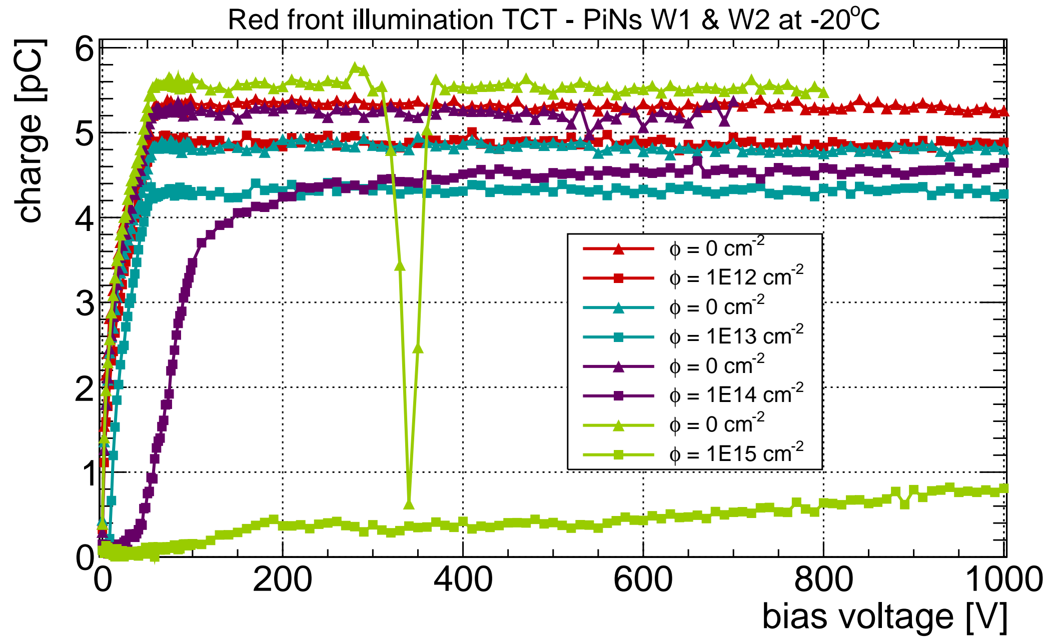

(a)

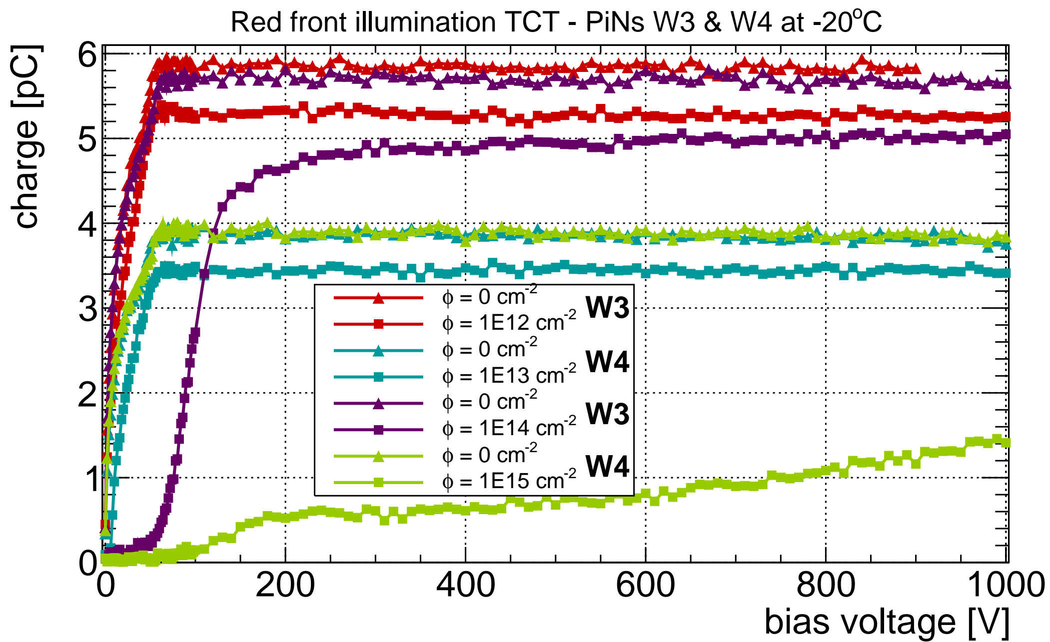

(b)

Figure 7.14: Red-front TCT voltage scans of PiN diodes at -20°C, both before and after proton irradiation. Results for PiN diodes from (a) W1 and W2, and (b) W3 and W4.

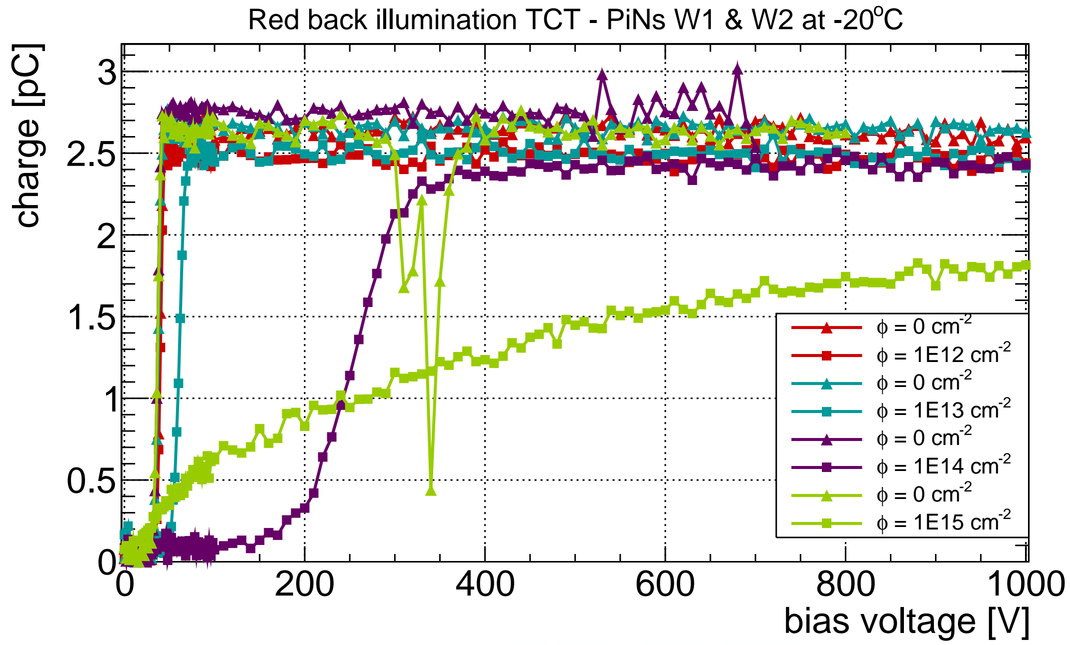

(a)

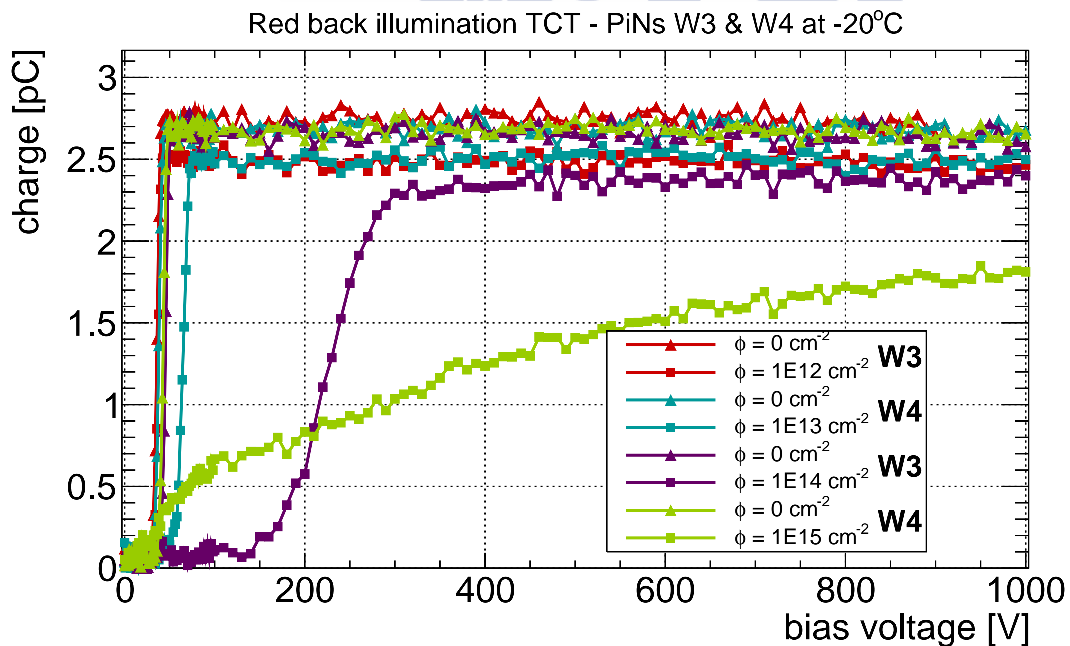

(b)

Figure 7.15: Red-back TCT voltage scans of PiN diodes at -20°C, both before and after proton irradiation. Results for PiN diodes from (a) W1 and W2, and (b) W3 and W4.

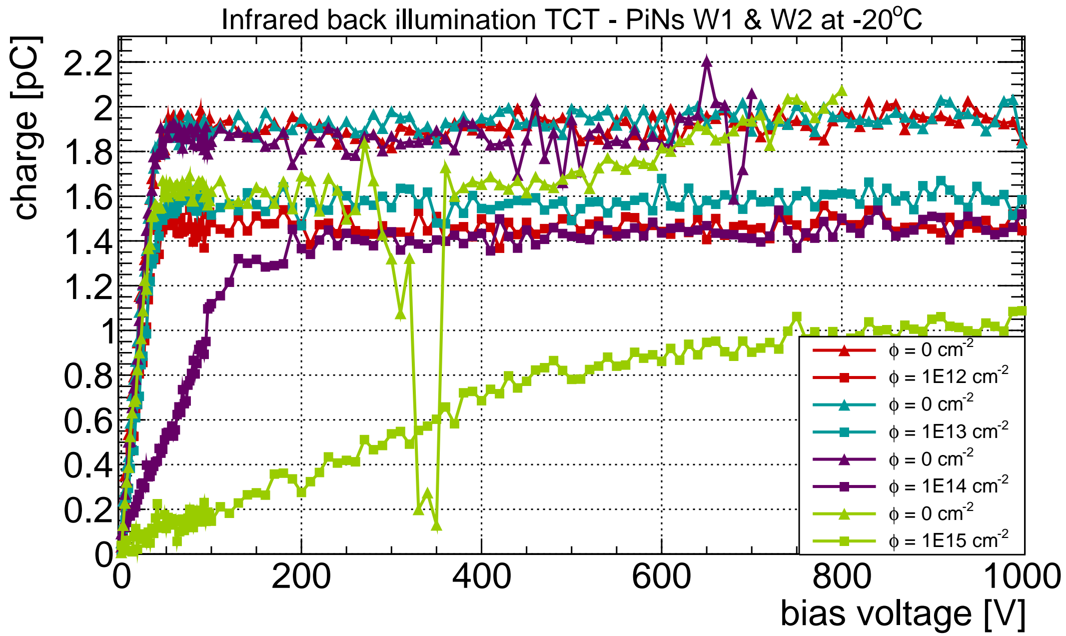

(a)

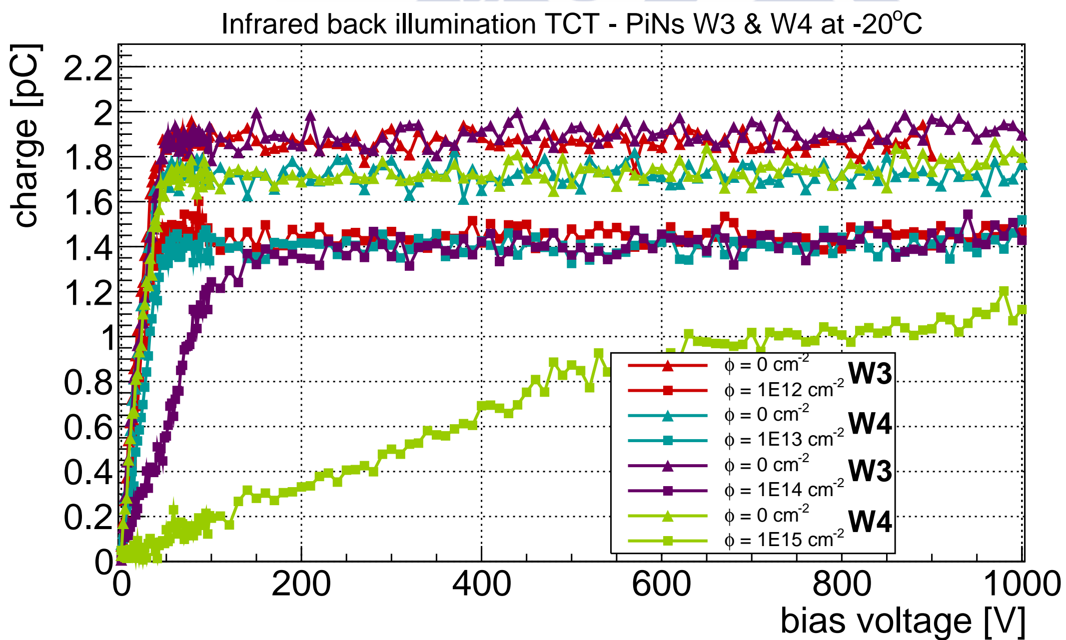

(b)

Figure 7.16: IR TCT voltage scans of PiN diodes at -20°C, both before and after proton irradiation. Results for PiN diodes from (a) W1 and W2, and (b) W3 and W4.

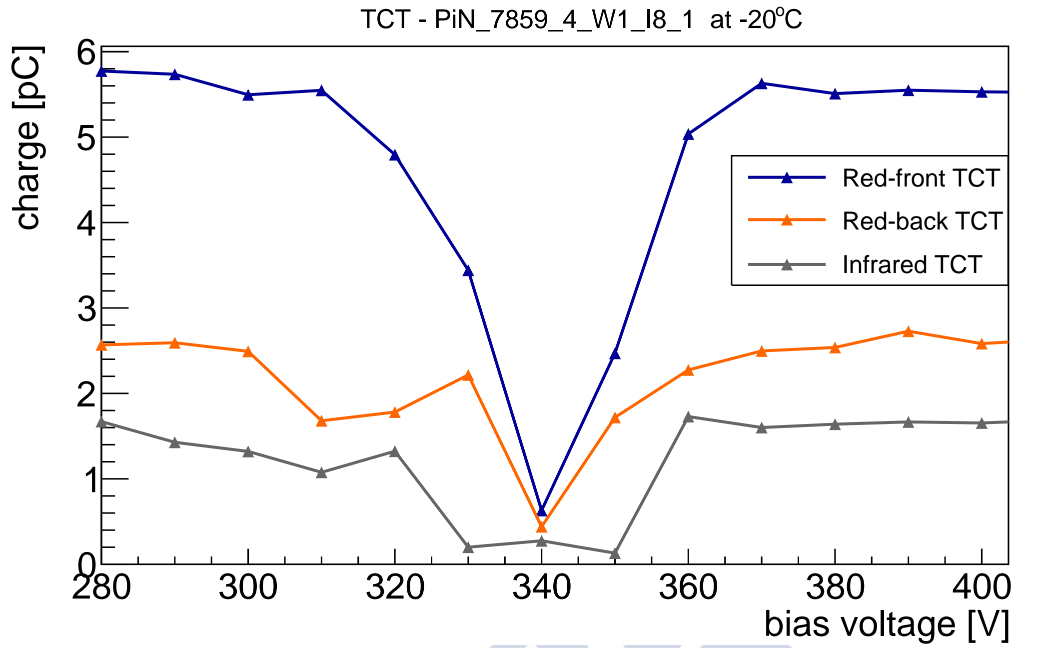

(a)

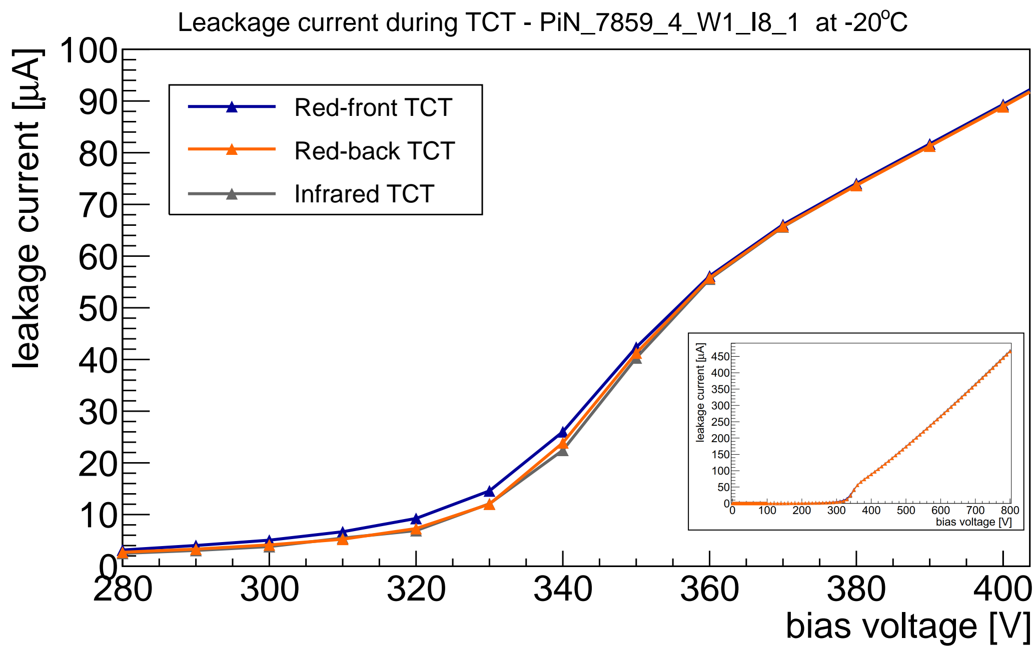

(b)

Figure 7.17: (a) Detail of the voltage region where PiN_7859_4_W1_I8_1 presents a drop in the collected charge. (b) Leakage current, of the same sample, measured during the TCT scans.

After irradiation, the behaviour is fairly analogous to that observed before irradiation. The samples that present a somewhat different behaviour are those irradiated to the highest fluences. In particular, the two PiN diodes irradiated to 10^{15} n_{eq}/cm^2 do not reach a clear plateau. This is related to the defects introduced by radiation, which act as traps and recombination centres. In principle, the charge collection efficiency can be at least partly restored by increasing the bias above full depletion voltage. This increases the drift velocity, thus decreasing the drift time, and with it the probability of charge trapping. In practice, at such high irradiation levels, the voltage required to saturate the efficiency of the device is higher than the operational voltage range defined to remain below breakdown.

As regards LGADs, Figures 7.18 to 7.20 presents all the voltage scan obtained with LGADs. By comparing the charge collection values of LGADs and PiN diodes, it is possible to see the significant effect of internal multiplication in the collected charge. It is clear as well that charge collection decreases with fluence for both types of devices. In fact, at a fluence of 10^{15} n_{eq}/cm^2 the charge collected by an LGAD is almost the same as that obtained with a PiN diode exposed to the same fluence (regardless of the type of injection).

The information that can be taken from the voltage scans, particularly for hole injection (red-front TCT), extends beyond what has just been discussed. To be specific, the shape of the charge collection curves provides significant information regarding the behaviour of the devices. By observing the red-front TCT charge collection curves for LGADs, it becomes evident that for voltages below 30 V, for W1 and W2, and 32 V, for W3 and W4, no charge is collected; and afterwards the collected charge increases dramatically. This threshold voltage ensues from the full depletion of the multiplication layer. To actually have impact ionisation the p+ layer must be depleted, therefore the threshold voltage indicates the full depletion voltage of the p+ layer.

According to the results in [10], the multiplication-onset voltage (also known as threshold voltage) decreases with fluence as a consequence of acceptor removal. As explained in Chapter 3, if the effective doping of the multiplication layer decreases, its depletion voltage decreases as well. Interestingly, as it can be seen in Figure 7.21, the opposite effect was found in this study, where an increase in the threshold voltage is observed as a result of irradiation in LGADs of similar characteristics.

In addition, when analysing the charge collection for electron injection (red-back TCT) it was found that, before irradiation no charge collection is observed at bias voltages below full depletion (Figures 7.19a and 7.19b). On the other hand, after irradiation, already at a fluence of 10^{13} n_{eq}/cm^2, there is charge collection at low voltages. Said scans are obtained by means of a red laser, which has an absorption length in silicon of only a few μm. The laser in question is illuminating the back side of the device. When performing red-back TCT before irradiation, at bias voltages below full depletion the e^-/h^+ pairs produced by the laser get recombined and produce no signal. It is only when the device is fully depleted that the e^-/h^+ pairs can drift and induce a signal. The only plausible

explanation for the observed charge collection at low voltages for electron injection (red-back TCT) after irradiation is that there is a depletion region growing from the back side of the device. Such an effect could be caused by a change in the space charge due to charge carrier trapping in irradiation-induced defects (see Chapter 3). Before irradiation there are no deep-level traps in the silicon and the depletion region grows from the junction in the front of the sensor, where the p+ multiplication layer is. After irradiation the number of defects is substantial. For this reason, holes produced by dark current and possibly secondary holes, originating from the multiplication in the gain layer, can get trapped. If the amount of trapped holes is significantly large, the space charge will change sign, i.e. it will effectively behave as if it were n-type silicon [40]. This implies the formation of a pn-junction on the back of the sensor, this is known as the *double-junction effect* [105]. Under these conditions, the depletion at reverse bias grows from the back junction, instead of from the frontal pn-junction at the p+ multiplication layer region. Consequently, after irradiation, the sensor collects charge with electron injection (red-back TCT) even at low voltages. Also, this means that until almost full depletion either the charge carriers cannot reach the multiplication layer within the time frame relevant for the signal, or the electric field in the multiplication layer is not high enough to produce charge multiplication. This would undoubtedly explain the observed increase of the multiplication-onset voltage with fluence (Figure 7.18a and Figure 7.18b). A detailed study of these unexpected behaviour was performed and can be found in Section 7.5 of this same chapter.

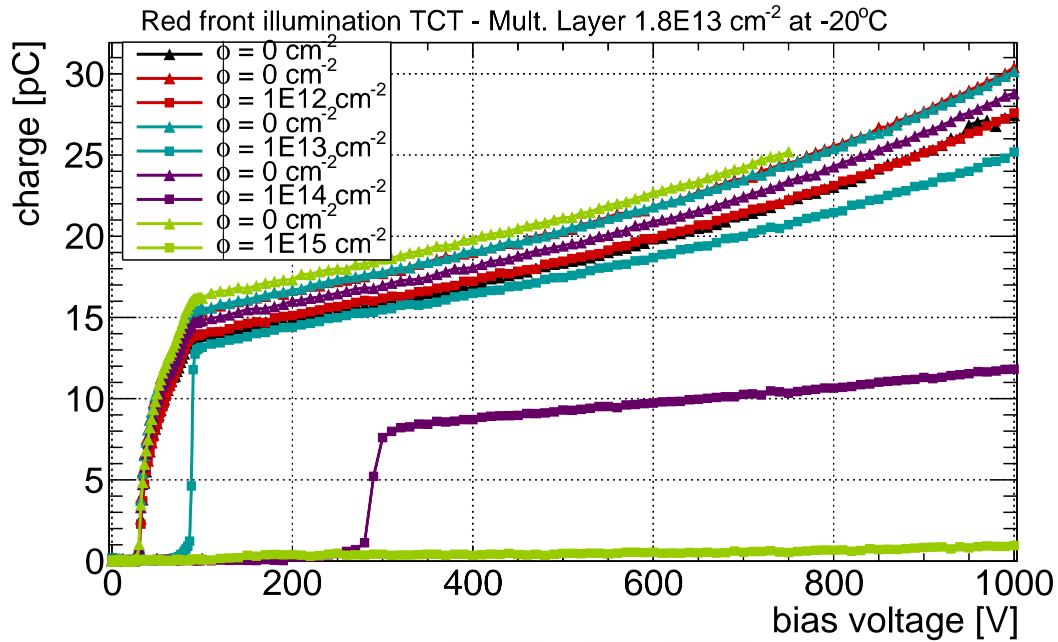

(a)

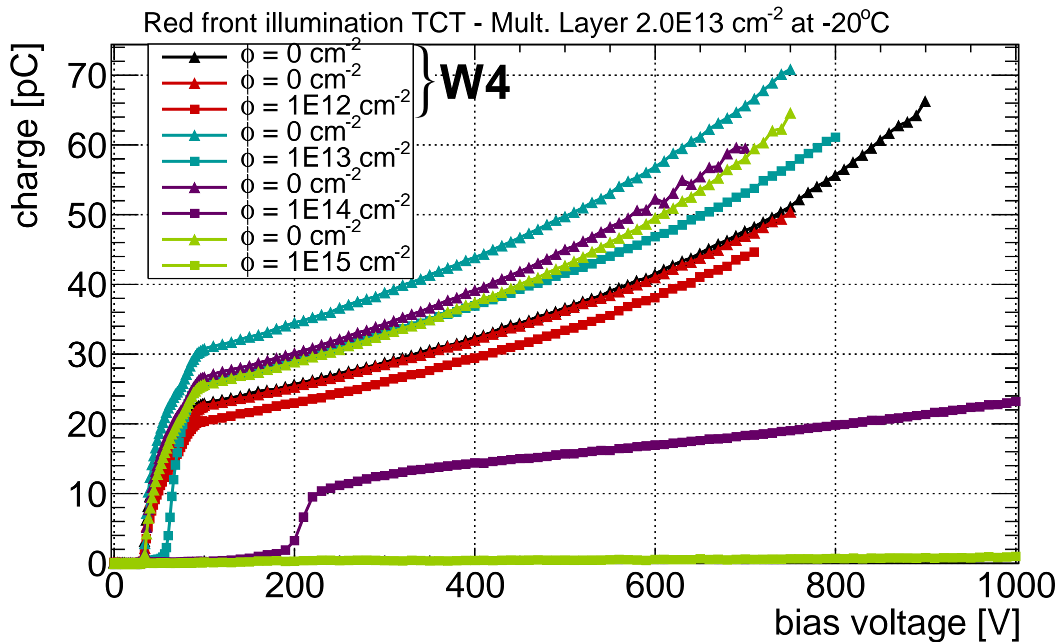

(b)

Figure 7.18: Red-front TCT voltage scans of LGADs at -20°C both before and after proton irradiation. Results for LGADs from (a) W1 and W2 (mult. layer dose: 1.8×10^{13} cm^{-2}), and from (b) W3 and W4 (mult. layer dose: 2.0×10^{13} cm^{-2}).

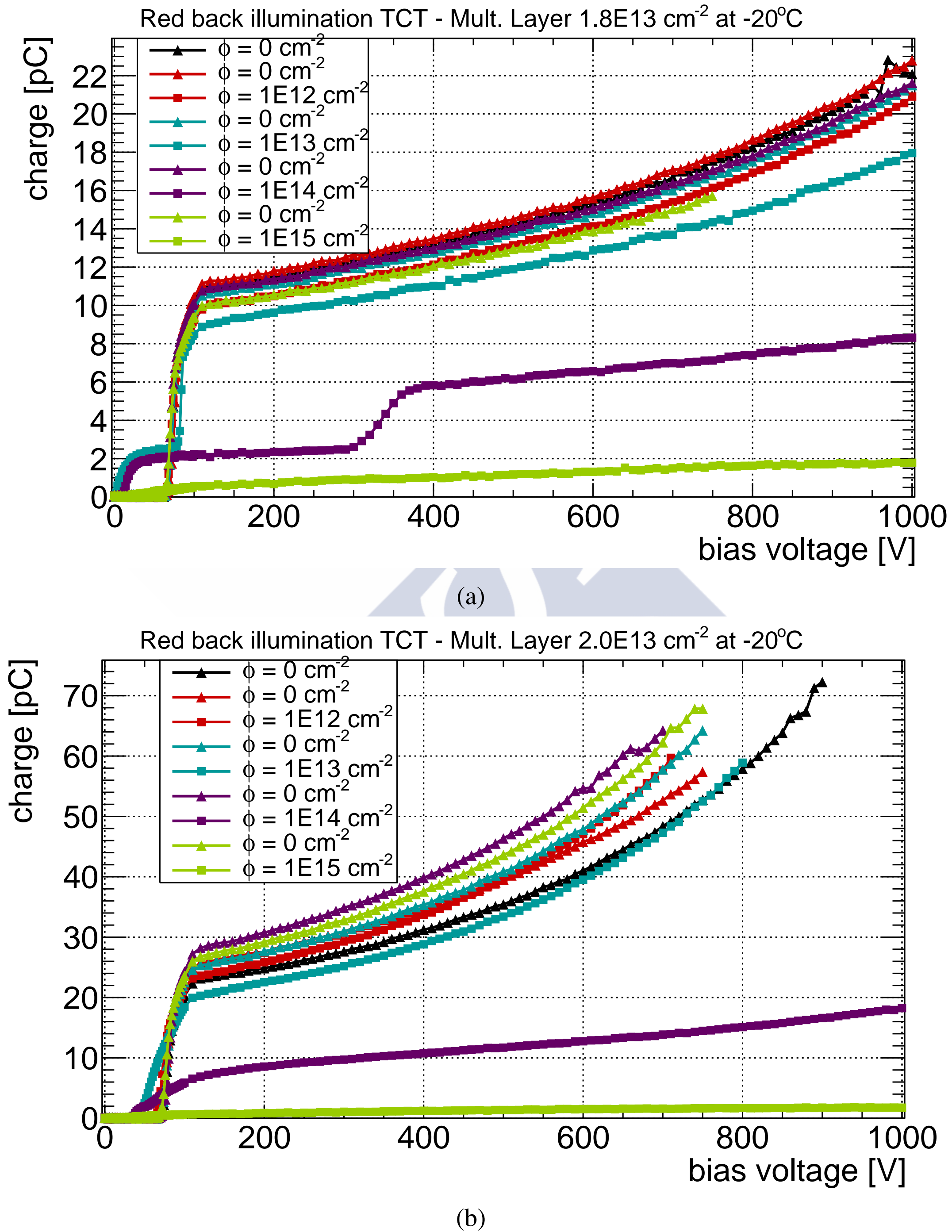

Figure 7.19: Red-back TCT voltage scans of LGADs at -20°C both before and after proton irradiation. Results for LGADs from (a) W1 and W2 (mult. layer dose: 1.8×10^{13} cm^{-2}), and from (b) W3 and W4 (mult. layer dose: 2.0×10^{13} cm^{-2}).

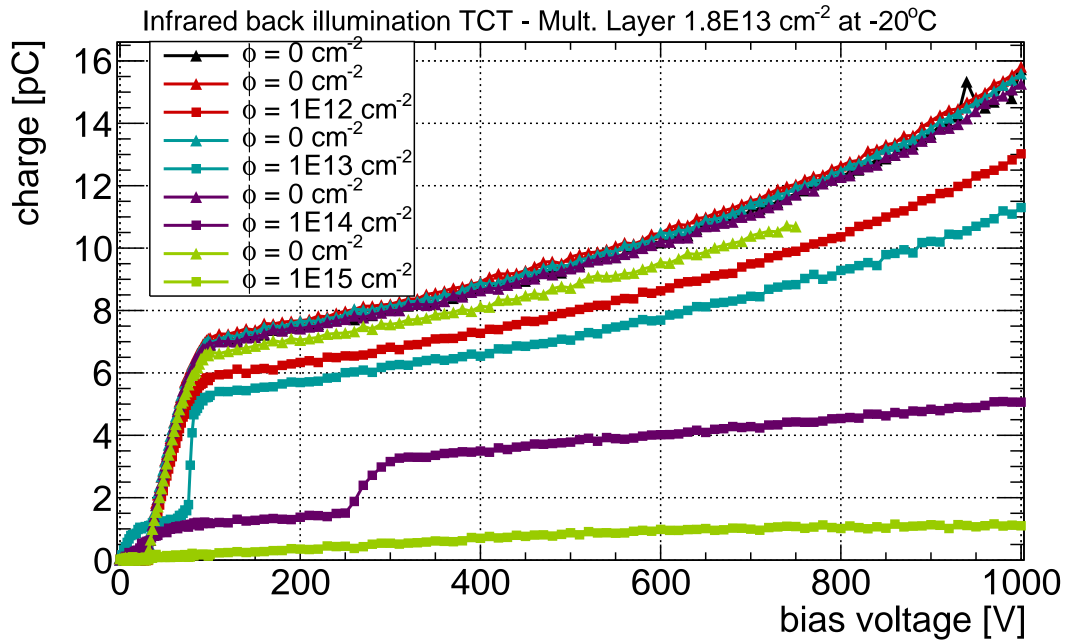

(a)

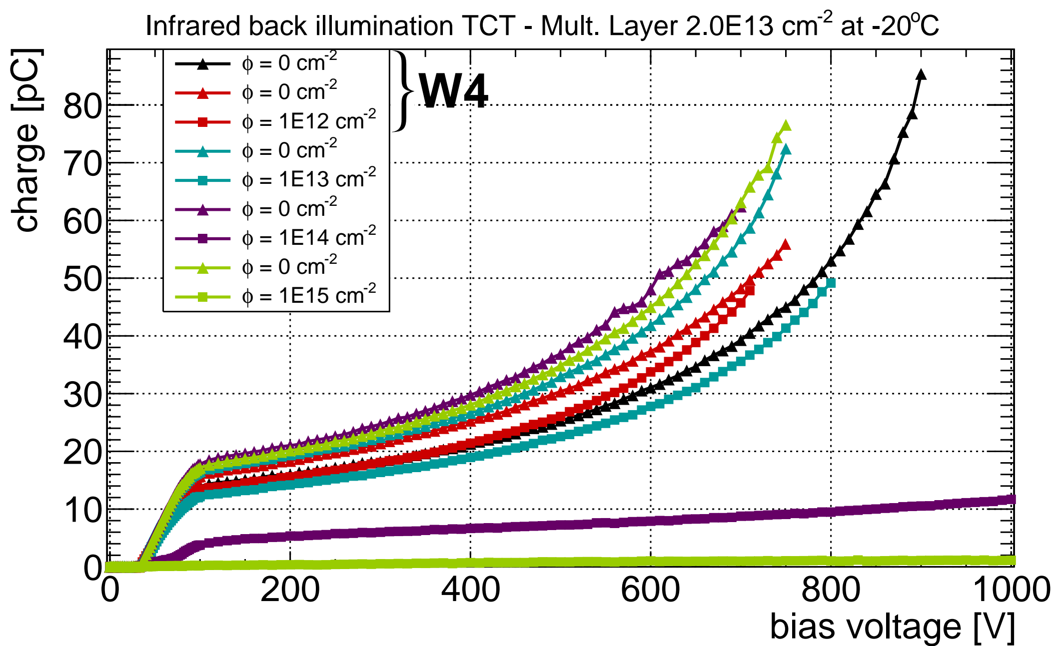

(b)

Figure 7.20: IR TCT voltage scans of LGADs at -20°C both before and after proton irradiation. Results for LGADs from (a) W1 and W2 (mult. layer dose: 1.8×10^{13} cm^{-2}), and from (b) W3 and W4 (mult. layer dose: 2.0×10^{13} cm^{-2}).

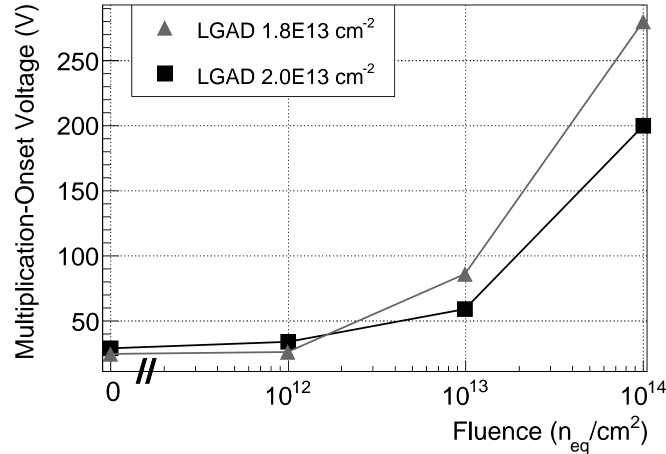

Figure 7.21: Multiplication-onset voltage as a function of fluence.

7.4 Gain study

One of the most critical parameters to evaluate in LGADs before and, most importantly, after irradiation is gain. Paradoxically, there is no established convention for its calculation. Firstly, it is important to clarify that when calculating (and indicating) the gain, it is important to do so at a specific voltage and temperature. The internal multiplication of silicon detectors depends on both parameters [90]. In this thesis, two gain-calculation methods are used and compared. The first, which will be referred to as *type-1 gain*, consists in the ratio between the charge collected by an LGAD and the charge collected by a reference PiN diode (irradiated with the same particles and up to the same fluence). In the case of TCT measurements, both charge values are normalised by the laser power[4]. This is done to unambiguously state that different gains are due to an actual difference in sensor behaviour and not just an effect of a laser-intensity fluctuation. The second method, which will be referred to as *type-2 gain*, consists in the ratio between the charge induced by electrons injected through red-back illumination TCT, and the charge induced by secondary holes. This method allows for the calculation of the gain of an LGAD without the need to compare it to a PiN diode.

The *type-1 gain* was calculated for IR pulses, hole (red-front TCT) and electron (red-back TCT) injection. The chosen temperature for evaluating the gain was -20°C. The bias voltage used was 700 V, to have the certainty that all devices were fully depleted, regardless of their level of irradiation. Since the gain depends on the doping of the multiplication layer, the gain was calculated separately for devices coming from wafers with different doping. After irradiation each LGAD was compared to an equally irradiated PiN diode coming from the same set of wafers, i.e. LGADs from wafers 1&2 (3&4) were

[4]During TCT measurements the laser intensity is monitored by means of a reference photodiode, see Chapter 4. These data are stored together with that from the DUT. The eventual reflection losses on the DUT are considered to be the same for each wafer and illumination.

always compared to PiN diodes from wafers 1&2 (3&4). Before irradiation, the gain was calculated as the ratio between the mean normalised charge of all the LGADs and PiN diodes from a given wafer set. The results obtained can be found in Figure 7.22.

As described in the previous section, in red-front and IR TCT scans the charge collected by PiN diodes from W4 was lower than that of PiN diodes from W3, seef Figure 7.23. Evidently, such a difference in measured charge could not be neglected when calculating the gain. As a result, in the case of hole injection (red-front TCT) and IR pulses, the gain was calculated independently for each wafer, i.e. LGADs from W3 (W4) were compared to PiN diodes from W3 (W4). As a more general result, the plots in Figure 7.22 show that, as expected, gain is proportional to multiplication-layer doping. Another conclusion that can be drawn is that the gain values obtained are dependent on the type of illumination used. Lastly, it is apparent that regardless of the type of charge carrier injection, the gain decreases with fluence. As a matter of fact, at a fluence of 10^{15} n_{eq}/cm^2, the gain, irrespective of the multiplication-layer dose, is ~ 1, i.e. the charge collection is equal to that of a PiN diode, there is no internal amplification due to the multiplication layer.

The *type-2 gain* was determined for all devices and fluences, with the exception of 10^{15} n_{eq}/cm^2, since the signal waveforms were too distorted. The results can be seen in Figure 7.22c. In this instance, the before-irradiation values were calculated as the mean of the gain values obtained for all the LGADs from each set of differently doped wafers. As expected, the behaviour of the *type-2 gain* is analogous to that of *type-1 gain*: the gain is proportional to multiplication-layer doping; and it decreases with fluence. Although the *type-2 gain* could not be determined at 10^{15} n_{eq}/cm^2, the *type-1 gain* could actually be computed. As with all other illuminations, at a fluence of 10^{15} n_{eq}/cm^2 the gain is ~ 1, regardless of the initial multiplication-layer doping.

Furthermore, an exhaustive study of the *type-1 gain* obtained with IR pulses was performed. The particular interest in IR pulses comes from the fact that they imitate the behaviour of MIPs (see Section 4.2). It is because of this that the gain for IR pulses was calculated, both before an after irradiation, as a function of voltage, see Figure 7.24. As in Figure 7.22b, before irradiation the gain was calculated as the ratio between the mean normalised charge of all the LGADs and PiN diodes from a given wafer set. In the case of W3 and W4, there are two different curves before irradiation, this is due to the aforementioned difference in measured charge between these two wafers. Also, the before-irradiation gain values between 320 V and 360 V for W1 and W2 were omitted due to the abnormal behaviour of one of the PiN diodes (see discussion in Section 7.3.2).

Several conclusions can be drawn from the results in Figure 7.24. Firstly, it is, once again, confirmed that higher multiplication-layer doping translates into higher gain, and that gain decreases with irradiation. Secondly, it is observed that at a fluence of 10^{14} n_{eq}/cm^2 it is no longer possible to recover the gain to before-irradiation values by increasing the applied bias voltage. Finally, as seen previously (Figure 7.22), at a fluence of 10^{15} n_{eq}/cm^2 there is no amplification, no matter the initial multiplication-layer doping. The observed decrease in gain may be related to the double-junction effect men-

tioned in Section 7.3. Before irradiation, at a specific bias voltage the electric field has a clear maximum in the multiplication layer. After irradiation, at the same specific bias voltage there are now two *competing* electric field peaks; one in the back of the device, and one in the front. This implies that a higher bias voltage is required to reach the same electric-field intensity in the multiplication layer as before irradiation, and hence the same gain. It is also possible that the cause for this decrease in gain is actually a combination of two effects, namely, the double-junction effect and effective acceptor removal. Acceptor removal would cause and decrease in the effective doping concentration of the multiplication layer, which would lead to a decrease in the gain.

Finally, the *type-1 gain* was also calculated with the charge collection results obtained through ^{90}Sr voltage scans. As mentioned in Section 7.3.1, the measurements could only be performed before irradiation, due to high noise levels afterwards. The *type-1 gain* values obtained at 700 V and 20°C are shown in Table 7.2. These gain values are rather lower than those obtained with IR TCT, this is due to the difference in temperature. The TCT measurements were done at -20°C, whilst the ^{90}Sr scans were done at 20°C.

Table 7.2: *Type-1 gain* values obtained through ^{90}Sr measurements on LGADs from run 7859 before irradiation, at 700 V, and 20°C.

	Multiplication-layer dose	
	1.8×10^{13} cm^{-2}	2.0×10^{13} cm^{-2}
Gain	4.3 ± 0.5	12 ± 2

UNIVERSIDADE DE SANTIAGO DE COMPOSTELA

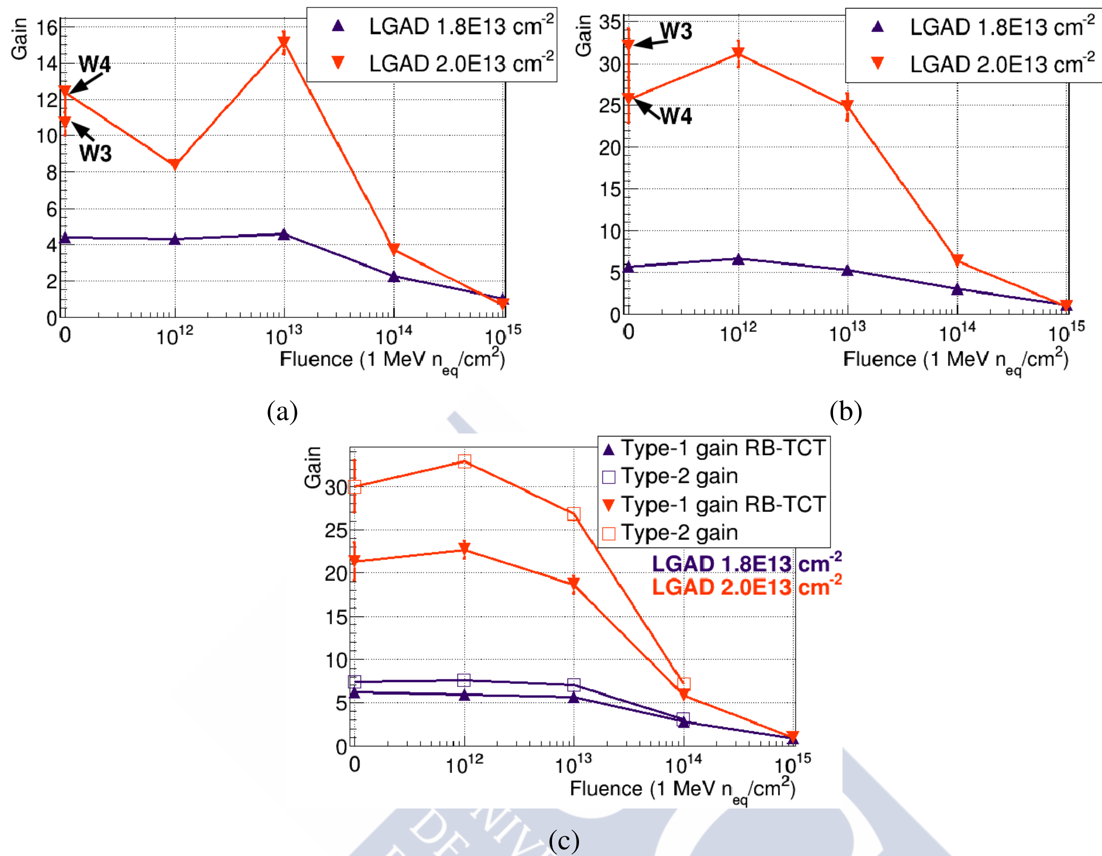

Figure 7.22: Gain at 700 V and -20°C as a function of fluence. *Type-1 gain* (ratio between Q_{LGAD} and Q_{PiN}) for (a) hole injection (red-front TCT), (b) IR pulses, and (c) electron injection (triangular markers, red-back TCT). *Type-2 gain* as a function of fluence is plotted in (c). *Type-2 gain* is calculated as the ratio between the injected electrons (red-back TCT) and the secondary holes produced.

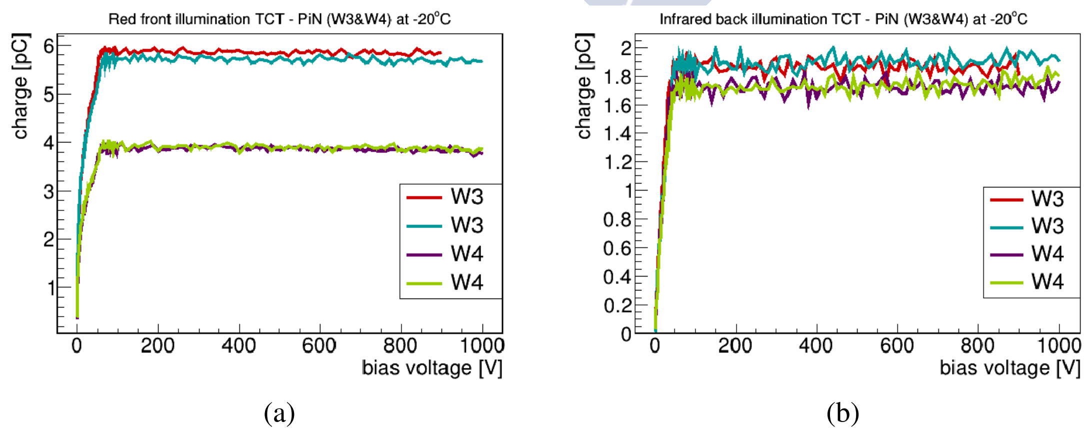

Figure 7.23: Before-irradiation voltage scans of the PiN diodes from wafers 3 and 4. (a) Red-front TCT (hole injection), and (b) IR TCT. Temperature: -20°C.

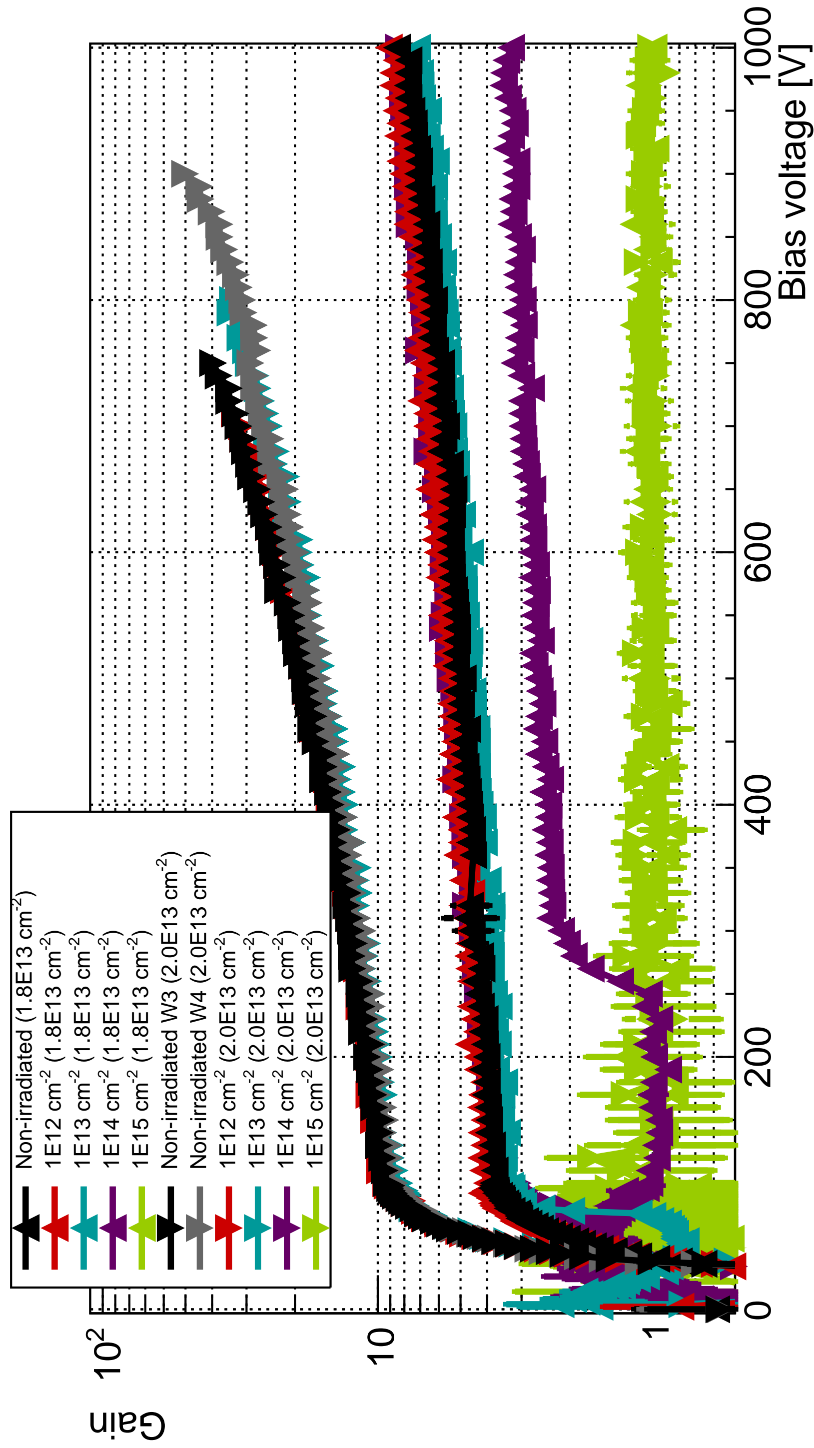

Figure 7.24: *Type-1 gain* of LGADs as a function of voltage and fluence for IR pulses. The multiplication-layer doping is indicated in brackets in the legend.

7.5 Detailed study of samples irradiated up to 10^{14} n_{eq}/cm^2

In order to have more conclusive proof of the inversion of space charge sign due to hole trapping mentioned in Section 7.3.2, further studies were performed on the samples irradiated up to 10^{14} n_{eq}/cm^2 (LGAD_7859_4_W2_I3_1 and LGAD_7859_7_W3_C2_3), as the effect was most noticeable in these devices.

7.5.1 Waveforms at different temperatures

The first step was to study the waveforms obtained from red TCT voltage scans at different temperatures. The motivation for this is that both the occupation probability of traps, and the emission probability (or trapping time) are dependent on temperature. The lower the temperature the higher the occupation probability of traps, meaning that trapping is more likely at lower temperatures [36]. Additionally, the emission probability of charge carriers from deep-level traps decreases with decreasing temperature, ergo the lower the temperature the longer the charges remain trapped [25]. Consequently, if the inversion of space charge sign is due to hole trapping, the effect should be reduced at higher temperatures, this was actually seen for the firs time in [40]. This means that, if after irradiation the depletion region grows from the back at -20°C, as seen in Section 7.3.2, at 20°C the devices may deplete from the front side.

To get a clearer picture of the behaviour of the devices, red TCT voltage scans were done at 5 different temperatures: 20°C, 10°C, 0°C, -10°C, and -20°C. For completeness, not only LGADs were measured, but also the PiN diodes irradiated to 10^{14} n_{eq}/cm^2. For future reference, these measurement were carried out in April 2016, this detail will prove to be important after the discussion in Section 7.5.3. The results obtained for LGADs are summarised in Figures 7.25 and 7.26. Here the full voltage scans obtained at all 5 different temperatures, both with red-front and red-back TCT, are also included. It should be mentioned that the voltage steps used for the scans were rather large, so it is not possible to determine the multiplication-onset voltage with precision, however, it is enough to examine its evolution with temperature. Additionally, the waveforms obtained with both LGADs at 300 V for all 5 different temperatures, both with red-front and red-back TCT are shown. The Figures with all the obtained waveforms for both LGADs and PiN diodes can be found in Appendix B. It should be noted that no double-junction effect or space charge sign inversion of the bulk was observed in PiN diodes.

Let us first focus on the sensor from W2 (LGAD_7859_4_W2_I3_1, mult. layer dose: 1.8×10^{13} cm^{-2}). Figures 7.25a and 7.25c show the charge collection with respect to voltage for this sample at all 5 different temperatures. The minimum bias voltage required to get a signal through red-front TCT increases as temperature decreases: between 50 and 100 V at 20°C and 10°C, above 100 V at 0°C, more than 180 V at -10°C, and above 260 V at -20°C. Meanwhile, through red-back TCT, already at voltages between 0 and 50 V there is charge collection at all temperatures. Moreover, the waveforms obtained with red-front TCT at 300 V (Figure 7.25b) show clearly that at -20°C and, less noticeably, at -10°C there is a peak in the electric field on the back of the device. Said peak is not present at temperatures above 0°C. Finally, the waveforms obtained with red-back TCT at 300 V (Figure 7.25d) show clearly that at -20°C the electric field is growing from the back side of the sensor. In fact, the pulse shape corresponds to that expected from the movement of electrons in a PiN diode with an electric field growing from the back. The expected pulse shape due to the electrons injected in the back reaching the multiplication layer and creating an avalanche of holes is not present.

The LGAD from W3 (LGAD_7859_7_W3_C2_3, mult. layer dose: 2.0×10^{13} cm^{-2}) presented a similar response. Figures 7.26a and 7.26c show the charge collection with respect to voltage for this sample at all 5 different temperatures. The minimum voltage to get a signal through red-front TCT increased as temperatures decreased below 0°C, requiring 180-220 V at -20°C. At the same time, a voltage of 50 V resulted in an observable signal through red-back TCT at all temperatures. Regarding the waveforms, as in the other LGAD, red-front TCT (Figure 7.26b) revealed a peak in the electric field on the back of the device at -20°C and -10°C. On the other hand, the waveforms from red-back TCT (Figure 7.26d) did not differ greatly, besides the expected gain dependence with temperature (see Chapter 6).

All these observations point towards the presence of a maximum of the electric field in the back side of the LGADs irradiated up to 10^{14} n_{eq}/cm^2, most pronouncedly so in the device with the lowest multiplication-layer dose (1.8×10^{13} cm^{-2}). Such a result is consistent with the existence of a back junction in proton-irradiated LGADs. The measurements also show that the back junction is most noticeable at lower temperatures. This is in line with the hypothesis of a trap-induced space charge sign inversion of the p-type bulk.

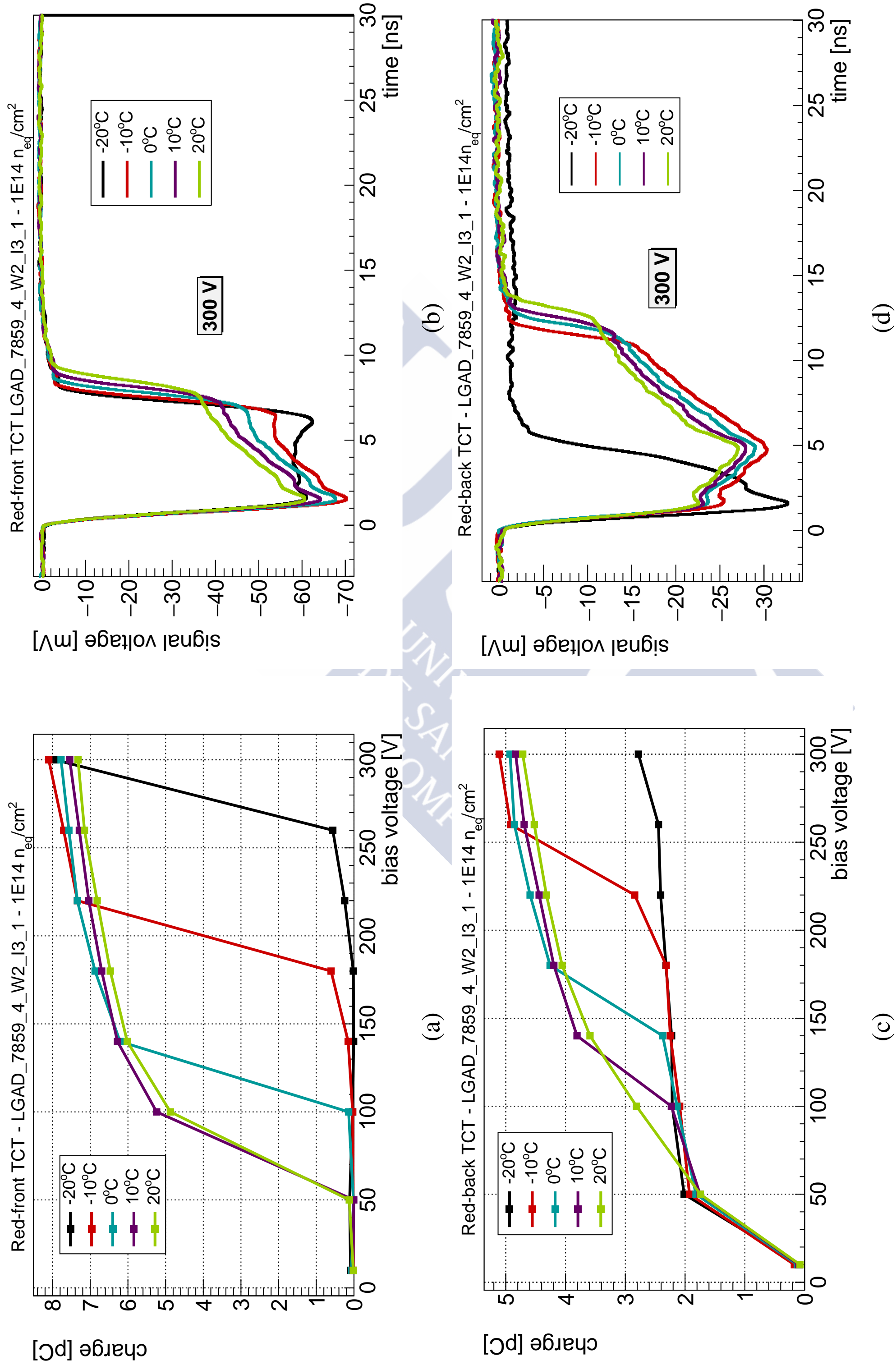

Figure 7.25: (top) Red-front and (botton) red-back TCT (a,c) voltage scans and (b,d) waveforms at 300 V of LGAD_7859_4_W2_I3_1 (mult. layer dose: 1.8×10^{13} cm^{-2}, fluence: 10^{14} n$_{eq}$/cm^2) at 20, 10, 0, -10, and -20°C.

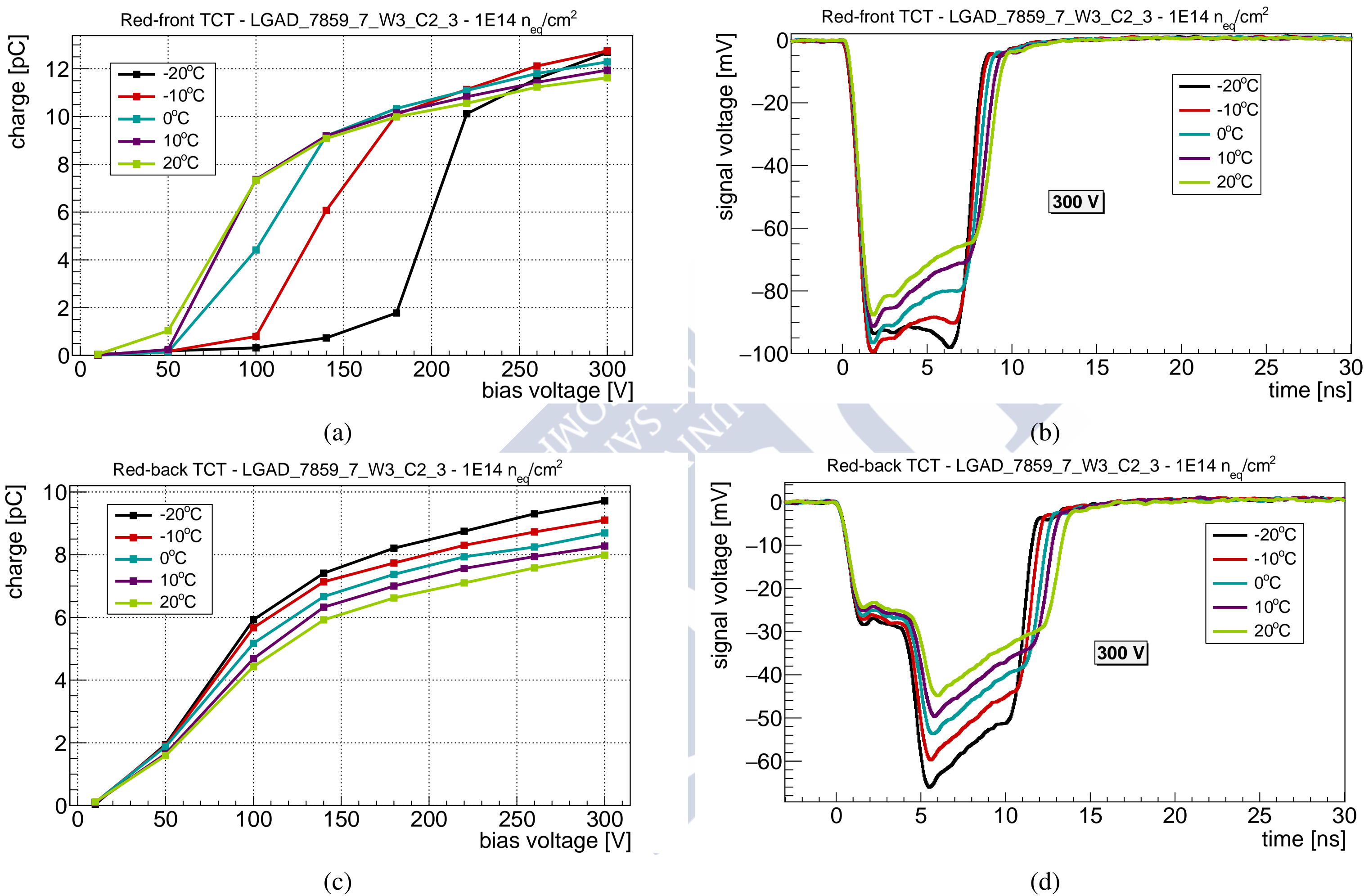

Figure 7.26: (top) Red-front and (botton) red-back TCT (a,c) voltage scans and (b,d) waveforms at 300 V of LGAD_7859_7_W3_C2_3 (mult. layer dose: 2.0×10^{13} cm^{-2}, fluence: 10^{14} n$_{eq}$/cm^2) at 20, 10, 0, -10, and -20°C.

7.5.2 Leakage current

The space charge sign inversion of p-type silicon in LGADs was observed before in [106], however, it was indicated that it only occurred in LGADs with a total leakage current higher than 1 μA at full depletion voltage, and 20°C, before irradiation. According to [106], LGADs with a lower leakage current did not show an inversion of space charge, but a reduction of gain due to acceptor removal in the multiplication layer, as seen in [10]. To verify that the LGADs considered in the present study had a sufficiently low leakage current, where space charge sign inversion is not expected, the before-irradiation IV curves of both devices irradiated up to 10^{14} n_{eq}/cm^2 were carefully inspected. Figure 7.27 shows the leakage current as a function of voltage before irradiation at 20°C for both LGADs that were later on irradiated to 10^{14} n_{eq}/cm^2. It can be seen, particularly in 7.27b, that both devices have a total (pad + GR) leakage current significantly lower than 1 μA at full depletion voltage, and 20°C.

It should be noted that the devices in [106] have an active area of 5×5 mm^2 and a thickness of 300 μm. On the other hand, the devices studied in this thesis have an active area of 3×3 mm^2, and a thickness of 285 μm. Assuming that the leakage current is proportional to the active volume of the device, in the LGADs from this thesis the current threshold set to 1 μA in [106] would actually be of 0.34 μA. As can be seen in 7.27b, both samples have a total leakage current below 0.34 μA at full depletion voltage and 20°C.

7.5.3 Annealing and influence of the guard ring on TCT scans

Since, within the EP-DT-DD SSD team at CERN, TCT measurements had always been performed without grounding the GR, a thorough study of the possible influence of the GR grounding was performed. Firstly, an LGAD, kept unirradiated for reference, was tested at -20°C and 20°C, with and without the GR grounded, see Figure 7.28. No GR-induced changes were found. Before irradiation the onset of multiplication voltage remains constant regardless of the temperature (as expected) and connection of the GR. The only changes observed are that the multiplication is higher at -20°C. This result is independent of the GR connection, and comes as no surprise based on the relation between gain and temperature described in Chapter 6.

To properly evaluate the effects of the GR after irradiation, various variables were considered when studying the samples irradiated up to 10^{14} n_{eq}/cm^2, namely: temperature, connection of the GR, multiplication-onset voltage, gain, and date (month and year) when each measurement was performed. In the case of the LGAD from W2 (multiplication-layer dose: 1.8×10^{13} cm^{-2}), Figure 7.29a presents the multiplication-onset voltage measured with and without the GR at -20°C, as well as one measurement at 20°C. In this plot the results are shown with respect to the date when each measurement occurred. When comparing measurements from the same date it is found that at -20°C the GR con-

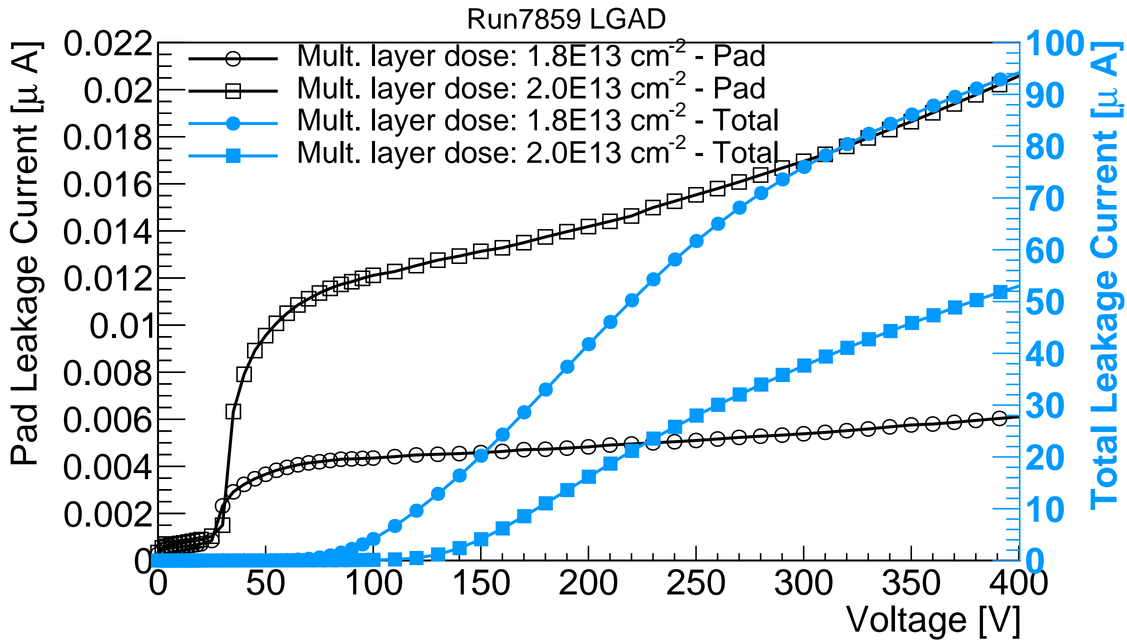

(a)

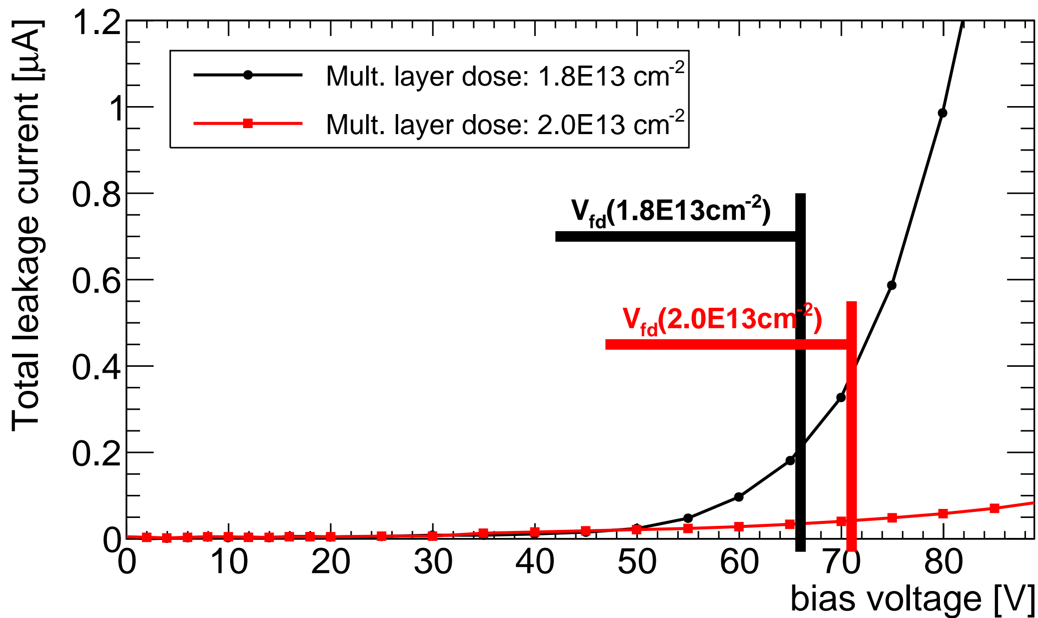

(b)

Figure 7.27: (a) Pad and total (pad + GR) leakage currents at 20°C, before irradiation. (b) Detail of the total leakage current around full depletion. Samples LGAD_7859_4_W2_I3_1 and LGAD_7859_7_W3_C2_3, irradiated uo to 10^{14} n_{eq}/cm^2.

nection shifts the onset of multiplication. Also, the multiplication-onset voltage is lower at high temperatures, reaching almost the before-irradiation value of $\sim$ 30 V. This observation is consistent with the hypothesis of trap-induced space charge sign inversion of the bulk, as the effect is less marked at higher temperatures. What is actually most striking, is the decrease in multiplication-onset voltage with time. This change might be related to reverse annealing introducing negative space charge, since in between each set of measurements there were periods of involuntary annealing (due to the transport of the samples, measurements at temperatures above 0°C, etc.). As regards the influence of the GR on the gain, and its evolution with time, Figure 7.29b shows the type-1 gain measured through red-front TCT at -20°C and 400 V, with and without the GR, as a function of the date when each measurement took place. Whilst the GR connection scheme does not seem to have much of an effect, the gain increases with time. This would mean that annealing aids the recovery of gain after irradiation. As a matter of fact, the latest measurement presents a gain equal to 70 % of the before-irradiation gain value of $\sim$ 3.45, under the same temperature and voltage conditions.

Similarly, the LGAD from W3 (multiplication-layer dose: 2.0×10^{13} cm^{-2}), presents a multiplication-onset voltage that decreases with time, i.e. with annealing (see Figure 7.29c). Indeed, the latest measurements indicate that the multiplication-onset voltage has shifted to values close to that before irradiation, around 32 V. Curiously, in this sample the GR connection causes no significant changes, and neither does the temperature. Such a behaviour is almost identical to the one expected from a non-irradiated LGAD (Figure 7.28). In addition, the gain is also not affected by the GR connection, and with time/annealing it has gone up to about 60 % of the before-irradiation value of $\sim$ 6.83, under the same temperature and voltage conditions.

Finally, to discard any other possible set-up-related influences on the measurements, besides testing the effect of the GR connection on the multiplication-onset, different bias and read-out schemes were examined. Regardless of whether the biasing and read-out were done through the front (n-side), or if the biasing was applied to the back (p-side) and the read-out performed through the front (n-side), the results were always the same, as seen in Fig 7.30.

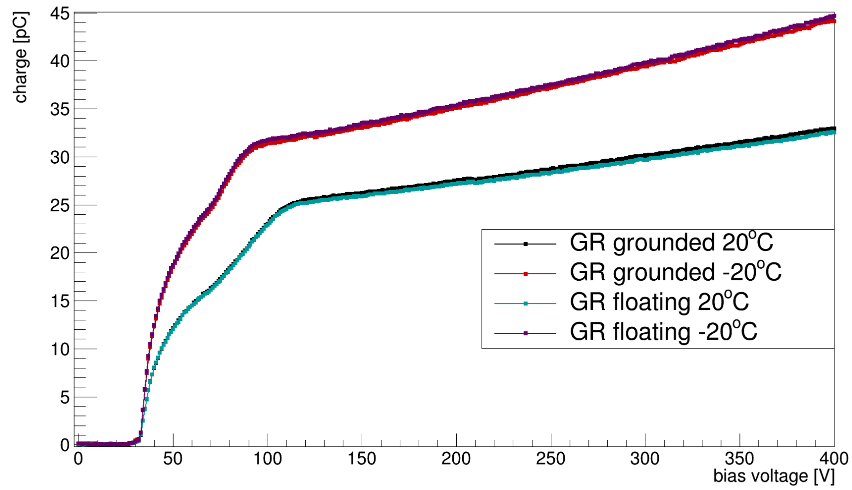

Figure 7.28: Charge collection as a function of voltage obtained with red-front TCT on an unirradiated LGAD at 20°C and -20°C, with and without a GR connection.

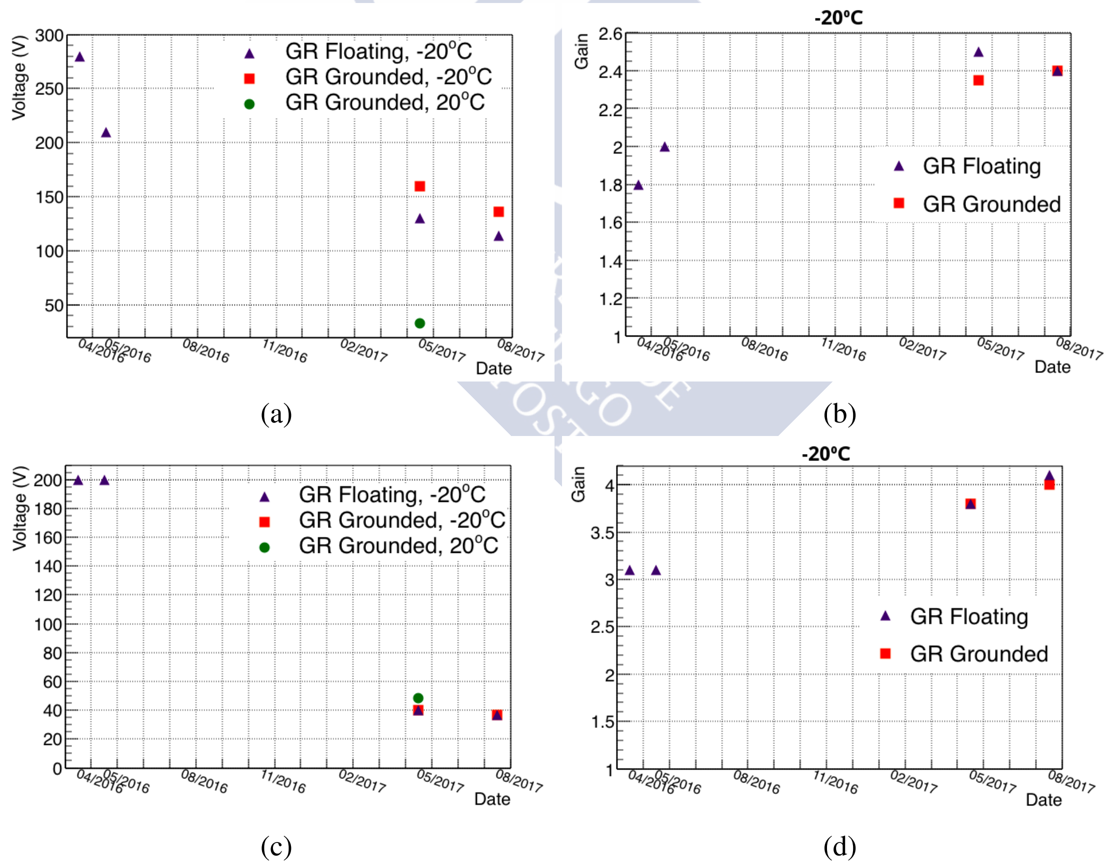

Figure 7.29: Evolution with time of the (left) multiplication-onset voltage (red-front TCT) and the (right) *type-1 gain* measured through red-front TCT at -20°C, and 400 V for LGAD_7859_4_W2_I3_1 (top), and LGAD_7859_7_W3_C2_3 (bottom) irradiated up to 10^{14} n_{eq}/cm^2.

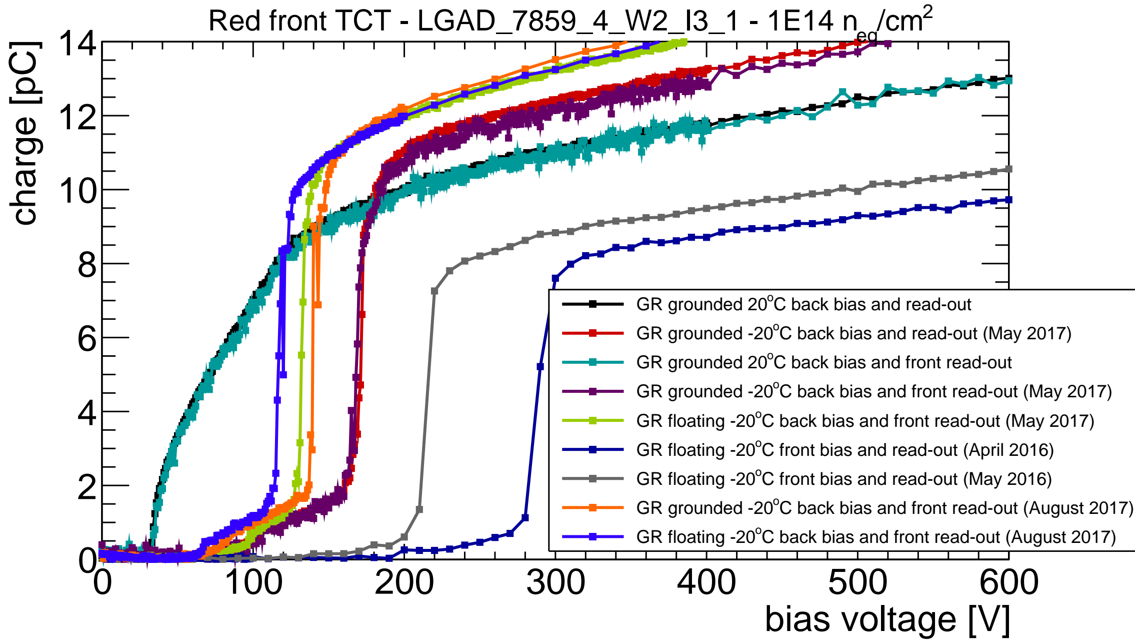

(a)

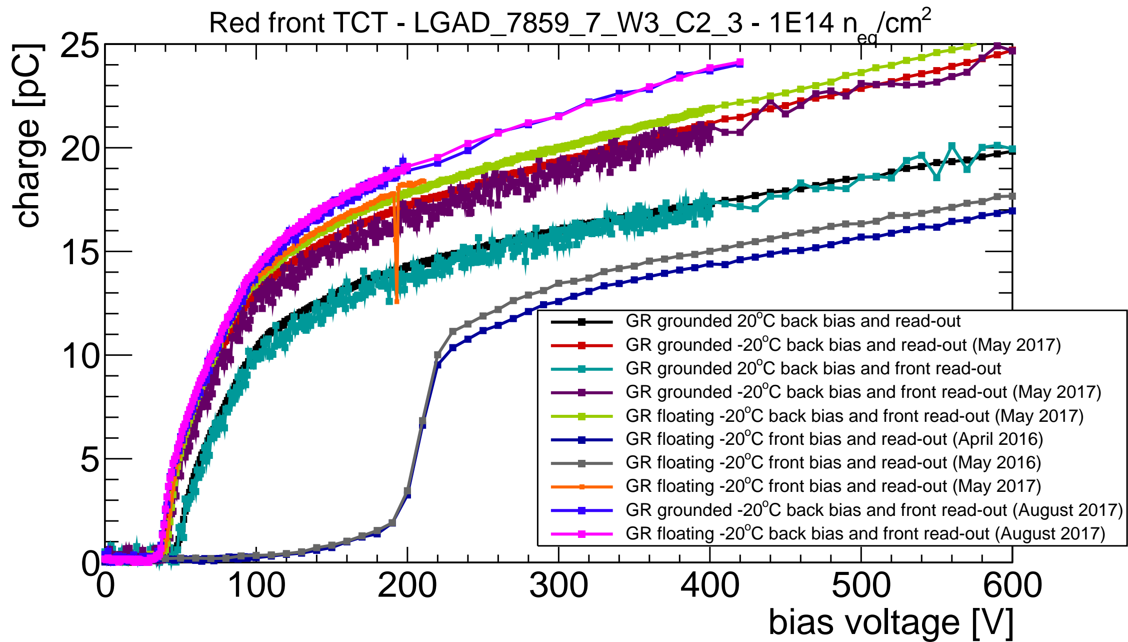

(b)

Figure 7.30: Red-front TCT voltage scans performed on both LGADs irradiated up to 10^{14} n_{eq}/cm^2 at 20°C, and -20°C; on several dates; and using different GR, biasing, and read-out schemes. (a) LGAD_7859_4_W2_I3_1 (multiplication-layer dose: 1.8×10^{13} cm^{-2}) and (b) LGAD_7859_7_W3_C2_3 (multiplication-layer dose: 2.0×10^{13} cm^{-2}).

7.5.4 Characterisation of the electric field

In order to understand how the electric field evolves with voltage and temperature TPA-TCT and eTCT measurements, see Chapter 4, were performed. For the eTCT measurements, the side of the devices that was going to be illuminated was thoroughly polished. The LGAD from W3 (LGAD_7859_7_W3_C2_3, mult. layer dose: 2.0 $\times$ 10^{13} cm^{-2}) underwent, in September 2017, eTCT Z-scans, i.e. scanning the device all through its thickness, at different voltages and at -20°C and 20°C, see Figure 7.31. The results show that temperature does not seem to affect dramatically the profile of the drift velocity, which is proportional to the electric field. This is consistent with the behaviour of a non-irradiated LGAD, just as the multiplication onset results commented in Section 7.5.3. However, at 20°C there is an unexpected narrow peak in the electric field on the back of the device. Unfortunately, due to time constraints and the availability of the TPA-TCT facility, it was not possible to do TPA-TCT scans on the device, which may have shed some light on this peculiarity.

Edge-TCT scans were also performed on the LGAD from W2 (LGAD_7859_4_W2_I3_1, mult. layer dose: 1.8 $\times$ 10^{13} cm^{-2}) in August 2017. The Z-scans can be found in Figure 7.32, and in Figure 7.33 ZY-scans can be seen, i.e. maps of the electric field all through the thickness and width of the device at a given voltage. The Z-scans show that at 20°C the drift velocity, and thus the electric field, is higher on the front of the device. Also, at higher voltages the velocity tends to be more homogeneous throughout the device. On the other hand, at -20°C the behaviour is quite different. At voltages below $\sim$ 85 V the electric field on the back side of the LGAD is either higher or comparable to that on the front. Above 85 V the field peaks at the front side, and at voltages higher than $\sim$ 235 V, the field tends to be more homogeneous throughout the thickness of the sensor. The same behaviour was observed in the ZY-scans. Figure 7.33 shows not only the ZY-scans, but also the red-front TCT voltage scan done on the very same sample, and used to choose the voltage values for each ZY-scan. Even though the illuminated surface of the sensor was polished, the resolution in these scans is not optimal. In order to achieve a better and clearer understanding of the behaviour of the electric field inside this device, in July 2017, TPA-TCT Z-scans were carried out on this LGAD.

TPA-TCT Z-scans consist in illuminating the sample from the front and making the laser beam spot move all through the thickness of the sensor. Said scans were performed on device LGAD_7859_4_W2_I3_1 at -20°C and 0°C, with bias voltages ranging between 0 and 700 V, see Figure 7.32. At both temperatures, -20°C and 0°C, the electric field clearly begins growing from the back of the device. At 0°C, already at low voltages ($\sim$ 30 V) there is also a peak on the front side. In fact, at $\sim$ 45 V the electric field on the front side has approximately the same intensity as on the back, giving a profile consistent with a *double junction*. At -20°C, the double peak profile of the electric field appears at $\sim$ 96 V. Successively, at a voltage between 150 and 200 V (for both temperatures) the electric field in the front side overpowers the field in the back, resulting in a unique peak on the front. Finally, at voltages above 200 V, the electric field recovers its before-irradiation shape.

Space charge sign inversion of p-type silicon due to hole trapping explains the growth of the electric field from the back of the device, as well as the presence of a double junction. Also, it is consistent with the observation that at lower temperatures a higher voltage is needed to increase the intensity of the electric field on the front side of the sensor. This is due to the temperature dependency of trapping, and thus of trap-induced space charge sign inversion [40, 41]. However, space charge sign inversion alone does not account for the electric field at higher voltages, nor the intermediate state with just one peak on the front. A comprehensive explanation has not yet been found due to the complexity of the various phenomena at play.

A possible explanation to the observed behaviour could be the presence of a *triple junction*. Space charge sign inversion of the p-type bulk, resulting in an n-like bulk, in the LGAD could be creating an n+/p+/n/p++ structure, see Figure 7.34a. This would cause the formation of three junctions. One in the front (n+/p+), between the n+ implantation layer of the LGAD and the p+ multiplication layer, which would be reverse biased. One in the back (n/p++), between the n-like bulk and the p++ back implantation of the LGAD, which would also be reverse biased. And, finally, one in the middle (p+/n), between the p+ multiplication layer and the n-like bulk, which would be forward biased. A potential explanation to the behaviour of the electric field was obtained through a qualitative TCAD simulation of the device in question[5] [107]. According to it, the multiplication layer is depleted at ~ 30 V, even after irradiation. In spite of this, as higher voltages are applied, the electric field begins growing from the back of the sensor towards the front. It is not until the depletion region reaches the front side that the electric field starts increasing on the front side of the detector, and the *standard* double-junction effect appears. Afterwards, the space charge starts to change sign from positive to the original negative in the bulk.

Further support to the *triple junction* hypothesis was found in IV curves. Before irradiation, the pad leakage current presents a rapid increase at the multiplication-onset voltage, and then it continues to increase slowly, remaining almost constant. After irradiation, the general behaviour of the pad leakage current is the same. These results, which can be seen clearly in Figure 7.34b, imply that the multiplication layer is, in fact, depleted and active at the same voltage even after irradiation. However, as observed in TCT voltage scans, this activation of the multiplication layer is not observed in TCT measurements. It might be that the defects caused to the bulk by radiation may be changing how the signal propagates inside the sensor, thus not allowing the measurements of the signal at voltages below full depletion. As regards the space charge change from the sign-inverted positive state (n-like) to the original negative state (p-type bulk), this could be explained based on the characteristic of the deep-level traps. If the occupation probability of the produced traps is highly dependent on the electric field, the increase in voltage may reduce the number of trapped holes. This would cause a flip in space charge sign, with the bulk going back to the original p-type behaviour.

[5] The simulation work was carried out by Dr. Michael Moll.

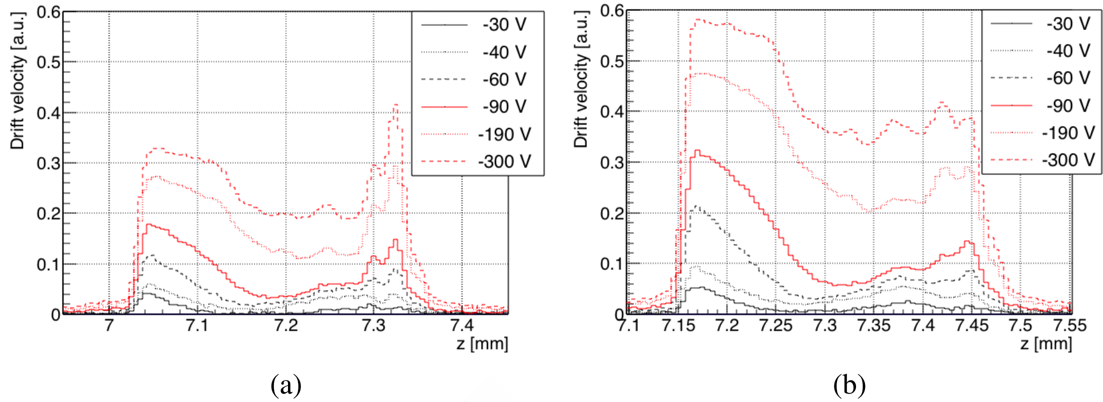

(a) (b)

Figure 7.31: Drift velocity profiles obtained through eTCT on LGAD_7859_7_W3_C2_3 (mult. layer dose: 2.0 $\times$ 10^{13} cm^{-2}), irradiated up to 10^{14} n_{eq}/cm^{2}, at (a) 20°C and (b) -20°C. In each plot the front side of the device corresponds to the left side of the graph.

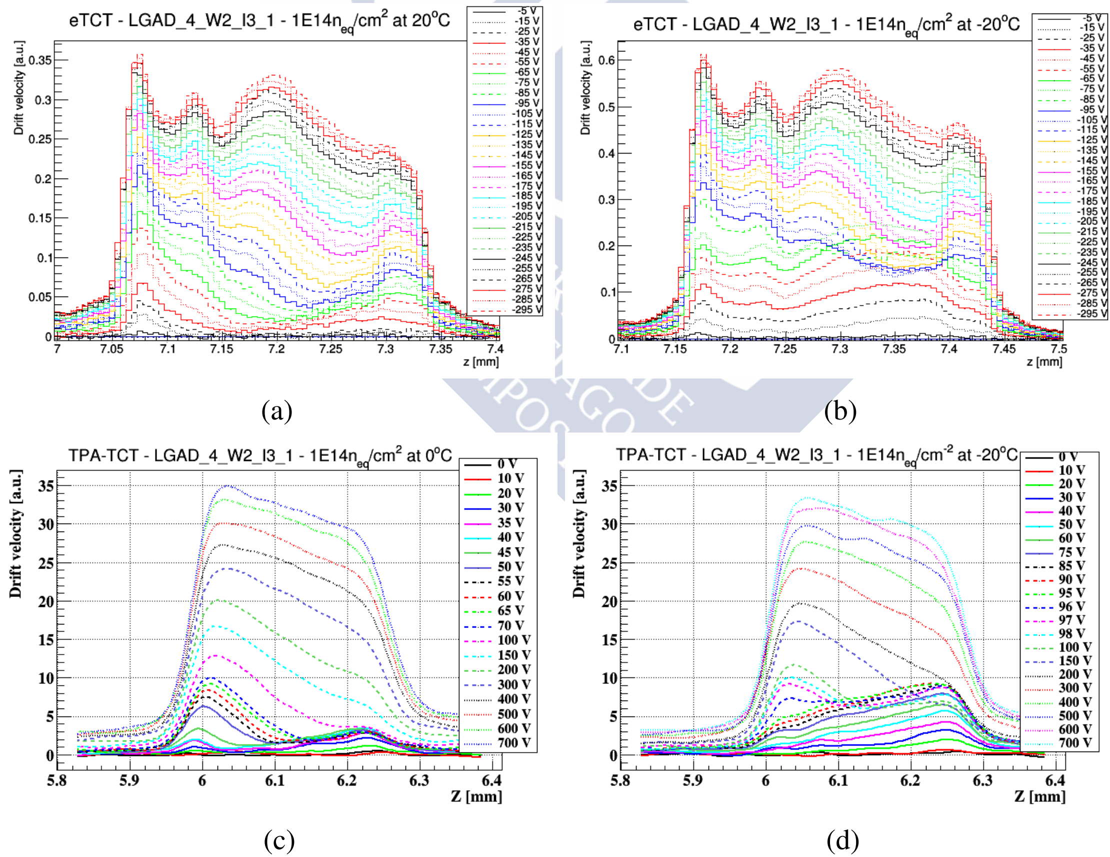

(a) (b)

(c) (d)

Figure 7.32: Drift velocity profiles obtained through eTCT and TPA-TCT (bottom) on LGAD_7859_4_W2_I3_1 (mult. layer dose: 1.8 $\times$ 10^{13} cm^{-2}), irradiated up to 10^{14} n_{eq}/cm^{2}. eTCT scans were done at (a) 20°C and (b) -20°C. TPA-TCT scans were done at (e) 0°C and (f) -20°C. In each plot the front side of the device corresponds to the left side of the graph.

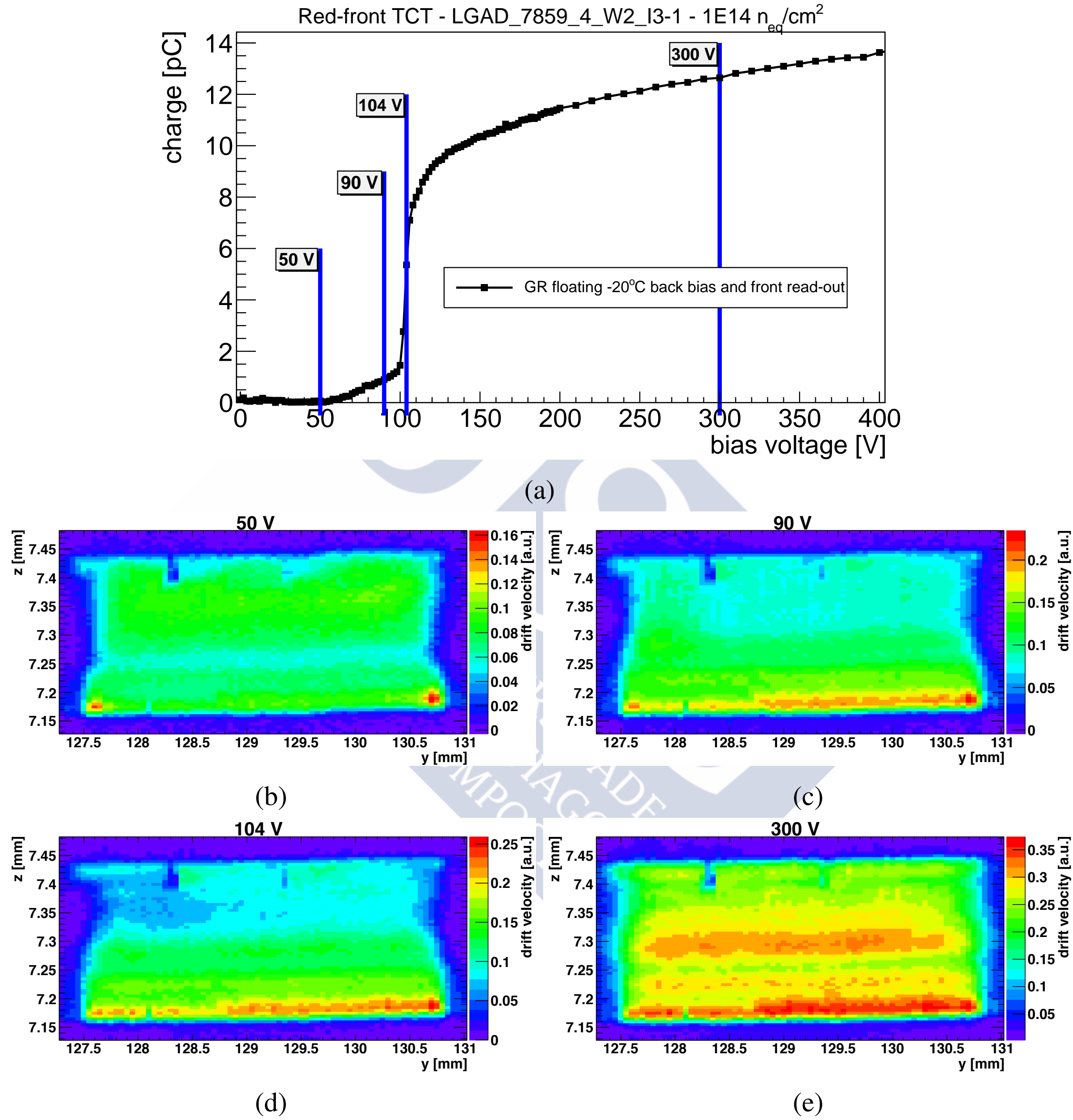

Figure 7.33: (a) Red-front TCT voltage scan of LGAD_7859_4_W2_I3_1 (mult. layer dose: 1.8×10^{13} cm^{-2}, fluence: 10^{14} n_{eq}/cm^2) to determine the voltages of interest for eTCT ZY-scans. (b)-(e) eTCT ZY-scans at 50, 90, 104, and 300 V. The front (back) side of the device corresponds to the bottom (top) of the 2D map. Temperature: -20°C.

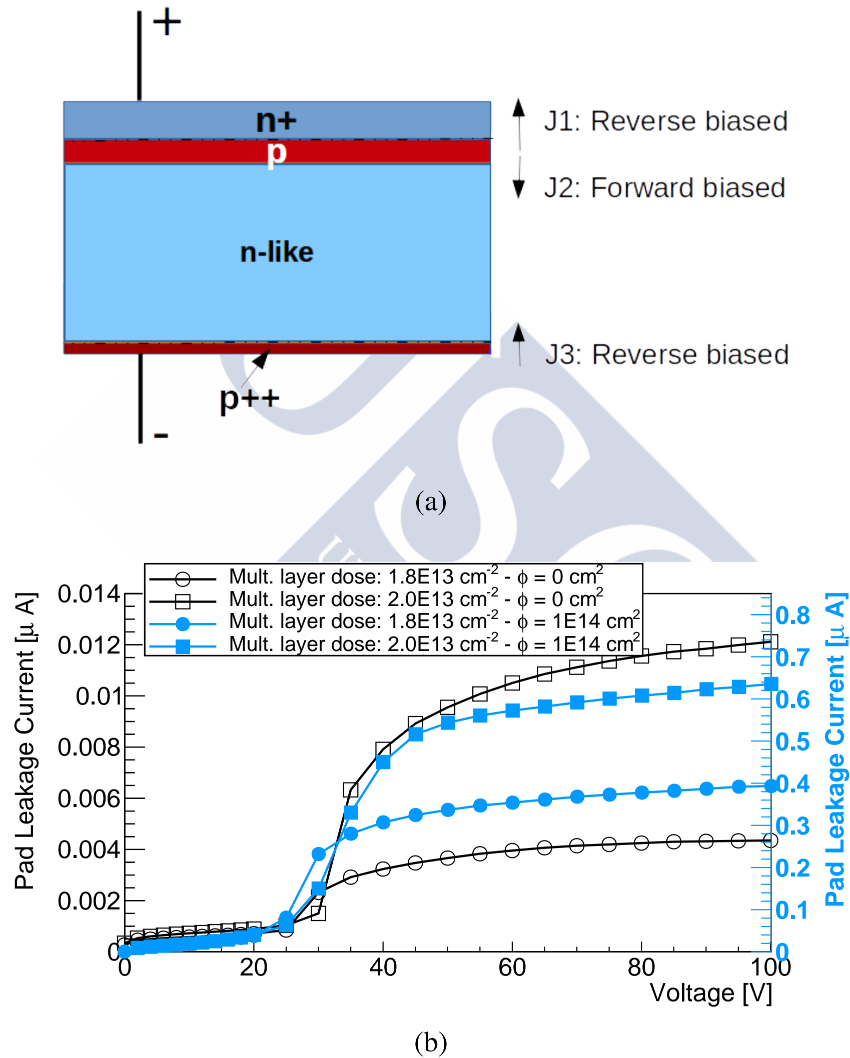

Figure 7.34: (a) Schematic of the hypothetical *triple-junction* structure in an LGAD. (b) Detail at low voltages of the pad leakage current, before and after irradiation, for the two LGADs that were irradiate up to 10^{14} n_{eq}/cm^2.

Chapter 8

Characterisation of DD-APDs

The effect of neutron irradiation on Deep Diffused APDs (DD-APDs), introduced in Chapter 6, was studied in this thesis. In order to do this, two sets of 2×2-mm^2 DD-APDs were characterised before and after neutron irradiation. Although the radiation effects were studied in these devices, the sensors considered for timing use in HEP experiments have an active area of 8×8 mm^2. In this thesis, two 8×8-mm^2 devices were characterised, although only before irradiation. In fact, the objective of that study was to analyse the signal amplitude uniformity, and whether it could be improved through surface metallisation. This was done by performing TCT surface scans.

The characterisation of all 2×2-mm^2 DD-APDs included TCT surface and voltage scans, as well as measurements of the capacitance and leakage current with respect to voltage. Measurements of the signal produced by electrons from a radioactive source (^{9}0Sr, see Section 4.4) were considered for the characterisation. However, the presence of the alumina support below the sensor made the measurements impracticable. Moreover, the ceramic support implied that there was no access to the back of the 2×2-mm^2 sensors, thus only red-front and IR-front TCT scans were performed on those. The average peak power of the laser beams used were 87 μW for red TCT, and 129 μW for IR TCT.

It should be noted that some small alterations had to be made to the TCT set-up for measurements to be feasible. These devices had to be biased up to 1.8 kV, whilst the bias T integrated in the amplifier used for TCT can only withstand a maximum of 1 kV. Hence, a simple customised bias T was devised, with a 1-MΩ resistor and a 4.4-nF capacitor, that could withstand 2 kV. Furthermore, the amplifier in question had to be changed as well in order to work at high voltages. This change meant that the amplifier was more robust in case of micro-discharges. On the downside, it also introduced a slight undershoot in the signal. Lastly, before the input of the 40-dB amplifier, an attenuator had to be connected, resulting in an effective amplification of 10 dB. This had to be done as the linear range of the amplifier is ± 1 V, without the attenuator the signals reached an amplitude of up to 3 V. Although some preliminary tests were done without an amplifier, it was finally decided not to dispense with the amplifier altogether, to avoid a direct connection between the DD-APDs and the oscilloscope.

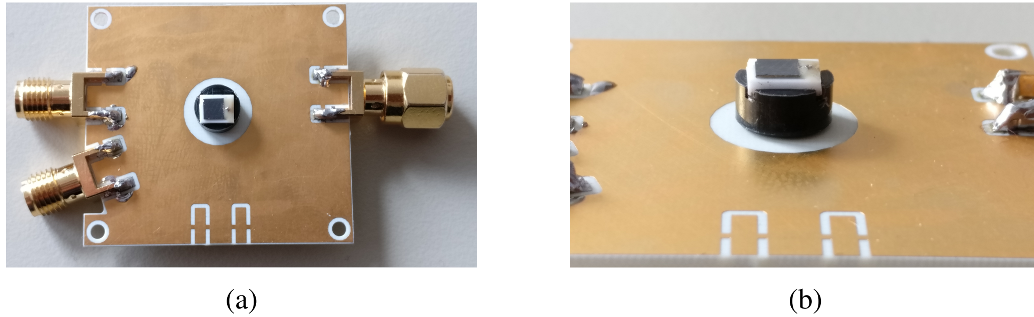

(a) (b)

Figure 8.1: View of a 2×2-mm^2 DD-APD mounted on a TCT PCB by means of a custom-made adaptor.

As explained in Section 6.2, 2×2-mm^2 DD-APDs are mounted on a ceramic support, and the electrical connections are done through two leads glued to the electrodes of the sensor. Because of their design, it was not possible to directly attach the devices to the PCBs used in the TCT set-up of the CERN EP-DT-DD SSD team. An adaptor was specially designed[1] for this purpose, allowing not only for the mounting of the DD-APDs on the PCBs, but also ensuring that the devices are not vertically tilted, which would cause differences in the incidence of light. Figure 8.1 shows a DD-APD mounted on a TCT PCB my means of one of this tailor-made adaptors. The aforementioned *packaging* of the devices, i.e. the combination of DD-APD+alumina support+leads, makes it impossible to perform CV/IV measurements in the usual probe station described in Section 4.1.1. However, CV/IV measurements could be performed in the CV/IV set-up developed inside a climate chamber (Section 4.1.2) with the DD-APDs already mounted on PCBs.

8.1 First Set of 2×2-mm^2 DD-APDs

Initially, a set of 7 DD-APDs with an active area of 2×2 mm^2 was characterised. From this first set of detectors, 2 devices were left unirradiated as reference, whilst the remaining 5 were sent for neutron irradiation at the Jožef Stefan Institute in Ljubljana, Slovenia. Table 8.1 indicates the fluence to which each device was exposed. The detectors were not subjected to annealing after irradiation. Nevertheless, it was estimated that, due to their handling, the samples underwent a total annealing of 60 min at 21°C.

[1]The design and production of these adaptors was carried out by Miranda Van Stenis, at the Glass and Ceramic Workshop of the CERN EP-DT-EF Thin Films & Glass service, and by the EP-DT Mechanical Workshop.

UNIVERSIDADE DE SANTIAGO DE COMPOSTELA

Table 8.1: Irradiation details for all $2 \times 2\text{-mm}^2$ DD-APDs from the first set of sensors analysed.

Fluence [n_{eq}/cm^2]	Device name	Fluence [n_{eq}/cm^2]	Device name
0	394-1-7 394-1-8	3×10^{14}	394-1-4 394-1-5
3×10^{13}	394-1-1	1×10^{15}	394-1-6
6×10^{13}	394-1-3	-	

8.1.1 Homogeneity analysis

TCT surface scans were performed in order to verify the homogeneity of charge collection in this set of DD-APDs. These scans were done with both the red and the IR laser. The devices were biased to 1700 V from the back (n-side), whilst kept at a temperature of -20°C. The charge maps obtained with the unirradiated samples are shown in Fig 8.2. The red-front scans look entirely homogeneous, only sample 394_1_7 has a small region on the right side with higher charge collection. This inhomogeneity is merely an optical effect, caused by the reflection of light on a blob of glue on top of the lead connected to the front side of the device, as can be seen in Figure 8.3a. On the other hand, the IR TCT scans present a ring of high charge around their centre, also the area surrounding it has a charge collection that is ~ 30 % higher than that in the external areas and the centre of the devices. The central ring coincides in diameter with the circularly shaped mesa structure on the back of $2 \times 2\text{-mm}^2$ DD-APDs. So this high-charge ring could be a consequence of reflections of the IR laser on that structure. As to the other, more amorphous, areas of higher charge collection, they seem to be caused by reflections on the glue used for connecting the leads to the back electrode and to attach each DD-APD to its ceramic support. Pictures of two different alumina supports (those of samples 394_1_7 and 394_1_5), after the removal of the silicon sensors, can be found in Figure 8.3. The elimination of the silicon unveils the pattern created by the silver glue used for connections, as well as the non-conducting underfill material injected between the silicon and the alumina.

The IR scan of sample 394_1_8, along with those of all irradiated samples, covers a wider region than that of sample 394_1_7. These wider range scans bring to light the existence of regions of charge collection outside the active area of the devices. In fact, they are outside the silicon die, which has a size of 2.8×2.8 mm. This feature had already been observed during the preliminary tests performed before this study. Therefore, a brief investigation was carried out to understand the effect, the results of which can be found in Appendix C. It was revealed that these areas were a consequence of the IR light reflecting on the underfill material which protrudes from below the silicon sensor.

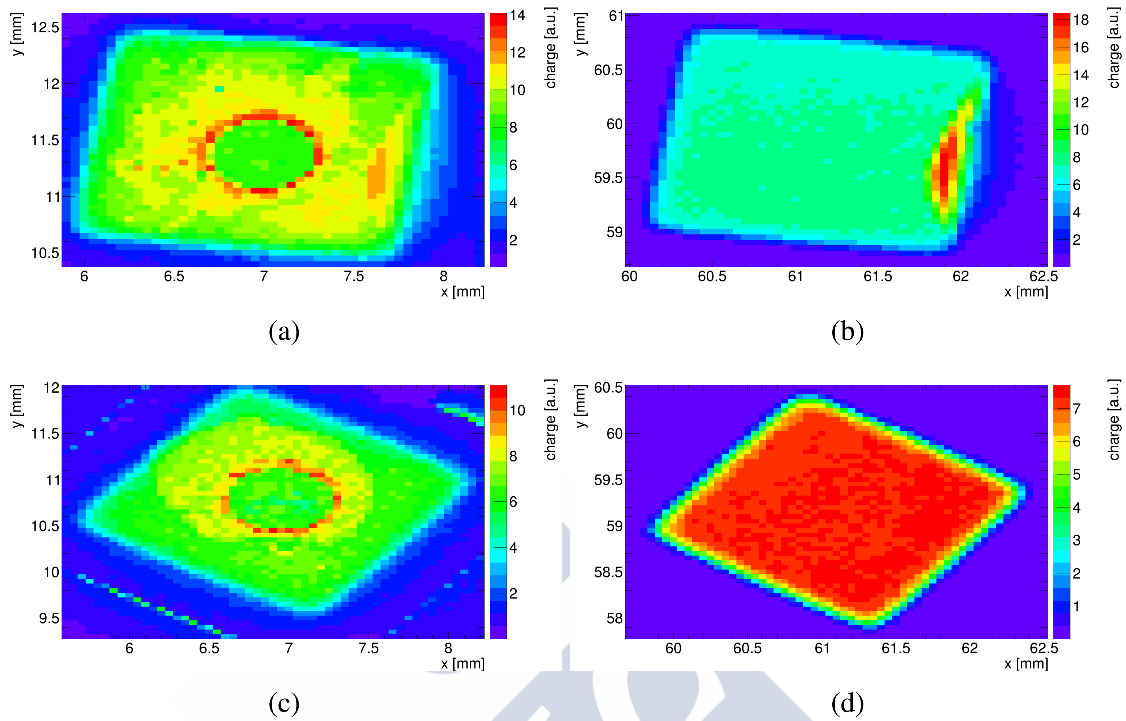

Figure 8.2: (Left) IR and (right) red-front TCT surface scans at -20°C and 1700 V on both samples kept unirradiated: sample 394_1_7 (top), sample 394_1_8 (bottom).

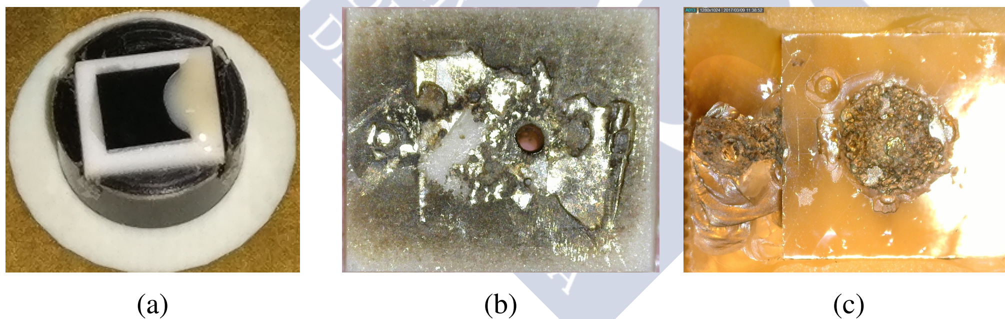

Figure 8.3: (a) Close-up of sample 394_1_7, a blob of glue is visible on the right-hand side of the sensor. (b),(c) Alumina supports from samples 394_1_7 and 394_1_5, after elimination of the silicon sensors.

The XY scans obtained for the two lowest fluences can be found in Figures 8.4 and 8.5. At a fluence of 3×10^{13} n_{eq}/cm^2 the scans look similar to those obtained with the unirradiated devices. The most significant change is the reduction of the charge collection. Interestingly, after a fluence of 6×10^{13} n_{eq}/cm^2, although the IR scan looks similar, the red-front scan shows an unexpected circular inhomogeneity in the centre. Said increase is caused by the lengthening of the pulse-width, and the increase in amplitude of the induced signal. This can be seen in Figures 8.5c and 8.5d, where the waveforms obtained all along the line $y = 59.4$ mm are shown. The source of this change in waveform-shape for red-front TCT has not been determined yet.

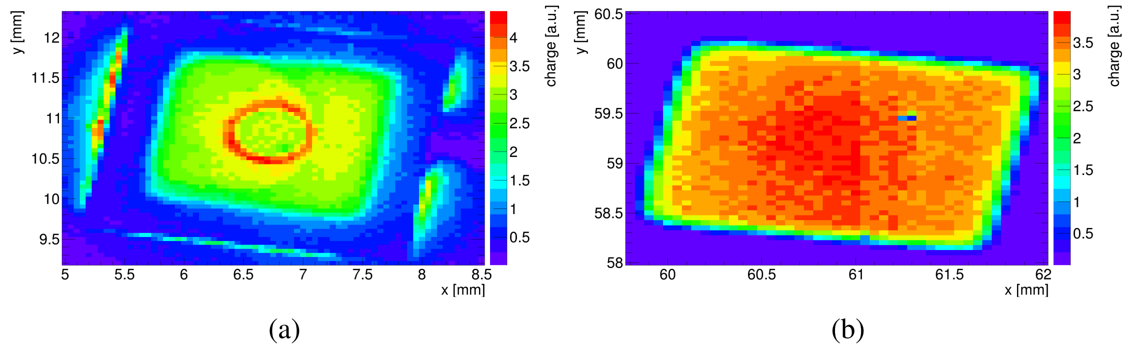

Figure 8.4: (Left) IR and (right) red-front TCT surface scans at -20°C and 1700 V on the DD-APD irradiated up to 3×10^{13} $\mathrm{n_{eq}/cm^2}$ (sample 394_1_1).

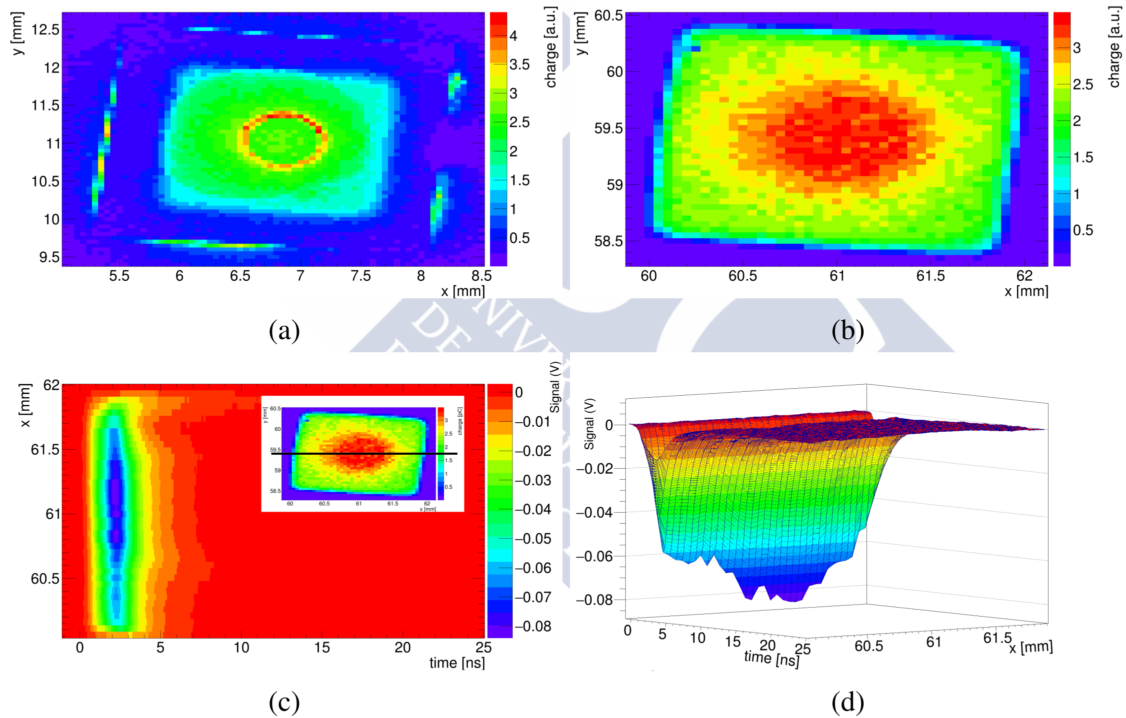

Figure 8.5: (a) IR and (b) red-front TCT surface scans at -20°C and 1700 V on the DD-APD irradiated up to 6×10^{13} $\mathrm{n_{eq}/cm^2}$ (sample 394_1_3). (c),(d) Red-front TCT waveforms obtained at every position in x along the line $y = 59.4$ mm of the surface scan.

Surface scans were also performed on both samples irradiated up to 3×10^{14} $\mathrm{n_{eq}/cm^2}$, see Figure 8.6. The scan on sample 394_1_4 had to be performed at 1500 V, instead of the usual 1700 V. At 1530 V the leakage current of the sensor reached compliance[2], which, for device-security purposes, was set at a conservative 10μA. This makes sample 394_1_5,

[2]The *compliance current* is a limit set, by means of the power supply, to the maximum current that should be allowed to go through the DUT.

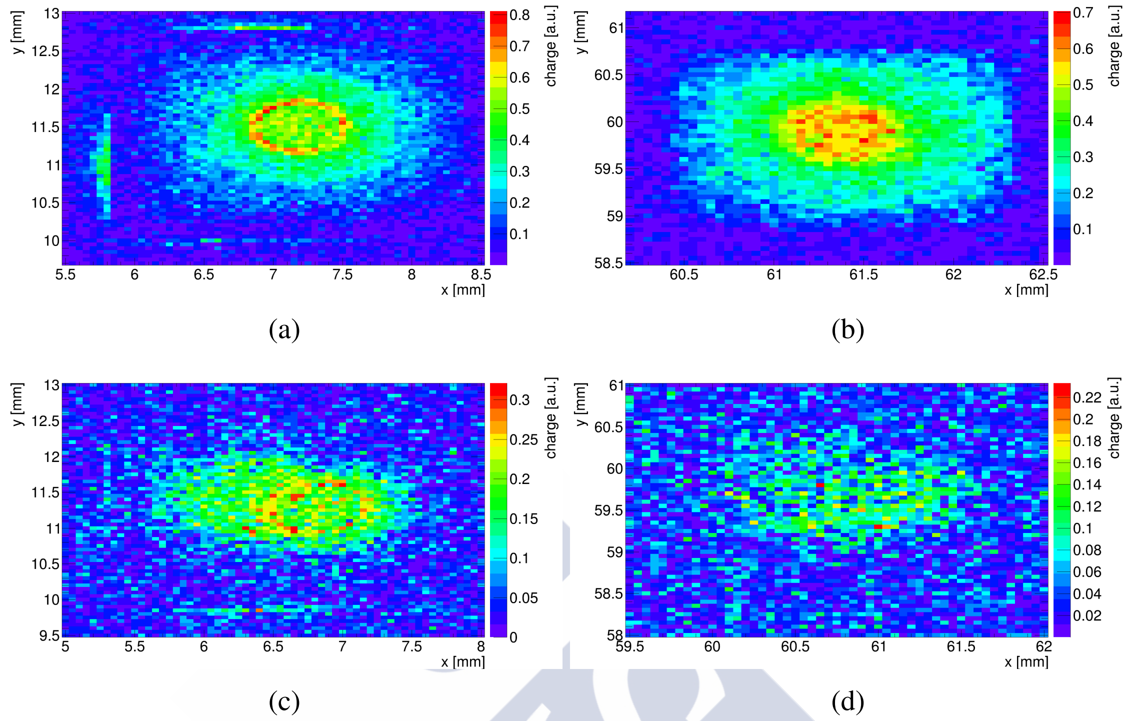

Figure 8.6: (Left) IR and (right) red-front TCT surface scans at -20°C on both samples irradiated up to 3×10^{14} n_{eq}/cm^2: sample 394_1_5, bias voltage 1700 V (top); sample 394_1_4, bias voltage 1500 V (bottom).

which could be biased up to 1700 V, a better candidate for comparison with the previously discussed devices. In any case, both sensors show a clear reduction in the active area of the DD-APDs after irradiation. Identically to the others, the red-front TCT scan of sample 394_1_5 presents a high-collection region at its centre. What is most surprising about these results is the fact that both sensors, irradiated up to the exact same fluence, present such different behaviours.

Finally, no charge collection maps were obtained for sample 394_1_6, irradiated up to 1×10^{15} n_{eq}/cm^2, as its leakage current reached compliance at 600 V.

UNIVERSIDADE DE SANTIAGO DE COMPOSTELA

8.1.2 Charge collection with voltage

In order to study the changes in charge collection with irradiation, IR TCT voltage scans were performed. During these, the IR laser continuously pointed at the centre of the device, whilst the voltage (applied on the n-side) was ramped up between 2 and 1800 V. Sample 394_1_4 (irradiated up to 3×10^{14} n_{eq}/cm^2) was biased only up to 1500 V as the leakage current reached compliance at 1530 V. Sample 394_1_1 was inadvertently taken up to 1700 V only. The sample irradiated up to 1×10^{15} n_{eq}/cm^2 (394_1_6) was not measured at all, as its leakage current reached compliance at 600 V.

The charge collection curves obtained are found in Figure 8.7. When inspecting these scans, the first thing that becomes evident is that, in the case of DD-APDs, multiplication begins at $\sim$ 1200 V. Another aspect that is immediately visible is that charge collection decreases with fluence. By fitting the curves, from 1500 V onwards, with an exponential function, it was possible to estimate the voltage needed after irradiation to recover the before-irradiation charge at 1700 V. For the lowest fluences, the charge collection could be recovered by ramping up the voltage to 1800-1900 V. At a fluence of 3×10^{14} n_{eq}/cm^2, however, the detectors should be biased at about 2500 V, which is well beyond the operational range of the devices.

Another chief detail is that detectors that should, in principle, behave identically, such as the unirradiated ones or those irradiated up to the same fluence, responded quite differently. Most surprising of all was the significant difference in charge collection between both unirradiated DD-APDs. In fact, at 1700 V, sample 394_1_7 collects 43 % more charge than sample 394_1_8. After consulting RMD, the manufacturer, about this, it transpired that the sensors we were given could come from different wafers. If so, their gain, doping profile, thickness, and pn-junction depth could differ as well. We were also informed that they could not provide any traceability information; leading to the conclusion that, in future irradiation campaigns, it would be crucial to test absolutely all devices before irradiation.

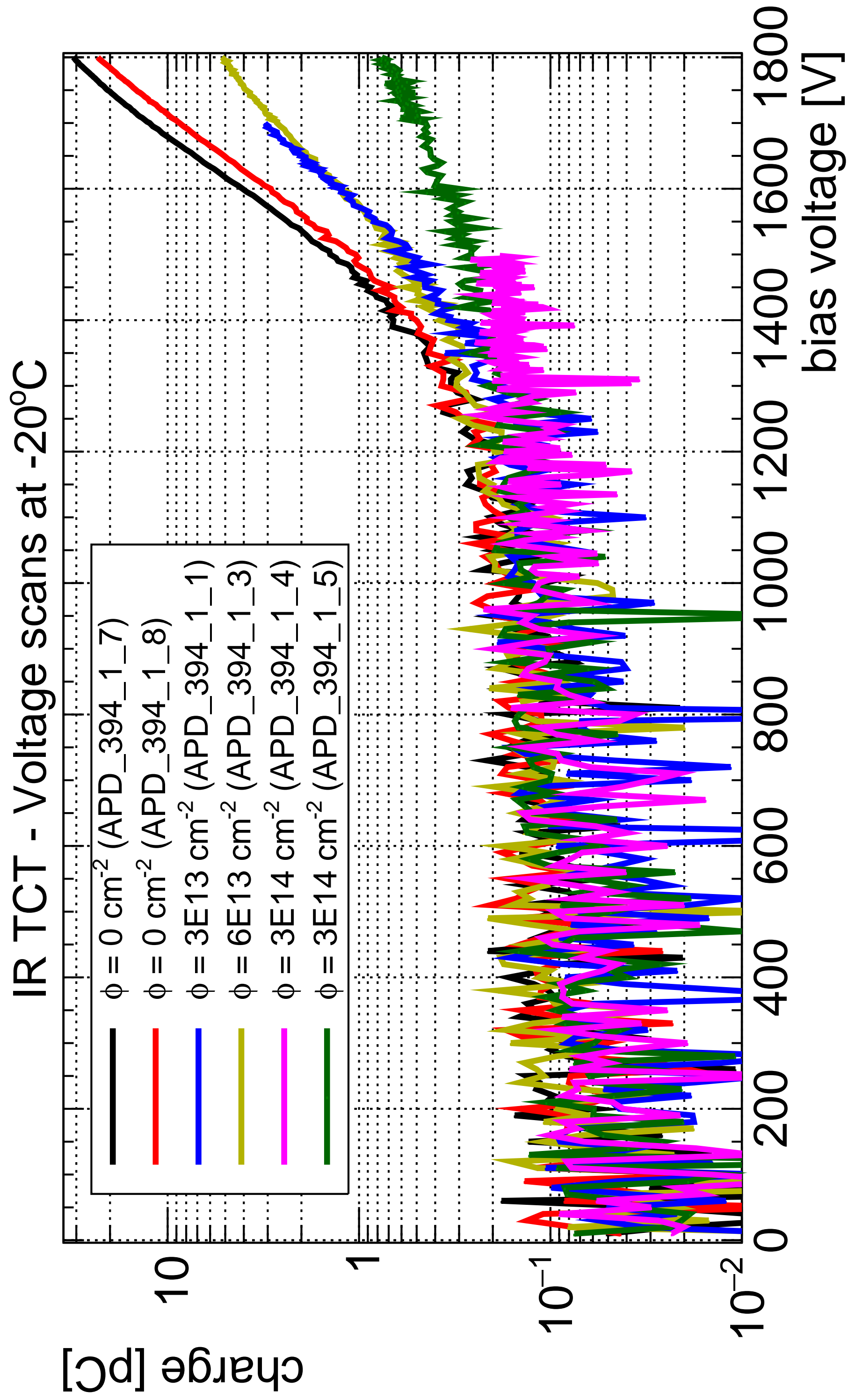

Figure 8.7: IR TCT voltage scans of all 2×2-mm^2 DD-APDs from the first set, with the omission of sample 394_1_6 ($\phi = 1 \times 10^{15}$ n_{eq}/cm^2) as it could only be biased up to 600 V. All scans were done at -20°C.

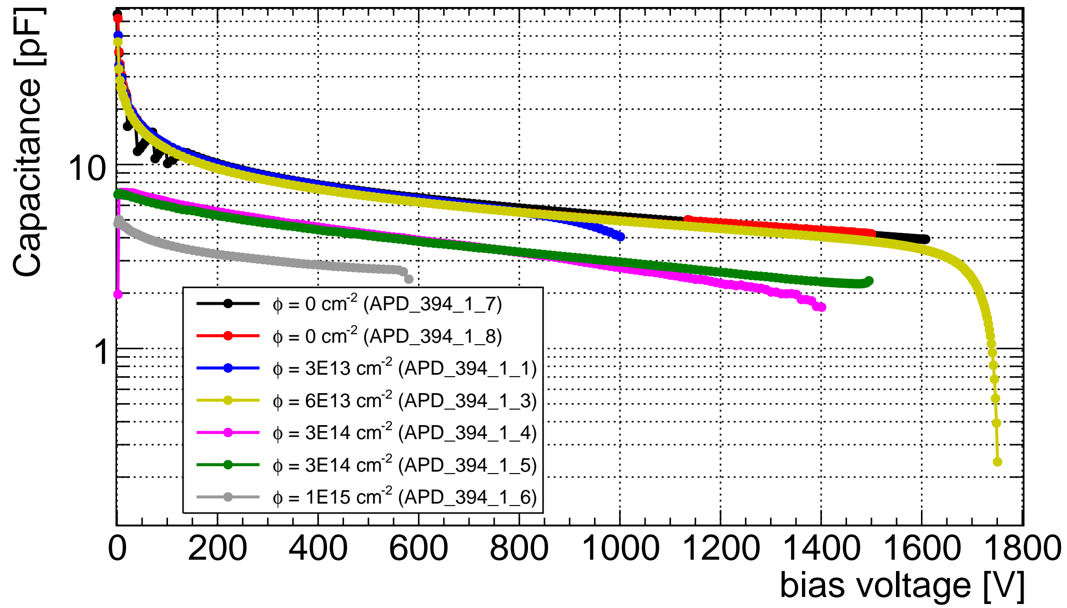

Figure 8.8: Capacitance with respect to voltage for all 2×2-mm^2 DD-APDs from the first set.

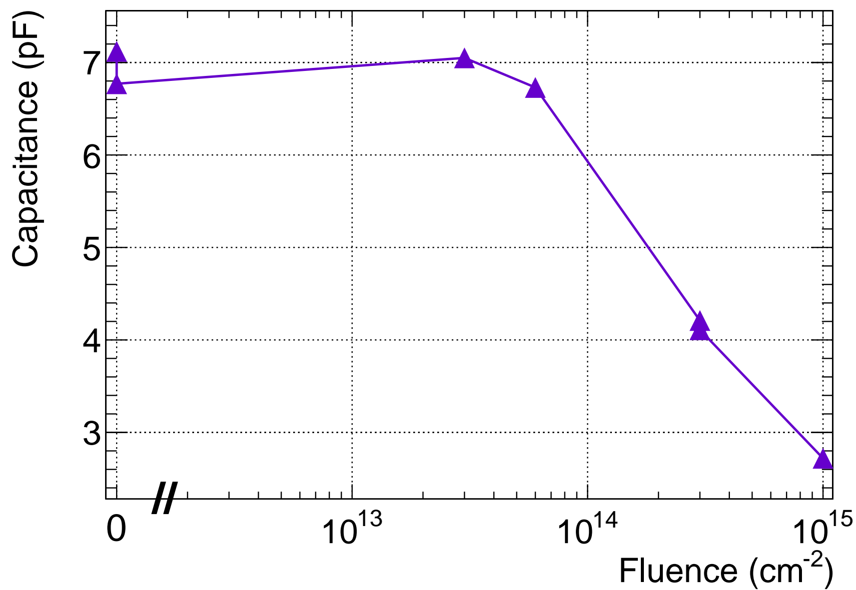

Figure 8.9: Capacitance at 500 V with respect to fluence. Measurements done at -20°C and 1 kHz.

8.1.3 Capacitance

The characterisation of these devices included obtaining their CV curves, plus analysing the dependence of capacitance with fluence. The CV measurements were carried out at -20°C, at a frequency of 1 kHz, and applying back (n-side) biasing. The full CV curves and the capacitance at 500 V with respect to fluence are shown in Figures 8.8 and 8.9. There is a clear decrease in capacitance with increasing irradiation. Since capacitance is inversely proportional to depletion width (see Equation 2.6), the lower the capacitance the longer the depletion width, assuming a constant active area. These results have the same tendency as those obtained through TCAD simulations of the same devices by R. Dalal from the University of Dehli [108]. Having said that, the results obtained through TCT surface scans show a reduction in the active area of the devices with fluence, which would also lead to a decrease in capacitance. Basically, the decrease in capacitance with irradiation could be due to a combination of both a decrease in active area, and an increase in depletion width.

8.1.4 Leakage current

To fully characterise the devices, IV measurements were performed on all sensors at -20°C, and with n-side biasing. The curves can be found in Figure 8.10. Generally speaking, leakage current is seen to increase with fluence. At a fluence of 1×10^{15} n_{eq}/cm^2 (sample 394_1_6) the device had an abrupt increase in leakage current at 590 V, making it impossible to operate. Analogously to the results presented in the previous sections, differences in behaviour were observed between devices that, in principle, should have behaved similarly. Once again, both unirradiated samples behave differently. Not only is the overall leakage current higher in sample 394_1_7, but the breakdown voltage is higher too. As for the pair irradiated up to 3×10^{14} n_{eq}/cm^2, sample 394_1_4 has a higher leakage current and lower breakdown voltage than its counterpart, sample 394_1_5.

The leakage current was the last property to be measured on these devices. It is thus interesting to see how some of the sensors changed behaviour with respect to the first measurements carried out (TCT). In particular, samples 394_1_8 (unirradiated), and 394_1_1 (3×10^{13} n_{eq}/cm^2) could, at the beginning, be taken up to 1800 V, by the end of the measurement campaign they could only be biased up to 1610 V and 1050 V, respectively. It is thought that these changes in breakdown voltage may be attributable to humidity. This implies that besides controlling the humidity levels during measurements, which is already done, the samples should be kept for a certain amount of time in a dry box before being measured. This may prove complicated in the case of irradiated samples, as they are stored in freezers to avoid annealing, and the amount of time they are kept at room temperature is kept to the minimum.

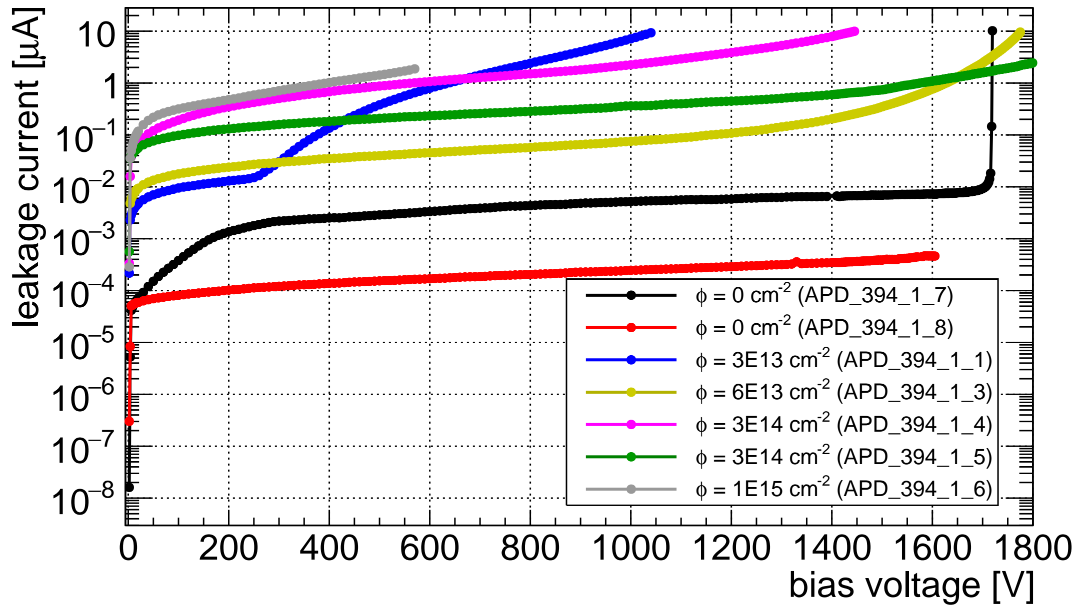

Figure 8.10: Leakage current for all 2×2-mm^2 DD-APDs from the first set. Measurements done at -20°C.

As regards the contributions to the leakage current, before irradiation, at voltages below 1600 V the leakage current is barely affected by multiplication. After irradiation, the voltage at which the leakage current is influenced by multiplication decreases, being around 1200 V for a fluence of 6E13. The explanation for this could be that the main contribution to the current is surface generation. As a consequence, the bulk current (which is affected by multiplication) only becomes dominant when the gain is high enough. After irradiation, defects increase the bulk generation current, hence its amplification due to internal multiplication becomes noticeable at a lower voltage. This hypothesis is also supported by the results found by fitting the curves up to 800 V following the relation $I \propto V^n$. For bulk generation current it is expected that $n = 0.5$ (see Equation 3.21). However, even before irradiation, the relation between current and voltage was far from $I \propto \sqrt{V}$. In fact, the only sample that could be accurately parameterised by $I \propto \sqrt{V}$ was 394_1_1 up to 200 V, at higher voltages the increase in leakage is much steeper (as seen in Figure 8.10).

A study of the fluence dependence of leakage current at -20°C was performed. The objective was to verify if in DD-APDs the increase in leakage current is proportional to the fluence, as described by Equation 3.20. In order to do this, the leakage current for a specific bias voltage had to be determined. The voltage chosen in this instance was 200 V, given that at such a low voltage there is no multiplication that could affect the level of leakage current ($I(200\text{ V})$). Also, Equation 3.20 describes the relation between fluence and the difference between leakage currents measured before and after irradiation. Nevertheless, before irradiation $I(200\text{ V})$ is below 0.1-1 nA, and after it is between 20 to 480 nA. Hence, the before-irradiation current was considered to be negligible and not

taken into account. The leakage current values at 200 V were plotted with respect to the fluence, and fitted with a linear function, forcing the intercept to the origin. For comparison, the expected curve at -20°C for a PiN diode with the same active volume as an unirradiated DD-APD (6×10^{-4} cm^3), and the same annealing state was plotted, see Fig 8.11. From the fit to the data, it was possible to calculate the *current related damage rate* (α), i.e. the proportionality constant between current and fluence. The value obtained is an estimation, as for α to be extracted the active volume of the device must be known. Normally, devices are fully depleted and thus their active volume is constant, as long as the leakage current is measured above full depletion. DD-APDs are never fully depleted, and as seen in Sections 8.1.1 and 8.1.3, their active volume changes with fluence. This issue was not considered when estimating α from the experimental data, and the active volume was considered to be constant and equal to that expected before irradiation. To plot the curve expected from an equivalent PiN diode, its current related damage rate was calculated. Both this theoretical value and the experimental one estimated for DD-APDs, appear in Table 8.2. It should be noted that, since the devices did not undergo an annealing step, but due to their handling they were kept at room temperature some times, their annealing was estimated to be 60 min at 21°C.

Table 8.2: *Current related damage rates* (α), after 60 min at 21°C, obtained from the experimental data at 200 V, and calculated for a PiN diode with active volume 6×10^{-4} cm^3.

	DD-APDs	Equivalent PiN diode
α [A/cm]	8.22×10^{-19}	11.8×10^{-19}

Finally, the temperature dependence of the leakage current was analysed for one of the irradiated devices. Previously, it was mentioned that IV measurements point in the direction of surface generation current being dominant at lower voltages. In any case, as explained in Chapter 3, the same temperature dependence is expected for either surface or bulk generation current. By obtaining the IV curves of a given sample at different temperatures, and then plotting the current at a precise voltage with respect to temperature, Equation 3.25 can be used to fit the data, and the effective energy can be extracted.

Here, the temperature dependence of the leakage current of sample 394_1_5, irradiated up to 3×10^{14} $\mathrm{n_{eq}/cm^2}$, was analysed. IV curves were measured for sample 394_1_5 at 5 different temperatures (Fig 8.12a): 20°C, 10°C, 0°C, -10°C, and -20°C. Once again, the current at 200 V was the one used for this test, in order to exclude multiplication effects. Figure 8.12b shows $I(200\text{ V})$ with respect to $1/kT$, together with a fit of the data to Equation 3.25. The effective energy value obtained experimentally for sample 394_1_5 is (1.221 ± 0.008) eV, which is in agreement with the expected value.

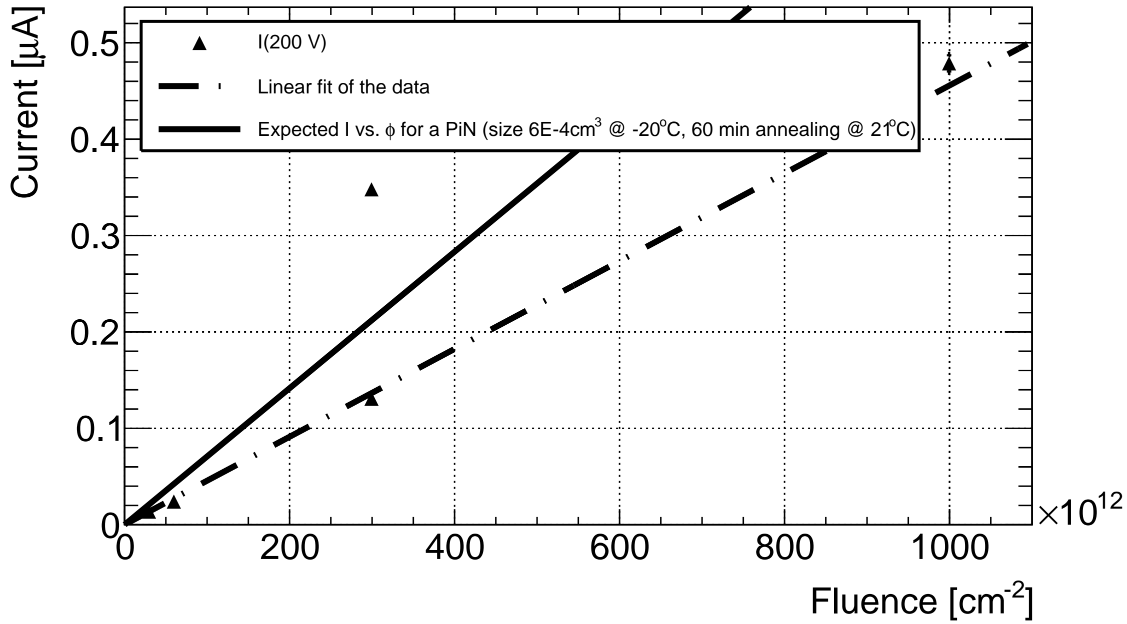

(a)

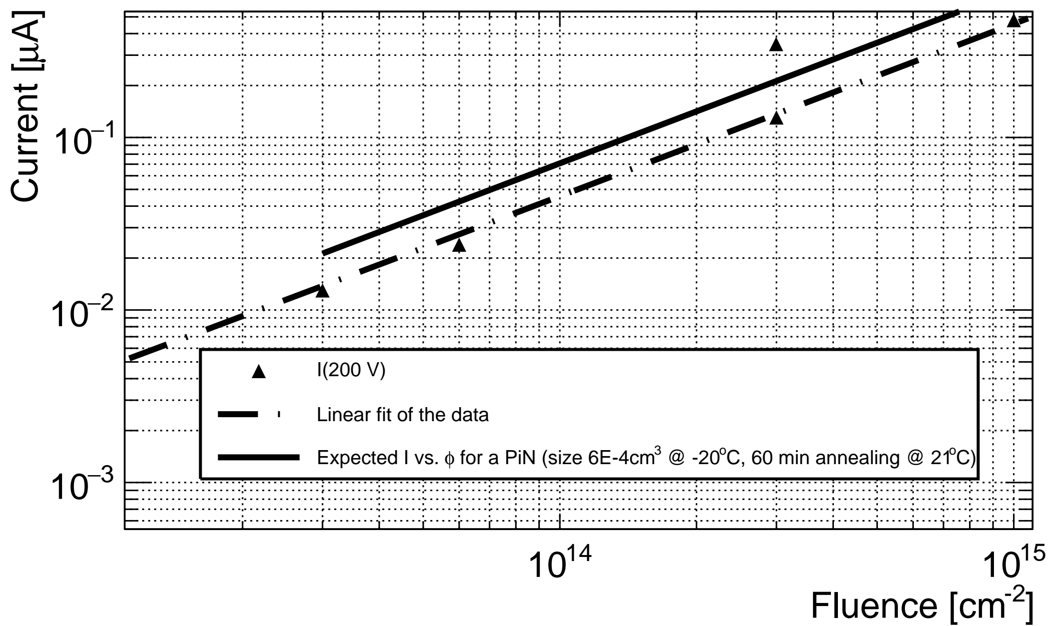

(b)

Figure 8.11: Leakage current at 200 V (where no multiplication is expected) and -20°C with respect to fluence. (a) In linear scale, (b) in logarithmic scale. The data were fitted with Equation 3.20. The expected dependency for a PiN diode under the same conditions, with the same active volume, and annealing history was plotted.

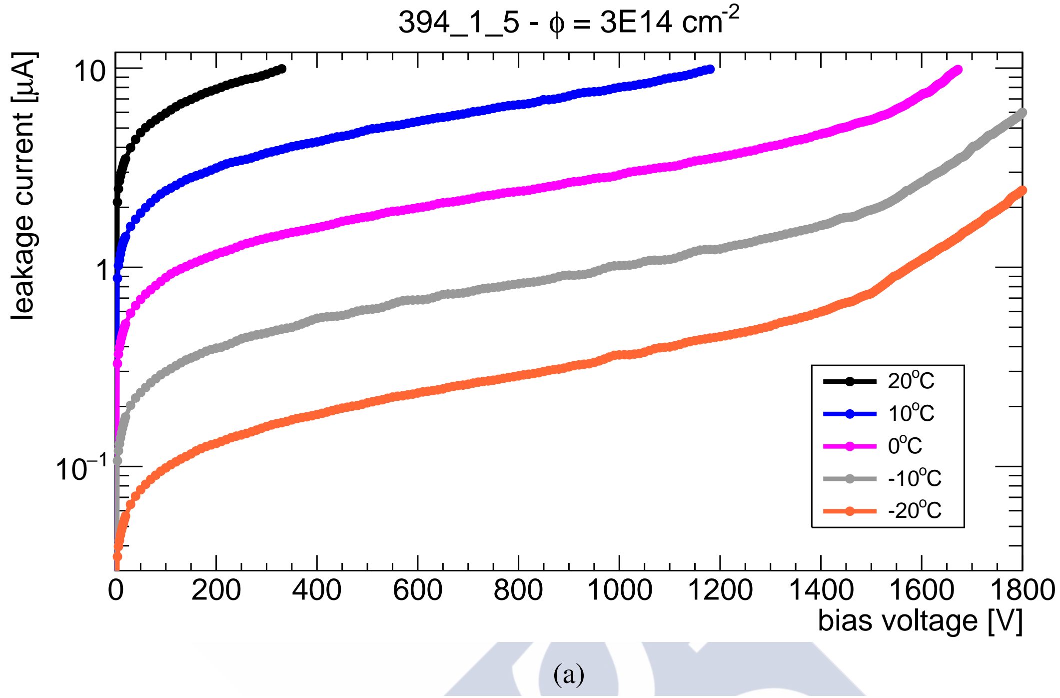

(a)

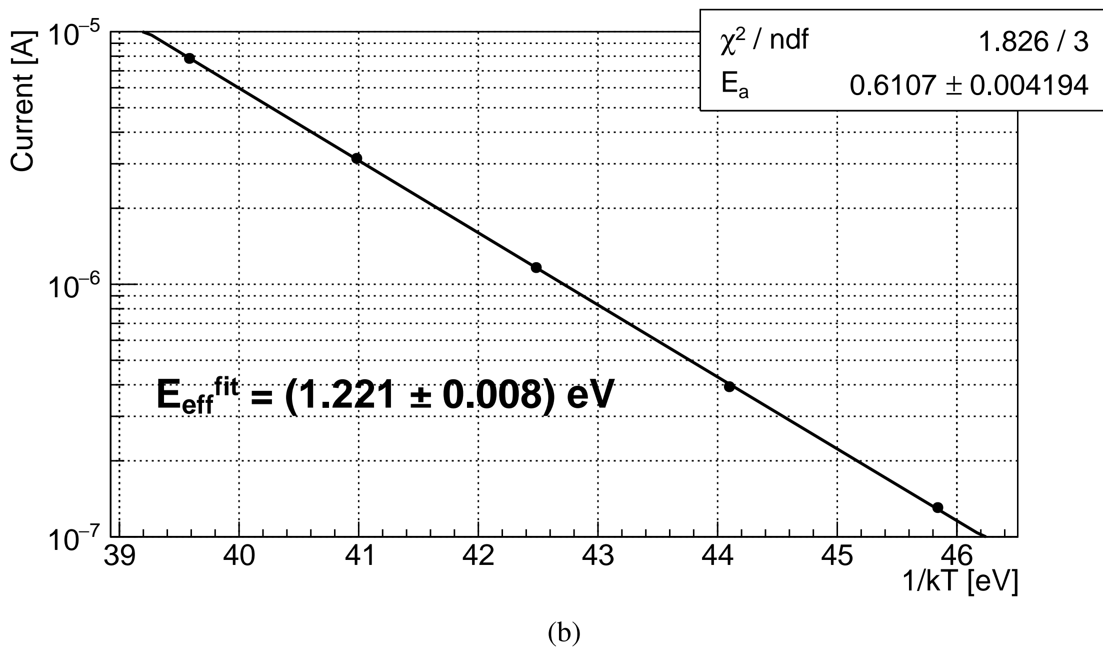

(b)

Figure 8.12: (a) Leakage current with respect to voltage for sample 394_1_5 at five different temperatures (20, 10, 0, -10, and -20°C). (b) Leakage current from sample 394_1_5 at 200 V with respect to $1/kT$, and a fit to the data using Equation 3.25.

8.2 Second Set of 2×2-mm^2 DD-APDs

One of the main conclusions reached after the study of the first set of 2×2-mm^2 DD-APDs was that all DD-APDs must be fully characterised before irradiation. This was a direct consequence of the samples possibly coming from different wafers with different gain, doping profile, thickness, and pn-junction depth. Since this was not known when working on the first set, the results were inconclusive. This is why a new set of 8 DD-APDs was requested to RMD, and all sensors were evaluated before starting the irradiation campaign. To have more conclusive results, all samples were irradiated in pairs, each pair being exposed to a different neutron fluence, see Table 8.3. The irradiation was carried out at the Jožef Stefan Institute in Ljubljana, Slovenia. No annealing steps were performed after irradiation. However, the final total annealing due to the handling of the samples, and the performance of measurements at different temperatures, was estimated to be of 73 min at 21°C. The tests performed on these new set of devices are the same as on the previous set.

Table 8.3: Irradiation details for all 2×2-mm^2 DD-APDs from the second set of sensors analysed.

Fluence [n_{eq}/cm^2]	Device name
3×10^{13}	APD_2B_1 APD_2B_3
6×10^{13}	APD_2B_5 APD_2B_11
3×10^{14}	APD_2B_4 APD_2B_6
1×10^{15}	APD_2B_7 APD_2B_9

8.2.1 Homogeneity analysis

Charge collection maps were obtained for each and every sample before irradiation, and for all that could be biased after irradiation. In the same way as with the previous set, the scans were done with both the red and the IR laser, at 1700 V (n-side bias), and at -20°C. Figures 8.13 to 8.20 show all the surface scans obtained before and after irradiation. Before irradiation all DD-APDs present a fairly similar behaviour, although the gain varies slightly from sensor to sensor. In particular, sample APD_2B_7 had a much lower gain. The mean charge collection was calculated for all devices (without computing the central high charge ring). The average of the mean charge collection for all samples, barring APD_2B_7, was of (20 ± 2) a.u. for IR-TCT, and (9 ± 2) a.u. for Red-TCT. In contrast, sample APD_2B_7 had a mean charge collection of (10 ± 2) a.u. for IR-TCT, and (3.7 ± 0.6) a.u. for Red-TCT. As expected, this same behaviour was observed during voltage scans, which will be discussed in Section 8.2.2. This could be merely due to the detector having a lower charge collection than the other devices, however, certain parameters were analysed to verify if there was another explanation. What was found was that, whilst the other samples had a leakage current lower than 0.7×10^{-3} μA at 1700 V, sample APD_2B_7 had a much higher leakage current. When the high voltage power supply was providing 1700 V, the leakage current in sample APD_2B_7 was of 0.8 μA during the IR TCT scans, and of 6.7 μA during the red-front TCT scans[3]. Since the biasing circuitry has resistors, amounting to a resistance of 13 MΩ, those levels of leakage current imply that, whilst the voltage provided by the power supply was of 1700 V, the actual voltage applied to the DD-APD was of 1690 V, during IR TCT, and 1613 V, during red-front TCT. At said voltages, the average charge collection observed in the other devices was of (16 ± 2) a.u. for IR TCT, and (6 ± 1) a.u. for red TCT. These values are closer to those found in sample APD_2B_7. Nevertheless, it is apparent that, even after taking into consideration the particularly high leakage current, sample APD_2B_7 is the sensor with the lowest charge collection of all analysed. Further information about the charge collection values of each sensor can be found in Section 8.2.2, and details about the voltage corrections necessary due to the bias circuit can be found in Appendix D.

A final comment regarding the before-irradiation scans should be made, a small region of extremely low charge collection was observed on sample APD_2B_6 for both IR and Red-TCT (see Figure 8.17). After visual examination with a microscope, a dent was found on the surface of the device in the exact spot were the charge collection is unusually low, thus clarifying this phenomenon.

[3] It should be clarified that this difference in leakage current between illuminations is in no way related to a change in circuitry nor temperature, it seems to be a difference in the sensor itself, as the red-front scans were performed some days after the IR scans.

After the first level of irradiation, i.e. 3×10^{13} n_{eq}/cm^2, the main variation observed was the decrease in charge collection (see Figures 8.13 and 8.14). Identically to what was seen in the first set of DD-APDs, at a fluence of 6×10^{13} n_{eq}/cm^2 (Figures 8.15 and 8.16) red-TCT XY scans present a central circular region where the charge collected is almost twice of that collected in the surrounding area. As for the IR-TCT scans, the charge collected decreased as well as the active area, particularly for sample APD_2B_11.

The irradiation up to 3×10^{14} n_{eq}/cm^2 resulted in one of the sensors, APD_2B_6, reaching a leakage current higher than 1.5 mA at only 7 V. Naturally, no measurements were done on said device after irradiation. On the other hand, the other sample irradiated up to this same fluence (APD_2B_4) could be tested, the results are shown in Figure 8.18. For both illuminations it was found that the charge collection decreased significantly, and that the active area was severely affected.

Finally, after irradiation up to 1×10^{15} n_{eq}/cm^2 the electrical behaviour of both DD-APDs exposed to this fluence was extremely different, although effectively the result is the same: little to no signal is detected, and with no multiplication. Therefore, neither of the devices (APD_2B_7 or APD_2B_9) is functional. Sample APD_2B_7 could not be biased beyond 480 V, as the leakage current of the sensor reached compliance (10 μA). Based on the studies performed on the first set of DD-APDs received, it was expected that the devices irradiated up to 1×10^{15} n_{eq}/cm^2 would be rendered non-operational. That is why this sample, with an odd leakage current behaviour before irradiation, was chosen to be exposed to such a level of irradiation. To ensure electrical stability, surface scans on sample APD_2B_7 were performed at 450 V. At such a voltage, no impact ionisation is expected in this type of device. As a result, little to no charge collection was found with IR-TCT, whilst with Red-TCT no charge collection was detected. Although sample APD_2B_9 could be biased up to 1700 V, the charge collection for both illuminations was extremely deteriorated. At the same time, the active area was seriously reduced, covering only a small fraction of the initial 2×2 mm^2. To all intents and purposes, at 1×10^{15} n_{eq}/cm^2 the damage to DD-APDs, as currently designed, is fatal.

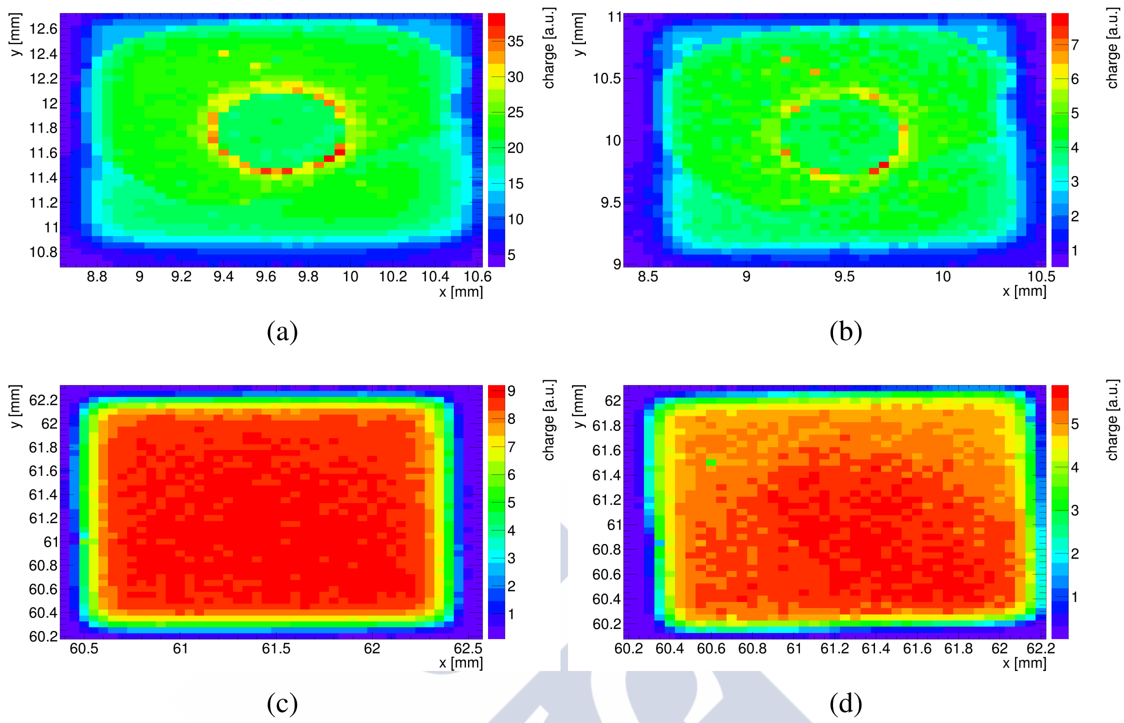

Figure 8.13: (Top) IR and (bottom) red-front TCT surface scans at -20°C and 1700 V on sample APD_2B_1 (left) before, and (right) after irradiation up to 3×10^{13} n_{eq}/cm^2.

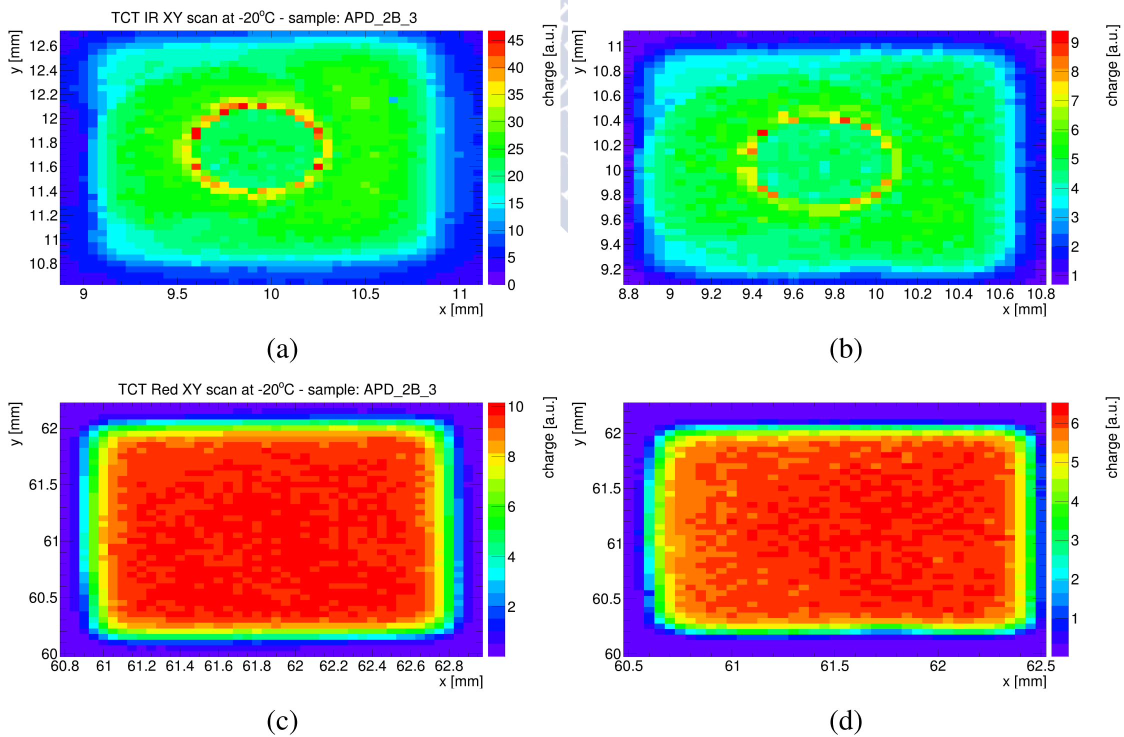

Figure 8.14: (Top) IR and (bottom) red-front TCT surface scans at -20°C and 1700 V on sample APD_2B_3 (left) before, and (right) after irradiation up to 3×10^{13} n_{eq}/cm^2.

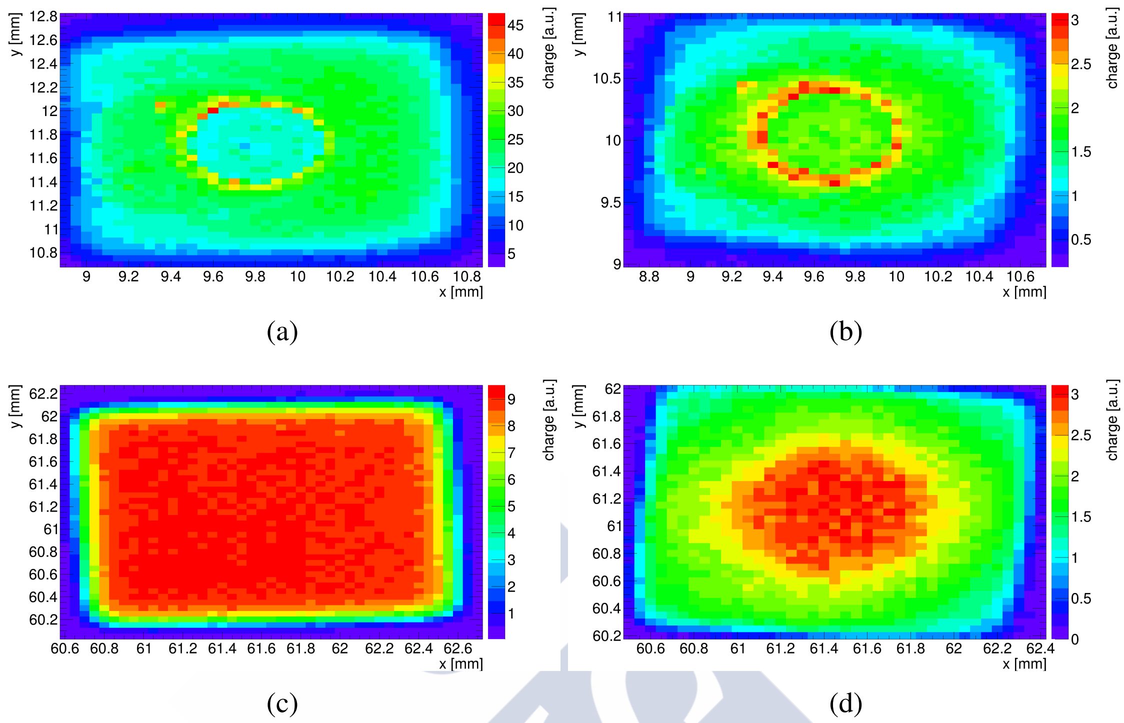

Figure 8.15: (Top) IR and (bottom) red-front TCT surface scans at -20°C and 1700 V on sample APD_2B_5 (left) before, and (right) after irradiation up to 6×10^{13} $\mathrm{n_{eq}/cm^2}$.

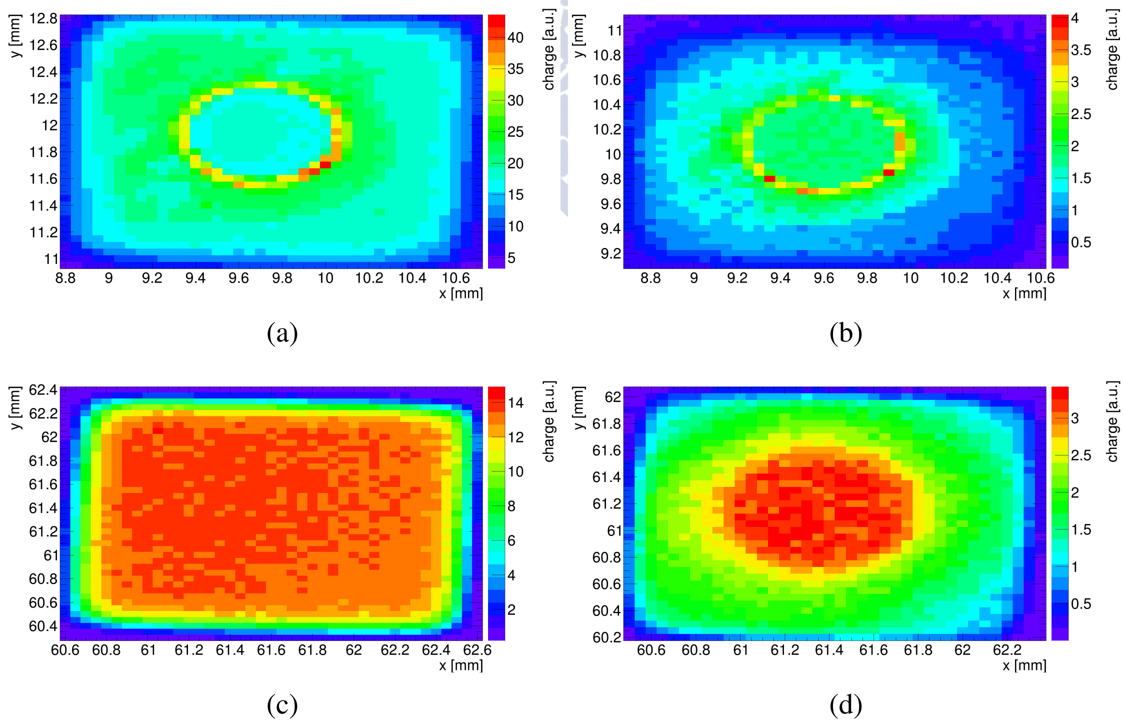

Figure 8.16: (Top) IR and (bottom) red-front TCT surface scans at -20°C and 1700 V on sample APD_2B_11 (left) before, and (right) after irradiation up to 6×10^{13} $\mathrm{n_{eq}/cm^2}$.

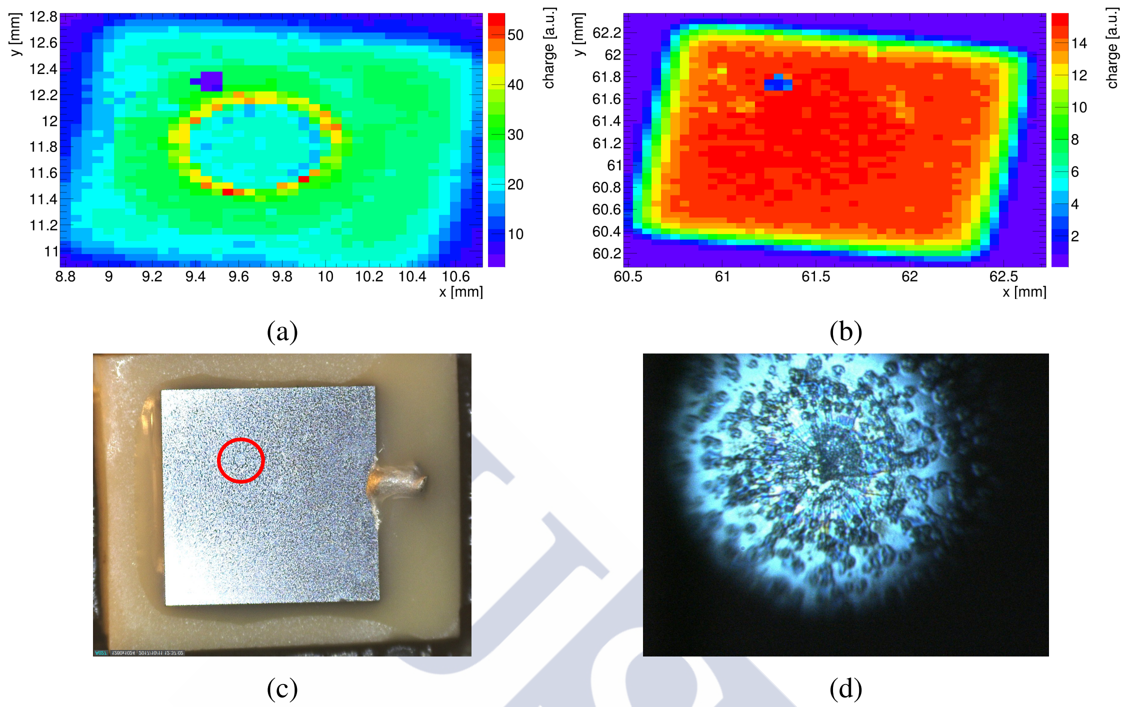

Figure 8.17: (a) IR and (b) red-front TCT surface scans at -20°C and 1700 V on sample APD_2B_6 before irradiation. (c) Frontal view of the sample. Circled in red a dent, see detail in (d). This coincides with the low-charge areas of the XY scans.

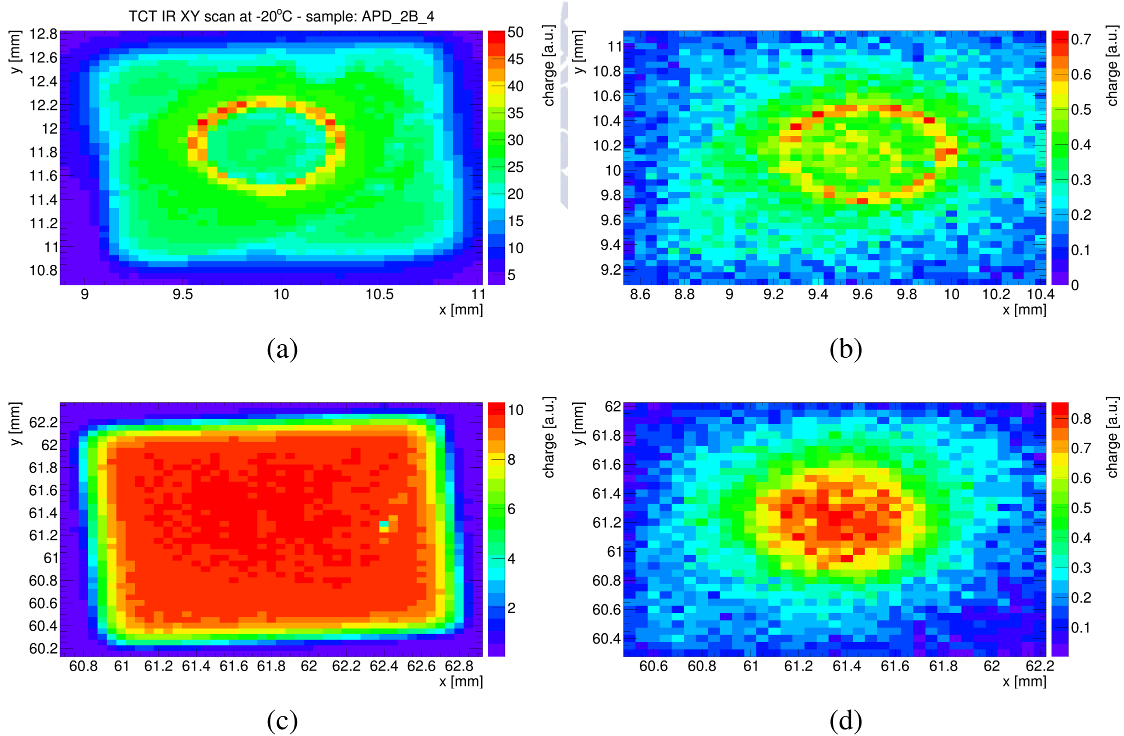

Figure 8.18: (Top) IR and (bottom) red-front TCT surface scans at -20°C and 1700 V on sample APD_2B_4 (left) before, and (right) after irradiation up to 3×10^{14} n_{eq}/cm^2.

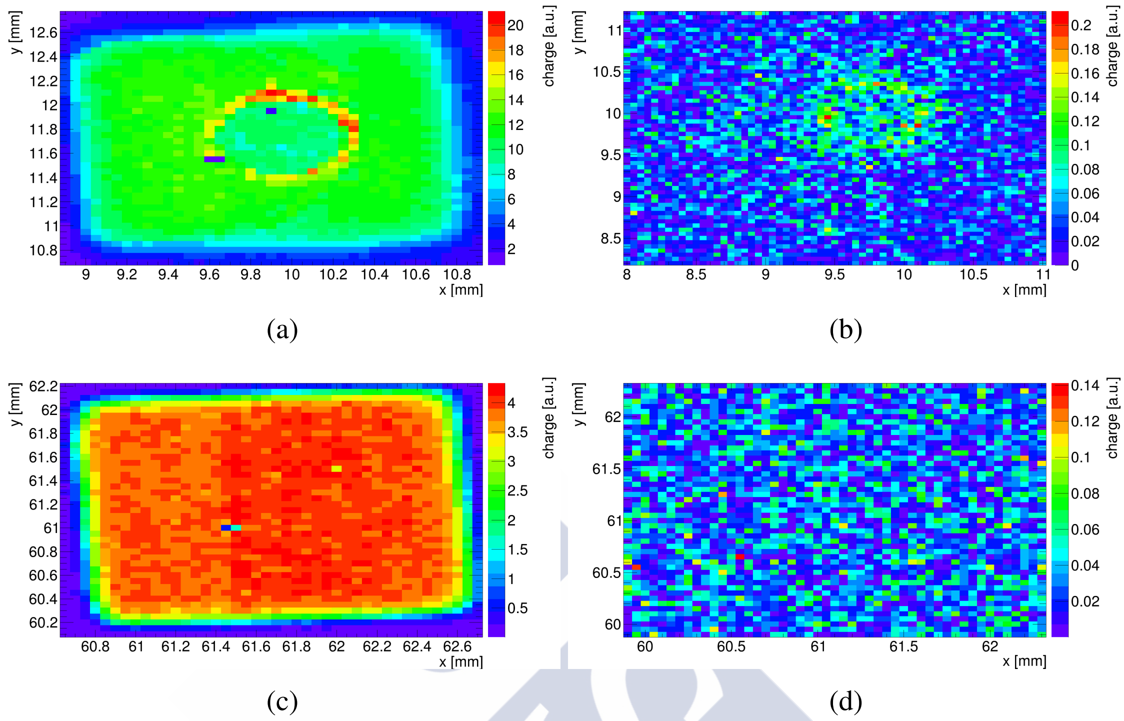

Figure 8.19: (Top) IR and (bottom) red-front TCT surface scans at -20°C on sample APD_2B_7 (left) at 1700 V before irradiation, and (right) at 450 V after irradiation up to 1×10^{15} n_{eq}/cm^2.

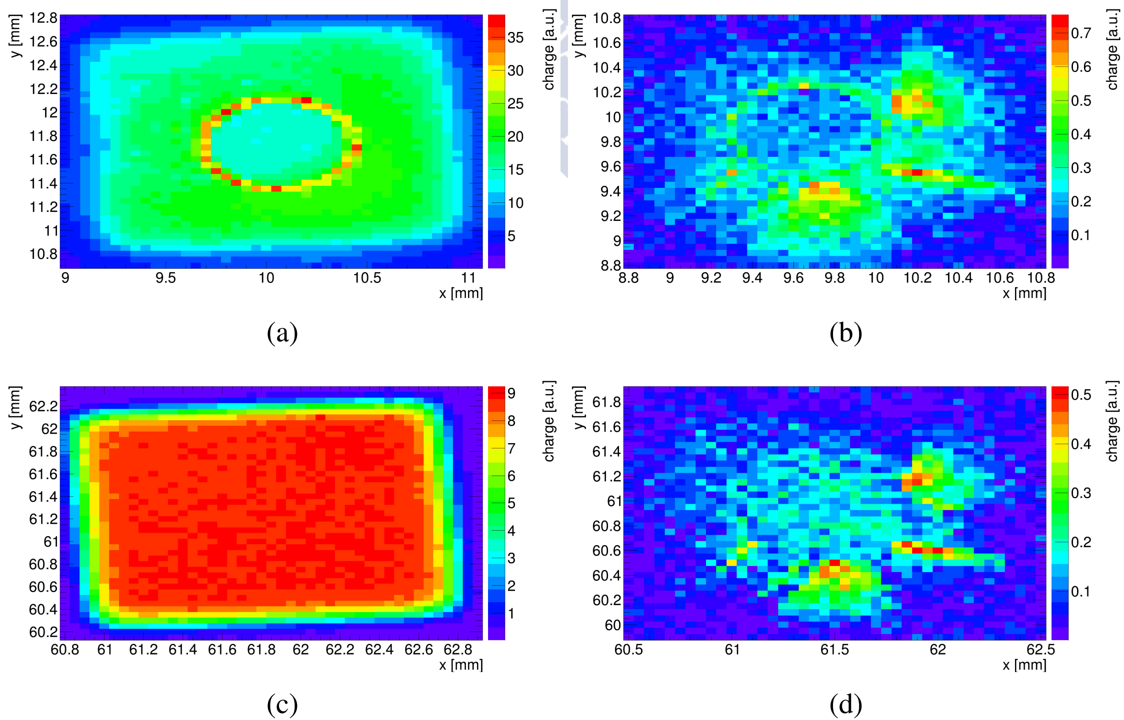

Figure 8.20: (Top) IR and (bottom) red-front TCT surface scans at -20°C and 1700 V on sample APD_2B_9 (left) before, and (right) after irradiation up to 1×10^{15} n_{eq}/cm^2.

8.2.2 Charge collection with voltage

Because it was already known that the devices could present different gain values depending on the wafer they came from, TCT voltage scans were performed on all devices before irradiation. These scans were later repeated after irradiation to observe the changes in charge collection caused by the irradiation. The voltage scans were performed at -20°C, and with both IR and red-front illumination. As regards the biasing, the voltage applied by the power supply went up to 1800 V. However, even before irradiation (mainly at voltages above 1740 V), all samples had such leakage current values that, due to the resistors in series with the DUT, the final voltage applied to the sensor was significantly lower than that provided by the power supply, with differences of up to 127 V. This was corrected during the data analysis by taking into consideration the leakage current associated to each data point, as well as the total resistance of the biasing circuit. The final results obtained are presented in Figures 8.21 and 8.22. For a detailed explanation of the correction method used see Appendix D. It should also be noted that, after irradiation, samples APD_2B_6 and APD_2B_7 were not measured due to their low breakdown voltage.

Before irradiation all sensors behave similarly, at least up to 1700 V, although the scale used conceals some differences. For more clarity, Figure 8.23 shows the charge collection curves between 1400 V and 1700 V. In these plots it is possible to see that not all sensors collect the same amount of charge. However, the variations are not so dramatic that they might lead to faulty conclusions after irradiation. At higher voltages these differences continue, yet, the most discordant is sample APD_2B_7, which has a lower charge collection than all other samples. In fact, the higher induction of charge occurring in the rest of the samples causes a phenomenon called *plasma effect* [109]. Put simply, because of the high gain, the charge carrier density is so high that a plasma of electrons and holes is created. The external layers of said plasma shield the interior ones from the electric field in the sensor, and the drift of charge carriers is slowed down. In charge versus voltage curves this is seen as a plateau towards the end of the scan, see Figure 8.24. The details regarding this effect, how it was detected, and its causes and consequences, can be found in Appendix D.

After irradiation, charge collection decreases with fluence. In fact, at a fluence of 1×10^{15} n_{eq}/cm^2 the charge collected is almost negligible in comparison to that before irradiation. As with the previous set of DD-APDs, the after-irradiation curves were fitted with an exponential at voltages higher than 1500 V. By doing so, it is possible to estimate the bias voltage that would be required to recover the charge collection obtained at 1700 V before irradiation. These fits revealed that 1800 V would be needed after 3×10^{13} n_{eq}/cm^2, 1900 V after 6×10^{13} n_{eq}/cm^2, nearly 3000 V after 3×10^{14} n_{eq}/cm^2, and roughly 8000 V after 1×10^{15} n_{eq}/cm^2. Evidently, after a fluence of 3×10^{14} n_{eq}/cm^2, it is not viable to attain charge collection values similar to those obtained before irradiation.

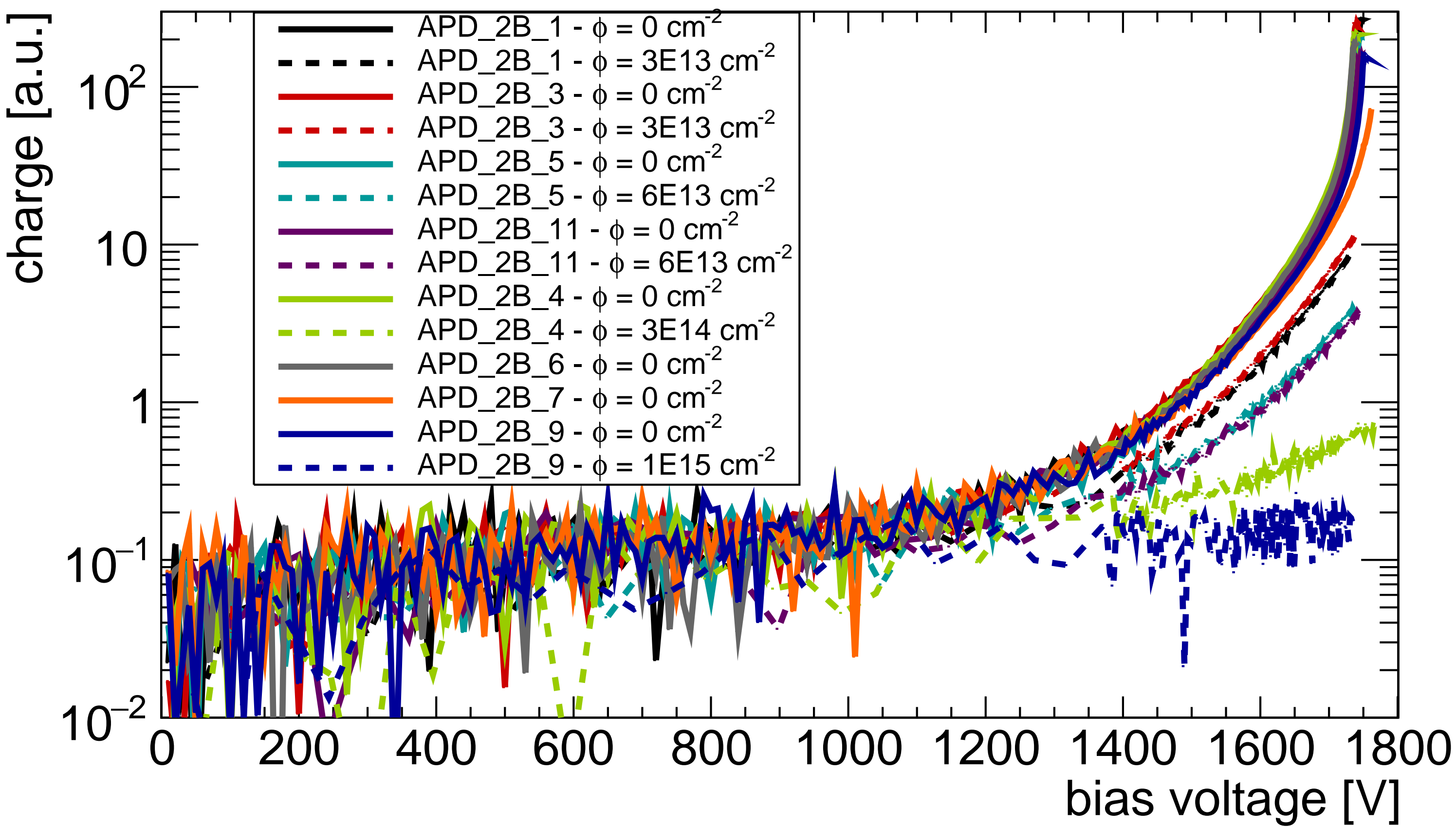

Figure 8.21: IR TCT voltage scans of all 2×2-mm^2 DD-APDs from the second set before and after irradiation. All scans were done at -20°C.

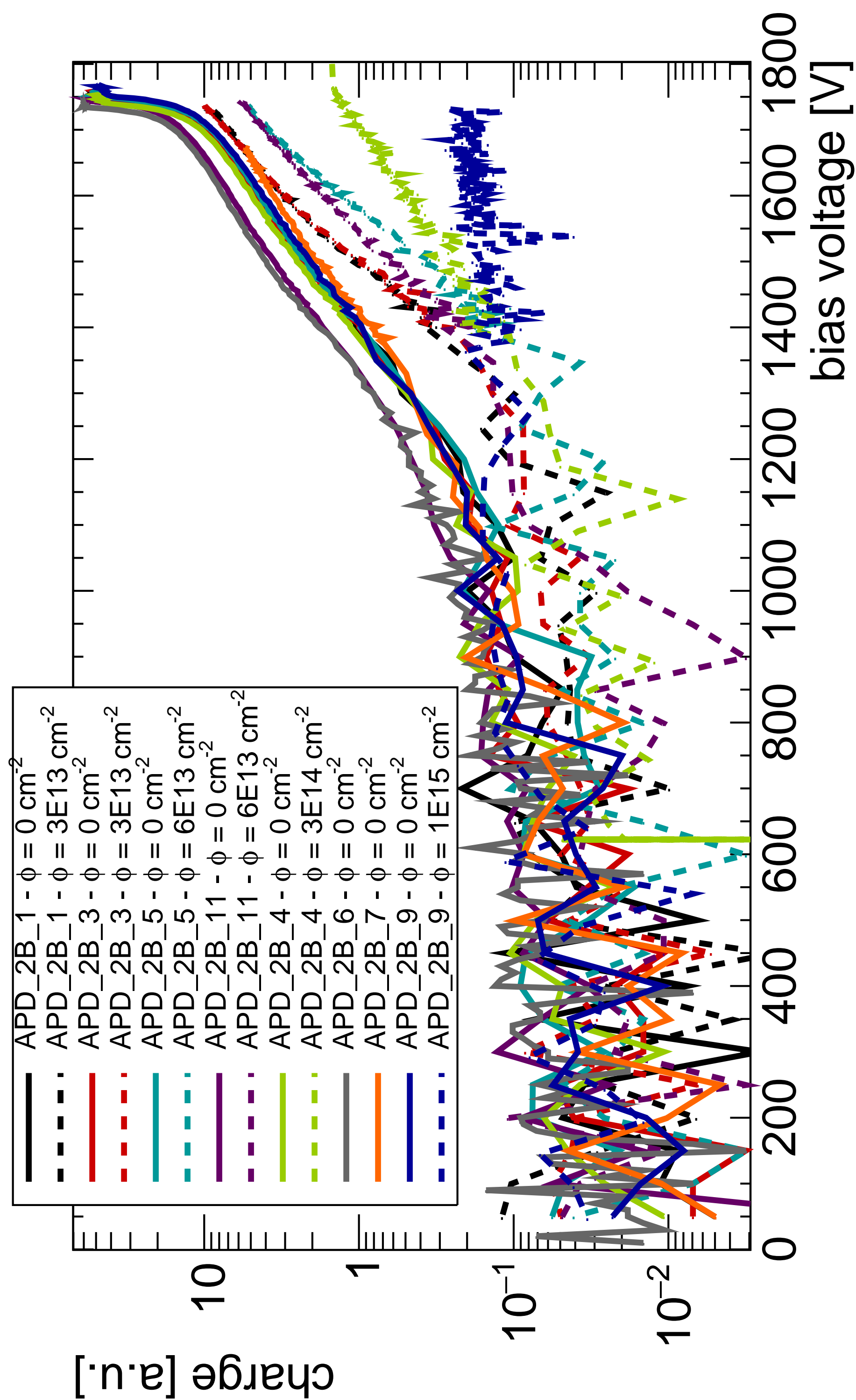

Figure 8.22: Red-front TCT voltage scans of all 2×2-mm^2 DD-APDs from the second set before and after irradiation. All scans were done at -20°C.

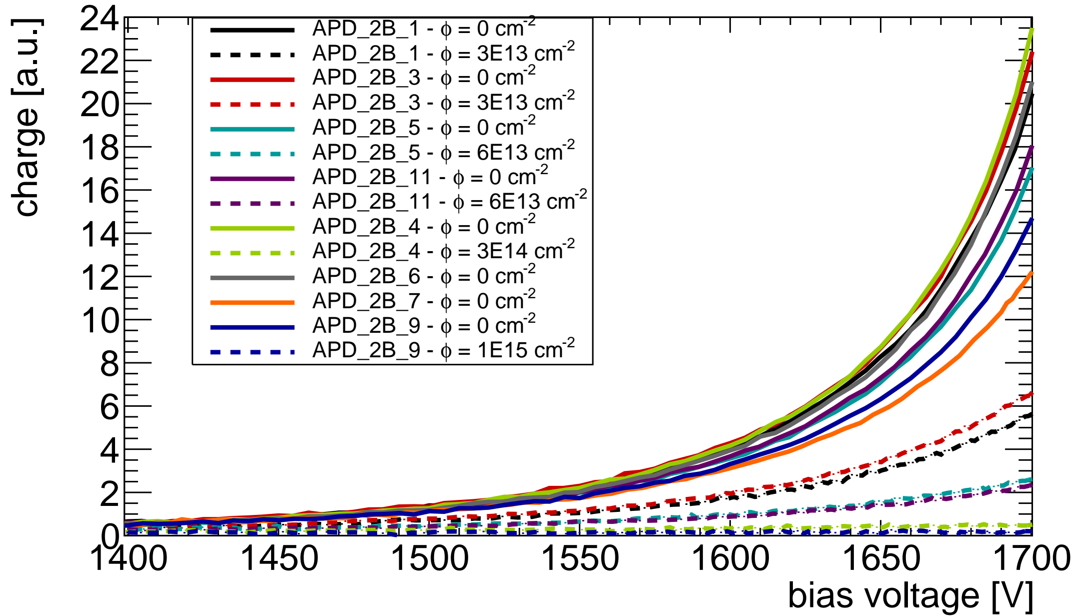

(a)

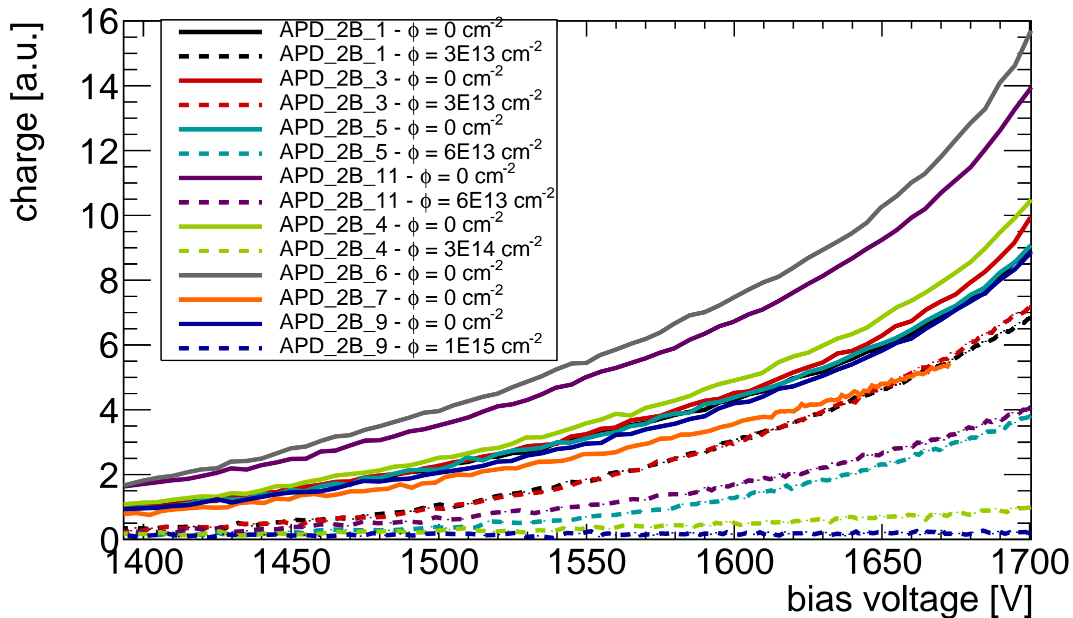

(b)

Figure 8.23: Detail at intermediate voltages of (a) IR TCT, and (b) red-front TCT voltage scans of all 2×2-mm^2 DD-APDs from the second set before and after irradiation. All scans were done at -20°C.

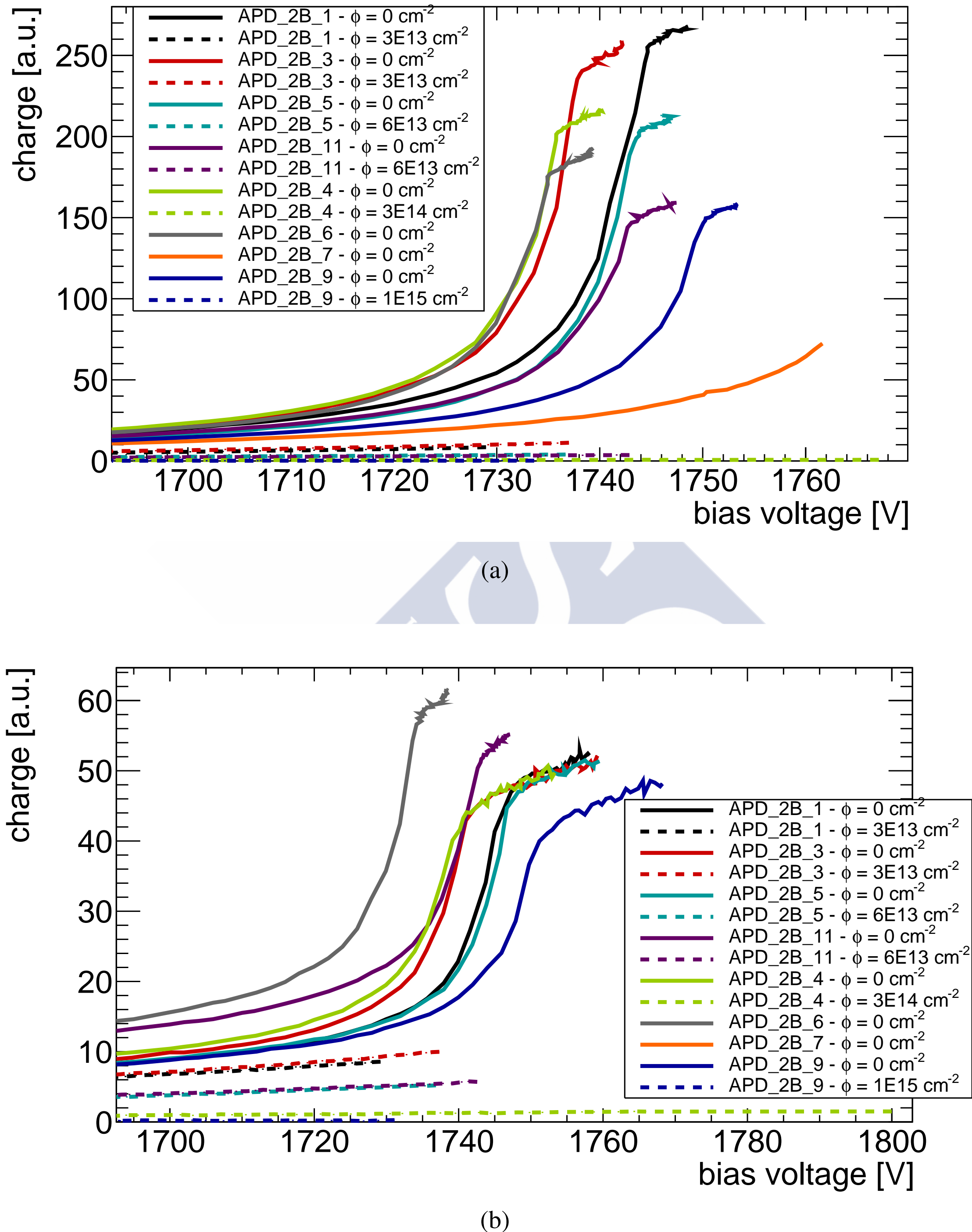

(a)

(b)

Figure 8.24: Detail at high voltages of (a) IR TCT, and (b) red-front TCT voltage scans of all 2×2-mm^2 DD-APDs from the second set before and after irradiation. All scans were done at -20°C.

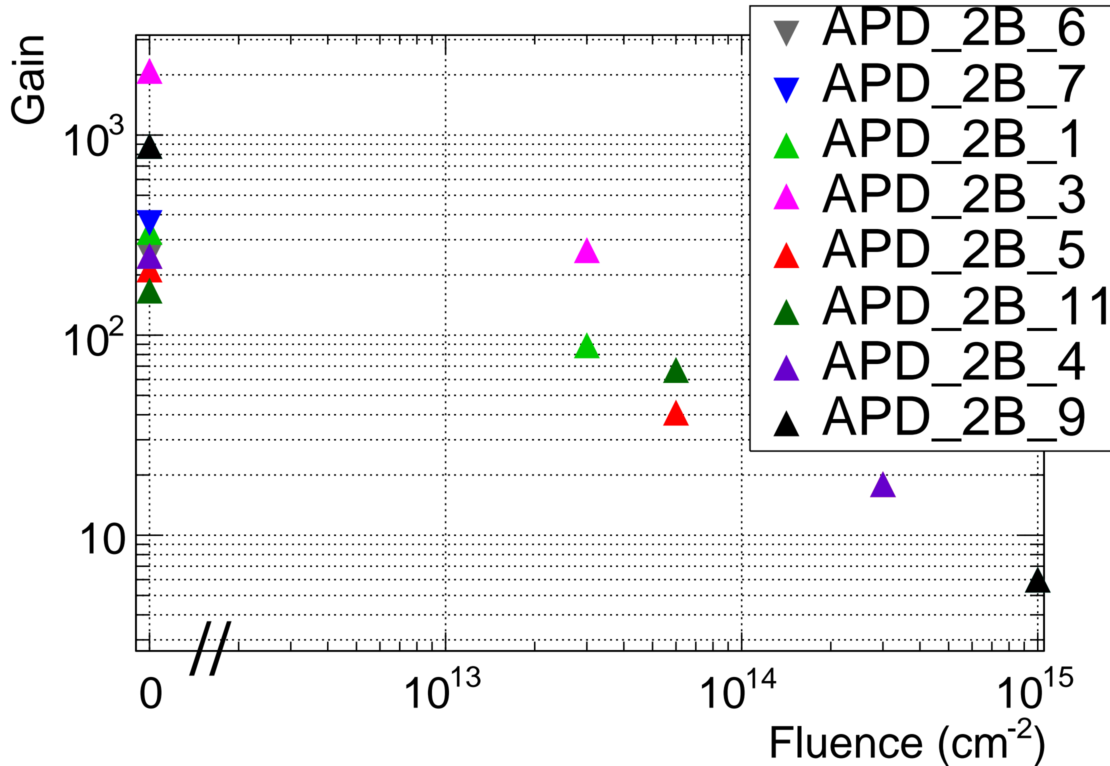

Figure 8.25: Gain as a function of fluence for 2×2-mm^2 DD-APDs from the second set before and after irradiation. The gain was calculated as the ratio between the charge at 1700 V and the charge at 200 V, where no impact ionisation is expected.

Finally, to have a more complete understanding of the workings of DD-APDs, the gain obtained through IR TCT at 1700 V was calculated for all devices, and it was analysed as a function of fluence. The gain was defined as the ratio between the collected charge of a given device at 1700 V, and its charge collection at 200 V, following [110]. The issue with this method is that at such low voltages, the fluctuations observed are of the same order of magnitude as the charge measured. This makes the comparison of gain values for different sensors at the same fluence rather complex. In fact, before irradiation, the two samples that present the highest gain are those with the lowest charge collection values at 200 V: less than 0.017 a.u.. On the contrary, the sample with the lowest gain before irradiation is that with the highest charge collection at 200 V: ~ 0.107 a.u.. All of these values can be found in Figure 8.25. Regardless of the approximative character of this method for the calculation of the gain, the results undoubtedly demonstrate that the gain of DD-APDs is gravely affected by radiation.

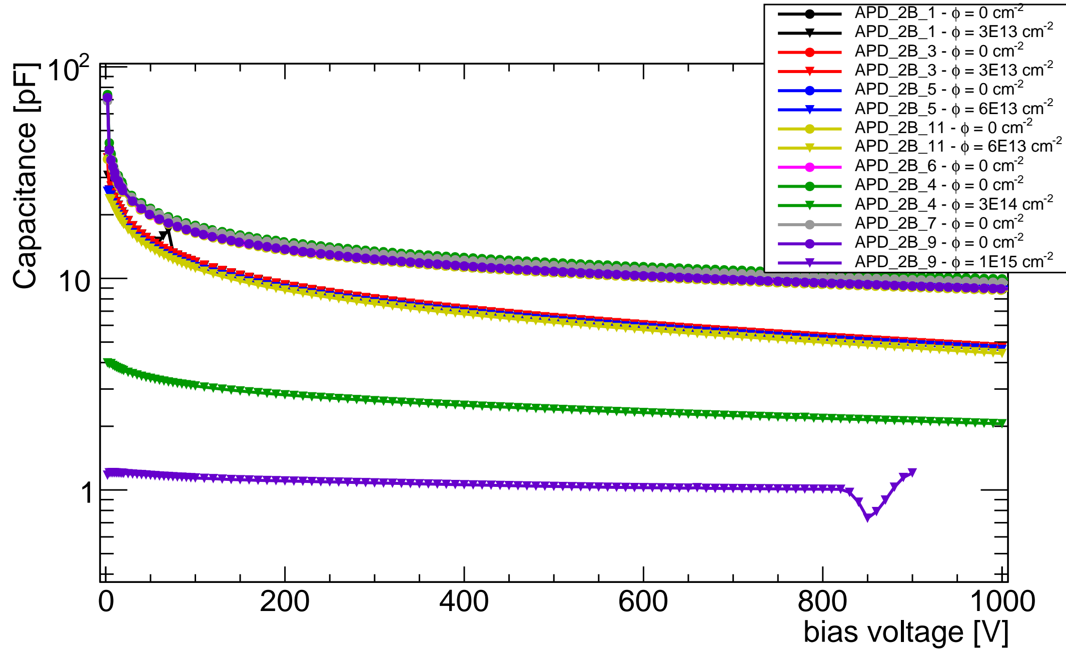

Figure 8.26: Capacitance with respect to voltage for all 2×2-mm^2 DD-APDs from the second set.

8.2.3 Capacitance

Part of the characterisation of DD-APDs consisted in the study of their capacitive behaviour before and after irradiation. Capacitance with respect to voltage curves were measured for all devices at -20°C, at a frequency of 10 kHz, and applying the biasing voltage to the n-side, see Figure 8.27. As with the first set of DD-APDs, the capacitance at 500 V was extracted from the full CV curves of all devices, and plotted as a function of fluence. The resulting plot, seen in Figure 8.28, shows that there is a substantial decrease in capacitance with irradiation. As explained in Section 8.1.3, this is equivalent to an increase in the depletion region width, which goes in the direction of the simulation results in [108]. At any rate, this decrease in capacitance could also originate from a reduction in the active area (see Equation 2.6). This would be consistent with the results obtained through TCT surface scans. In short, irradiation may be causing a decrease in active area, and an increase in depletion width, that would give rise to a decrease in capacitance.

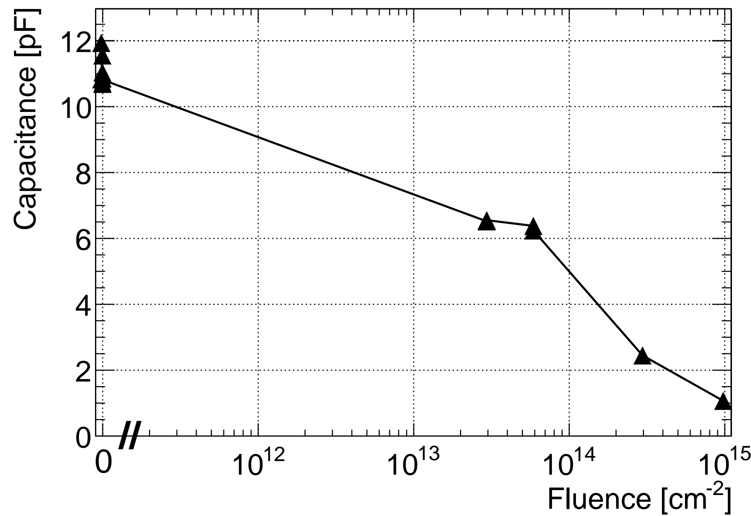

Figure 8.27: Capacitance at 500 V with respect to fluence. Measurements done at -20°C and 10 kHz.

8.2.4 Leakage current

IV curves were measured for all devices both before and after irradiation, see Figure 8.28. Before irradiation it was found that at voltages below 1600 V impact ionisation does not significantly affect the value of the current. In fact, up to 800 V, the curves can be parameterised with the relation $I \propto V^n$, with $n \sim 0.5$ for all devices. This proportionality relation is only valid for bulk generation current. A possible explanation to the lack of influence multiplication has, before irradiation, on the current at $V < 1600$ V is that the electric field is may not be high enough for the charge carriers to undergo impact ionisation. At voltages above 1600 V, the gain increases in such a way that the leakage current grows exponentially. After irradiation, the leakage current is higher, and at fluences of 3×10^{13} $\mathrm{n_{eq}/cm^2}$ and 6×10^{13} $\mathrm{n_{eq}/cm^2}$, multiplication has an influence on the current already at about 1400 V. Nevertheless, although the leakage current is higher with fluence, due to radiation-induced defects, the effective multiplication decreases. In fact, at fluences above 3×10^{14} $\mathrm{n_{eq}/cm^2}$, no exponential growth of the leakage current due to multiplication is observed. This is consistent with the charge collection curves obtained (Section 8.2.2), where it was seen that, after irradiation, higher voltages were required to reach the same gain as before irradiation. For completion, it should be noted that sample APD_2B_7 presented an unusual leakage current curve before irradiation. Two exponential increases where observed: one at 800 V, and another, much steeper, at approximately 1740 V. After irradiation up to 1×10^{15} $\mathrm{n_{eq}/cm^2}$, the device could only be biased up to 400 V.

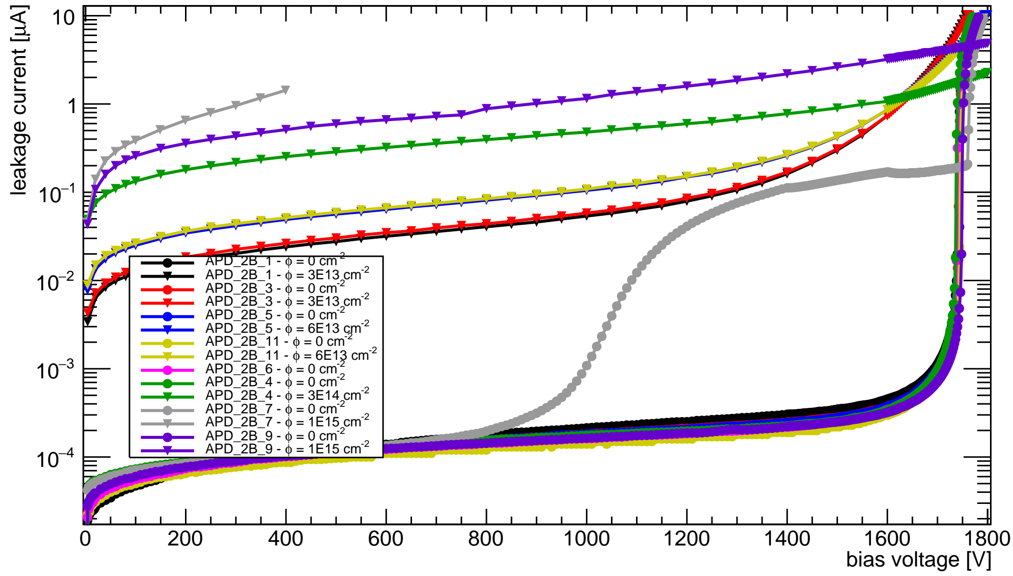

Figure 8.28: Leakage current for all 2×2-mm^2 DD-APDs from the second set. Measurements done at -20°C.

To better understand the dependencies between leakage current and fluence, the current at 200 V was compared for all devices and fluences, see Figure 8.29. The bias voltage was chosen to be 200 V so that multiplication did not play a role in the results. According to theory (see Chapter 3) the relation between these two parameters is linear. The proportionality constant (damage rate, α) gives a sense of the level of damage associated to irradiation. The results were thus fitted with a linear function, and α was extracted. The data were also compared to the leakage current values expected for a PiN diode of the same dimensions as the active volume of the DD-APDs before irradiation, and the same annealing history as the irradiated DD-APDs. Both the linear fit and the expected curve for a PiN diode can be seen in Figure 8.29. The experimental and the expected value of α can be found in Table 8.4.

Table 8.4: *Current related damage rates* (α), after 73 min at 21°C, obtained from the experimental data at 200 V, and calculated for a PiN diode with active volume 6×10^{-4} cm^3.

	DD-APDs	Equivalent PiN diode
α [A/cm]	8.66×10^{-19}	11.7×10^{-19}

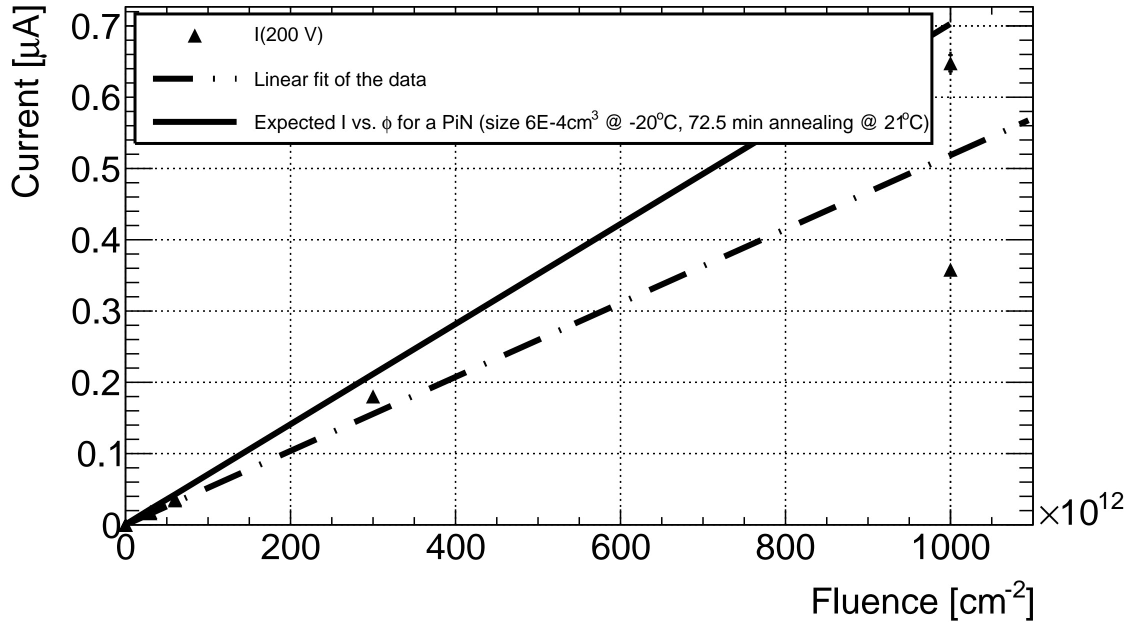

(a)

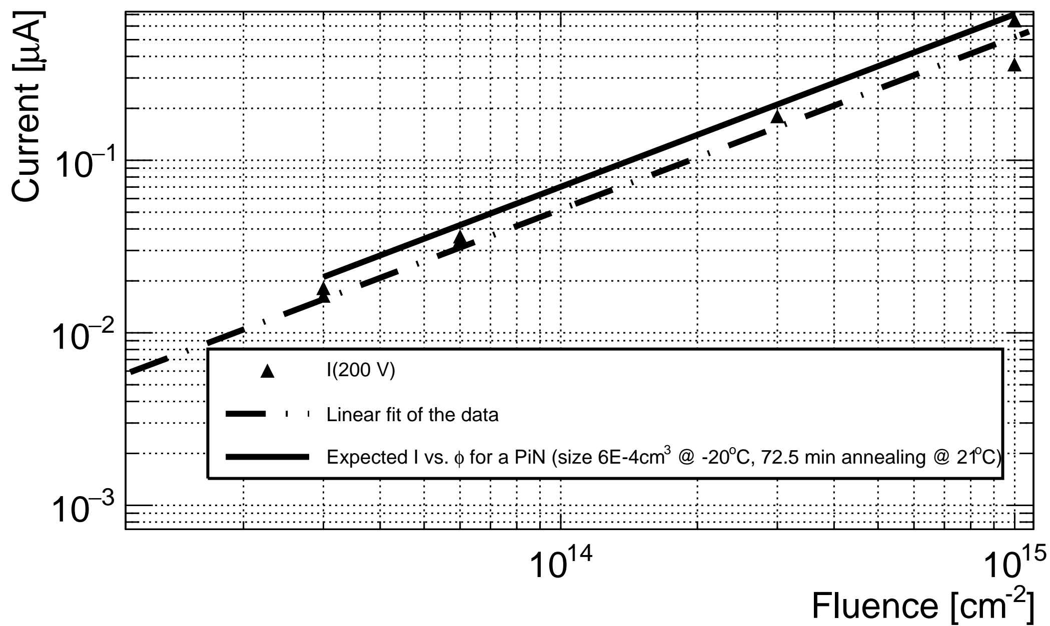

(b)

Figure 8.29: Leakage current at 200 V (where no multiplication is expected) and -20°C with respect to fluence. (a) In linear scale, (b) in logarithmic scale. The data were fitted with Equation 3.20. The expected dependency for a PiN diode under the same conditions, with the same active volume, and annealing history was plotted.

For further understanding of the devices, and for comparison of their behaviour to that expected from theory, the variation of leakage current with temperature was studied. Equation 3.25 was used to fit the leakage current at 200 V, where no multiplication is expected, with respect to the temperature (find the theoretical details in Section 8.1.4). This was done for all irradiated devices that could be biased, and for sample APD_2B_6 before irradiation, see Figures 8.30 and 8.31. To obtain these plots, the IV curves for all these devices had to be measured at several temperatures:

- For sample APD_2B_6 (before irradiation), 11 temperatures going from 20°C to -30°C.
- For samples irradiated up to 1×10^{15} n_{eq}/cm^2, 4 temperatures between 10°C and -20°C.
- For all other samples, 5 temperatures in the range 20°C to -20°C.

The full IV curves for all devices and temperatures can be found in Appendix E.

The values of E_{eff} obtained can be seen in Figure 8.32, where the expected value (1.21 eV) is also indicated. It can be seen that the E_{eff} obtained by fitting the data to Equation 3.25 is lower than that expected. It is worth noting that the χ^2/ndf of most fits differs significantly from unity. It is possible that the leakage current dependence with temperature for DD-APDs is not as straightforward as in Equation 3.25.

USC UNIVERSIDADE DE SANTIAGO DE COMPOSTELA

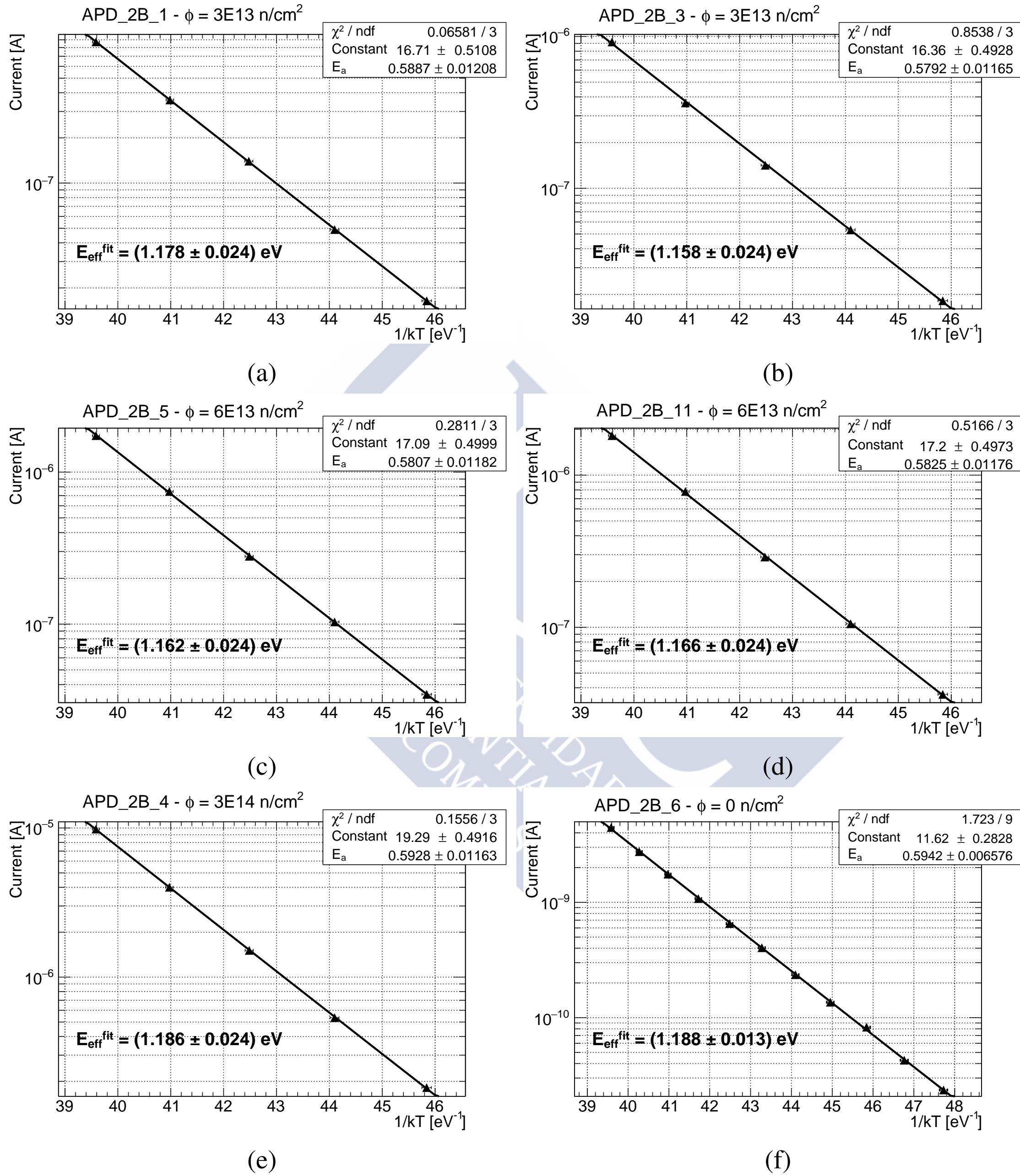

(a) (b)

(c) (d)

(e) (f)

Figure 8.30: Leakage current at 200 V with respect to $1/kT$, and a fit to the data using Equation 3.25, for samples irradiated up to 3×10^{13} n_{eq}/cm^2, 6×10^{13} n_{eq}/cm^2, 3×10^{14} n_{eq}/cm^2, and one unirradiated device.

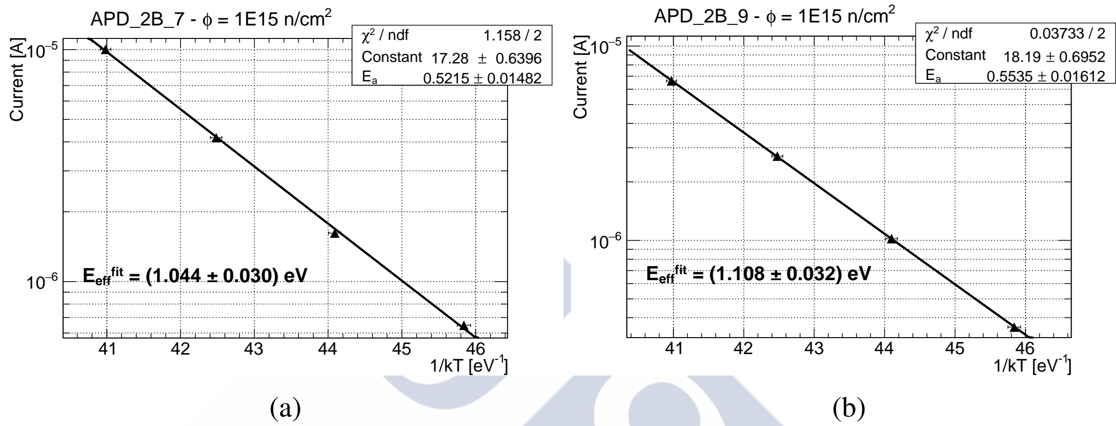

Figure 8.31: Leakage current at 200 V with respect to $1/kT$, and a fit to the data using Equation 3.25, for samples irradiated up to 1×10^{15} $\mathrm{n_{eq}/cm^2}$.

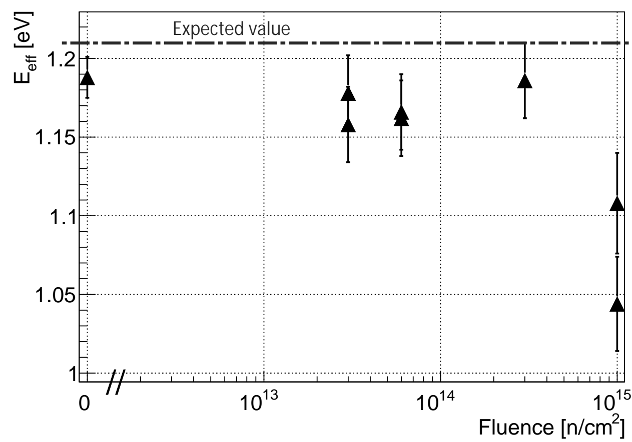

Figure 8.32: Effective energy as a function of fluence. The expected value (1.21 eV [49]) is also indicated.

8.3 8×8-mm^2 DD-APDs

The previous sections of this chapter focused on the effects of radiation on DD-APDs. This section, however, will focus on the spatial dependence of the signal amplitude for 8×8-mm^2 DD-APDs. This is a particularly important issue for timing applications. If the signal amplitude depends on the position of incidence of the particle (or, as in this study, of the laser beam), then the timing resolution will not be homogeneous through the device. In the case of DD-APDs, it was found on previous studies [20] that the signal amplitude is highly dependent on position. It was based on those studies that emerged the idea of making a capacitive coupling between the front side of the DD-APD and a metallic mesh, using kapton as a dielectric. The objective of the study here presented is to verify this spatial dependence by means of TCT measurements, identify its cause, and test the possibility of employing a simpler method to fix the non-uniformity problem.

The proposed method consists in metallising the surface of the device by sputtering a layer of aluminium. This is done by, firstly, coating the sensor with a positive photoresist. The metallisation pattern is transferred through maskless lithography onto the photoresist, which is then developed. Afterwards, the aluminium is deposited on the surface of the sensor using a sputtering machine. The final step is the *lift-off*, where the remaining photoresist is dissolved, thus removing the aluminium from the regions that ought not to be metallised[4].

In this study, two 8×8-mm^2 DD-APDs were tested. Both of them were *unpackaged*, i.e. they were not mounted on a ceramic support and no leads were attached to them. One of the sensors was kept unaltered (without any metallisation), and the other one was metallised at CMi-EPFL[5]. Both devices were mounted on a PCB for TCT measurements. In the case of the non-metallised device, this was mounted with the front side (p-side) facing upwards. The electrical connection was done through a conductive wire glued to the sensor with silver paint, see Figure 8.33. On the other hand, the metallised device was glued with the back side (n-side) facing up. The reasoning behind flipping the device was to avoid any possible discharges due to the potential difference between the PCB and the p-type region surrounding the n+ electrode on the back. Because of this change in the mounting, and to allow for laser-probing over the full area of the sensor, the n-side was metallised with a grid pattern. The grid consisted of metallic strips of 50 μm and a spacing of 100 μm. The p-side, however, was uniformly metallised with only one 2-mm hole in the centre, see Fig 8.34a. For this sample, the read-out and biasing were done on the n-side (facing upwards) through wirebonds, see Fig 8.34b.

[4]Further information about the process can be found in `https://cmi.epfl.ch/process/Photolithography.php`

[5]This work was performed in collaboration with M. Centis Vignali, J. Bronuzzi, and A. Mapelli.

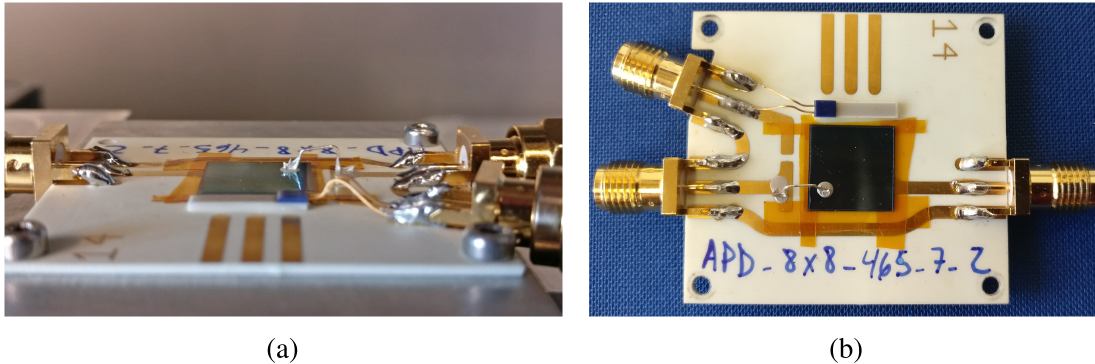

(a) (b)

Figure 8.33: (a) 8×8-mm^2 DD-APD with no surface metallisation. The read-out and biasing were done through a wire glued with silver paint onto the front side (p-side) of the sensor.

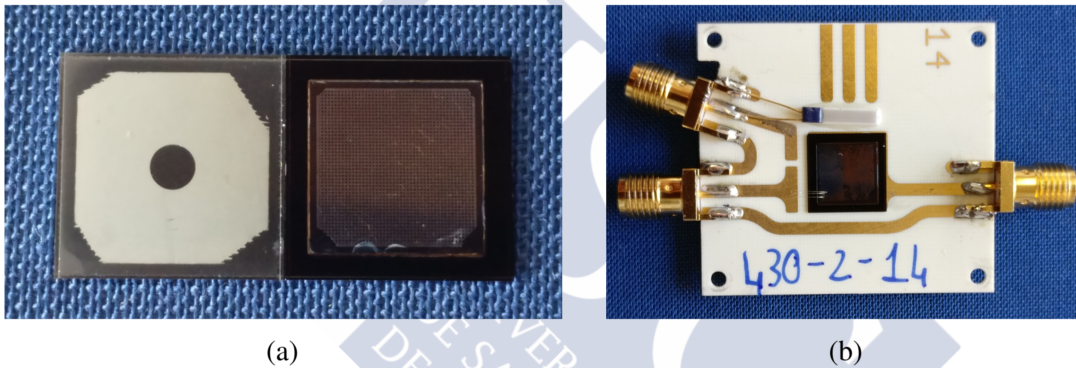

(a) (b)

Figure 8.34: (a) Metallisation pattern, and (b) electrical connection of the metallised 8×8-mm^2 DD-APD studied. The read-out and biasing were done through wirebonds connected to the n-side of the sensor (facing upwards in this configuration).

To perform the TCT surface scans, as the read-out and biasing were done through the same electrode, a customised bias T (the same described at the beginning of this chapter) had to be used. Also, to avoid reaching signal amplitudes beyond the linear range of the amplifier, all measurements were done with a 40 dB amplifier with a 30 dB attenuator connected to its input. Unlike in previous sections, the aim of the TCT surface scans in this study was not to test the homogeneity of charge collection, but the homogeneity of the signal amplitude. When IR-front TCT scans were done on the non-metallised sample, various structures were found, see Figure 8.35. These inhomogeneities were not due to the intrinsic behaviour of the DD-APD, but due to reflections of the laser on the PCB, on the edge of the mesa structure of the back electrode, and on the silver paint used to glue the sensor. In order to compensate for these optical effects, the ratio between the signal amplitude and the collected charge was computed and plotted, see Figure 8.35c.

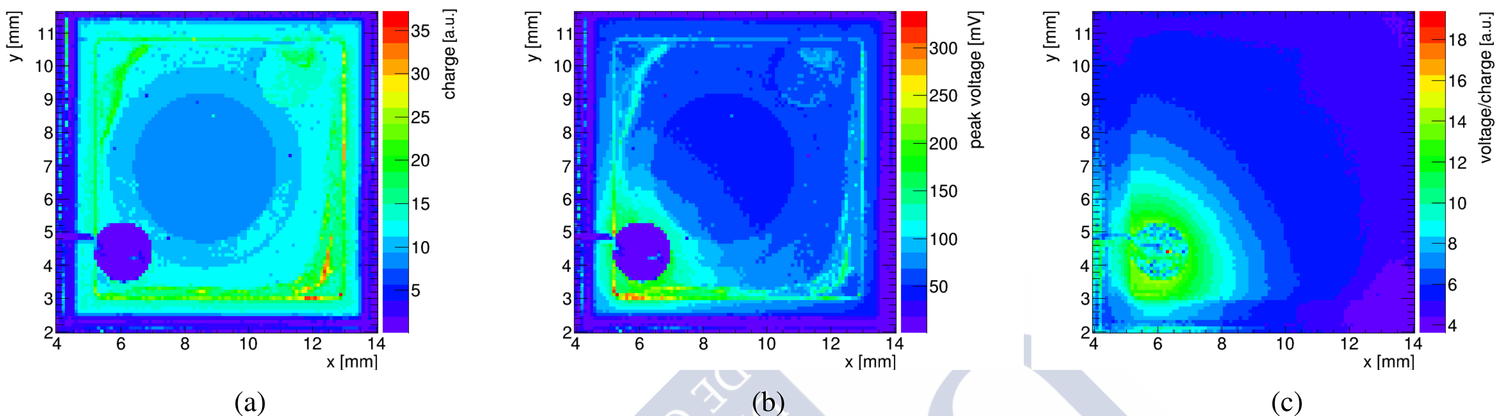

Figure 8.35: (a) Charge collection, (b) signal amplitude, and (c) amplitude/charge ratio maps obtained with IR-front TCT on the p-side of an 8×8-mm^2 DD-APD with no surface metallisation.

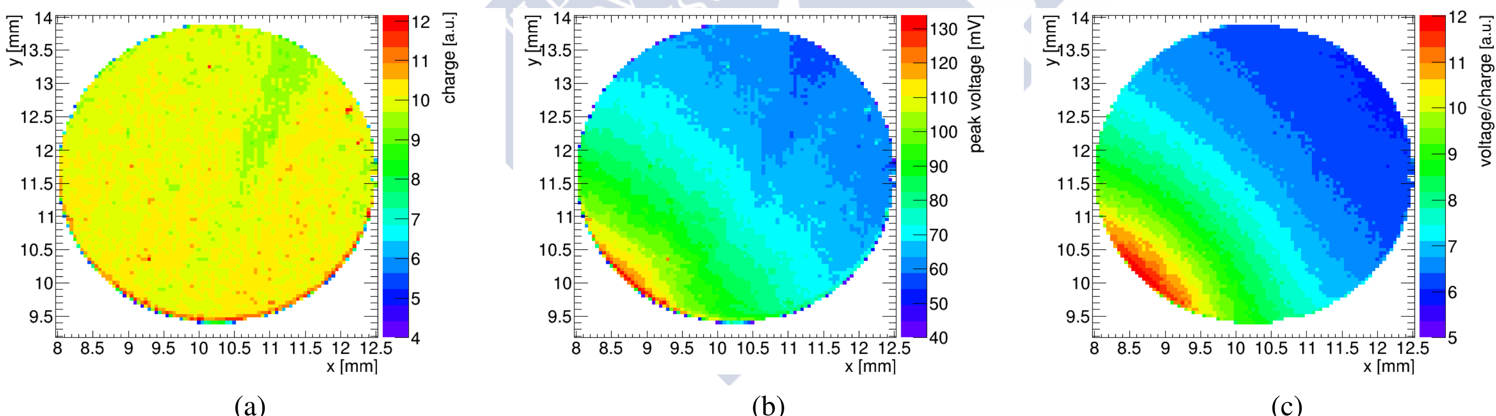

Figure 8.36: (a) Charge collection, (b) signal amplitude, and (c) amplitude/charge ratio maps obtained with IR-back TCT on the n-side of an 8×8-mm^2 DD-APD with no surface metallisation.

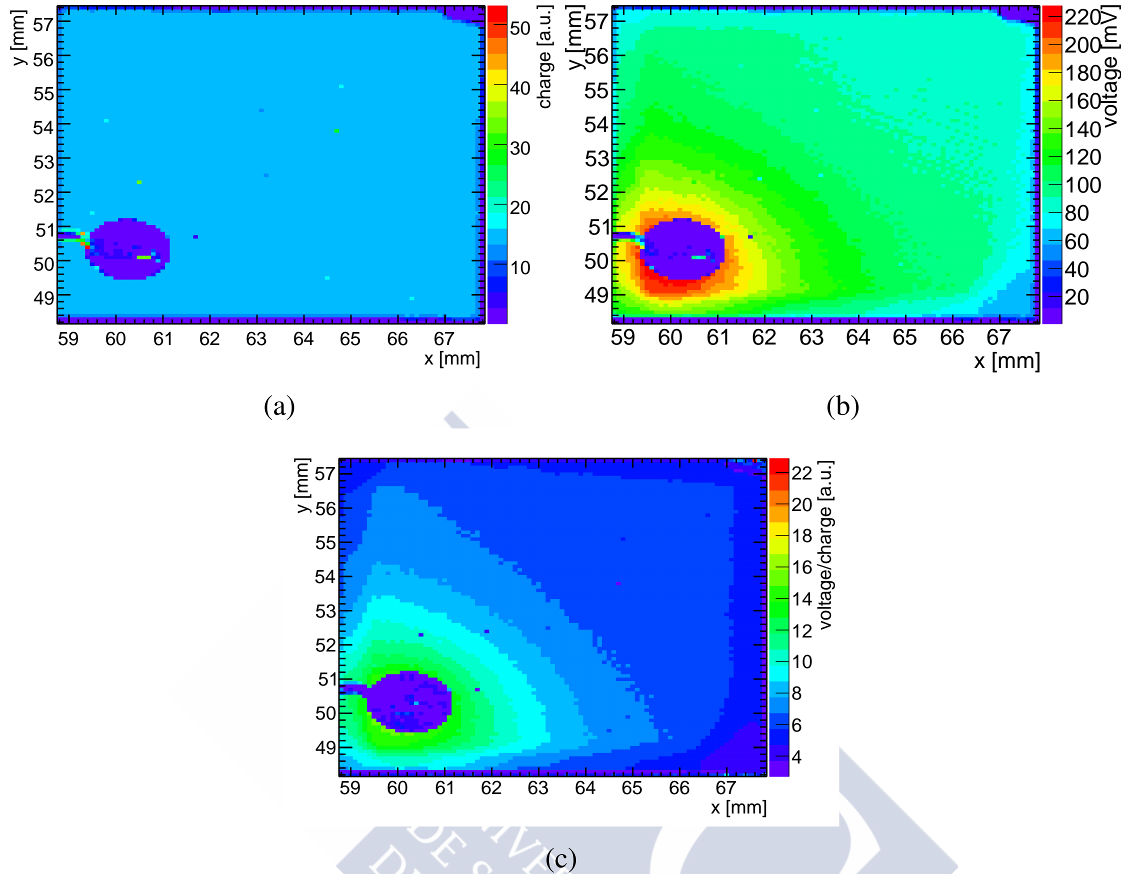

Figure 8.37: (a) Charge collection, (b) signal amplitude, and (c) amplitude/charge ratio maps obtained with red-front TCT on the p-side of an 8×8-mm^2 DD-APD with no metallisation.

The non metallised sample was not only subjected to IR-front TCT surface scans, but also to IR-back, and red-front TCT scans. All of these were carried out at 1700 V and -20°C. For all illuminations, charge collection, peak signal amplitude, and amplitude over charge maps were obtained, these can be seen in Figures 8.35 to 8.37. In the case of the front illumination scans, it should be noted that the circular area of low charge collection on the bottom left coincides with the silver paint blob used to glue the biasing wire on the sensor. Also for the frontal illumination, it can be seen that the amplitude/charge ratio maps show a clear dependency with the distance to the read-out point (the silver paint blob connected to the wire). In fact, the closer to the read-out point, the higher the amplitude/charge ratio. This is also seen in IR-back TCT scans, where there is a clear amplitude gradient, with its maximum towards the area below the blob on the front. The maximum difference[6] in amplitude/charge ratio observed through IR TCT was of about 75 % over a distance of 7 mm. A qualitative study of this effect was performed in [21], and it was found that the ratio between signal amplitude and charge depends on the

[6]The percentage difference was calculated using: $\Delta\ \% = \frac{(\max-\min)}{(\max+\min)/2} \times 100\ \%$.

distance to the contact due to the non-negligible surface resistivity. Since the amplitude signal inhomogeneity is caused by the high resistivity of the sensor surface, applying a conductive layer on the surfaces of the device could be a solution, i.e. the aforementioned aluminium metallisation.

Given that, with TCT, the signals obtained with the IR laser are the most similar to those expected during operation, for the metallised DD-APD only IR TCT scans were done. These measurements were done at 20°C and applying 1800 V. Firstly, a coarse IR-front TCT surface scan was done to identify the full area of the n-side of the sensor. Let it be remembered that for this sample, the n-side was facing upwards (contrary to the situation for the non-metallised device). In view of the presence of a metallic grid with a spacing of 100 μm on the surface of the n-electrode, obtaining a detailed enough scan of the full 8×8 mm^2 would have taken too long. Instead, based on the initial coarse scan, four 0.5×0.5-mm^2 regions of the sensor were chosen to carry out very detailed scans. The full charge collection scan of the device, and the four maps with the ratio between signal amplitude and charge can be found in Figure 8.38. In these last four plots, to have better contrast in the colour scale, the regions corresponding to the metallic grid (where little to no signal is obtained) have been filtered out (they appear in white). The grid pattern is not clear in all maps, in fact in some regions the edges of the expected rectangles from the grid pattern (the areas where the Si is not metallised) are blurry and fuse with adjacent charge-collection areas. This is because the measurements were done on the first device to be metallised, and it presented some defects in the metallisation. Figure 8.39 shows a picture of the metallic grid on the first DD-APD to be metallised[7]. The technique has now been optimised for these sensors, resulting in the clean-cut metallisation patterns shown in Figure 8.34. Figure 8.39 also shows were the wirebonds providing the bias and read-out were connected.

From the measurements here presented (Figure 8.38) it was found that the metallised DD-APD has a much better amplitude/charge ratio uniformity than the sensor with no metallisation. The mean value of the amplitude/charge ratio was calculated for each of the four scans, the values can be found also in Figure 8.38. There is a slight increase in the amplitude/charge ratio towards the region where the wirebonds are connected, i.e. the area covered by the XY scan in Figure 8.38d. However, considering the standard deviation, the mean amplitude/charge ratio of the other 3 surface maps are in agreement. By comparing the mean amplitude/charge ratio between the diagonally opposed surface scans seen in Figures 8.38c and 8.38d, it is possible to determine the maximum difference in amplitude/charge ratio observed. If the mean value of each surface scan is associated to the centre point of said scan, this difference corresponds to the amplitude/charge ratio variation over 7 mm. The maximum difference in amplitude/charge ratio observed was of about 8 %. This value may improve in devices with an even metallisation pattern, as that in Figure 8.34. However promising these first results are, further studies must be performed to confirm the viability of this method.

[7]The picture has been correspondingly flipped so that it can be directly compared to the map obtained through TCT (Figure 8.38a).

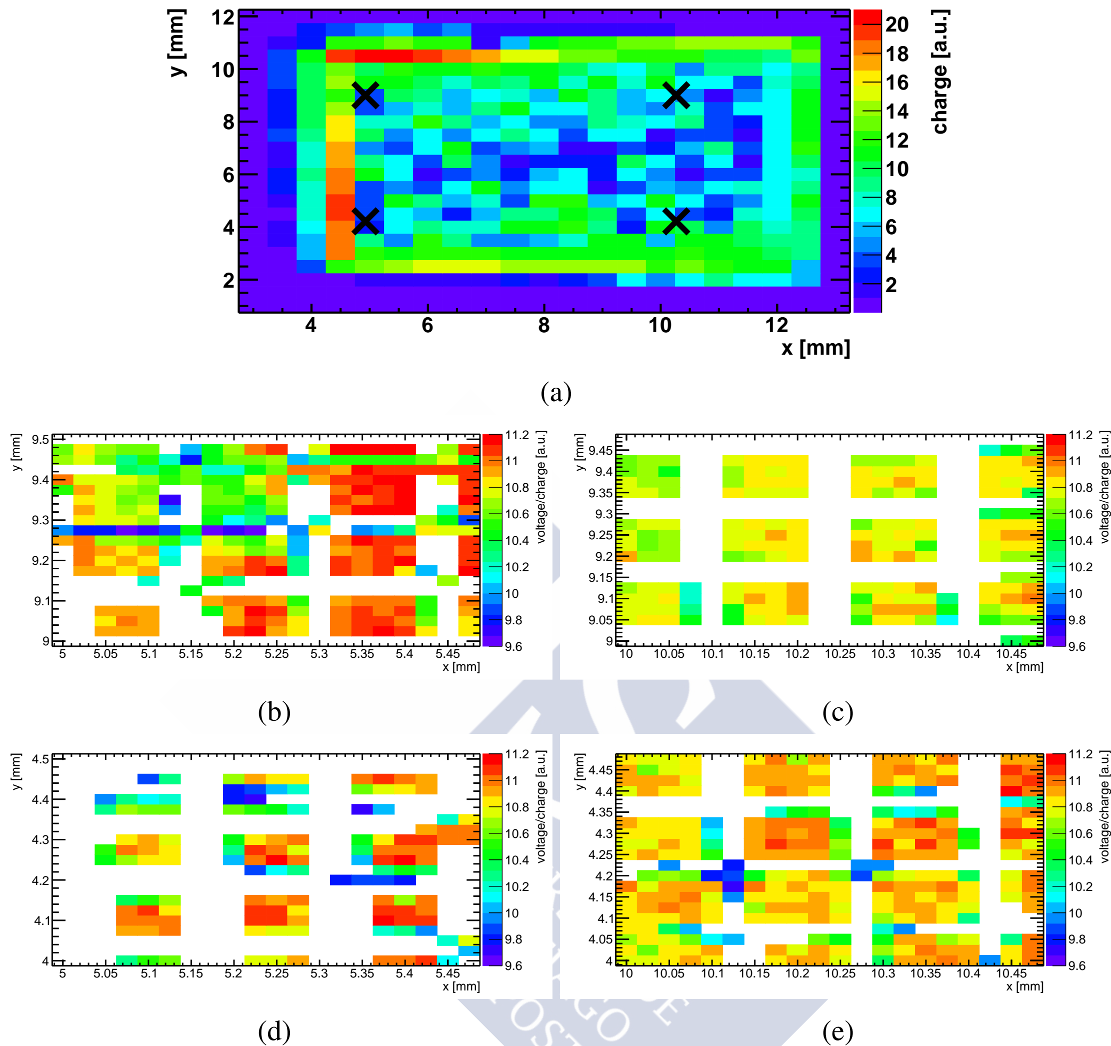

Figure 8.38: IR-front TCT scans done to the n-side of a metallised 8×8-mm^2 DD-APD. (a) Coarse charge collection scan of the full surface of the device. (b) to (e) Detailed amplitude/charge ratio maps of small regions centred around the points indicated with crosses on (a). The mean and standard deviation of each scan are specified.

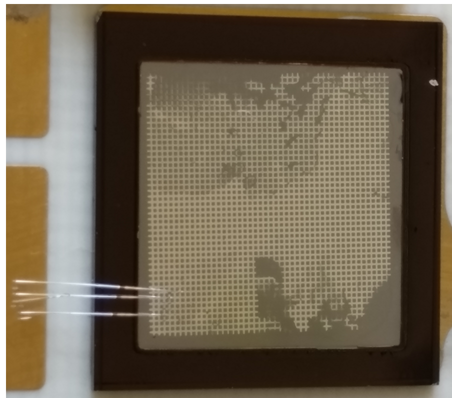

Figure 8.39: Picture of the metallic grid on the 8×8-mm^2 DD-APD measured. This was the first device to be metallised.

Chapter 9

Conclusions

This thesis, performed in the framework of the RD50 Collaboration and the CERN Doctoral Student Programme (within the EP-DT-DD SSD team), has as its main objective to contribute to the research and development of radiation tolerant silicon sensors for the High Luminosity upgrade of the CERN Large Hadron Collider (HL-LHC). This work goes in parallel with the many efforts from ATLAS, CMS, RD50 and other sensor R&D projects developing devices capable of withstanding the radiation levels expected at the HL-LHC, which will reach up to about 1.6×10^{16} fast hadrons/cm^2 at the innermost detectors [4]. The increased luminosity of the HL-LHC implies a rise in the expected pile-up. To cope with it, new technologies are being put forward to attain MIP timing resolutions of the order of $\sim$ 10 ps without losing spatial accuracy [5]. Moreover, another major challenge arises from the high levels of radiation expected, the degradation of charge collection efficiency, and the subsequent loss of sensor performance. In order to tackle these issues, one line of research investigates the possibility of producing radiation tolerant silicon sensors with intrinsic charge gain. The aim is to improve the signal height after irradiation as well as the timing capabilities of the devices.

In this thesis, the focus was set on two of the proposed technologies for precision timing detectors in future high luminosity colliders: Low Gain Avalanche Detectors (LGADs) [7], and Deep Diffused Avalanche Particle Detectors [8]. Both types of devices rely in the same basic principle: intrinsic charge gain due to impact ionisation. The internal multiplication of said sensors should improve their timing capabilities as well as increase their signal height, even after irradiation.

LGADs and DD-APDs were characterised before and after irradiation to analyse the performance degradation (loss of signal and gain, inhomogeneous spatial response, etc.) as a function of radiation fluence. The objective of these studies is to help understand the fundamental physical processes leading to the deterioration of the gain mechanism in silicon devices with intrinsic gain. Furthermore, this thesis sheds light on the many phenomena occurring inside silicon devices after heavy irradiation, both with protons and neutrons. Finally, whilst aiming for performance optimisation, clear application limits for LGADs and DD-APDs in terms of radiation hardness were obtained. These findings will serve the HL-LHC and other experiments as guideline for considering the use of devices

with intrinsic gain for tracking, calorimetry or timing applications.

Low Gain Avalanche Detectors

LGADs and PiN diodes, manufactured by CNM-Barcelona, were characterised before and after proton irradiation. All the devices have a thickness of 285 μm, an active area of 3×3 mm^2, a guard ring (GR), and a junction termination extension (JTE). The characterisation of the sensors was done by performing CV/IV measurements, radioactive source measurements, TCT scans, eTCT and TPA-TCT scans at different voltages and temperatures. The objective was to analyse the effects of radiation on the gain; the charge collection homogeneity; the multiplication onset; and the evolution with voltage, fluence and temperature of the electric field, the collected charge, and the space charge. PiN diodes were measured to serve as a reference for gain calculations.

The samples studied come from CNM run 7859, and from four different wafers:

- W1 and W2 with a multiplication-layer implant dose of 1.8×10^{13} cm^{-2},
- W3 and W4 with a multiplication-layer implant dose of 2.0×10^{13} cm^{-2}.

Regarding the electrical parameters of these sensors, before irradiation, they all had an end capacitance of ~ 4.1 pF, and a total leakage current (pad + GR) of less than 0.21 μA at full depletion and 20°C. The results obtained in this thesis are compared to previous studies [10, 106]. According to [106] LGADs can be discriminated based on their leakage current before irradiation, defining low leakage current devices as those with a leakage current below 1 μA at full depletion voltage and 20°C. Assuming that the leakage current is proportional to the active volume of the device, in the LGADs from this thesis the current threshold set to 1 μA in [106] would correspond to 0.34 μA due to the smaller active volume. As already indicated, all samples (barring LGAD_4_W4_I3_1, later irradiated up to 10^{12} n$_{eq}$/cm^2) have a leakage current below 0.21 μA at full depletion and 20°C.

The samples were sent to be irradiated with 24-GeV/c protons at the CERN IRRAD facility, with fluences between 10^{12} and 10^{15} n$_{eq}$/cm^2. After irradiation, and before their characterisation, the detectors were annealed at 60°C for 80 min.

The spatial distribution of charge collection was examined on specific devices, before and after irradiation, through red TCT measurements. The distribution was found to be homogeneous before irradiation, with a maximum deviation from the mean below 5 %. After irradiation at fluences not higher than 10^{14} n$_{eq}$/cm^2, the maximum deviation from the mean ranged between 2 % and 20 %, depending on the sample and the illumination (front or back). However, at a fluence of 10^{15} n$_{eq}$/cm^2 significant inhomogeneities were found. In fact, a striped pattern of different charge collection levels was seen, and the maximum deviation from the mean varied between 13 % up to a staggering 100 % (seen

in red-back TCT). To better understand the source of these inhomogeneities, scans were carried out on a PiN diode irradiated up to 10^{14} n_{eq}/cm^2. The charge collection spatial distribution turned out to be much more homogeneous than for an LGAD irradiated up to the same fluence. It is therefore reasonable to conclude, that the main source of charge collection inhomogeneities is the effect of radiation on the p+ multiplication layer.

One of the main aims of this work was to analyse the evolution with fluence of the multiplication-onset voltage. A previous study [10] on similar LGADs irradiated with neutrons, 200-MeV/c pions, and 800-MeV/c protons was taken as reference. In [10], it was found that the multiplication-onset voltage decreased with fluence. This effect would be a consequence of what is generally referred to as acceptor removal. However, in this thesis, where LGADs irradiated with 24-GeV/c protons were characterised, the study of charge collection with voltage showed that in these devices, and with this type of irradiation, the multiplication-onset voltage increases with fluence. This is consistent with space charge sign inversion of the initially p-type bulk towards n-type due to hole trapping. Furthermore, through TPA-TCT measurements, and TCAD simulations, which allowed the analysis of the electric field evolution inside one of the LGADs irradiated up to 10^{14} n_{eq}/cm^2, it was possible to infer that there is a *triple junction effect* occurring in the type-inverted device. Interestingly, it was also discovered that with annealing the multiplication-onset voltage decreases, and the gain is recovered to 60-70 % of the value before irradiation. As samples get annealed, they tend towards an unirradiated-like state. This implies that annealing is playing an important role for LGAD performance and might be exploitable for LGAD long term operation. Further irradiation campaigns and systematic annealing studies should be performed on similar samples to better comprehend these phenomena.

On the matter of gain, it was shown that this parameter decreases with increasing fluence. Up to fluences below 10^{14} n_{eq}/cm^2, it is possible to recover the gain by increasing the bias voltage. However, at higher fluences, it is no longer possible to recover the gain to before-irradiation values by increasing the applied bias voltage. As a matter of fact, at the maximum fluence evaluated (10^{15} n_{eq}/cm^2) the charge collected by the LGADs, independently of their multiplication-layer doping, was almost equal to that of a normal PiN diode with no internal multiplication of charge. This decrease in the internal gain can be attributed to the aforementioned triple junction, or more specifically, to the space charge sign inversion due to hole trapping. Before irradiation, at a specific bias voltage the electric field has a clear maximum in the multiplication layer. After irradiation, at the same specific bias voltage there are now two *competing* electric field peaks; one in the back of the device and one in the front. This implies that a higher bias voltage is required to reach the same electric-field intensity in the multiplication layer as before irradiation, and hence the same gain. It is also possible that the cause for this decrease in gain is actually a combination of two effects, namely the space charge sign inversion, and effective acceptor removal. Further studies, particularly at 10^{15} n_{eq}/cm^2, must be performed in order to determine if the observed decrease in gain is due to a combination of the triple-junction effect and effective acceptor removal.

Deep Diffused Avalanche Particle Detectors

Two sets of 2×2-mm^2 DD-APDs were characterised, before and after neutron irradiation, in order to evaluate their radiation hardness. The characterisation of all 2×2-mm^2 DD-APDs included TCT surface and voltage scans, as well as capacitance and leakage current with respect to voltage measurements. This thesis contains the most comprehensive study so far on the radiation hardness of DD-APDs. Also two 8×8-mm^2 devices were characterised, although only before irradiation, to analyse their signal amplitude uniformity.

2×2 mm^2

The effect of neutron irradiation on 2×2-mm^2 DD-APDs was studied in this thesis. In order to do this, two sets of 2×2-mm^2 DD-APDs were characterised before and after neutron irradiation. The first set consisted of 7 DD-APDs, and the second of 8. After the study of the first set, it was understood that all DD-APDs must be fully characterised before irradiation. This was a direct consequence of the samples possibly coming from different wafers with different gain, doping profile, thickness, and pn-junction depth. Since this was not known when working on the first set, the results were inconclusive. This is why a second set of DD-APDs was requested to RMD, and all sensors were evaluated before starting the irradiation campaign.

Five out of the seven DD-APDs from the first set were irradiated with neutrons up to fluences between 3×10^{13} n_{eq}/cm^2 and 1×10^{15} n_{eq}/cm^2. The remaining 2 devices were kept unirradiated as reference. The detectors were not subjected to annealing after irradiation. Nevertheless, it was estimated that, due to their handling, the samples underwent a total annealing of 60 min at 21°C.

TCT surface scans were performed to analyse the spatial homogeneity of the charge collection. The unirradiated samples showed inhomogeneities due to purely optical effects. After irradiation, it was found that there was a reduction with fluence of the active area of the sensors. Also, a region of higher charge collection appeared at the centre of the devices in the red laser scans of samples irradiated to a $\phi \geq 6 \times 10^{13}$ n_{eq}/cm^2, this occurrence has yet to be understood.

IV curves showed that in this set the leakage current seems to be dominated by surface generation current. As expected, there is an increase in current with fluence. From the IV measurements at 200 V, where no internal multiplication is expected to occur, it was possible to estimate the current related damage rate α. The obtained value of 8.22×10^{-19} A/cm resulted of the expected order of magnitude. The dependence between leakage current and temperature was evaluated for one of the samples irradiated up to 3×10^{14} n_{eq}/cm^2 and the effective energy was determined. The value obtained was (1.221 ± 0.008) eV, which is in agreement with the expected 1.21 eV [49, 50].

From CV measurements, it was found that at a specific voltage the capacitance decreases with fluence. Assuming a similar active area, this would imply an increase in the depletion region thickness with increasing irradiation, which goes in the direction of the simulation results in [108]. Having said that, surface scans showed a reduction in active area. The decrease in capacitance could be a combination of both effects.

TCT voltage scans were performed to evaluate the change in charge collection with fluence, which was found to decrease. In fact, it was found that for a fluence of 3×10^{14} n_{eq}/cm^2 a bias voltage of ~ 2500 V would have to be applied in order to recover the before-irradiation charge collection value at 1700 V. However, the most important conclusion drawn from these measurements was in fact not related to the operational voltage after irradiation. By comparing scans from devices that, in principle, should have behaved identically, it was found that there were significant variations in response. This was observed even in the unirradiated DD-APDs. Such variations were also found during CV/IV measurements. After consulting with the manufacturer, RMD, it emerged that sensors could come from different wafers. This implied that their gain, doping profile, thickness, and pn-junction depth could differ as well. Hence, it became apparent that it was crucial to measure and test all samples before an irradiation campaign. Finally, based on these results, it was decided that a new set of DD-APDs had to be studied to have a better understanding of their behaviour.

The new set of devices consisted of 8 DD-APDs, which were all characterised before being irradiated with neutrons. To have more conclusive results, all samples were irradiated in pairs, each to a different fluence: 3×10^{13}, 6×10^{13}, 3×10^{14}, and 1×10^{15} n_{eq}/cm^2. No annealing steps were performed after irradiation. However, the final total annealing due to the handling of the samples, and the performance of measurements at different temperatures, was estimated to be of 73 min at 21°C. The tests performed on this new set of devices were the same as on the previous set.

Equally to what was observed in the previous set, TCT surface scans showed that there was a reduction in the active area with fluence. Also, at fluences higher than 6×10^{13} n_{eq}/cm^2, the same inhomogeneity at the centre of the detector in red TCT XY scans was seen.

IV curves presented the expected increase with fluence, and the leakage current appeared to be dominated by bulk generation current, before and after irradiation. Once again, from the leakage current measurements at 200 V the current related damage rate α was estimated to be 8.66×10^{-19} A/cm, and resulted of the expected order of magnitude. An analysis of the dependence of leakage current with temperature was also carried out. One unirradiated sample, and all irradiated sensors were tested at various temperatures. The effective energy was determined for each and every one of them. The mean value of the effective energy over all sensors, and its standard deviation were calculated. The value obtained was (1.15 ± 0.05) eV, which is slightly below the expected 1.21 eV [49].

As for CV measurements, the results were analogous as for the previous set. The capacitance decreases with fluence, which could imply an increase in the depletion region thickness with fluence, consistent with simulation results in [108]. Nevertheless, it could also be explained by a reduction in active area, which is actually observed in TCT XY scans. Perhaps, the capacitance decrease seen is caused by a combination of both effects.

Lastly, TCT voltage scans show a decrease in charge collection with fluence, which was to be expected. In this set, the results were fairly consistent between each other for samples irradiated up to the same fluence, and amongst all samples before irradiation. Measurements showed that for fluences of up to 6×10^{13} n_{eq}/cm^2, charge collection could be recovered by increasing the bias voltage. On the contrary, for fluences above 3×10^{14} n_{eq}/cm^2, the bias voltage required to recover before-irradiation charge collection levels could not be reached, as it was estimated to be higher than 3000 V.

Further studies should be performed in the range between 6×10^{13} and 3×10^{14} n_{eq}/cm^2 in order to obtain more accurate operational limits for DD-APDs. That said, the performed radiation-hardness studies point towards DD-APDs not being that promising a technology for HEP applications with radiation levels higher than 3×10^{14} n_{eq}/cm^2.

8×8 mm^2

The work done on 8×8-mm^2 DD-APDs focused on the homogeneity of the signal amplitude over the detector area, a particularly important issue for timing applications. On previous studies [20] it was found that the signal amplitude in DD-APDs is highly dependent on position. Based on those studies the idea of making a capacitive coupling between the front side of the DD-APD and a metallic mesh, using kapton as a dielectric, was proposed. The objective of the study carried out in this thesis was to verify this spatial dependence by means of TCT measurements, identify its cause, and test the possibility of employing a simpler method to fix the non-uniformity problem.

Two 8×8-mm^2 DD-APDs were tested through TCT surface scans. One device was kept unaltered, and the other one was metallised at CMi-EPFL through the sputter deposition of aluminium. To avoid the interference of optical effects (such as reflections) in the evaluation of the spatial uniformity of the signal amplitude, the ratio between the signal amplitude and the collected charge were analysed.

The non metallised sample was subjected to IR-front, IR-back, and red-front TCT scans. For the frontal illumination, it could be seen that the amplitude/charge ratio maps had a clear dependency with the distance to the read-out point. The closer to the read-out point, the higher the amplitude/charge ratio. The same was observed in IR-back TCT scans, where there is a clear amplitude gradient, with its maximum towards the area below the read-out point on the front. The maximum difference in amplitude/charge ratio observed through IR TCT was of about 75 % over a distance of 7 mm. It was discovered, by means of a qualitative study of this phenomenon [21], that the ratio between signal amp-

litude and charge depended on the distance to the contact due to the surface resistivity of the device. Consequently, applying a conductive layer on the surface of DD-APDs, the aforementioned aluminium metallisation, could be a solution to the spatial non-uniformity of the signal amplitude.

Only IR TCT scans were done on the metallised DD-APD, as the signals obtained with the IR laser are the most similar to those expected during operation. A coarse IR-front TCT surface scan was done to identify the full area of the sensor. Based on the initial coarse scan, four 0.5×0.5-mm^2 regions of the sensor were chosen to carry out very detailed scans. These measurements demonstrated that the amplitude/charge ratio uniformity of DD-APDs could be remarkably improved by metallising the surface of the devices. The final uniformity was better than 8 %, when comparing the difference in amplitude/charge ratio over a distance of 7 mm. These first results are quite promising, nonetheless, further studies ought to be performed to confirm the viability of this method.

Final remarks

To summarise, the work done on LGADs proved that these devices can maintain their gain capabilities up to fluences of 1×10^{14} n_{eq}/cm^2. In fact, below that level of irradiation, it is possible to recover the gain by increasing the applied bias voltage. It was also concluded that the devices can be manufactured to possess a homogeneous response over their full active area. Finally, in the case of exposure to highly energetic protons, the annealing of samples could potentially improve the performance of these devices during their use in HEP experiments.

From the radiation-hardness studies performed on DD-APDs it emerged that this is not as promising a technology for HEP applications with radiation levels higher than 3×10^{14} n_{eq}/cm^2. At higher fluences, the voltages required to recover before-irradiation gain values are well beyond the operational range of the sensors. The design of DD-APDs should be adapted in order to use this type of detectors in the HL-LHC environment.

USC UNIVERSIDADE DE SANTIAGO DE COMPOSTELA

USC
UNIVERSIDADE
DE SANTIAGO
DE COMPOSTELA

Appendices

USC
UNIVERSIDADE
DE SANTIAGO
DE COMPOSTELA

Appendix A

Silicon crystal growth

The manufacture of silicon sensors relies on the growth of monocrystalline ingots of silicon that can then be sawed into wafers. The starting material in this process is silicon dioxide, which is chemically processed to obtain a high-purity polycrystalline silicon. Several techniques area available for growing monocrystalline silicon, namely: Czochralski, float-zone, and epitaxial. A brief description of these processes will be given in this appendix, for further details see [30].

Czochralski process

The Czochralski process is the most common, particularly for industrial applications. This technique involves the use of an apparatus called a *crystal puller*, see Figure A.1. The main components of the puller are a furnace, a crystal-pulling mechanism, and an ambient control. In the crystal-growing process, polycrystalline silicon is placed in a silica crucible inside the furnace, which is heated above the melting point of silicon (1412°C). The crucible is mounted on a rotating platform to prevent the formation of local hot or cold regions during the growth. Suspended over the crucible in a seed holder there is a suitably oriented seed crystal (e.g· $\langle 111 \rangle$, $\langle 100 \rangle$, etc.). The seed is dipped into the silicon melt, and is then slowly lifted. As the seed is slowly pulled upwards, it is also rotated in the opposite direction to the movement of the crucible. The molten silicon adheres to the crystal and it solidifies using th crystal seed as a template [30]. FigureA.2 shows a schematic of the process.

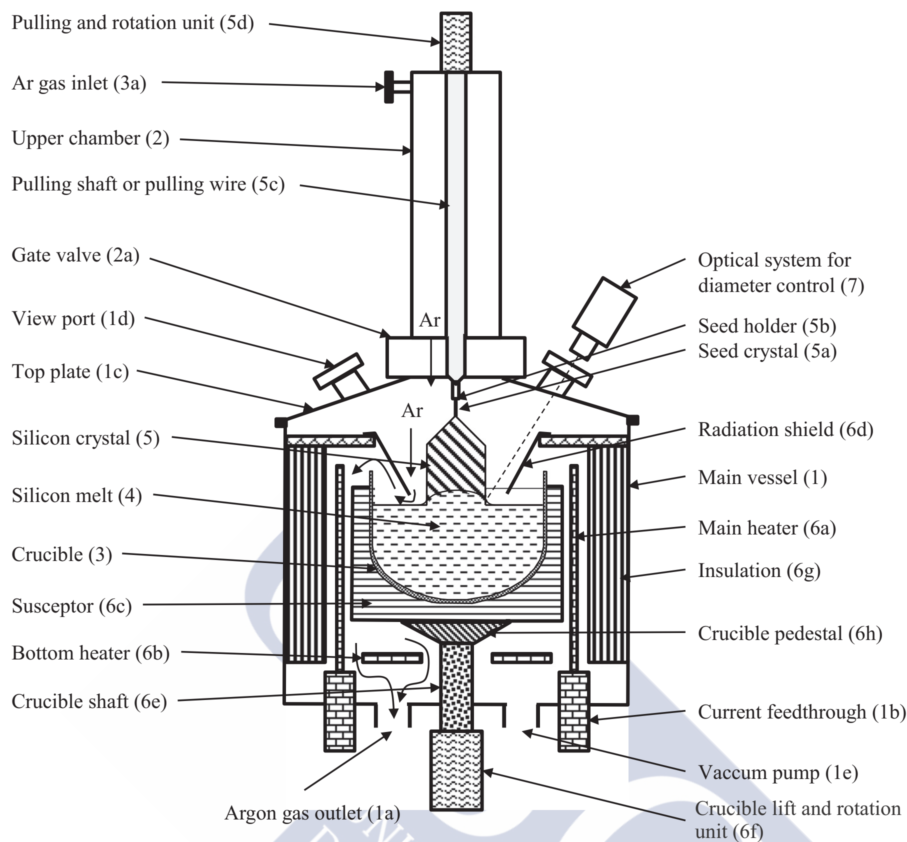

Figure A.1: Schematic drawing of the Czochralski crystal puller. From Rudolph 2015 [111]. ©Elsevier Science B.V., reproduced with permission.

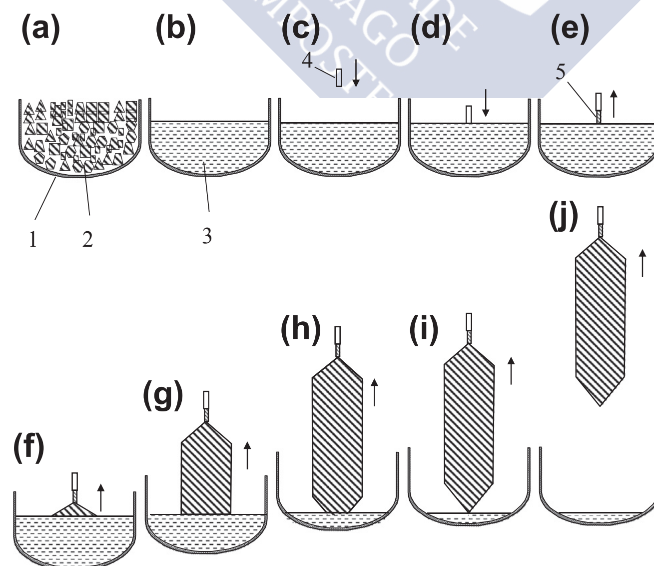

Figure A.2: Schematic of the different steps of the Czochralski process. (a) Polycrystalline Si is put in a crucible where it is (b) melted. (c, d) The Si seed crystal is dipped into the melt, and (e-i) slowly pulled upwards. (j) The full ingot is lifted and cooled. From Rudolph 2015 [111]. ©Elsevier Science B.V., reproduced with permission.

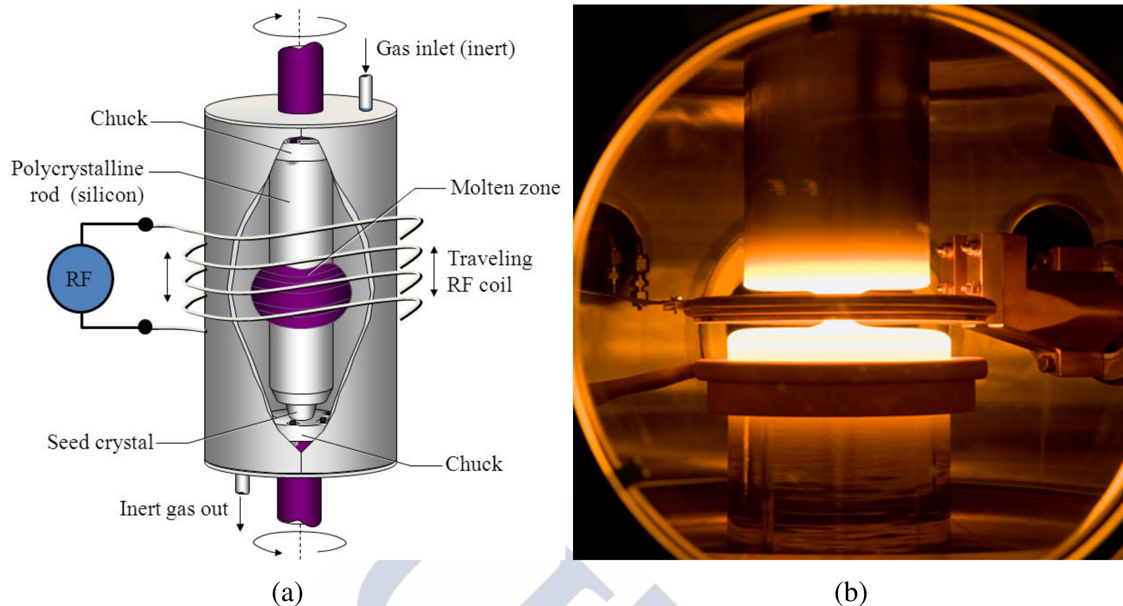

(a) (b)

Figure A.3: (a) Schematic drawing of the float-zone process [112], and (b) a photograph taken during the procedure [113].

Float-zone process

The process consists in holding vertically, and rotating a high-purity polycrystalline rod with a seed crystal at the bottom. During the process, the rod is kept within an inert atmosphere. By means of a radio-frequency heater, a region of a few centimetres in length is kept molten. This molten zone is referred to as the *floating zone*, which is retained by surface tension. The rod is slowly dropped so that the floating zone moves upwards from the seed towards the top end of the rod. As the floating zone moves upwards, a monocrystalline silicon rod grows below the molten zone as an extension of the seed crystal. Figure A.3 shows both a schematic of the process and a photograph taken during the procedure. The silicon obtained through the float-zone process is purer than that obtained with the Czochralski method. Consequently, materials with higher resistivity can be obtained through the float-zone process than through the Czochralski process [30].

Epitaxial process

In the epitaxial process, a monocrystalline silicon layer is grown on top of a substrate wafer. The monocrystalline silicon substrate is used as the seed crystal. The epitaxial layer and the substrate materials may or may not be the same. There are several epitaxial growing methods, but the most common for silicon device production is chemical-vapour deposition (CVD), also known as vapour-phase epitaxy (VPE). CVD consists in the deposition of an epitaxial layer through a chemical reaction between gaseous compounds, such as silicon tetrachloride ($SiCl_4$), dichlorosilane (SiH_2Cl_2), trichlorosilane ($SiHCl_3$), and silane (SiH_4). Silicon tetrachloride is one of the most studied and used in the industry. The reaction of $SiCl_4$ that results in the deposition of a Si layer occurs at 1200°C and is the following

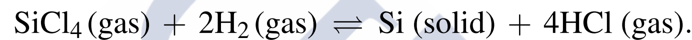

$$SiCl_4\,(\text{gas}) + 2H_2\,(\text{gas}) \rightleftharpoons Si\,(\text{solid}) + 4HCl\,(\text{gas}).$$

In parallel to this, there is an additional competing reaction taking place:

$$SiCl_4\,(\text{gas}) + Si\,(\text{solid}) \rightleftharpoons 2SiCl_2\,(\text{gas}).$$

If the silicon tetrachloride concentration is too high, etching rather than growth of silicon will take place. Whilst, initially, the growth rate increases with the concentration of $SiCl_4$, at a specific mole fraction[1] the growth rate reaches a maximum. Beyond that, the growth rate starts to decrease and eventually etching of the silicon will occur [30].

UNIVERSIDADE DE SANTIAGO DE COMPOSTELA

[1] Amount of a constituent divided by the total amount of all constituents in the mixture [114].

Appendix B

LGADs and PiN diodes: waveforms at different temperatures

Part of the study of the change in space charge and electric field distribution in irradiated LGADs involved the study of the waveforms obtained during TCT voltage scans. In particular, red-front and red-back TCT voltage scans, ranging from 10 to 300 V, were done on the two pairs of LGADs and PiN diodes irradiated up to 10^{14} n_{eq}/cm^2:

- LGAD_7859_4_W2_I3_1 (1.8×10^{13} cm^{-2}),
- LGAD_7859_7_W3_C2_3 (2.0×10^{13} cm^{-2}),
- PIN_7859_7_W1_C9_3,
- PIN_7859_4_W3_I8_1.

Said scans were performed at 5 different temperatures: 20°C, 10°C, 0°C, -10°C, and -20°C. The results were summarised and discussed in Section 7.5. Here, the complete set of measurements is shown in Figures B.1 to B.8. These measurement were carried out in April 2016, i.e. before the performance of TPA-TCT and eTCT measurements, which took place in July and August 2017.

UNIVERSIDADE DE SANTIAGO DE COMPOSTELA USC

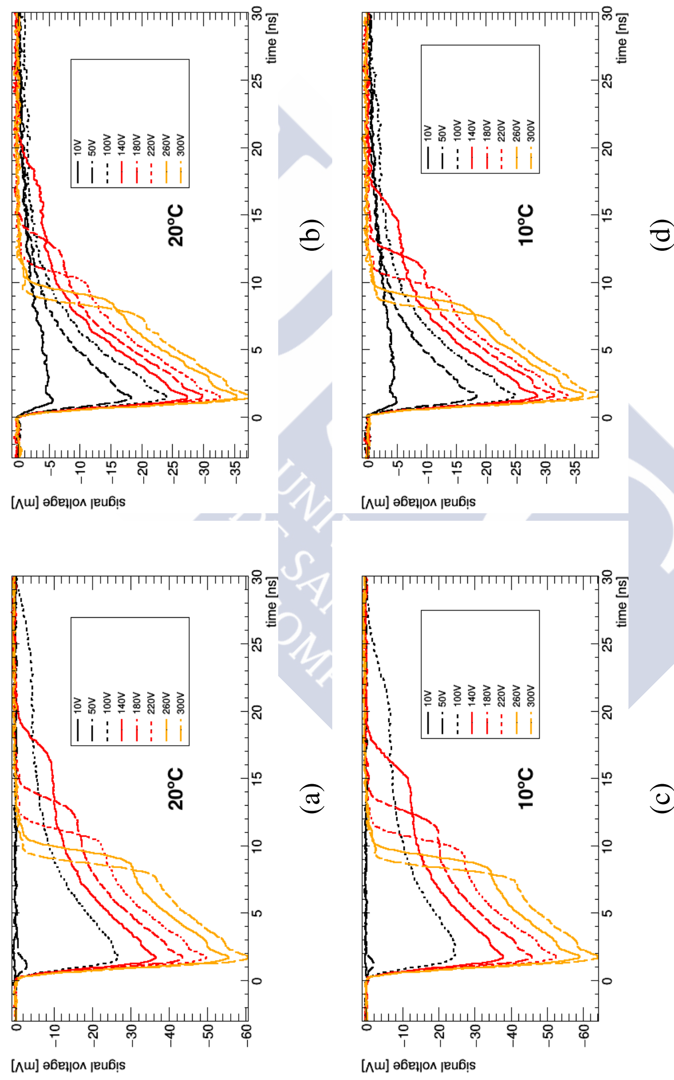

Figure B.1: Red-front TCT waveforms from (left) LGAD_7859_4_W2_I3_1 (1.8 × 10^{13} cm^{-2}) and (right) PiN_7859_7_W1_C9_3 (PiN diode), from W2 and W1, irradiated up to 10^{14} n_{eq}/cm^2, at 20, and 10°C.

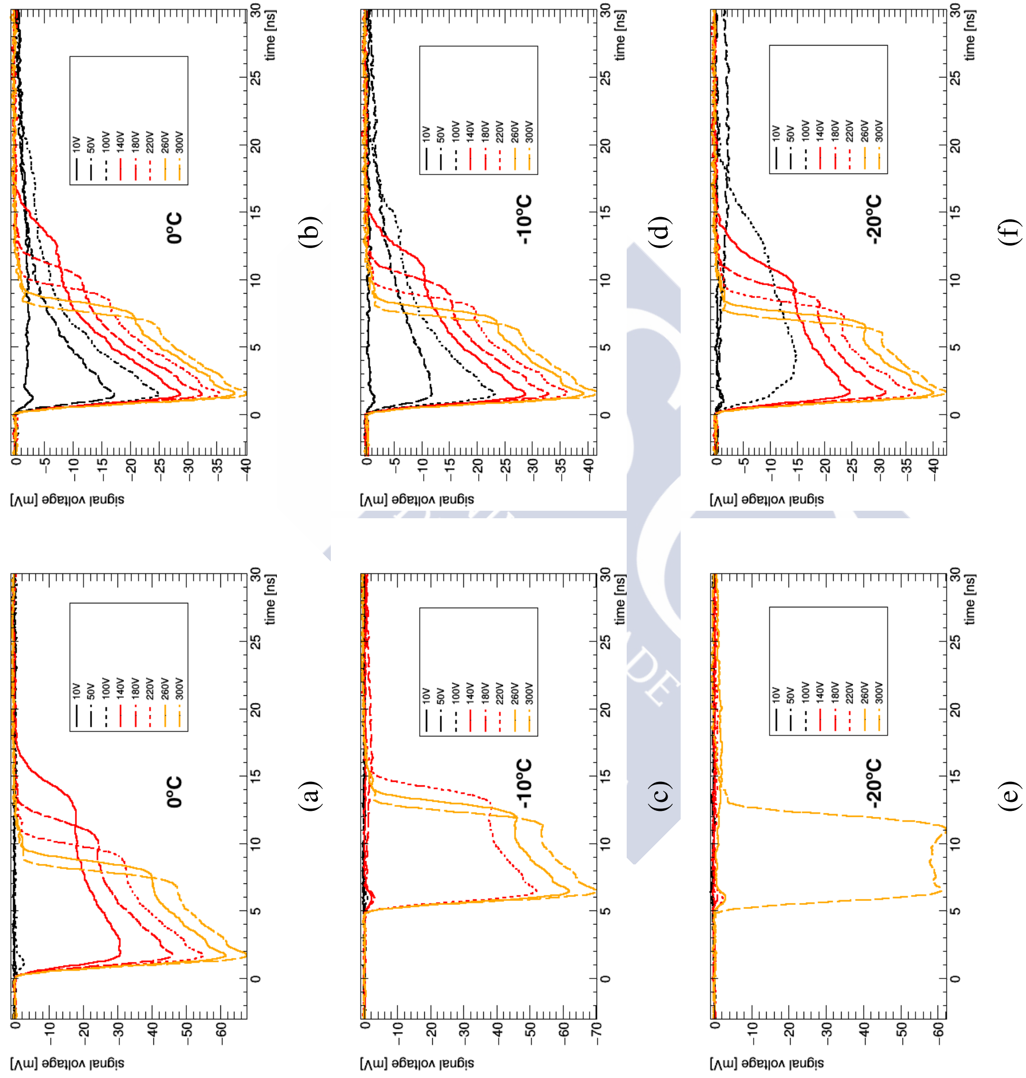

Figure B.2: Red-front TCT waveforms from (left) LGAD_7859_4_W2_I3_1 (1.8×10^{13} cm^{-2}) and (right) PiN_7859_7_W1_C9_3 (PiN diode), from W2 and W1, irradiated up to 10^{14} n_{eq}/cm^2, at 0, -10, and -20°C.

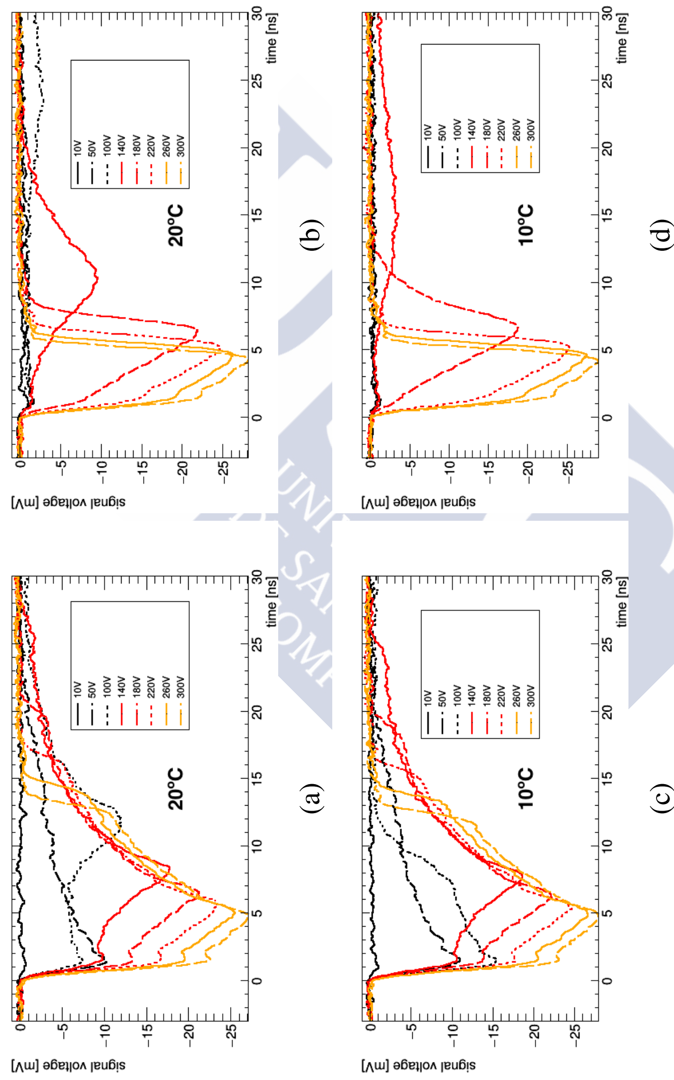

Figure B.3: Red-back TCT waveforms from (left) LGAD_7859_4_W2_I3_1 (1.8×10^{13} cm^{-2}) and (right) PiN_7859_7_W1_C9_3 (PiN diode), from W2 and W1, irradiated up to 10^{14} n_{eq}/cm^2, at 20, and 10°C.

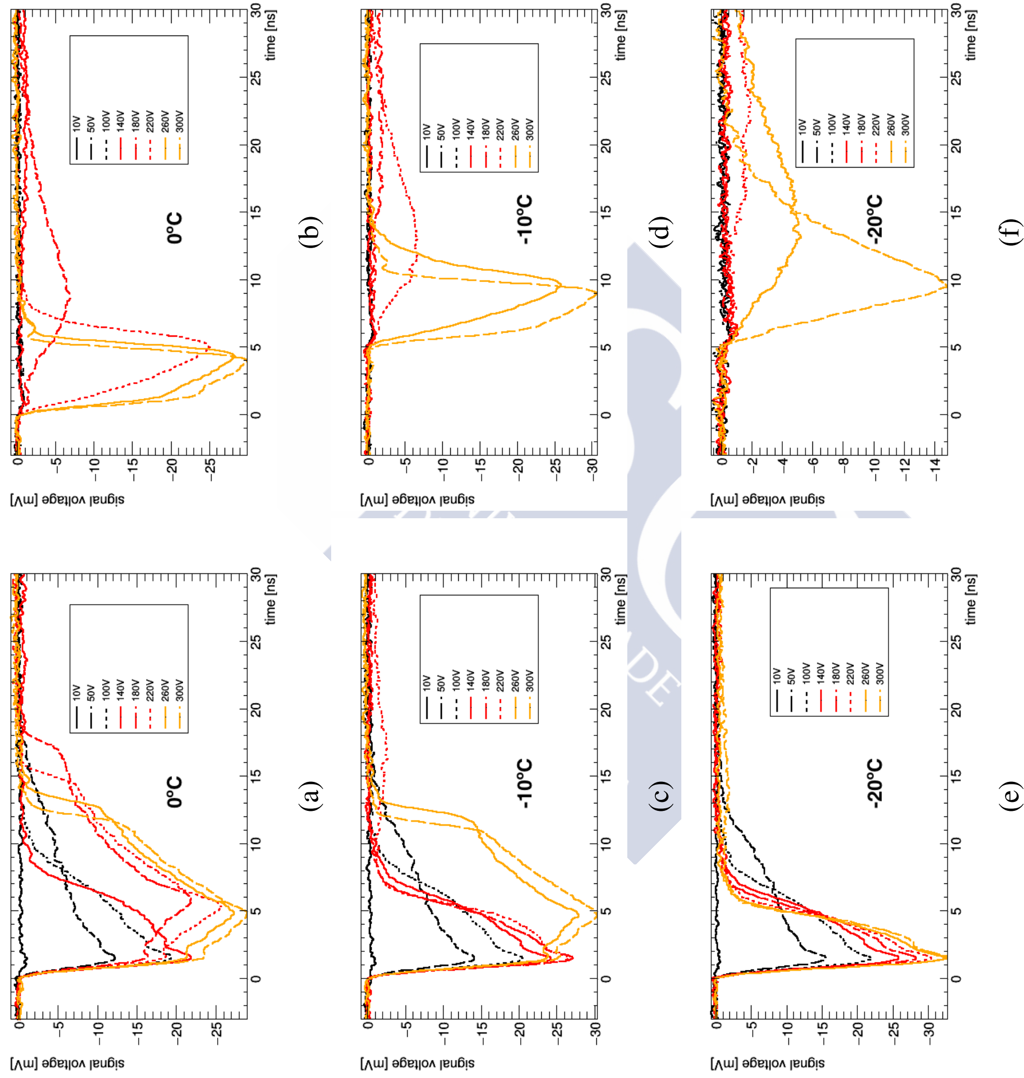

Figure B.4: Red-back TCT waveforms from (left) LGAD_7859_4_W2_I3_1 (1.8×10^{13} cm^{-2}) and (right) PiN_7859_7_W1_C9_3 (PiN diode), from W2 and W1, irradiated up to 10^{14} n_{eq}/cm^2, at 0, -10, and -20°C.

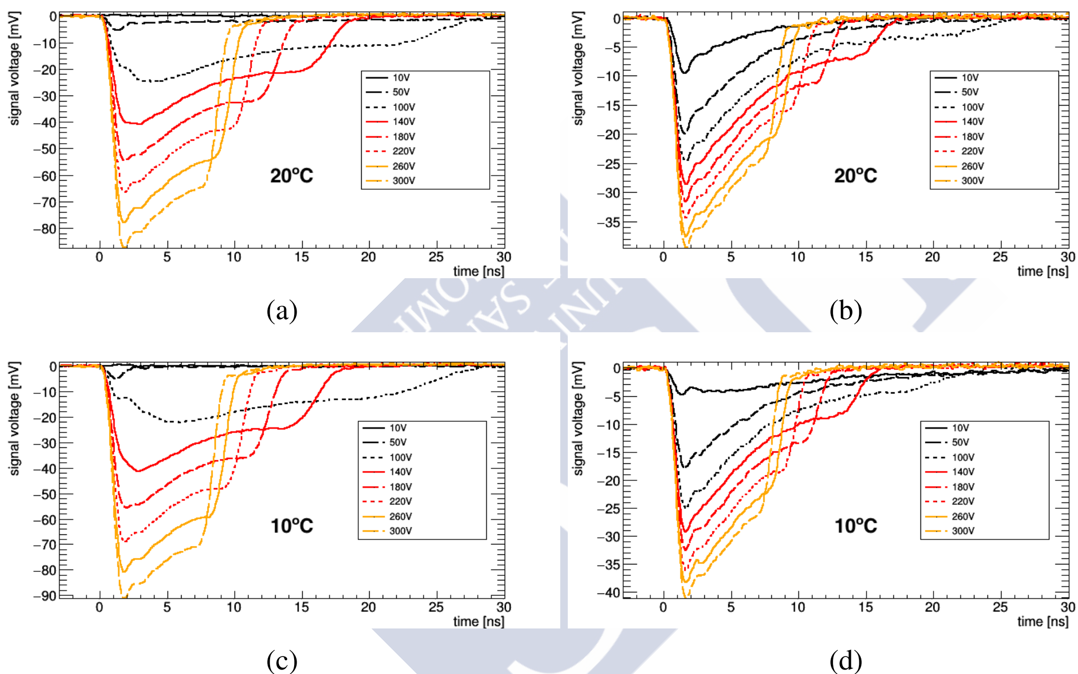

Figure B.5: Red-front TCT waveforms from (left) LGAD_7859_7_W3_C2_3 (2.0×10^{13} cm^{-2}) and (right) PIN_7859_4_W3_I8_1 (PiN diode), from W3, irradiated up to 10^{14} n$_{eq}$/cm^2, at 20, and 10°C.

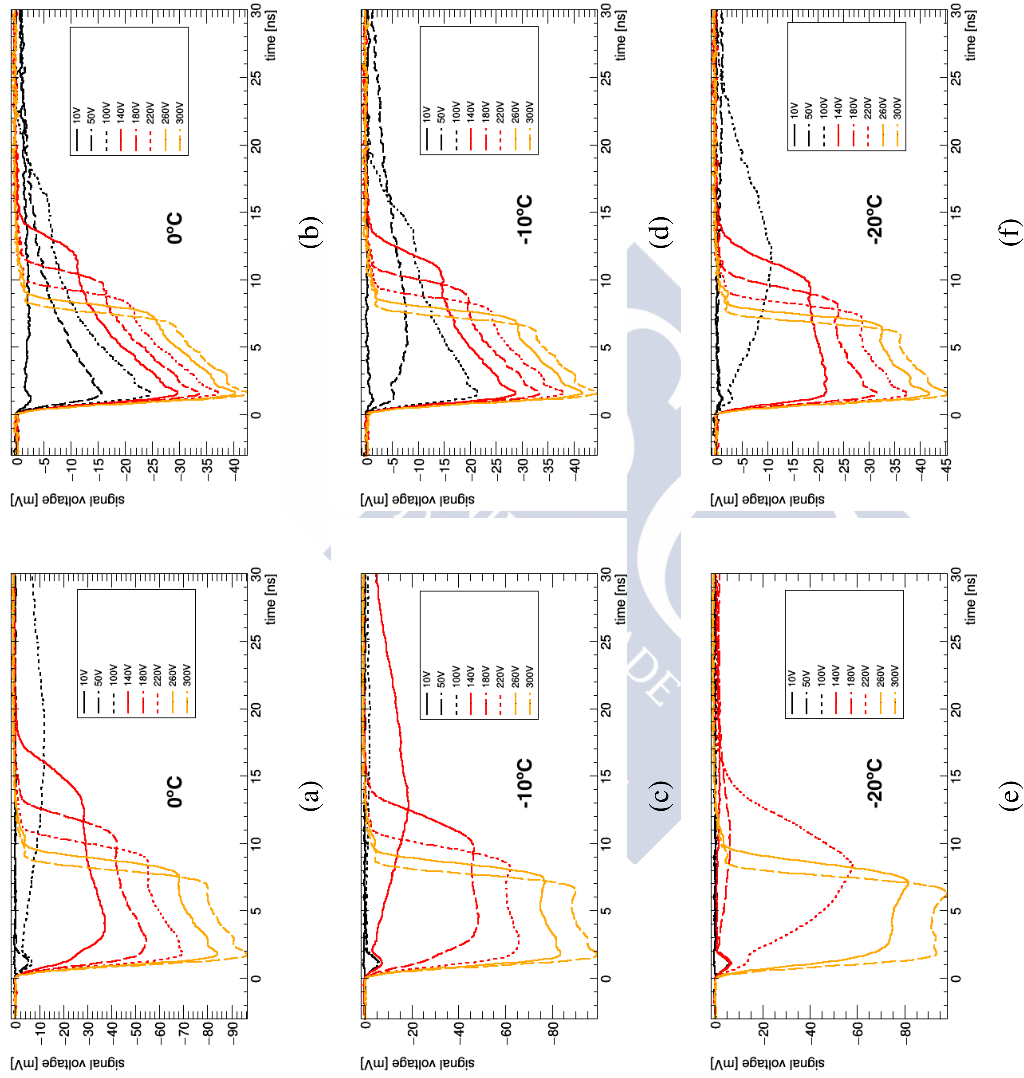

Figure B.6: Red-front TCT waveforms from (left) LGAD_7859_7_W3_C2_3 (2.0×10^{13} cm^{-2}) and (right) PIN_7859_4_W3_I8_1 (PiN diode), from W3, irradiated up to 10^{14} n_{eq}/cm^2, at 0, -10, and -20°C.

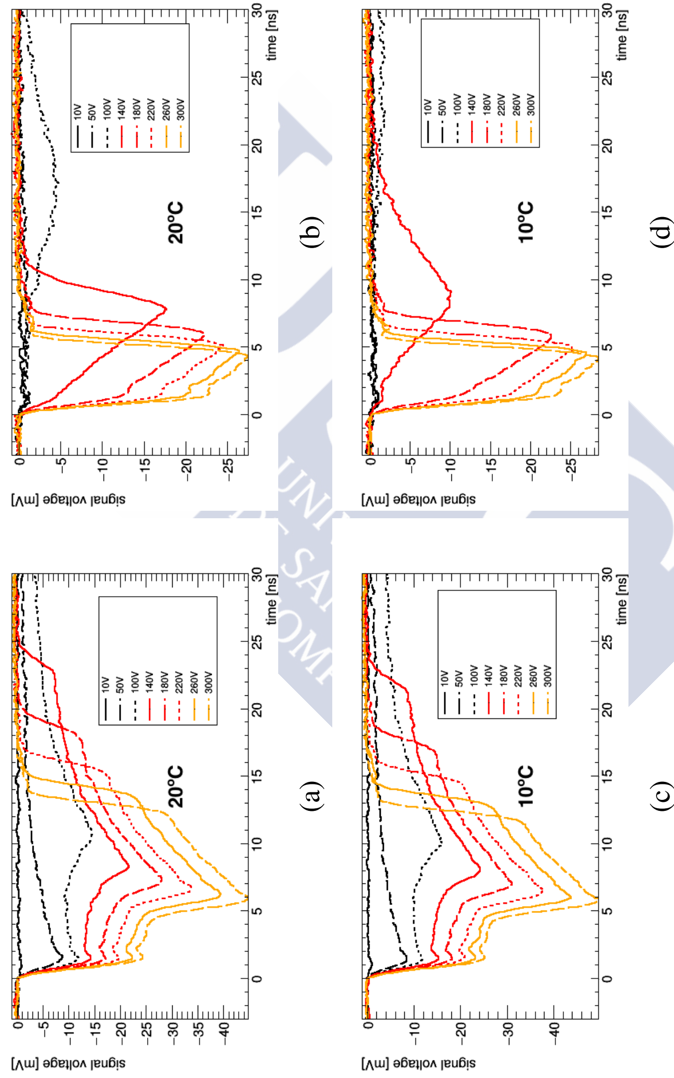

Figure B.7: Red-back TCT waveforms from (left) LGAD_7859_7_W3_C2_3 (2.0×10^{13} cm^{-2}) and (right) PIN_7859_4_W3_I8_1 (PiN diode), from W3, irradiated up to 10^{14} n_{eq}/cm^2, at 20, and 10°C.

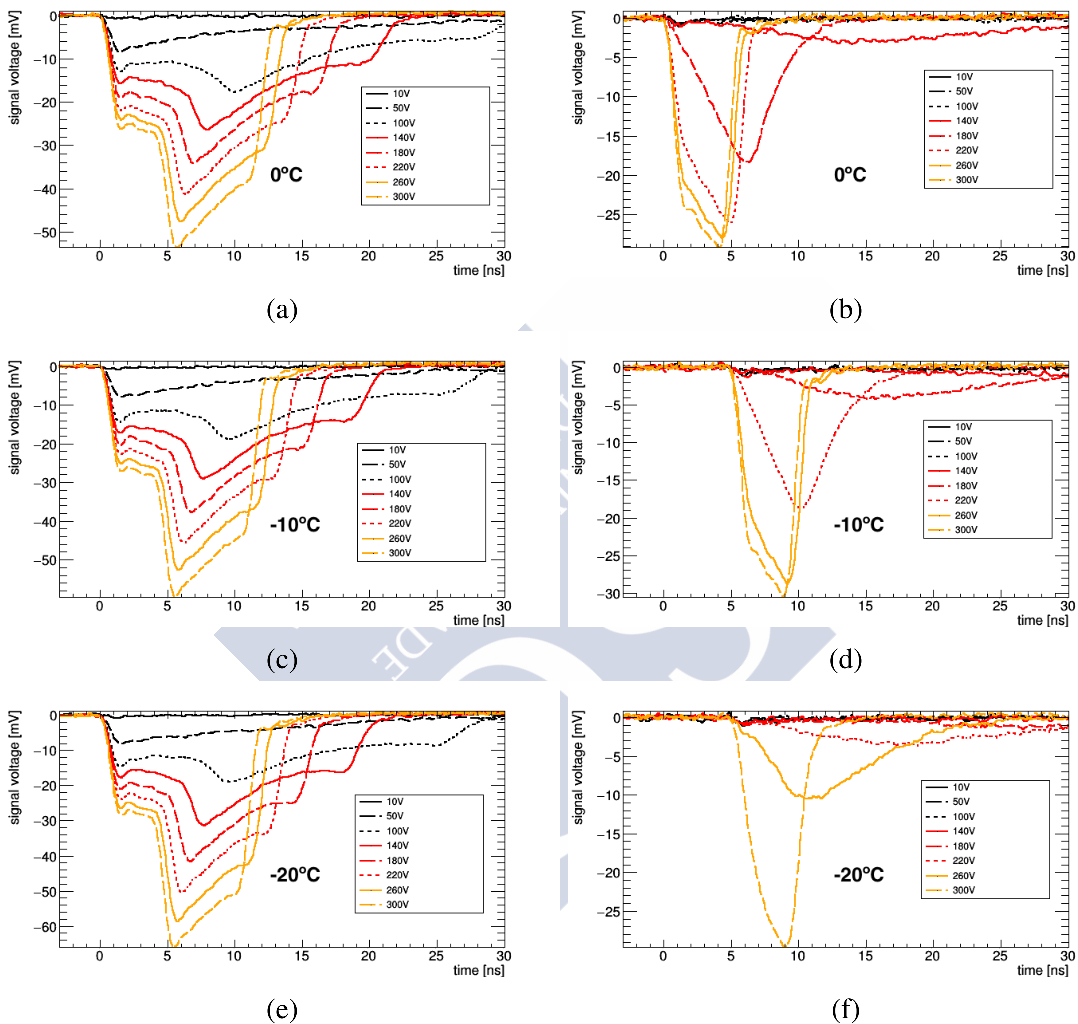

Figure B.8: Red-back TCT waveforms from (left) LGAD_7859_7_W3_C2_3 (2.0×10^{13} cm^{-2}) and (right) PIN_7859_4_W3_I8_1 (PiN diode), from W3, irradiated up to 10^{14} n$_{eq}$/cm^2, at 0, -10, and -20°C.

USC
UNIVERSIDADE
DE SANTIAGO
DE COMPOSTELA

Appendix C

Optical effects caused by glue on 2×2-mm^2 DD-APDs

Before carrying out the study on DD-APDs presented previously in this thesis, a series of preliminary tests were performed. One of these analyses had the aim of determining the source of some observed charge collection areas outside the active area, and even the die area, of the 2×2-mm^2 DD-APDs during IR TCT surface scans. On close inspection of the devices, the unexpected charge areas observed in TCT surface scans outside the die seemed to coincide with the glue/underfill around the silicon (see Figure C.1). The following hypothesis was put forward, IR light might be reflecting on the glue and entering the device, thus creating these spurious charge collection regions outside the actual device. To verify this, part of the sensor was covered with kapton tape, and the latter was covered with black insulating tape. The black insulating tape was not directly attached to the DD-APDs to stop it from leaving any glue residues on the device. Figure C.2 shows a picture of the covered device and an IR TCT surface scan. When comparing the XY scans obtained before and after partially covering the sensor, it is seen that the spurious charge collection disappears in the region covered by the tape. It was thus concluded that the charge collection areas observed outside the active area of the DD-APD are due to the reflection of the IR laser on the glue/underfill.

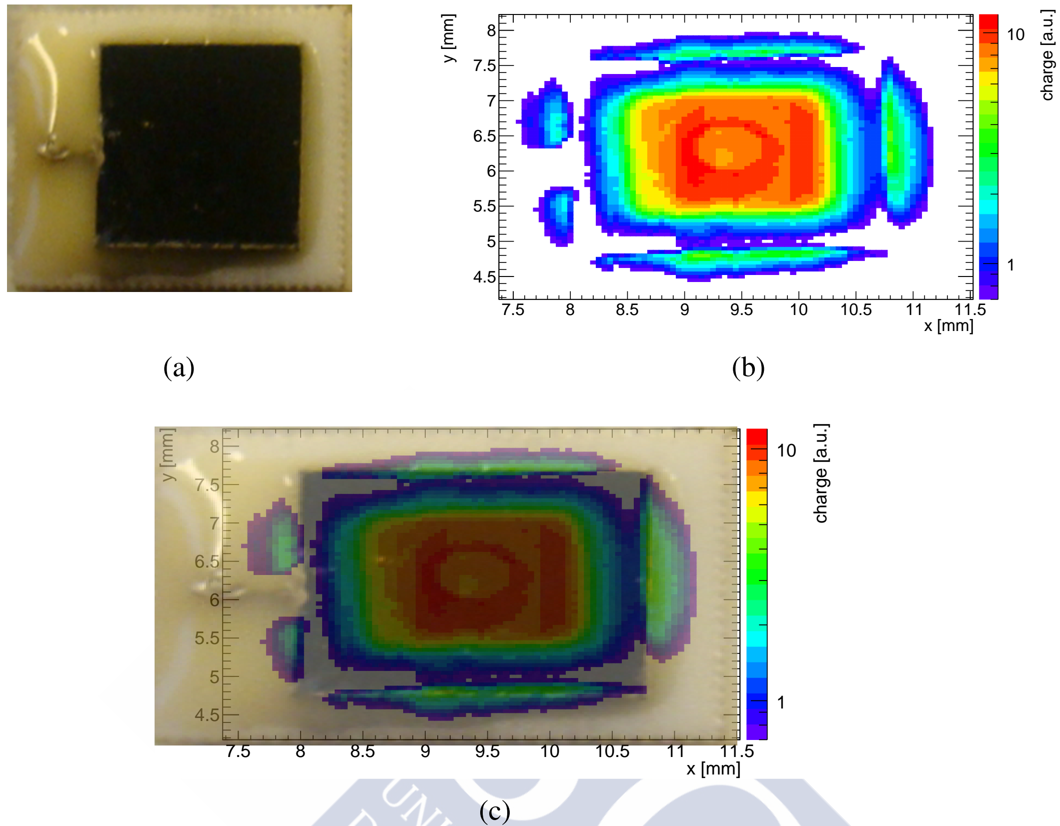

Figure C.1: (a) 2×2-mm^2 DD-APD used for preliminary tests, including the study of unexpected charge collection areas outside the silicon die in IR TCT surface scans. (b) IR TCT surface scan at 1700 V and 20°C on the DD-APD shown in the previous picture. The regions with no charge collection have been filtered out, and the z-axis set to log scale to improve contrast. (c) Scaled superposition of the photo of the DD-APD and its TCT scan.

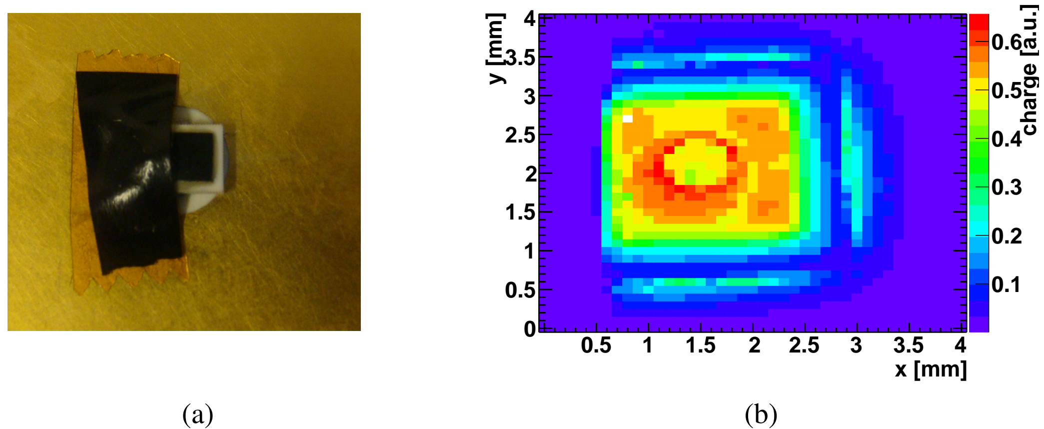

Figure C.2: (a) Partially covered DD-APD. (b) IR TCT surface scan at 1500 V and 20°C of the covered sample. The pattern of charge collection previously observed on the left has disappeared.

Appendix D

About voltage scans on 2×2-mm^2 DD-APDs with very high gain

As described in Section 8.2.2, all 2×2-mm^2 DD-APDs from the second set received were tested before and after irradiation. During red and IR TCT scans before irradiation, it was found that at voltages above 1740 V all samples, except APD_2B_7, reached a plateau, where charge collection remained fairly constant with respect to voltage. This can be seen in Figure D.1. In order to understand what was occurring, the leakage current with respect to voltage curves obtained during TCT scans were checked, see Figure D.2. It was found that all samples, barring APD_2B_7, went from a leakage current lower than 0.7 nA at 1700 V to a maximum current at 1800 V of 4.7 μA. This increase coincided in voltage range with the plateau observed in the charge collection curves. In the particular case of sample APD_2B_7, during the IR TCT scan, the leakage current at 1700 V was already above 0.5 μA, and at 1800 V its value was $\sim$ 3 μA. During the red TCT voltage scans, which were performed a few days later, the leakage current at 1700 V increased up to 6.7 μA, and at 1800 V it reached almost 9.8 μA. As regards the voltage scans for this specific device, the charge collection at high voltages was lower than for other sensors. In fact, at 1800 V the charge collected with IR TCT by APD_2B_7 was $\sim$ 2 times lower than that of the next device with low charge collection.

All these observations seemed to lead towards a relation between low or stagnant charge collection and higher values of leakage current. A deeper examination of the circuitry used for the biasing and read-out of the devices during TCT measurements brought to light the cause of such behaviour. Figure D.3 gives an outline of the circuitry in question, from which one can derive that during TCT DD-APDs are connected in series with a total resistance of 13 MΩ. Having such a high resistance in series with the device can cause drops in the voltage that is actually applied to the sensor. For most samples, before irradiation and at voltages below 1740 V, the leakage current was of the order of 1 nA, which translates into a voltage drop of only 13 mV. However, even a leakage current of 1 μA can cause a drop of 13 V. Considering that the highest leakage current observed (without including sample APD_2B_7) was of 4.7 μA, that would account for a 61.1 V drop. This means that whilst the power supply may be providing a voltage as high as

1800 V, that is not the actual voltage reaching the sensor under bias. This explains why the charge collection becomes almost constant. The power supply provides 1800 V, and that is the value stored by the DAQ. However, the actual bias voltage is $\sim$ 60 V lower, i.e. $\sim$ 1740 V. As regards the special case of sample APD_2B_7, the drop in potential begins at lower voltages. So much so, that during the red TCT scan, when the power supply provides 1800 V, the actual biasing is of merely $\sim$ 1673 V. Evidently, to conduct an accurate study of these scans, it was necessary to correct the voltage values from those provided by the power supply to those actually applied to the sensors. The resulting charge collection curves before irradiation can be seen in Figure D.4, as well as in Section 8.2.2. The voltage correction was also applied on the scans obtained after irradiation.

After correcting for the resistance-induced voltage drop, another particularity was found in the before-irradiation curves. Although the plateau caused by the misidentified voltages was fixed, the curves continued to present a lower slope at the highest voltages. The only sensor that did not show this same behaviour was sample APD_2B_7. The main differences between the latter and the other samples were the lower charge collection, and the lower gain. As a matter of fact, with IR TCT at 1740 V sample APD_2B_7 had a gain 27 times lower than that of the sample with the highest gain (APD_2B_3). To better understand the phenomenon causing this reduction in slope at high voltages, the waveforms obtained for all samples during TCT voltage scans were compared and contrasted. Figure D.5 shows the waveforms obtained during IR and red TCT voltage scans on sample APD_2B_7, and on sample APD_2B_1, which displays the abnormal behaviour and has more than twice the gain of sample APD_2B_7 at 1740 V (IR TCT). The waveforms obtained with both illuminations on sample APD_2B_7 look as expected: the higher the voltage the higher the amplitude. In addition, the pulses from APD_2B_7 fit well within 25 ns, the integration time used for calculating charge collection. On the contrary, sample APD_2B_1 reaches an approximately constant amplitude at 1744 V and 1747 V for IR and red TCT respectively. Furthermore, in this device the pulses are much longer, reaching a width of more than 25 ns. In the case of IR TCT waveforms, the falling edge can be approximately fitted with an exponential decay function. As a result it was found that the time constant at 1749 V for sample APD_2B_1 was $\sim$ 7 times that of APD_2B_7. No fits were done to the falling edges of red TCT waveforms, however, at voltages above 1730 V sample APD_2B_1 presents a tail at the end of the pulses that increases in amplitude and length with voltage. These tails were not seen in sample APD_2B_7, having said that, this sample could only be biased up to 1673 V, and at those voltages the waveforms in APD_2B_1 had no tails.

All of these observations regarding sample APD_2B_1 (and all the others except for APD_2B_7) are consistent with a phenomenon called *plasma effect*, first observed and documented in [109]. Such an effect can be caused by heavily ionising particles, high-intensity laser injection or high impact ionisation inside the device. Under these circumstances, a dense *plasma column* made up of charge carriers is created. As the device is biased, the plasma is polarised in such a way that the external electric field is screened by the charges in the outermost layer of the plasma [115]. The applied reverse bias field

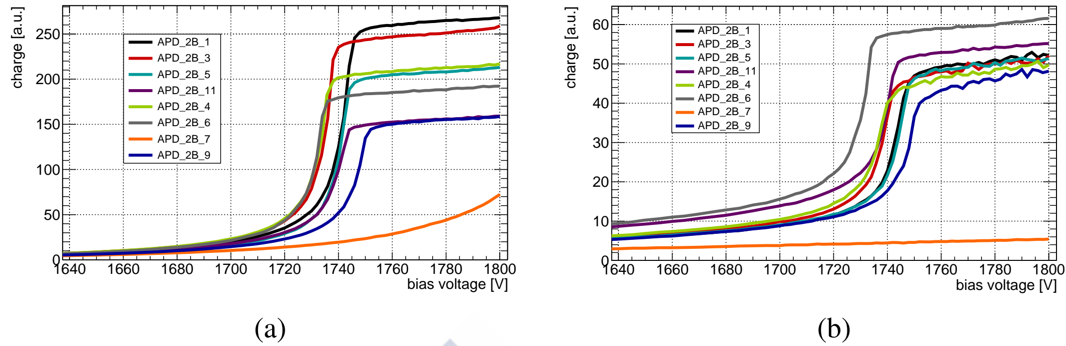

Figure D.1: High-voltage detail of (a) IR and (b) red TCT charge collection scans. The voltage indicated is that provided by the power supply, yet not the one actually being applied to the sensors.

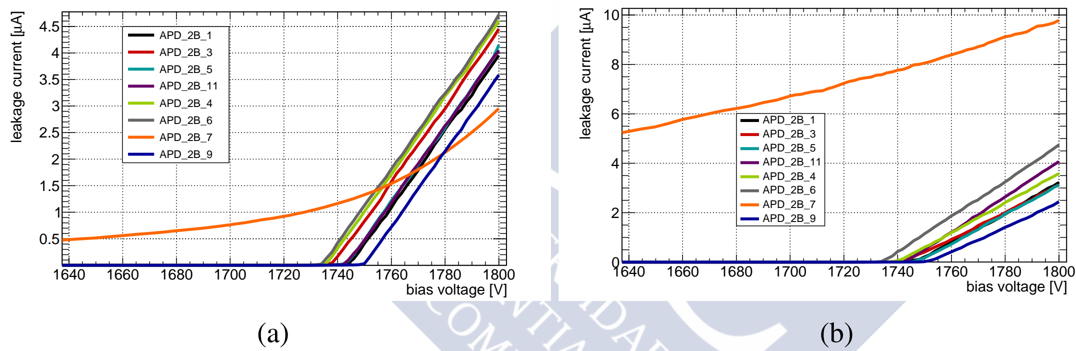

Figure D.2: High-voltage detail of the leakage current with respect to voltage during (a) IR and (b) red TCT voltage scans. The voltage here shown is that provided by the power supply.

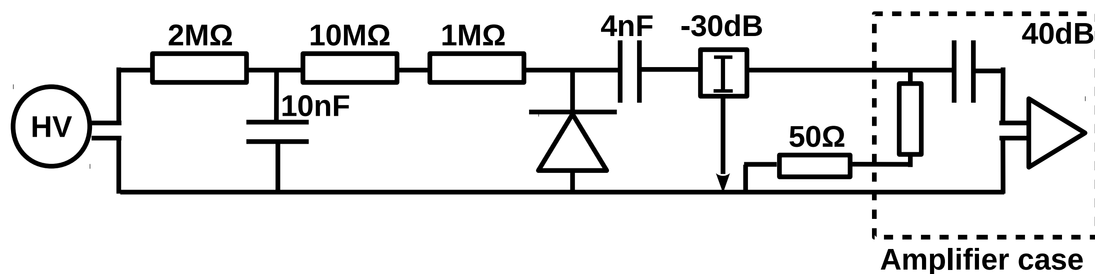

Figure D.3: Schematic of the biasing and read-out circuitry used during TCT measurements on DD-APDs.

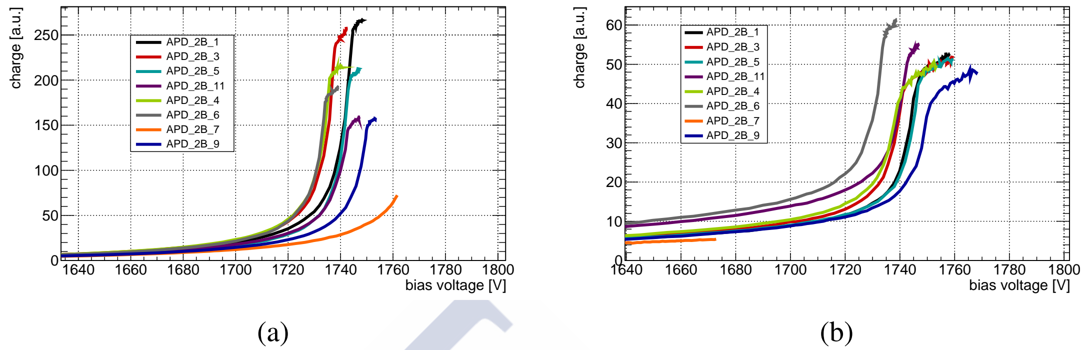

(a) (b)

Figure D.4: High-voltage detail of (a) IR and (b) red TCT charge collection scans after correcting for the resistance-induced voltage drop. The voltage indicated is the actual bias voltage applied to the sensor.

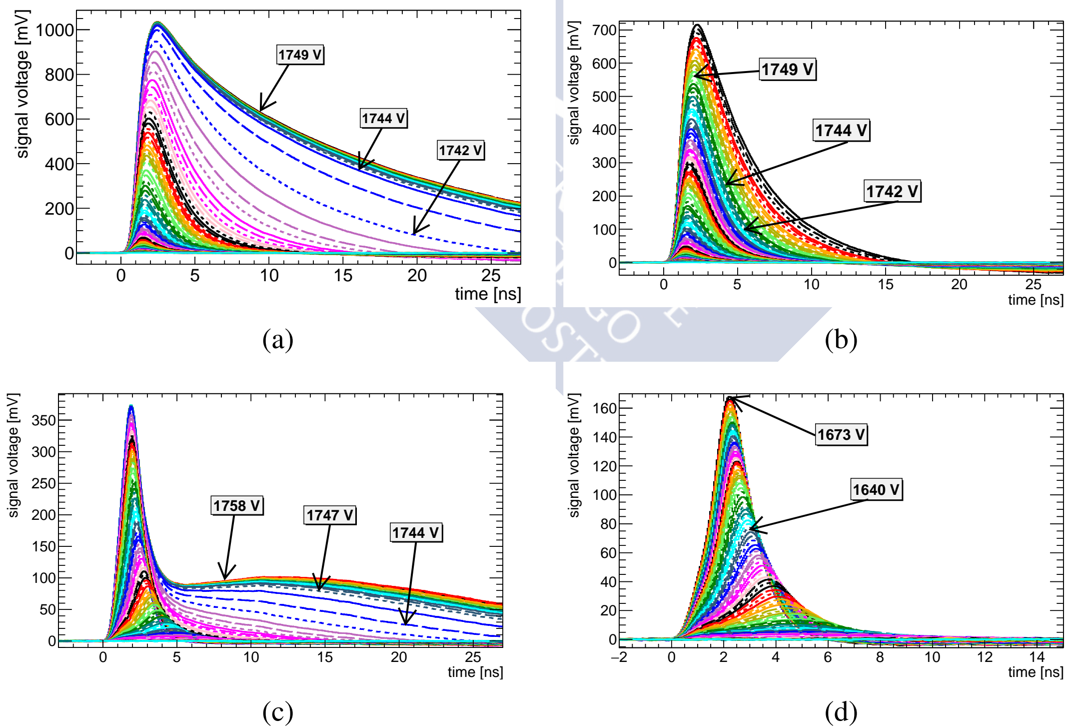

(a) (b)

(c) (d)

Figure D.5: Waveforms obtained at -20°C, before irradiation, through (top) IR and (bottom) red TCT on samples (left) APD_2B_1 and (right) APD_2B_7.

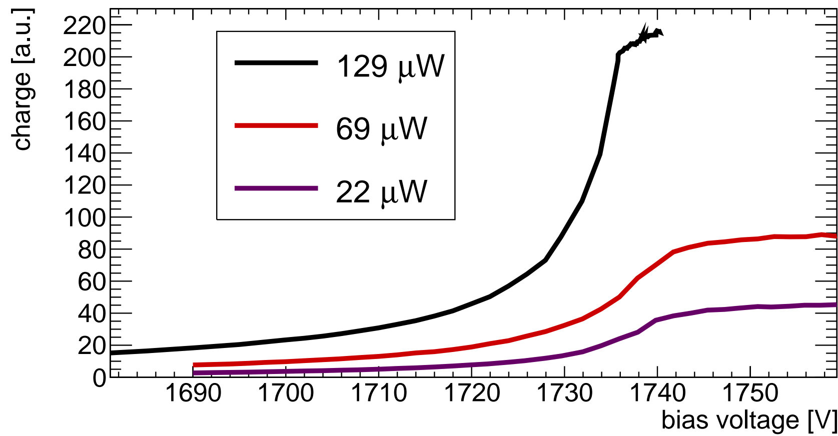

Figure D.6: IR TCT voltage scans obtained from sample APD_2B_4 with three different intensities: 129 μW (the IR intensity used throughout this thesis to measure DD-APDs), 69 μW, and 22 μW.

causes the outermost layer of charges to drift towards the electrodes, thus removing those charges and reducing the density of the plasma. At the same time, the plasma column expands radially, thus increasing its surface and volume, due to the radial diffusion[1] of charge carriers. This expansion causes a decrease in charge carrier density of the plasma. Eventually, a critical density is reached at which the internal plasma field equals the external applied bias field, and the plasma column collapses. [116]. Evidently, this phenomenon delays the transport of charge carriers, which leads to the charge collection time being longer than anticipated, and it can affect the charge collection efficiency of the sensor in question [115].

Finally, measurements were done at different laser intensities to verify if this was the cause of the plasma effect in DD-APDs. Figure D.6 shows the IR TCT voltage scans obtained from sample APD_2B_4 with three different intensities: 129 μW (the IR intensity used throughout this thesis to measure DD-APDs), 69 μW, and 22 μW. The scans for the lowest intensities were done only for voltages above 1690 V, and they reached higher voltages than the scan at 129 μW because the leakage current was lower during the measurements. Naturally, the bias voltage indicated in Figure D.6 is the voltage that was actually applied to the device, i.e. it has been corrected to account for the resistance-induced voltage drop. What can be observed in the scans shown in Figure D.6 is that even at the lowest intensity the plasma-induced plateau is present. Therefore, the origin of the plasma effect in these devices in particular seems to be the high gain of the sensors.

[1]Radial diffusion: towards the edges of the sensor.

USC
UNIVERSIDADE
DE SANTIAGO
DE COMPOSTELA

Appendix E

IV curves of 2×2-mm^2 DD-APDs at different temperatures

The following pages present all the IV curves obtained with 2×2-mm^2 DD-APDs, from the second set, at different temperatures. These measurements were done on APD_2B_6 before irradiation, and on all irradiated devices except APD_2B_6, which could not be biased after irradiation (I(7 V) $\sim$ 1.5 mA). Both before and after irradiation, it is seen that the onset of multiplication occurs at lower voltages for lower temperatures. This is due to the dependence on temperature of impact ionisation, see Chapter 6. Also, it is seen that, as expected, the leakage current increases with temperature and with fluence (see Chapter 3).

USC
UNIVERSIDADE
DE SANTIAGO
DE COMPOSTELA

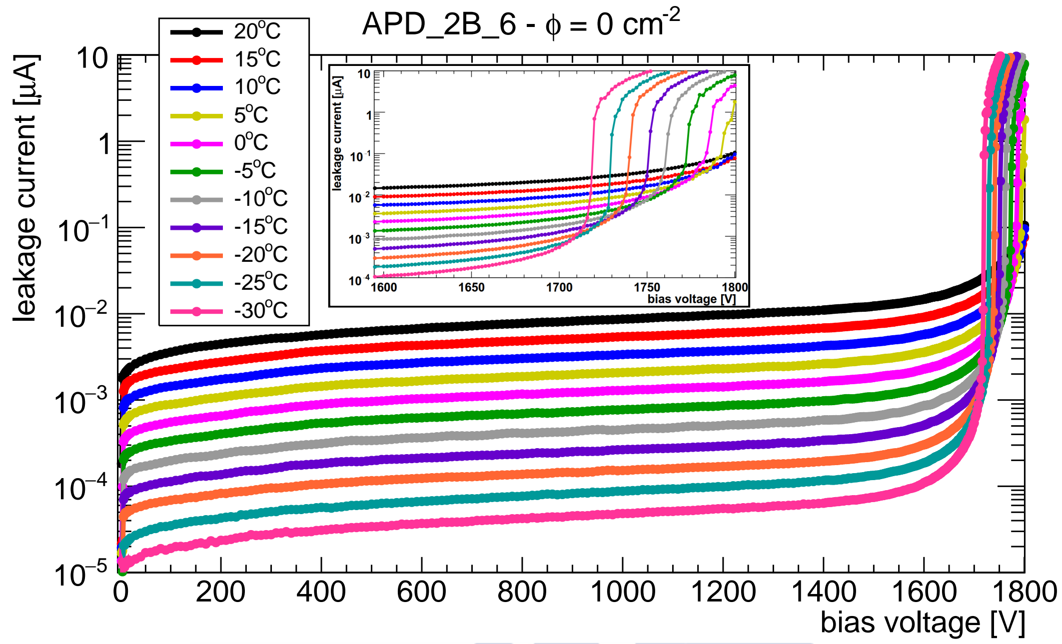

Figure E.1: Leakage current at different temperatures before irradiation, sample APD_2B_6.

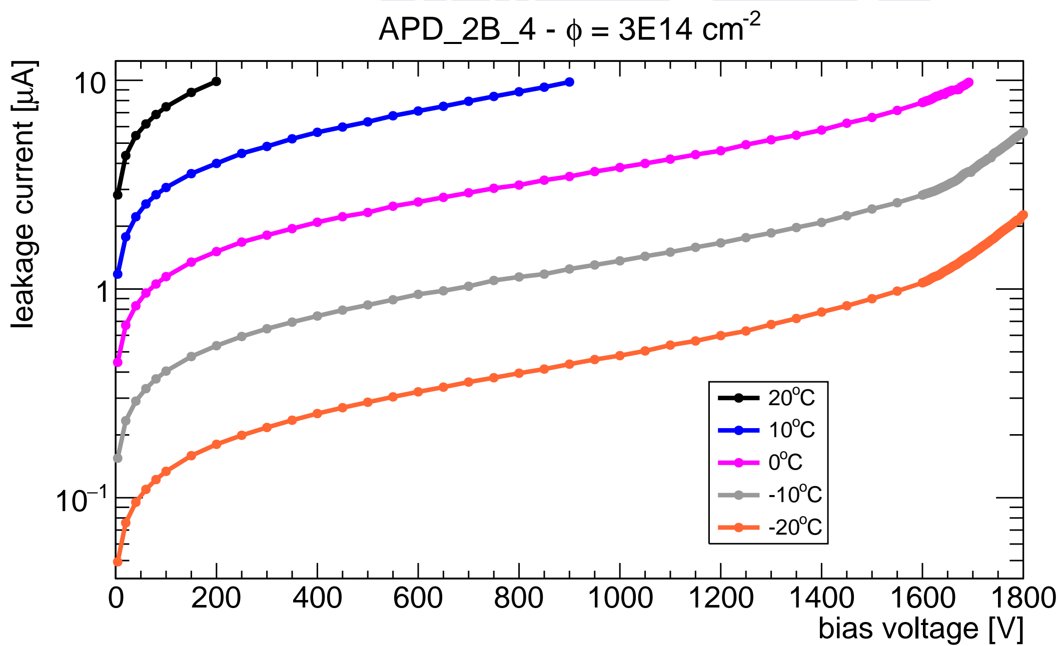

Figure E.2: Leakage current at different temperatures after irradiation to 3×10^{14} n_{eq}/cm^2, sample APD_2B_4.

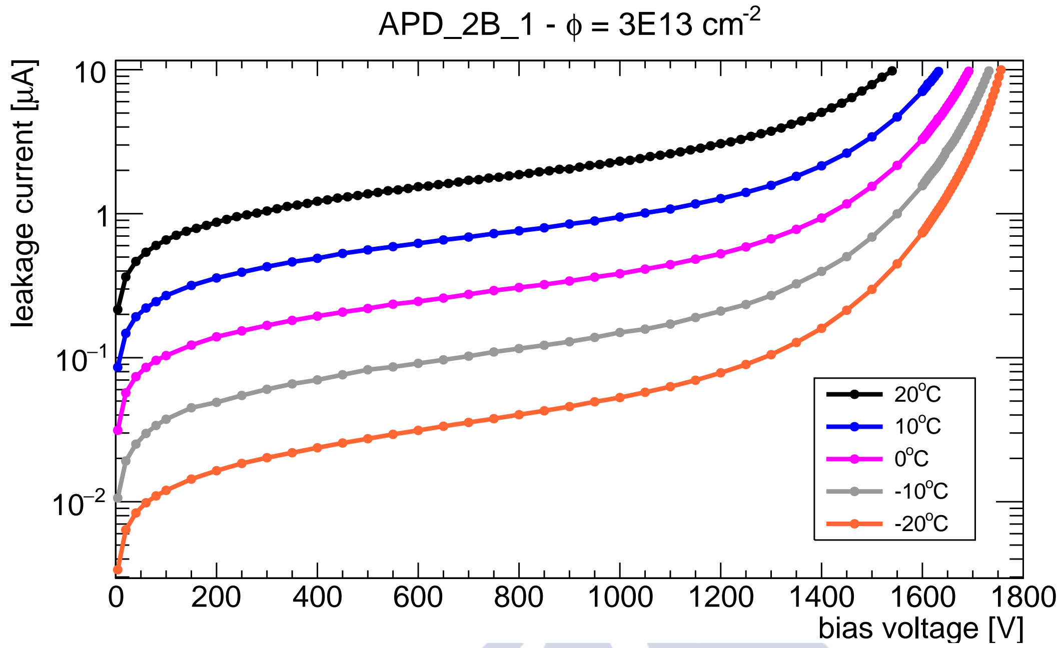

Figure E.3: Leakage current at different temperatures after irradiation to 3×10^{13} n_{eq}/cm^2, sample APD_2B_1.

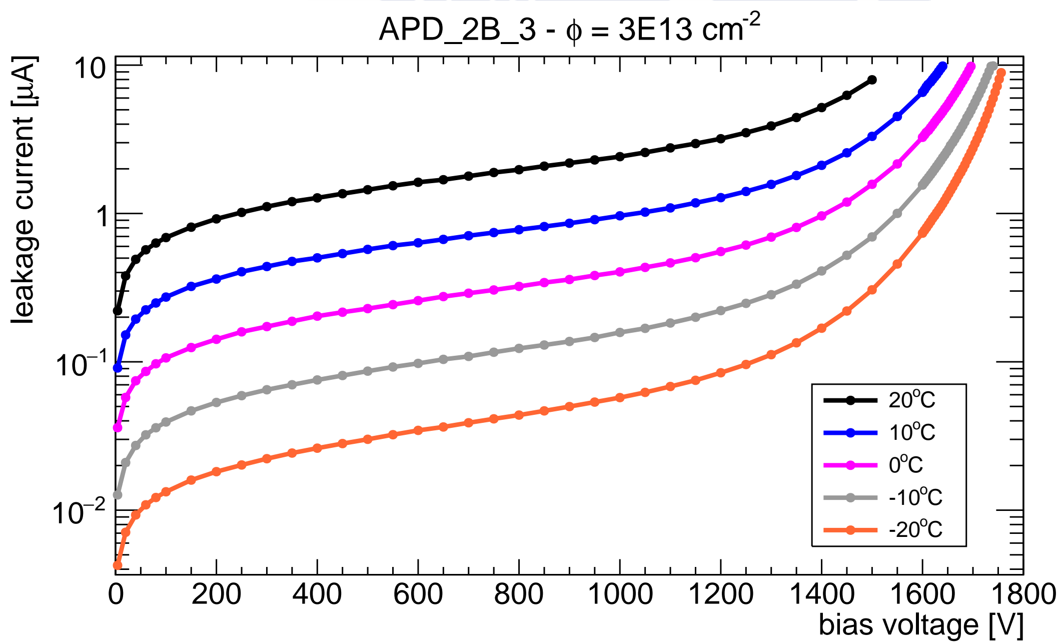

Figure E.4: Leakage current at different temperatures after irradiation to 3×10^{13} n_{eq}/cm^2, sample APD_2B_3.

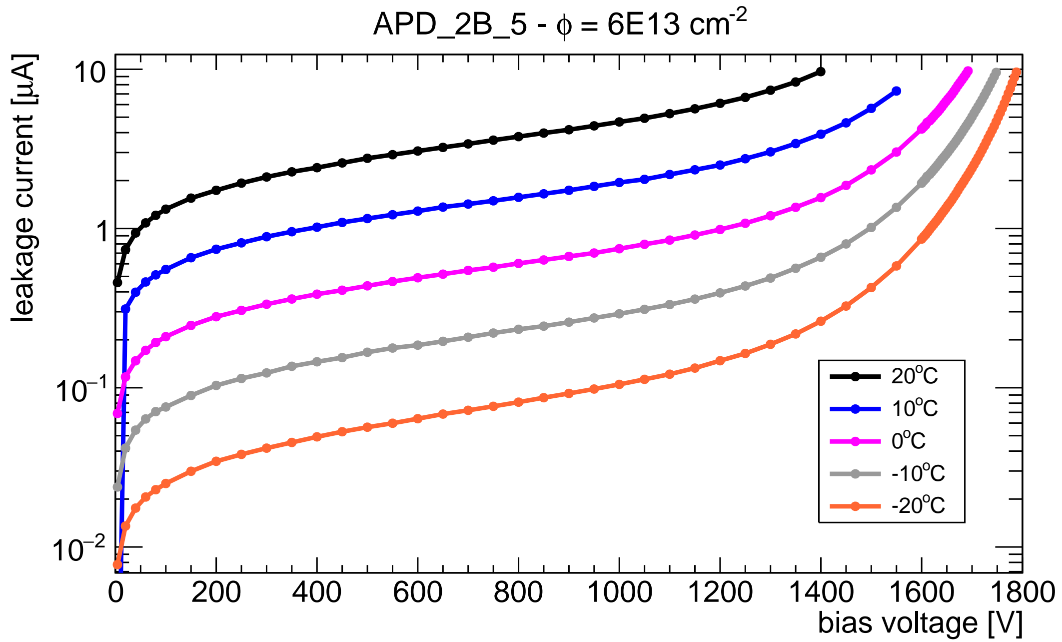

Figure E.5: Leakage current at different temperatures after irradiation to 6×10^{13} n_{eq}/cm^2, sample APD_2B_5.

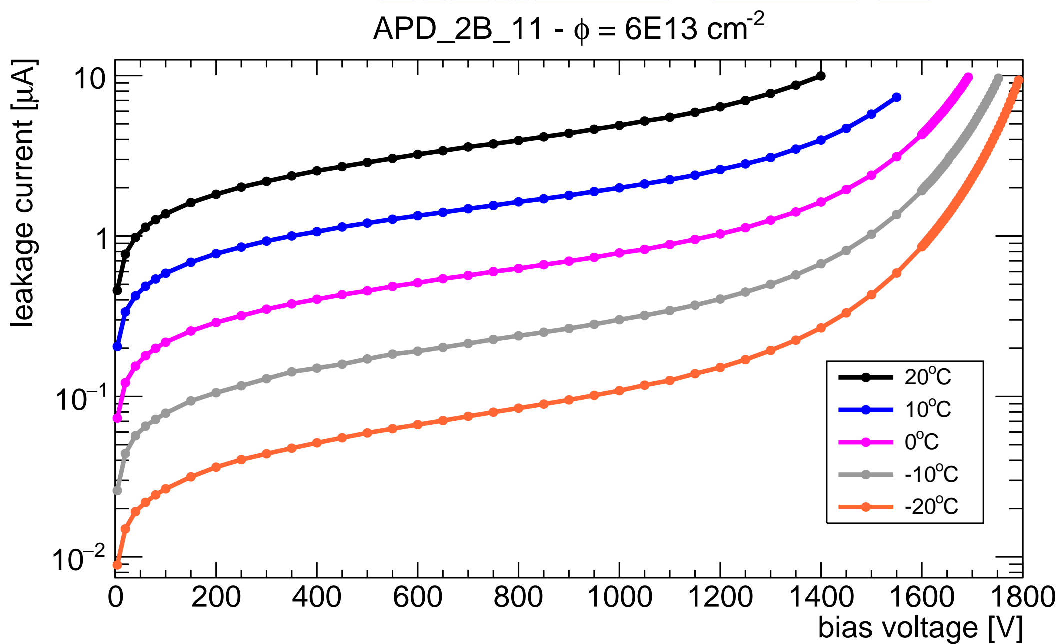

Figure E.6: Leakage current at different temperatures after irradiation to 6×10^{13} n_{eq}/cm^2, sample APD_2B_11.

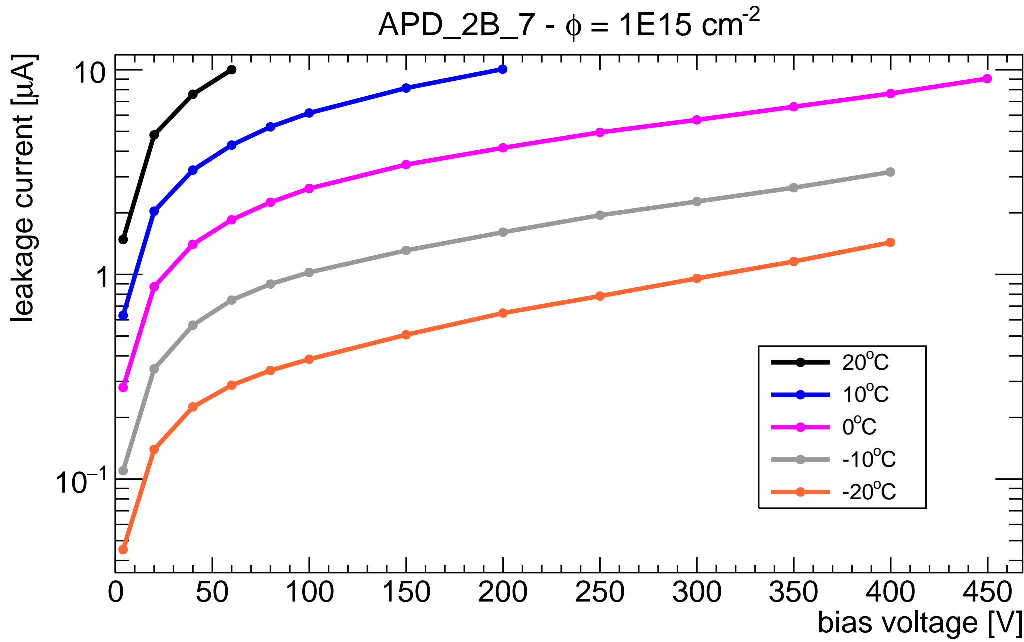

Figure E.7: Leakage current at different temperatures after irradiation to 1×10^{15} n_{eq}/cm^2, sample APD_2B_7.

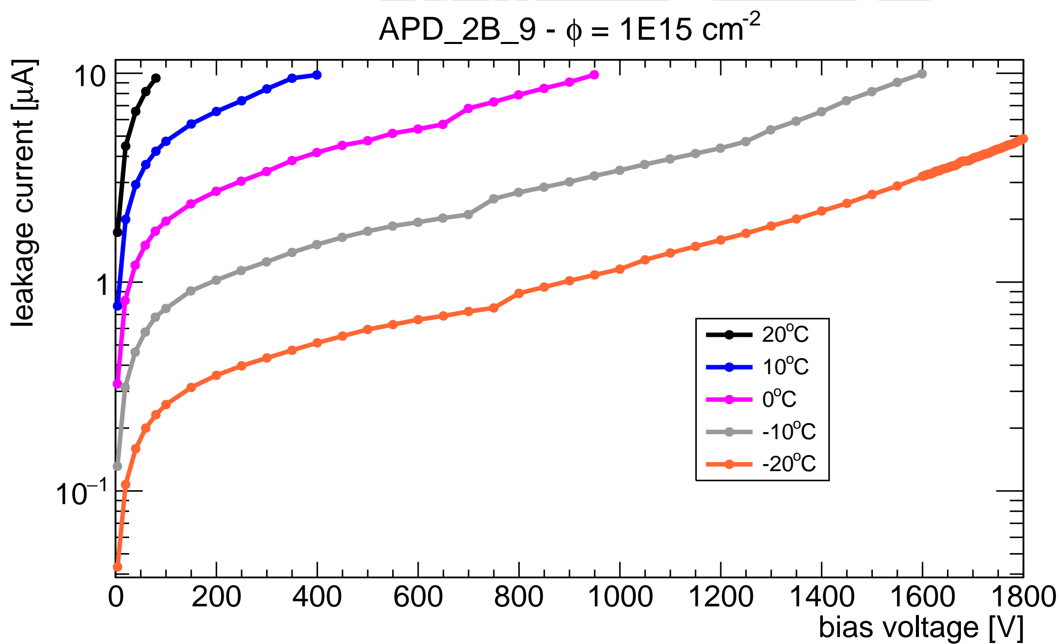

Figure E.8: Leakage current at different temperatures after irradiation to 1×10^{15} n_{eq}/cm^2, sample APD_2B_9.

USC
UNIVERSIDADE
DE SANTIAGO
DE COMPOSTELA

Bibliography

[1] G. Apollinari *et al.*, *High-Luminosity Large Hadron Collider (HL-LHC): Technical Design Report V. 0.1*, ser. CERN Yellow Reports: Monographs. Geneva: CERN, 2017. [Online]. Available: https://cds.cern.ch/record/2284929

[2] F. Pastore; on behalf of the ATLAS Collaboration, "ATLAS Run-2 status and performance," *Nucl. Part. Phys. Proc.*, vol. 270-272, pp. 3 – 7, 2016, 18th Montpellier International Conference on Quantum Chromodynamics (QCD 15). [Online]. Available: http://www.sciencedirect.com/science/article/pii/S2405601416000031

[3] D. Contardo *et al.*, "Technical Proposal for the Phase-II Upgrade of the CMS Detector," CERN, Geneva, Tech. Rep. CERN-LHCC-2015-010. LHCC-P-008. CMS-TDR-15-02, Jun 2015. [Online]. Available: https://cds.cern.ch/record/2020886

[4] F. Gianotti *et al.*, "Physics potential and experimental challenges of the LHC luminosity upgrade," *Eur. Phys. J. C*, vol. 39, no. 3, pp. 293–333, 2005. [Online]. Available: http://dx.doi.org/10.1140/epjc/s2004-02061-6

[5] H.F.-W. Sadrozinski *et al.*, "Sensors for ultra-fast silicon detectors," *Nucl. Instrum. Meth. A*, vol. 765, pp. 7 – 11, 2014, Proceedings of the 9th International "Hiroshima" Symposium on Development and Application of Semiconductor Tracking Detectors. [Online]. Available: http://www.sciencedirect.com/science/article/pii/S0168900214005051

[6] G. Kramberger *et al.*, "Electric field in heavily irradiated silicon detectors based on Edge-TCT measurements," in *Proceedings of the 21st International Workshop on Vertex Detectors: Jeju Island, Republic of Korea, September 16-21, 2012 — PoS(Vertex 2012)*, vol. 167, 2013, p. 022. [Online]. Available: https://doi.org/10.22323/1.167.0022

[7] G. Pellegrini *et al.*, "Technology developments and first measurements of Low Gain Avalanche Detectors (LGAD) for high energy physics applications," *Nucl. Instrum. Meth. A*, vol. 765, pp. 12 – 16, 2014, Proceedings of the 9th International "Hiroshima" Symposium on Development and Application of Semiconductor Tracking Detectors. [Online]. Available: http://www.sciencedirect.com/science/article/pii/S0168900214007128

[8] M. Mcclish *et al.*, “A Reexamination of Deep Diffused Silicon Avalanche Photodiode Gain and Quantum Efficiency,” *IEEE Transactions on Nuclear Science*, vol. 53, no. 5, pp. 3049–3054, Oct 2006.

[9] Centre Nacional de Microelectrònica, IMB-CNM-CSIC, Barcelona, Spain. [Online]. Available: http://www.imb-cnm.csic.es/index.php/en/

[10] G. Kramberger *et al.*, “Radiation effects in Low Gain Avalanche Detectors after hadron irradiations,” *JINST*, vol. 10, no. 07, p. P07006, 2015. [Online]. Available: http://stacks.iop.org/1748-0221/10/i=07/a=P07006

[11] E. Cavallaro *et al.*, “First measurements of segmented silicon tracking detectors with built-in multiplication layer,” *Nucl. Instrum. Meth. A*, vol. 796, no. Supplement C, pp. 136 – 140, 2015, proceedings of the 10th International Conference on Radiation Effects on Semiconductor Materials Detectors and Devices. [Online]. Available: http://www.sciencedirect.com/science/article/pii/S0168900215006336

[12] G. Pellegrini *et al.*, “Recent technological developments on LGAD and iLGAD detectors for tracking and timing applications,” *Nucl. Instrum. Meth. A*, vol. 831, pp. 24 – 28, 2016, Proceedings of the 9th International “Hiroshima” Symposium on Development and Application of Semiconductor Tracking Detectors. [Online]. Available: http://www.sciencedirect.com/science/article/pii/S0168900216304557

[13] N. Cartiglia *et al.*, “Beam test results of a 16 ps timing system based on ultra-fast silicon detectors,” *Nucl. Instrum. Meth. A*, vol. 850, no. Supplement C, pp. 83 – 88, 2017. [Online]. Available: http://www.sciencedirect.com/science/article/pii/S0168900217300219

[14] C. Gallrapp *et al.*, “Study of gain homogeneity and radiation effects of Low Gain Avalanche Pad Detectors,” *Nucl. Instrum. Meth. A*, vol. 875, pp. 27 – 34, 2017. [Online]. Available: http://www.sciencedirect.com/science/article/pii/S0168900217307799

[15] S. Otero Ugobono *et al.*, “Radiation Tolerance of Proton-Irradiated LGADs,” *IEEE Transactions on Nuclear Science*, vol. 65, no. 8, pp. 1667–1675, Aug 2018.

[16] S. Otero Ugobono *et al.*, “Multiplication onset and electric field properties of proton irradiated LGADs,” to be published in Proceedings, 26th International Workshop on Vertex Detectors (Vertex 2017): Asturias, Spain, September 10-15, 2017.

[17] C. Agapopoulou, “A High-Granularity Timing Detector for the Phase-II upgrade of the ATLAS Detector System,” CERN, Geneva, Tech. Rep. ATL-LARG-PROC-2017-004, Nov 2017. [Online]. Available: http://cds.cern.ch/record/2293126

[18] The CMS and TOTEM Collaborations, “CMS-TOTEM Precision Proton Spectrometer,” CERN, Tech. Rep. CERN-LHCC-2014-021. TOTEM-TDR-003. CMS-TDR-13, Sep 2014. [Online]. Available: https://cds.cern.ch/record/1753795

USC UNIVERSIDADE DE SANTIAGO DE COMPOSTELA

[19] CMS Collaboration, "Technical Proposal for a MIP Timing Detector in the CMS Experiment Phase 2 Upgrade," CERN, Geneva, Tech. Rep. CERN-LHCC-2017-027. LHCC-P-009, Dec 2017. [Online]. Available: https://cds.cern.ch/record/2296612

[20] S. White, "Hyperfast Sensor Development for the HL-LHC era," presented at Joint Instrumentation Seminar, June 12th 2015, DESY, Hamburg, Germany. [Online]. Available: https://instrumentationseminar.desy.de/e187807/

[21] M. Centis Vignali *et al.*, "Characterization of Irradiated APDs for Timing Applications," presented at the *31st RD50 Workshop*, CERN, Geneva, Switzerland, 2017.

[22] R. Grazioso *et al.*, "Radiation hardness of high gain avalanche photodiodes," in *2001 IEEE Nuclear Science Symposium Conference Record (Cat. No.01CH37310)*, vol. 1, Nov 2001, pp. 240–244 vol.1.

[23] M. C. Vignali *et al.*, "Characterization of irradiated APDs for picosecond time measurements," *Journal of Instrumentation*, vol. 13, no. 01, p. C01041, 2018. [Online]. Available: http://stacks.iop.org/1748-0221/13/i=01/a=C01041

[24] M. Centis Vignali *et al.*, "Deep Diffused APDs for Charged Particles Timing Applications," to be published.

[25] H. Spieler, *Semiconductor Detector Systems*. Oxford, Great Britain: Oxford University Press, 2005.

[26] M. Moll, "Radiation Damage in Silicon Particle Detectors," Ph.D. thesis, Universität Hamburg, 1999. [Online]. Available: https://mmoll.web.cern.ch/mmoll/thesis/

[27] LHCb Collaboration, "LHCb VELO Upgrade Technical Design Report," CERN, Tech. Rep. CERN-LHCC-2013-021. LHCB-TDR-013, Nov 2013. [Online]. Available: https://cds.cern.ch/record/1624070

[28] S. Sze and K. N. Kwok, *Physics of Semiconductor Devices; 3rd ed.* Hoboken, NJ: Wiley, 2007. [Online]. Available: https://cds.cern.ch/record/1092737

[29] G. Lutz, *Semiconductor Radiation Detectors: Device Physics*. Berlin; New York: Springer, 1999.

[30] S. Sze and M.-K. Lee, *Semiconductor devices: physics and technology; 3rd ed.* Hoboken, NJ: Wiley, 2012. [Online]. Available: https://cds.cern.ch/record/1632394

[31] E. Fluck, "New notations in the periodic table," *Pure and Applied Chemistry*, vol. 60, no. 3, pp. 431–436, jan 1988. [Online]. Available: https://doi.org/10.1351/pac198860030431

USC UNIVERSIDADE DE SANTIAGO DE COMPOSTELA

[32] L. Gimmestad Johansen, "Radiation hard silicon microstrip detectors for use in ATLAS at CERN," Ph.D. thesis, Universitetet i Bergen, 2005. [Online]. Available: https://inis.iaea.org/collection/NCLCollectionStore/_Public/36/117/36117215.pdf

[33] P. Riedler, "Radiation Damage Effects and Performance of Silicon Strip Detectors using LHC Readout Electronics," Ph.D. thesis, Universität Wien, 1998. [Online]. Available: https://cds.cern.ch/record/423114

[34] M. Huhtinen, "Simulation of non-ionising energy loss and defect formation in silicon," *Nucl. Instrum. Meth. A*, vol. 491, no. 1, pp. 194 – 215, 2002. [Online]. Available: http://www.sciencedirect.com/science/article/pii/S0168900202012275

[35] G. Lindström, S. Watts, and F. Lemeilleur, "3rd RD48 status report: the ROSE collaboration (R&D on silicon for future experiments)," CERN, Tech. Rep. CERN-LHCC-2000-009, 1999. [Online]. Available: https://cds.cern.ch/record/421210

[36] G. Kramberger *et al.*, "Effective trapping time of electrons and holes in different silicon materials irradiated with neutrons, protons and pions," *Nucl. Instrum. Meth. A*, vol. 481, no. 1, pp. 297 – 305, 2002. [Online]. Available: http://www.sciencedirect.com/science/article/pii/S0168900201012633

[37] G. Lutz, "Effects of deep level defects in semiconductor detectors," *Nucl. Instrum. Meth. A*, vol. 377, no. 2, pp. 234 – 243, 1996, proceedings of the Seventh European Symposium on Semiconductor. [Online]. Available: http://www.sciencedirect.com/science/article/pii/0168900296000253

[38] A. S. Grove, *Physics and technology of semiconductor devices*. New York, NY: Wiley, 1967.

[39] D. Pitzl *et al.*, "Type inversion in silicon detectors," *Nucl. Instrum. Meth. A*, vol. 311, no. 1, pp. 98 – 104, 1992. [Online]. Available: http://www.sciencedirect.com/science/article/pii/016890029290854W

[40] V. Eremin, Z. Li, and I. Iljashenko, "Trapping induced Neff and electrical field transformation at different temperatures in neutron irradiated high resistivity silicon detectors," *Nucl. Instrum. Meth. A*, vol. 360, no. 1, pp. 458 – 462, 1995, proceedings of the Sixth Pisa Meeting on Advanced Detectors. [Online]. Available: http://www.sciencedirect.com/science/article/pii/0168900295001123

[41] G. Kramberger *et al.*, "Field engineering by continuous hole injection in silicon detectors irradiated with neutrons," *Nucl. Instrum. Meth. A*, vol. 497, no. 2, pp. 440 – 449, 2003. [Online]. Available: http://www.sciencedirect.com/science/article/pii/S0168900202019277

[42] E. Fretwurst *et al.*, "Investigation of damage-induced defects in silicon by TCT," *Nucl. Instrum. Meth. A*, vol. 388, no. 3, pp. 356 – 360, 1997, radiation Effects on Semiconductor Materials, Detectors and Devices. [Online]. Available: http://www.sciencedirect.com/science/article/pii/S0168900297000028

[43] J. W. Corbett, *Electron radiation damage in semiconductors and metals*. New York, NY: Academic Press, 1966. [Online]. Available: https://cds.cern.ch/record/109891

[44] G. Lindström, M. Moll, and E. Fretwurst, "Radiation hardness of silicon detectors – a challenge from high-energy physics," *Nucl. Instrum. Meth. A*, vol. 426, no. 1, pp. 1 – 15, 1999. [Online]. Available: http://www.sciencedirect.com/science/article/pii/S0168900298014624

[45] R. Wunstorf *et al.*, "Investigations of donor and acceptor removal and long term annealing in silicon with different boron/phosphorus ratios," *Nucl. Instrum. Meth. A*, vol. 377, no. 2, pp. 228 – 233, 1996, proceedings of the Seventh European Symposium on Semiconductor. [Online]. Available: http://www.sciencedirect.com/science/article/pii/0168900296002173

[46] J. Adey, "Boron related point defects in silicon," Ph.D. thesis, University of Exeter, 2004. [Online]. Available: https://newton.ex.ac.uk/research/qsystems/people/adey/adey-thesis.pdf

[47] P. G. Dias de Almeida *et al.*, "Characterization of acceptor removal in epitaxial silicon pad diodes," to be published.

[48] D. K. Schroder, *Semiconductor material and device characterization*. USA: John Wiley & Sons, Inc., 2006.

[49] A. Chilingarov, "Temperature dependence of the current generated in Si bulk," *Journal of Instrumentation*, vol. 8, no. 10, p. P10003, 2013. [Online]. Available: http://stacks.iop.org/1748-0221/8/i=10/a=P10003

[50] J. Zhang *et al.*, "Investigation of X-ray induced radiation damage at the Si-SiO_2 interface of silicon sensors for the European XFEL," *Journal of Instrumentation*, vol. 7, no. 12, p. C12012, 2012. [Online]. Available: http://stacks.iop.org/1748-0221/7/i=12/a=C12012

[51] V. Eremin *et al.*, "Development of transient current and charge techniques for the measurement of effective net concentration of ionized charges (Neff) in the space charge region of p-n junction detectors," *Nucl. Instrum. Meth. A*, vol. 372, no. 3, pp. 388 – 398, 1996. [Online]. Available: http://www.sciencedirect.com/science/article/pii/0168900295012958

[52] G. Kramberger *et al.*, "Investigation of Irradiated Silicon Detectors by Edge-TCT," *IEEE Transactions on Nuclear Science*, vol. 57, no. 4, pp. 2294–2302, Aug 2010.

[53] I. Vila *et al.*, "TPA-TCT: A novel Transient Current Technique based on the Two Photon Absorption (TPA) process," presented at the *25th RD50 Workshop*, Geneva, Switzerland, 2014.

[54] L. Franconi, "Insertable B-Layer integration in the ATLAS experiment and development of future 3D silicon pixel sensors," Ph.D. thesis, University of Oslo, 2018. [Online]. Available: https://cds.cern.ch/record/2313668

[55] N. Pacifico and M. De Palma, "Radiation damage study on innovative silicon sensors for the CMS tracker upgrade," Ph.D. thesis, Università degli Studi di Bari Aldo Moro, 2012. [Online]. Available: https://cds.cern.ch/record/2130663

[56] M. Tanabashi *et al.*, "Review of Particle Physics," *Phys. Rev. D*, vol. 98, p. 030001, Aug 2018. [Online]. Available: https://link.aps.org/doi/10.1103/PhysRevD.98.030001

[57] G. Kramberger, "Signal development in irradiated silicon detectors," Ph.D. thesis, Univerza v Ljubljani, 2001. [Online]. Available: http://www-f9.ijs.si/~gregor/papers/dok_eng.pdf

[58] C. Gallrapp *et al.*, "The TCT+ setup - a system for TCT, eTCT and timing measurements," presented at the *1st TCT Workshop*, DESY, Hamburg, Germany, 2015.

[59] Image by Steve Ruzin and Holly Aaron, UC Berkeley. [Online]. Available: http://microscopy.berkeley.edu/courses/tlm/2P/index.html

[60] M. Göppert-Mayer, "Über elementarakte mit zwei quantensprüngen," *Annalen der Physik*, vol. 401, no. 3, pp. 273–294, 1931. [Online]. Available: http://dx.doi.org/10.1002/andp.19314010303

[61] M. Fernández García *et al.*, "TPA-TCT of a neutron irradiated HVCMOS," presented at the *29th RD50 Workshop*, Geneva, Switzerland, 2016.

[62] J. Daintith, *A Dictionary of Physics*, ser. Oxford Paperback Reference. OUP Oxford, 2009. [Online]. Available: https://books.google.fr/books?id=N2PEAQAACAAJ

[63] Chart of Nuclides, National Nuclear Data Center, Brookhaven National Laboratory. [Online]. Available: https://www.nndc.bnl.gov

[64] H. Spieler, "Introduction to Radiation Detectors and Electronics - Lecture notes Physics 198," Spring Semester 1999.

[65] S. Hancock *et al.*, "Energy-loss distributions for single particles and several particles in a thin silicon absorber," *Nucl. Instrum. Meth. B*, vol. 1, no. 1, pp. 16 – 22, 1984. [Online]. Available: http://www.sciencedirect.com/science/article/pii/0168583X84904725

[66] P. La Rocca and F. Riggi, "Absorption of beta particles in different materials: an undergraduate experiment," *European Journal of Physics*, vol. 30, no. 6, p. 1417, 2009. [Online]. Available: http://stacks.iop.org/0143-0807/30/i=6/a=019

USC UNIVERSIDADE DE SANTIAGO DE COMPOSTELA

[67] E. Currás Rivera, "Advanced silicon sensors for future collider experiments," Ph.D. thesis, Universidad de Cantabria, 2017. [Online]. Available: https://cds.cern.ch/record/2291517

[68] AIDA project. [Online]. Available: http://aida2020.web.cern.ch/

[69] F. Ravotti *et al.*, "The Beam Profile Monitoring System for the CERN IRRAD Proton Facility," no. AIDA-2020-CONF-2016-005, p. 4, Oct 2016. [Online]. Available: https://cds.cern.ch/record/2235850

[70] PS IRRAD Proton Facility, CERN. [Online]. Available: https://ps-irrad.web.cern.ch/

[71] I. Mateu *et al.*, "NIEL hardness factor determination for the new proton irradiation facility at CERN," *AIDA-2020-SLIDE-2016-002*, Jun 2016. [Online]. Available: https://cds.cern.ch/record/2162852

[72] V. Cindro, "Transnational access to TRIGA Mark III reactor," presented at the *AIDA Final Meeting*, CERN, Geneva, Switzerland, 2014.

[73] Jožef Stefan Institute webpage for the AIDA2020 project. [Online]. Available: http://aida2020.web.cern.ch/content/jsi

[74] ATLAS Collaboration, "ATLAS Phase-II Upgrade Scoping Document," CERN, Geneva, Tech. Rep. CERN-LHCC-2015-020. LHCC-G-166, Sep 2015. [Online]. Available: https://cds.cern.ch/record/2055248

[75] K. Grimm *et al.*, "Primary vertex reconstruction at the ATLAS experiment," CERN, Geneva, Tech. Rep. ATL-SOFT-PROC-2017-051. 4, Feb 2017. [Online]. Available: https://cds.cern.ch/record/2253428

[76] H. F.-W. Sadrozinski, A. Seiden, and N. Cartiglia, "4D tracking with ultra-fast silicon detectors," *Reports on Progress in Physics*, vol. 81, no. 2, p. 026101, 2018. [Online]. Available: http://stacks.iop.org/0034-4885/81/i=2/a=026101

[77] C. Tully, "Hadron Collider Environment," presented at the 40th SLAC Summer Institute, SLAC National Accelerator Laboratory, California, USA, 2012. [Online]. Available: https://indico.cern.ch/event/200595/contributions/381689/

[78] A. Holzner, "78 reconstructed vertices in event from high-pileup run 198609," Sep 2012, CMS Collection. [Online]. Available: https://cds.cern.ch/record/1479324

[79] L. Gray, "4 Dimensional Trackers," presented at Connecting The Dots/Workshop on Intelligent Trackers, LAL-Orsay, France, 2017. [Online]. Available: https://indico.cern.ch/event/577003/contributions/2476434/

[80] M. Fiorini *et al.*, “4D fast tracking for experiments at the High Luminosity LHC,” in *Proceedings of the 25th International Workshop on Vertex Detectors: La Biodola, Isola d’Elba, Italy, September 26-30, 2016 — PoS(Vertex 2016)* , vol. 287, 2017, p. 067. [Online]. Available: https://pos.sissa.it/287/067/pdf

[81] N. Neri *et al.*, “4D fast tracking for experiments at high luminosity LHC,” *Journal of Instrumentation*, vol. 11, no. 11, p. C11040, 2016. [Online]. Available: http://stacks.iop.org/1748-0221/11/i=11/a=C11040

[82] N. Cartiglia *et al.*, “Performance of ultra-fast silicon detectors,” *Journal of Instrumentation*, vol. 9, no. 02, p. C02001, 2014. [Online]. Available: http://stacks.iop.org/1748-0221/9/i=02/a=C02001

[83] [Online]. Available: https://commons.wikimedia.org/wiki/File:Constant_fraction_1.svg

[84] N. Cartiglia *et al.*, “Tracking in 4 dimensions,” *Nucl. Instrum. Meth. A*, vol. 845, pp. 47 – 51, 2017, proceedings of the Vienna Conference on Instrumentation 2016. [Online]. Available: http://www.sciencedirect.com/science/article/pii/S0168900216304715

[85] N. Cartiglia *et al.*, “First results on the timing resolution properties of LGAD,” presented at the *25th RD50 Workshop*, CERN, Geneva, Switzerland, 2014.

[86] A. Rivetti, “Fast front-end electronics for semiconductor tracking detectors: Trends and perspectives,” *Nucl. Instrum. Meth. A*, vol. 765, pp. 202 – 208, 2014, Proceedings of the 9th International “Hiroshima” Symposium on Development and Application of Semiconductor Tracking Detectors. [Online]. Available: http://www.sciencedirect.com/science/article/pii/S016890021400374X

[87] Y. Okuto and C. R. Crowell, “Ionization coefficients in semiconductors: A nonlocalized property,” *Phys. Rev. B*, vol. 10, pp. 4284–4296, Nov 1974. [Online]. Available: https://link.aps.org/doi/10.1103/PhysRevB.10.4284

[88] R. J. McIntyre, “A new look at impact ionization-Part I: A theory of gain, noise, breakdown probability, and frequency response,” *IEEE Transactions on Electron Devices*, vol. 46, no. 8, pp. 1623–1631, Aug 1999.

[89] P. Yuan *et al.*, “A new look at impact ionization-Part II: Gain and noise in short avalanche photodiodes,” *IEEE Transactions on Electron Devices*, vol. 46, no. 8, pp. 1632–1639, Aug 1999.

[90] D. R. Decker and C. N. Dunn, “Temperature dependence of carrier ionization rates and saturated velocities in silicon,” *Journal of Electronic Materials*, vol. 4, no. 3, pp. 527–547, Jun 1975. [Online]. Available: https://doi.org/10.1007/BF02666234

USC UNIVERSIDADE DE SANTIAGO DE COMPOSTELA

[91] I. Tapan *et al.*, “Avalanche photodiodes as proportional particle detectors,” *Nucl. Instrum. Meth. A*, vol. 388, no. 1, pp. 79 – 90, 1997. [Online]. Available: http://www.sciencedirect.com/science/article/pii/S0168900297003161

[92] A. Staiano *et al.*, “Development of Ultra-Fast Silicon Detectors for 4D tracking,” *Journal of Instrumentation*, vol. 12, no. 12, p. C12012, 2017. [Online]. Available: http://stacks.iop.org/1748-0221/12/i=12/a=C12012

[93] H.F.-W. Sadrozinski *et al.*, “Ultra-fast silicon detectors (UFSD),” *Nucl. Instrum. Meth. A*, vol. 831, pp. 18 – 23, 2016, proceedings of the 10th International “Hiroshima” Symposium on the Development and Application of Semiconductor Tracking Detectors. [Online]. Available: http://www.sciencedirect.com/science/article/pii/S0168900216301279

[94] H.-W. Sadrozinski *et al.*, “Low-Gain Avalanche Detectors,” presented at the 2014 IEEE Nuclear Science Symposium and Medical Imaging Conference (NSS/MIC), Seattle, USA, 2014. [Online]. Available: http://rd50.web.cern.ch/rd50/doc/talks/2014-11-IEEE-2014-LGAD-poster-4%203-sm.pdf

[95] V. Greco *et al.*, “Silicon Devices Optimised for Avalanche Multiplication,” in *Proceedings of the 23rd International Workshop on Vertex Detectors: Doksy, Czech Republic, September 15-19, 2014 — PoS(Vertex 2014)* , vol. 227, 2015, p. 031. [Online]. Available: http://pos.sissa.it/archive/conferences/227/031/Vertex2014_031.pdf

[96] N. Cartiglia *et al.*, “Design optimization of ultra-fast silicon detectors,” *Nucl. Instrum. Meth. A*, vol. 796, pp. 141 – 148, 2015, proceedings of the 10th International Conference on Radiation Effects on Semiconductor Materials Detectors and Devices. [Online]. Available: http://www.sciencedirect.com/science/article/pii/S0168900215004982

[97] V. A. K. Temple, “Junction termination extension (JTE), A new technique for increasing avalanche breakdown voltage and controlling surface electric fields in P-N junctions,” in *1977 International Electron Devices Meeting*, vol. 23, 1977, pp. 423–426.

[98] M. McClish *et al.*, “Characterization of very large silicon avalanche photodiodes,” in *IEEE Symposium Conference Record Nuclear Science 2004.*, vol. 2, Oct 2004, pp. 1270–1273 Vol. 2.

[99] R. Farrell *et al.*, “Radiation detection performance of very high gain avalanche photodiodes,” *Nucl. Instrum. Meth. A*, vol. 353, no. 1, pp. 176 – 179, 1994. [Online]. Available: http://www.sciencedirect.com/science/article/pii/0168900294916322

[100] F. Richard and V. Kofi, “Large Area Semiconductor Detector With Internal Gain,” U.S. Granted Patent US 7 268 339 B1, 09 11, 2007. [Online]. Available: https://lens.org/101-236-976-912-814

[101] International Atomic Energy Agency, *Neutron Transmutation Doping of Silicon at Research Reactors*. Vienna: International Atomic Energy Agency, 2012, IAEA-TECDOC-1681. [Online]. Available: http://www-pub.iaea.org/books/IAEABooks/8739/Neutron-Transmutation-Doping-of-Silicon-at-Research-Reactors

[102] Radiation Monitoring Devices Inc. [Online]. Available: http://rmdinc.com/

[103] M. McClish, private communication, 2016.

[104] C. Gallrapp *et al.*, "TCT measurements on neutron and proton irradiated LGAD pad sensors," presented at the *26th RD50 Workshop*, Santander, Spain, 2015.

[105] V. Eremin, E. Verbitskaya, and Z. Li, "The origin of double peak electric field distribution in heavily irradiated silicon detectors," *Nucl. Instrum. Meth. A*, vol. 476, no. 3, pp. 556 – 564, 2002, proc. of the 3rd Int. Conf. on Radiation Effects on Semiconductor Materials, Detectors and Devices. [Online]. Available: http://www.sciencedirect.com/science/article/pii/S0168900201016424

[106] G. Kramberger *et al.*, "Effects of irradiation on LGAD devices with high excess current," presented at the *25th RD50 Workshop*, Geneva, Switzerland, 2014.

[107] M. Fernández García, M. Moll, and S. Otero Ugobono, "The Transient Current Technique: laser characterization of silicon detectors," presented at DT Training Seminars, November 30th 2017, CERN, Geneva, Switzerland. [Online]. Available: https://indico.cern.ch/event/684193/

[108] S. Otero Ugobono *et al.*, "Characterisation of HFS Detectors," presented at the *29th RD50 Workshop*, CERN, Geneva, Switzerland, 2016.

[109] G. L. Miller *et al.*, "Silicon p-n Junction Radiation Detectors," *IRE Transactions on Nuclear Science*, vol. 7, no. 2-3, pp. 185–189, June 1960.

[110] M. McClish *et al.*, "Characterization of very large silicon avalanche photodiodes," in *IEEE Symposium Conference Record Nuclear Science 2004.*, vol. 2, Oct 2004, pp. 1270–1273 Vol. 2.

[111] J. Friedrich, W. von Ammon, and G. Müller, "2 - Czochralski Growth of Silicon Crystals," in *Handbook of Crystal Growth (Second Edition)*, second edition ed., ser. Handbook of Crystal Growth, P. Rudolph, Ed. Boston: Elsevier, 2015, pp. 45 – 104. [Online]. Available: http://www.sciencedirect.com/science/article/pii/B978044463303300002X

[112] Float-zone process. [Online]. Available: https://slideplayer.com/slide/10797189/38/images/4/Float+Zone+Crystal+Growth.jpg

[113] Topsil GlobalWafers A/S. [Online]. Available: http://www.topsil.com/media/56109/fz_proces.jpg

[114] A. D. Mcnaught and A. Wilkinson, *IUPAC. Compendium of Chemical Terminology, 2nd ed. (the "Gold Book").* WileyBlackwell; 2nd Revised edition edition, 1997.

[115] W. Seibt, K. Sundström, and P. Tove, “Charge collection in silicon detectors for strongly ionizing particles,” *Nucl. Instrum. Meth.*, vol. 113, no. 3, pp. 317 – 324, 1973. [Online]. Available: http://www.sciencedirect.com/science/article/pii/0029554X73904965

[116] J. England, G. Field, and T. Ophel, “Z-identification of charged particles by signal risetime in silicon surface barrier detectors,” *Nucl. Instrum. Meth. A*, vol. 280, no. 2, pp. 291 – 298, 1989. [Online]. Available: http://www.sciencedirect.com/science/article/pii/0168900289909200